COLLISIONAL DEPOLARISATION OF ROTATIONAL ANGULAR MOMENTUM IN THE OH RADICAL

GRANT PATERSON

(Submitted for the Degree of Doctor of Philosophy)

HERIOT-WATT UNIVERSITY
SCHOOL OF ENGINEERING AND PHYSICAL SCIENCES
MARCH, 2011

The copyright in this thesis is owned by the author. Any quotation from the thesis or use of any of the information contained in it must acknowledge this thesis as the source of the quotation or information.

Declaration

I hereby declare that the work presented in this entirely my own, except where due acknowledgement has been made to the work of others, and has not been presented previously, in whole or part, for any other degree or professional qualification.

---------- ----------

(Candidate) *(Date)*

ACKNOWLEDGEMENTS

First of all, I would like to thank both my supervisors in the same regard, Prof Ken McKendrick, for his guidance, extraordinary patience and ability to convey complex concepts on understandable terms; never failing to implant the physical picture. Dr Matt Costen, amongst many other examples, for his invaluable contributions to the PS experiments, showing me the laser alignment 'ropes' and re-wiring my LabVIEW routines so they actually run. Thanks to both of you for the numerous hours spent suggesting additions and alterations to this thesis, and also for your support during my years in the research group, in particular, my final year.

Drs Hilary Crichton and Graham Richmond deserve particular thanks for their contributions in the construction and development of the PS experiment prior to me joining the group. Thank you also to Dr Sarandis Marinakis for his *re*-construction of the experiment in addition to running all the scattering calculations. Iain Drummond and Alan Barton are due deserved acknowledgement for their important suggestions, alterations and additions to the PS experiment.

I want to thank Dr Dave Chandler for inviting me to Livermore, CA during my final year. Dr Jeffery Kay was an awesome host, colleague and friend during my time at Sandia National Laboratories.

The 5 enjoyable years I spent in the group saw the coming and going of various members each of whom have played their role (however small) during my PhD journey. In order of appearance those are: Dr Sven Kohler, Dr Azhagamnai Alagappan, Dr Mhairi Allan, Dr Paul Bagot, Iain Ballingall, Carla Waring, Dr Muthulingam Suresh, Stephen McGurk and Kerry King. There have also been a number of project students that have passed on 'my watch' so-to-speak. I thank them for their contributions to the research project and wish them all the best in the future.

Last, I want to thank some friends and family that have provided priceless support throughout my life and various (necessary) social events during my time at Heriot-Watt and when writing this thesis. So, thanks to: Mr and Mrs McComb for your awesome entertaining and obviously enjoying ours; the in-laws for meals-out, parties and holidays; Mum, Dad and my sister Lisa for literally everything; and my wife(!), Mrs P, for all your love. Carolanne is second only to me in feeling relief that this thesis is now complete.

Thank you all.

Abstract

Polarisation Spectroscopy (PS) has been used as a novel approach for measuring the collisional removal of bulk rotational orientation and alignment in OH (X $^2\Pi_{3/2}$, $v = 0$, $j = 1.5 - 6.5$, e) and OH (A $^2\Sigma^+$, $v = 1$, $N = 1 - 5$, f_1). Both one-colour degenerate PS (OCPS) and two-colour PS (TCPS) have been exploited. TCPS provides a route to measuring thermal rate constants (298 K) for the collisional evolution of rotational polarisations in *unique* rotational quantum states.

For OH (X), the dependence on the decay of the PS signal was investigated with a number of collision partners: He, Ar, Xe N_2 and O_2. The ability to remove PS signals increases across the series of noble gases He < Ar < Xe. In all cases the measured rate constant for loss of alignment is larger than that for orientation. This provides conclusive evidence that *elastic depolarisation* (the elastic redistribution of m_j-sublevels) contributes to the loss of PS signals. The efficiency of this contribution is found to be modest for He, but significant for Ar and Xe. Comparison of the PS measurements with quantum scattering calculations assists in the evaluation of the magnitude of elastic depolarisation for the atomic partners and also provides a rigorous test of the potential energy surfaces describing their interaction. Intriguing differences are found between the kinematically similar N_2 and O_2. A detailed cross comparison between colliders, comparison of the measurements to the potential energy surface and independent theoretical work suggest that the weaker long-range attractive forces play a significant role in elastic depolarisation.

The dynamics of OH (A) was measured with He and Ar only. PS experiments were compared to independent experimental and theoretical work carried out in parallel to this research. Distinctively different j-dependent trends for the removal of bulk rotational polarisations are observed for OH (X) + Ar and OH (A) + Ar. This comparative study emphasises the role of the attractive limbs of the potential energy surface in mediating elastic depolarisation.

Table of Contents

Chapter 1

Introduction

1.1 Important Concepts

A molecular collision occurs when molecular or atomic partners are sufficiently close to experience a force. The outcome of the encounter will depend on a number of factors, which include: the nature and strength of the force; the relative motion and orientation of the approaching partners; their internal energy distributions; and the identity of the species involved [1]. A special type of molecular collision is a chemical reaction, whereby molecular bonds are broken and new bonds form. More likely however, is an exchange of energy. Energy transfer (ET) is typically grouped into hierarchical classifications based on the degree of freedom, which are, in terms of decreasing complexity: electronic (EET), vibrational (VET) and rotational (RET). Combinations of these are possible and are collectively termed as *inelastic* collisions; they all progress with a change of internal energy, accompanied by a change of translational energy such that energy is conserved overall. Collisions which occur with only a change in velocity and/or plane of rotation without altering the internal energy distribution of the partners involved are termed *elastic*.

In the gas-phase, ET between molecules contributes to the complex interplay of chemical and physical processes that occur in important environments, such as combustion, the atmosphere and the interstellar medium [1]. In addition, laser-based techniques used to interrogate these environments are themselves inherently sensitive to collisional processes. A detailed understanding of energy transfer is therefore necessary for the successful modelling of the above environments and, ideally, the development of predictive models. At a fundamental level this means describing completely the interaction of colliding partners. The most ‘exact’ description is a full-dimensional

potential energy surface(s) (PES(s)) constructed from quantum first principles (*ab initio*). The gradient of this landscape (for a given set of coordinates) is equal to the force acting between molecules/atoms and governs the ensuing dynamics.

Experiments which measure the dynamics of molecular collisions, i.e. the branching over product degrees of freedom, from well-defined initial conditions, serve to test such theoretical descriptions and provide information for real-world applications. An added layer of detail is obtained by measuring the 'directional' or so-called vector properties of the system [2]. Technically these are more challenging experiments, but they provide an even deeper insight into the *anisotropy* of the interaction and thus provide a more rigorous test of state-of-the-art theoretical descriptions, in parallel to addressing fundamentally interesting questions.

The aim of the research presented here is to better understand the dynamics of molecular collisions involving important open-shell diatomics (namely OH) through the measurement of vector properties. Specifically, polarisation spectroscopy (PS) was exploited to measure the evolution of rotational angular momentum (AM) polarisations of OH in collisions with simple atomic and molecular collision partners. As such, these measurements are primarily sensitive to RET (change in the magnitude of rotational AM) and *elastic depolarisation* (change in the direction of the rotational AM).

This introductory chapter aims to address the conceptual framework for discussion and understanding of the results presented in the later chapters. It is split into two main sections: section 1.1 will introduce the concepts necessary for an understanding of the collisional dynamics of open-shell diatomic species, and section 1.2 will provide an overview of the PS technique.

1.1.1 The Hydroxyl Radical

OH is a suitable candidate for these studies because of its importance in the chemistry of gas-phase environments. Although present in low concentrations (typically 10^6 molecules cm^{-3}, or 0.1 ppt [3]), OH dominates daytime chemistry in the troposphere by removing trace constituents, and oxidising volatile organic species [3-5]. It is also ubiquitous in flames, due to incomplete combustion of organic compounds [5-7], and has astrophysical importance (e.g. OH maser emission) [8]. Experimentally, OH is easily produced *via* laser photolysis, and has accessible electronic transitions suitable

for the PS experiments. Because it is a hydride, the rovibonic transitions are also well separated [9]. In addition, the collision dynamics of OH with atomic and diatomic partners are theoretically tractable. Knowledge of the rotational structure and spectroscopy is vital to understanding the possible rotational energy processes.

Spectroscopy

Many of the laser-based techniques used to probe OH make use of the *A – X* electronic transition [10]. The ground electronic state of OH has a $(3\sigma^2)(\pi^3)$ valence electron configuration ($X^2\Pi$) and the first excited state has a $(3\sigma^1)(1\pi^4)$ electron configuration ($A^2\Sigma^+$). These two states are separated by ~ 32 000 cm^{-1} (figure 1). The total rotational angular momentum *(j)* is therefore not simply the nuclear rotation of the molecular framework *(R)*, but also involves the coupling of electronic orbital angular momentum *(L)*, and electronic spin *(S)*. These AM can couple in different ways, and are classified by limiting coupling schemes, known as the Hund's cases [11].

OH in its ground electronic state, at low-*j*, is best described by Hund's coupling case (a), where *L* couples strongly to *S*. The projection of these AM onto the internuclear axis are labelled Λ (= ±1) and Σ (= ±1/2), respectively. Their sum is labelled Ω (= Λ + Σ). This spin-orbit interaction results in two spin-orbit manifolds, $^2\Pi_{3/2}$ (F_1) and $^2\Pi_{1/2}$ (F_2), that are energetically separated by 139 cm^{-1} (i.e. OH(X) is irregular). The total electronic and spin projection onto the internuclear axis in turn couples to the nuclear rotation, *R*, and provides the total rotational angular momentum, *j*. The double degeneracy of the orbital angular momentum gives rise to Λ-type doublets. Second order spin-orbit and rotational-electronic Coriolis interactions with the remote $^2\Sigma$-state lifts this degeneracy [12]. In the high-*j* limit these take the conventional symmetry labels of *A′* (symmetric) and *A″* (anti-symmetric) with respect to inversion of the electronic spatial coordinates in the plane of rotation [13] (figure 1.2). The energy splitting increases with *j*. OH (X) therefore has four fine structure levels for every rotational level, *j*.

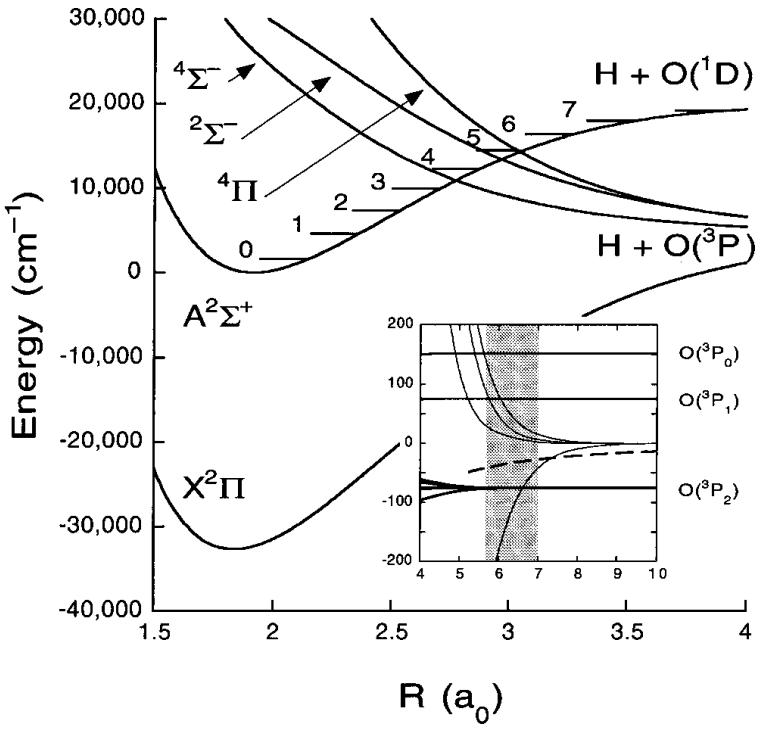

Figure 1.1: *Potential-energy curves for a selection of OH electronic states. The vibrational levels v' = 0 – 7 of the A $^2\Sigma^+$ state are indicated. Reprinted from [14].*

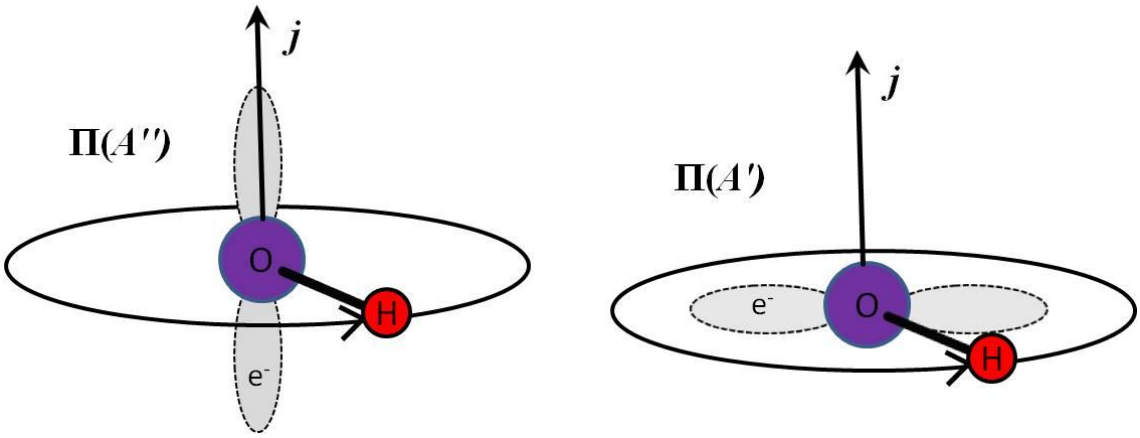

Figure 1.2: *Schematic of the Λ-doublet symmetry at high-j.*

It is common for open-shell diatomics to undergo spin-decoupling [12]. This occurs when the rotation of the molecular framework increases and the spin-rotation coupling becomes stronger than the spin-orbit coupling. The range of j over which this transition from case (a) to (b) occurs is related to the ratio A_v/B_v, where A_v and B_v are the vibrational-level dependent spin-orbit and rotational constants, respectively, (see table 1-1). For OH (X), case (a) describes the very lowest rotational levels, but an intermediate coupling case is a more accurate representation for $j \geq 2.5$. Figure 1.3 shows representative rotational ladders for OH (X) and OH (A).

OH (A) necessarily conforms to Hund's coupling case (b), because $\Lambda = 0$. By definition, there is no Λ-doubling. Generally for case (b) diatomics, the total angular momentum excluding electron spin, N, is a good quantum number. For Σ states this reflects purely the nuclear rotation, R. This couples to S, providing two spin-rotation levels for every value of N, except when $N = 0$. These are labelled f_1 ($j = N + 1/2$) and f_2 ($j = N - 1/2$).

Each rotational level is assigned a symmetry label, ε (= ±1), which indicates the total parity, i.e. symmetric or anti-symmetric with respect to an inversion operation on the molecular wave-function. This label alternates with j and the nearly degenerate Λ-doublets of the same j have opposite parity. Rotational levels with half integer j (true for OH) are labelled e if total parity is $+(-1)^{j-1/2}$ and f if they have total parity $-(-1)^{j-1/2}$ [13].

The one-photon selection rules, obtained by evaluating the matrix elements of the OH electric dipole moment, determine if rovibronic transitions are allowed or forbidden. For OH, two general selection rules apply. The first governs the change in j during a transition, and the second permits transitions connecting states of opposite parity; transitions between states of the same parity are forbidden.

i. $\Delta j = 0, \pm 1.$

ii. $+ \leftrightarrow -$

For Hund's case (a) and (b) systems the following selection rules hold:

iii. $\Delta \Lambda = 0, \pm 1.$

iv. $\Delta S = 0$

i.e. electronic bands connecting Σ – Σ and Σ – Π are allowed but Σ – Δ transitions are forbidden. Electronic transitions are also forbidden if the spin multiplicity is changed.

The $A - X$ electronic band of OH has, as a result of the selection rules, twelve branches; six main branches and six sub-branches. All twelve transitions are shown in figure 1.3 and they are labelled by convention:

$$^{\Delta N}\Delta j_{f\,F}(j)$$

For the main branches the superscript $\Delta N = \Delta j$ and $f = F$. In this case, the labels associated to the spectroscopic transition may be simplified by dropping the superscript

and having a single value for the subscript. For example, ${}^{P}P_{11}(j)$ may be simplified to $P_1(j)$. For the sub-branches $\Delta N \neq \Delta j$ and $f \neq F$. The rotational quantum number quoted in parenthesis represents the rotational level in the ground electronic state resonant with the transition.

Table 1-1: *Spectroscopic constants for the OH radical. The parameters are:* [a] *equilibrium internuclear distance / Å,* [b] *electronic term energy,* [c] *harmonic oscillator frequency,* [d] *equilibrium rotational constant,* [e] *spin-orbit coupling constant,* [f] *spin-rotation coupling constant. All parameters other than (a), which has units of distance, are measured in* cm^{-1}. *Data taken from ref. [11].*

Spectroscopic Property	***OH ($X^2\Pi$)***	***OH ($A^2\Sigma^+$)***
[a] r_e	*0.96966*	*1.0121*
[b] T_e	—	*32 687*
[c] ω_e	*3 737.8*	*3 178.4*
[d] B_e	*18.91*	*17.36*
[e] A_e	*-139.21*	—
[f] γ_e	—	*0.201*

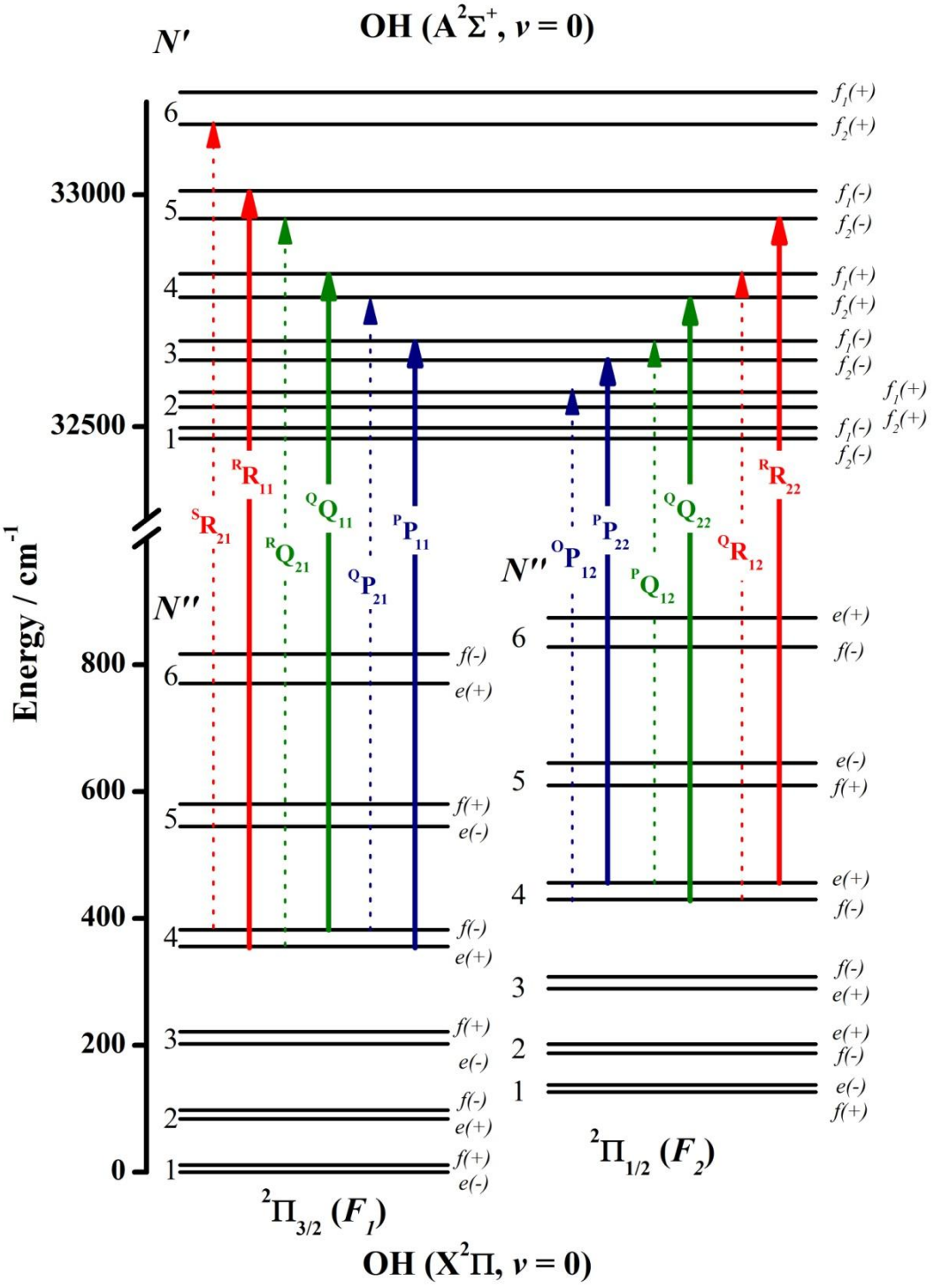

Figure 1.3: *Rotational energy level diagram for OH ($X\ ^2\Pi$, $v = 0$) and OH ($A\ ^2\Sigma^+$, $v = 0$). All levels are labelled by quantum number N. For OH (X), j = (N + ½) for the F_1 spin-orbit manifold and (N – ½) for the F_2 spin-orbit manifold. For OH (A), the spin-rotation manifolds represent j = (N + ½) (f_1) and (N – ½) (f_2). The twelve spectroscopic branches of the OH (A – X) (0,0) electronic band are shown: six main branches(solid arrows) and six sub-branches (broken arrows). The Λ-doublet splitting in OH (X) and the spin-rotation splitting on OH (A) are considerably exaggerated.*

1.1.2 The Potential Energy Surface

The potential energy surface (PES) describes the potential energy of the system over all nuclear coordinates (within the Born-Oppenheimer approximation), and thus also describes the forces that act between partners as they approach, collide, and then separate. The PES is required to perform scattering calculations, which may be used to predict collisional properties, for example, RET rate constants. Generally there are two main approaches: exact QM scattering calculations (at least, for A + BC collisions) or more approximate quasi-classical trajectory (QCT) calculations, which employ Newtonian mechanics. Since the QM scattering calculations are exact, then differences between these predictions and experimental observations would imply that there are inaccuracies in the PES.

For an atomic-diatomic system (relevant to the majority of the work in this thesis) the PES can be expressed as a function of three Jacobi co-ordinates: ***r*** (the internuclear axis of the diatomic), ***R*** (the vector connecting the centre of the atom and the centre-of-mass of the diatom), and θ (the angle between the vectors ***r*** and ***R***). For the OH-Rg systems discussed in this thesis $\theta = 0°$ always corresponds to the linear O-H-Rg geometry, while $\theta = 180°$ refers to the linear H-O-Rg geometry. In construction of the PES ***r*** is usually kept fixed at the mean intranuclear distance for a given vibrational level, to reduce the computational expense. To describe the electrostatic interaction, the dipole and quadrupole moments, as well as the dipole and quadrupole polarisabilities for OH, are taken into account. The latter two are included for the atom.

For OH ($X^2\Pi$), the perturbation of an approaching partner will lift the asymptotic symmetry of the diatomic, resulting in two adiabatic surfaces of $^2A'$ and $^2A''$ symmetry with respect to reflection of the electronic wave-function in the triatomic plane [15]. This is analogous to the symmetry labels of the Λ-doublet levels. For performing scattering calculations it is convenient to convert the PESs into a diabatic representation [15]. The corresponding linear combinations are given below:

$$V_{SUM}(R,\theta) = 0.5\left[V_{A''}(R,\theta) + V_{A'}(R,\theta)\right]$$

(Equation 1-1)

$$V_{DIFF}(R,\theta) = 0.5\left[V_{A''}(R,\theta) - V_{A'}(R,\theta)\right]$$

(Equation 1-2)

The V_{SUM} and V_{DIFF} defined in equations 1-1 and 1-2 are often referred to as the average and half-difference potentials, respectively. To construct $V_{A'}$ and $V_{A''}$, interaction energies are calculated for a finite grid of the nuclear coordinates, $\boldsymbol{R}$ and θ. However, for the scattering calculations, it is better to have a functional form for the PESs which are continuous. Equations 1-3 and 1-4 are a standard way of expressing the V_{SUM} and V_{DIFF} PESs [16-18]. Separating the radial part of the potential from the angular part also provides a useful tool for evaluating which angular components contribute to the collision dynamics (see section 1.1.3).

$$V_{\mathrm{SUM}}(R,\theta) = \sum_{\lambda=0}^{\lambda=\lambda_{\mathrm{MAX}}} V_{\lambda 0}(R) d_{00}^{\lambda}(\cos\theta)$$

(Equation 1-3)

$$V_{\mathrm{DIFF}}(R,\theta) = \sum_{\lambda=2}^{\lambda=\lambda_{\mathrm{MAX}}} V_{\lambda 2}(R) d_{20}^{\lambda}(\cos\theta)$$

(Equation 1-4)

Here $d_{mm'}^{\lambda}(\cos\theta)$ are reduced rotation matrices and are related to the Legendre polynomials, $P_{\lambda}(\cos\theta)$ [19]. λ_{MAX} is limited to the number of angles, θ, the PES was initially calculated for: (n-1), where n represents the number of angles.

For OH ($A^2\Sigma^+$) only one PES is required to describe the interaction with an atomic partner. Again this can be decomposed using reduced rotation matrices [17]:

$$V_{\Sigma}(R,\theta) = \sum_{\lambda=0}^{\lambda=\lambda_{\mathrm{MAX}}} V_{\lambda 0}(R) d_{00}^{\lambda}(\cos\theta)$$

(Equation 1-5)

For $^2\Sigma$ states with a neighbouring $^2\Pi$-state, there is an additional coupling PES for the interaction between the $^2\Sigma(A')$ and $^2\Pi(A')$ PESs [20]. This would be significant when the separation of two electronic states is small, for example CN ($X^2\Sigma^+$ and $A^2\Pi$) [20]. For OH, where the separation of the ground and first excited electronic states is ~ 32 000 cm^{-1}, this term is negligible. This means that scattering calculations performed on the OH (A) + Rg system may be reliably treated using only one PES and likewise OH(X) + Rg systems may be reliably treated using V_{SUM} and V_{DIFF} alone.

1.1.3 Rotational Energy Transfer

In comparison to EET and VET, RET is the most facile of inelastic processes, because of the relatively small energy gap between rotational quantum states in comparison to thermal energies. Consequently, RET plays an important role in various gas-phase transport phenomena. Experimentally, researchers measure rate constants (or cross-sections) for either a state-to-state process, k_{if}, where the subscript indicates the initial and final level, or the rate constant associated with total population removal from an initially populated level, k_{POP}:

$$k_{POP,i} = \sum_f k_{if} \ .$$

(Equation 1-6)

The rate constants may be converted to velocity averaged cross-sections, which accounts for the frequency of collisions:

$$\langle \sigma \rangle = \frac{k}{\langle v_{coll} \rangle}$$

(Equation 1-7)

$$\langle v_{coll} \rangle = \left(\frac{8 k_b T}{\pi \mu} \right)^{1/2}$$

(Equation 1-8)

Throughout this thesis the relationship in equation 1-7 will be used frequently. $\langle v_{coll} \rangle$, defined in equation 1-8, is the relative mean collision velocity. Here k_b is the standard

Boltzmann constant, T is the temperature of the system and μ is the reduced mass: $[m_1m_2/(m_1+m_2)]$.

Classically, the origin of RET comes from the coupling of the orbital motion of the colliding partners to the rotational motion of the diatomic molecule. The magnitude of orbital AM available is given by the following simple relationship [1]:

$$L = \mu v_{coll} b = b\sqrt{2E_{coll}\mu}$$

(Equation 1-9)

Here μ is the reduced mass of the collision system, v_{coll} and E_{coll} are the centre-of-mass collision velocity and energy, respectively, and b is the impact parameter – the hypothetical 'miss' distance between a pair of collision partners unperturbed from their initial trajectories.

This, together with research that is highlighted in section 1.1.4, forms the basis of a linear momentum (LM) – angular momentum (AM) model developed by McCaffery and co-workers [21,22], which qualitatively predicts trends in RET for single collision partners. The model takes account of only the repulsive core of the PES, since the collisions are assumed to be impulsive and sudden in nature. The anisotropy of the repulsive wall is treated using multiple ellipsoids representing contours of PE. For a given ellipsoid and atom-diatom collision trajectory, the collision is portrayed using the vector picture shown in figure 1.4. This model imposes AM and energy constraints on the degree of RET (Δj) that may be observed for a given system. In general, the larger the torque arm the larger the degree of RET. Although this model is useful for assessing whether a collision system is energy or AM constrained, it fails to predict the correct absolute magnitude of RET processes and even relative differences between various collision partners [23]. It is not suitable to describe the scattering of open-shell species, where the attractive part of the PES may become important, and interference between multiple PESs may dictate RET propensities. For this reason it is best to establish a QM treatment based on the PES coupling the initial and final quantum states.

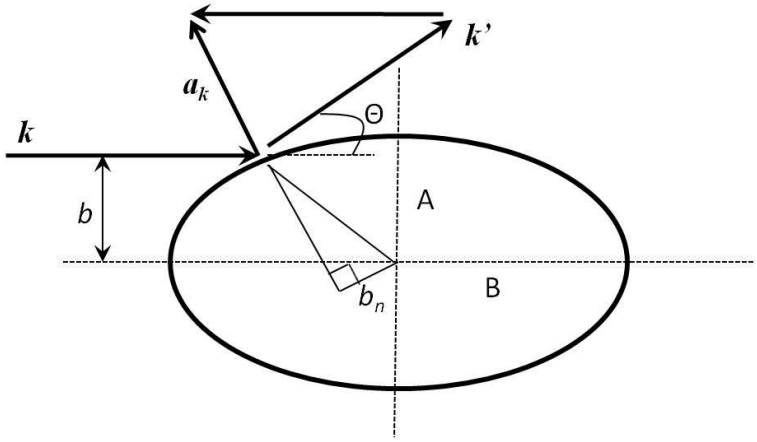

Figure 1.4: *Representation of the variables in this 2-D vector picture of an atom-diatom collision. (A – B) represents the anisotropy of the hard ellipsoid,* **k** *denotes linear momentum, b is the impact parameter,* b_n *is the effective impact parameter (torque arm) and* $\boldsymbol{a_k}$ *is the kinematic apse (=****k'-k****). Adapted from [22].*

QM Formalism

The convenience of the diabatic representation of the PES for interpreting the scattering dynamics of open-shell species with spherical partners becomes clearer when considering the formalism developed by Alexander *et al.* for describing the rotational scattering of $^2\Pi/^2\Sigma$ diatomics with structure-less ^{1}S partners [24-26]. QM scattering calculations solve a set of coupled differential equations (the close-coupled (CC) equations) to calculate the probability for molecular scattering between initial and final quantum states. The software used for the calculations discussed in chapter 5 was the Hibridon suite of codes [27]. The CC equations essentially have a kinetic energy term and a potential term. The first-order potential matrix elements in the equations, which connect the initial and final (labelled by convention with primes) rotational levels, take the form of equation 1-10 for $^2\Pi$ (case (a)) + ^{1}S systems [24]. It should be noted that in addition to these potential matrix elements there are additional higher order terms which contribute to the *exact* QM scattering calculation.

$$V^{JM}_{j'\Omega'\varepsilon'L',\, j\Omega\varepsilon L}(R) = (-1)^{J-\Omega+j+j'}[(2L+1)(2L'+1)(2j+1)(2j'+1)]^{1/2}$$

$$\times \sum_{\lambda} \begin{pmatrix} L' & \lambda & L \\ 0 & 0 & 0 \end{pmatrix} \begin{Bmatrix} j' & L' & J \\ L & j & \lambda \end{Bmatrix} \times F^{\lambda}_{j'\varepsilon',\, j\varepsilon}$$

$$\times \left[\begin{pmatrix} j' & \lambda & j \\ -\Omega' & 0 & \Omega \end{pmatrix} V_{\lambda 0}(R) - \varepsilon \begin{pmatrix} j' & \lambda & j \\ -\Omega' & 2 & -\Omega \end{pmatrix} V_{\lambda 2}(R) \right]$$

(Equation 1-10)

$$F^{\lambda}_{j'\varepsilon',\, j\varepsilon} = 1/2 \times [1 - \varepsilon\varepsilon'(-1)^{(j+j'+\lambda)}]$$

(Equation 1-11)

Here, j, Ω, and ε denote the diatom's total rotational angular momentum, spin-orbit manifold and parity, respectively. L, J and M represent the orbital angular momentum, total angular momentum and projection of the triatomic system, respectively, in a space-fixed frame. The expansion coefficients, $V_{\lambda\mu}$, are the same as those found in equations 1-3 and 1-4 and λ is the order of the Legendre moment. Wigner 3-j and 6-j symbols are represented by $(:::)$ and $\{:::\}$, respectively.

There are several important implications of this description in terms of the predicted propensities for RET. (Note: although the measurements presented in this thesis do not resolve individual product levels, the discussion of them will make use of these outcomes.) First, the 3-j symbol coefficient of $V_{\lambda 0}(R)$ in equation 1-10 will only be non-zero if $\Omega = \Omega'$, since the projections must sum to zero. Likewise, the 3-j symbol attached to $V_{\lambda 2}(R)$ will only be non-vanishing if $\Omega \neq \Omega'$. The implication of this is that, in the limit of pure Hund's case (a), the V_{SUM} potential will control the scattering *within* the same spin-orbit manifold and V_{DIFF} will promote transfer *between* spin-orbit manifolds. Second, the phase factor, F, expressed in equation 1-11, determines which λ-components of the expanded PES couple levels of the same, or different, total parity. Table 1-2 summarises the different combinations. In addition, the following general rules hold: $\sigma\,(e \rightarrow e) = \sigma\,(f \rightarrow f)$ and $\sigma\,(e \rightarrow f) = \sigma\,(f \rightarrow e)$. So, for experiments which begin with initial rotational level, j, and with equal Λ-doublet populations, the final product level will also have equal Λ-doublet populations.

Table 1-2: *A given rotational transition, Δj (= j-j′) can occur with conservation (ε = ε′) or breaking (ε ≠ ε′) of the total parity. The elements of this table show values of λ in the expanded PES which are non-zero and thus contribute to the scattering amplitude.*

	Non-Zero Coupling	
Δj	***ε = ε′***	***ε ≠ ε′***
Even	*λ = even*	*λ = odd*
Odd	*λ = odd*	*λ = even*

However, as noted above in section 1.1.1, OH (X) does not conform to pure Hund's case (a) at rotational levels populated in a thermal sample. Instead, OH (X) is better described by an intermediate Hund's case (a)/(b) indicated by the ratio: $Y = A_v/B_v$. In this case it is more correct to express the molecular wave-functions as linear combinations of the case (a) wave-functions due to the Ω-states being mixed by the spin-rotation term in the Hamiltonian [25]:

$$\left| jmF_i\varepsilon \right\rangle = \sum_{\Omega} C^{\Omega}_{jF_i\varepsilon} \left| jm\Omega\varepsilon \right\rangle$$

(Equation 1-12)

The potential matrix elements now take on the modified form:

$$V^{JM}_{j'\Omega'\varepsilon' L', j\Omega\varepsilon L}(R) = (-1)^{J+j+j'}[(2L+1)(2L'+1)(2j+1)(2j'+1)]^{1/2}$$

$$\times \sum_{l} \begin{pmatrix} L' & \lambda & L \\ 0 & 0 & 0 \end{pmatrix} \begin{Bmatrix} j' & L' & J \\ L & j & \lambda \end{Bmatrix}$$

$$\times F^{\lambda}_{j'\varepsilon', j\varepsilon}[A^{\lambda}_{j'\Omega'\varepsilon', j\Omega\varepsilon} V_{\lambda 0}(R) + \varepsilon B^{\lambda}_{j'\Omega'\varepsilon', j\Omega\varepsilon} V_{\lambda 2}(R)]$$

(Equation 1-13)

$$A^{\lambda}_{j'F_i'\varepsilon', jF_i\varepsilon} = C^{1/2}_{j'\Omega'\varepsilon'} C^{1/2}_{j\Omega\varepsilon} \begin{pmatrix} j' & \lambda & j \\ -1/2 & 0 & 1/2 \end{pmatrix} - C^{3/2}_{j'\Omega'\varepsilon'} C^{3/2}_{j\Omega\varepsilon} \begin{pmatrix} j' & \lambda & j \\ -3/2 & 0 & 3/2 \end{pmatrix}$$

(Equation 1-14)

$$B^{\lambda}_{j'F_i'\varepsilon',JF_i\varepsilon} = C^{3/2}_{j'\Omega'\varepsilon'}C^{1/2}_{j\Omega\varepsilon}\begin{pmatrix} j' & \lambda & j \\ -3/2 & 2 & -1/2 \end{pmatrix} - C^{1/2}_{j'\Omega'\varepsilon'}C^{3/2}_{j\Omega\varepsilon}\begin{pmatrix} j' & \lambda & j \\ -1/2 & 2 & -3/2 \end{pmatrix}$$

(Equation 1-15)

Now V_{SUM} and V_{DIFF} both contribute to the scattering within and between spin-orbit manifolds weighted by the coefficients A^{λ} and B^{λ}. Note that the propensities in table 1-2 still hold. However, interference between scattering on the two surfaces may now result in unequal Λ-doublet populations, even when starting from initial conditions where they are equally populated.

The potential matrix elements have also been described for a collision between a $^2\Sigma$-diatom and a structureless partner [26]. The formalism is simpler than that for degenerate electronic states, because there is only one PES which characterises the interaction. The main outcome of this, which will be useful for the discussion of results presented in chapter 6, is that specific PES components are responsible for *j*-changing and parity changing events, similar to that for $^2\Pi$ states. In fact, those outcomes for $^2\Pi$, presented in table 1-2, also hold true for $^2\Sigma$ states.

Spin Spectator Model

One important concept to consider for the scattering of $^2\Sigma^+$ diatoms with structureless partners is that the electronic spin may be reliably treated as a spectator to the collision dynamics. This has been used by a number of researchers when constructing theoretical formalisms for the rotational scattering dynamics of these systems [26,28,29]. For OH (A) the spin rotation splitting in the lowest rotational levels is approximately ≈ 0.3 cm^{-1}. Thus, the spin rotation interaction has a frequency of approximately 10 GHz and a corresponding interaction time of 100 ps. This is two orders of magnitude longer than the collision time, which is < 1 ps, based on the relative collision velocity of OH + Ar at 298 K over a distance comparable to the range of the PES, i.e. 10 a_0. Importantly, this means that spin rotation changing collisions, within this assumption, require substantial reorientation of the nuclear rotational AM, *N* (see figure 1.5). This will become a very important point for discussing the results of chapter 6.

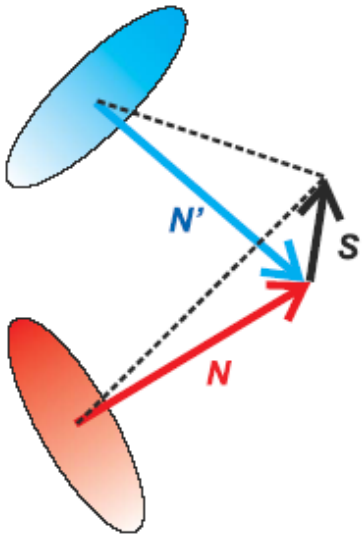

***Figure 1.5**: Illustration showing that, if electron spin is a spectator to the scattering dynamics, changes in spin-rotation state require collisions that cause significant reorientation of N. The dashed black lines indicate J and J'. Reprinted from ref. [29].*

Measuring RET

As noted already, open-shell diatomic species are present in turbulent environments such as flames. Measurements of RET may therefore be made within that environment directly using optical probes [30-32]. The advantage here is that the global RET observed is directly related to the system studied. The major disadvantage is that the measurements are heavily averaged over quantum states, velocities, collision partners, *etc*, and this makes it difficult to identify the conditions responsible for the observed process, and also to compare to theory. To learn more about individual interactions, it is better to perform measurements in more controlled environments, preferably with isolated collision partners. When investigating radical species this usually requires the *in situ* generation of the target molecule, unless it happens to be a stable radical, *e.g.* NO. Common methods of radical production are: electrical discharge [33]; chemical reaction [34-36]; and photolytic generation from a suitable precursor, which is presently the favoured method, especially with advances in laser technology. Another requirement is that the system must initially depart from equilibrium. There are two general approaches for achieving this and monitoring the subsequent RET: those using crossed molecular beams (CMBs), or those using optical-based measurements in bath-gas cells. They each measure different but complementary information and each have their pros and cons.

Molecular Beams (MBs) are produced by the supersonic expansion of a gas reservoir though a small aperture (nozzle). At the throat of the expansion the velocity becomes very anisotropic and there is also a high collision frequency, the net result being substantial cooling of the internal degrees of freedom to the lowest rotational levels in the ground electronic state and conversion of that internal energy to translation. In a CMB experiment the path of two MBs (one containing the investigated species and the other the collision partner) cross each other and the scattered products are detected. Traditionally a rotatable time-of-flight mass-spectrometer (TOF-MS) is used for detection. The arrival time of a particular mass fragment will be related to the degree of internal energy transfer as a result of the collision. In this way the *integral* (ICS) and *differential* (DCS) cross-sections can be measured even for rotationally inelastic collisions. The DCS, in this context, is a measure of the scattering probability for a given inelastic process as a function of scattering angle. The integral cross-section is the integral of this function and is related to the total scattering probability. The DCS falls into the category of vector properties, which are discussed further in section 1.1.4.

For higher resolution of the internal energy distribution in the products, CMB experiments have more recently been coupled with optical detection schemes. This is especially desirable when measuring the collision dynamics of open-shell species that contain fine-structure. The two most commonly used optical detection schemes are laser-induced fluorescence (LIF) and resonance-enhanced multi-photon ionisation (REMPI). LIF involves promoting molecules to an accessible higher lying electronic state and observing the spontaneous fluorescence. Fluorescence will only be observed when the excitation laser is resonant with a spectroscopic transition connected to populated rotational quantum states in the ground electronic state. REMPI involves the generation of ions which are accelerated toward an ion detector, for example a charged micro-channel plate (MCP). The 'resonance-enhanced' part provides the state specificity. Alternatively, the kinetic energy of the ejected photoelectron could be used as a measure of the internal energy distribution of the parent molecule (photoelectron spectroscopy).

The major limitation of the CMB technique is clearly the restriction of the initial quantum state to the lowest rotational levels in the ground electronic state. (Although, experiments have been able to state-prepare vibrationally and electronically excited levels [37,38].) This is often not well matched to the environments in which radical species exist. In addition, only *relative* collision cross-sections can be measured and not

absolute cross-sections or rate-constants. A distinct advantage however, is that the MBs are well collimated and have a narrow speed distribution, which consequently means a narrow collision energy distribution. On top of this, CMB methods allow the collision energy to be tuned by varying the crossing angle of the MBs [39], by varying parameters such as the seeding gas or reservoir pressure/temperature, or by introducing a stark decelerator [40,41]. CMB measurements can therefore provide a powerful test of theoretical calculations, especially with respect to the near threshold onset of rotational excitation.

Bath-gas (or thermal cell) experiments on the other hand measure collisional processes under *isotropic* conditions and allow the measurement of *absolute* thermal rate-constants by measuring the kinetics of the collisional process. The term bath-gas comes from the fact that the investigated molecule is studied within a bath of the collision partner. The generation of radical species will naturally lead to a state of disequilibrium and researchers have exploited this 'hot' distribution to monitor RET as the system evolves back to equilibrium [42]. Otherwise, researchers tend to allow translational and rotational moderation of the system after radical generation. Optical methods are then used to pump molecules to higher lying quantum states, e.g. rovibrational or rovibronic, and the collision dynamics within that manifold are monitored by a suitable detection scheme. When monitoring the ground electronic state a second probe laser is usually used, which is either resonant with the initially pumped level to monitor total RET removal of that state, or is resonant with a different rotational level to monitor the state-to-state cross-section or rate-constant. These schemes are commonly referred to as optical-optical double resonance methods (OODR). For monitoring the dynamics of electronically excited species the spontaneous fluorescence is usually dispersed using a monochromator. The time-dependence of the rotational populations will provide RET rates. This does require that the lifetime of the emitting state is long relative to the collision time-scale.

The disadvantages of the above approach are that the RET rates are averages over a Boltzmann distribution of thermal velocities. There is not much scope for tuning the collision energy and DCS cannot be measured. (Note: PHOTO-LOC techniques do not fall into the category of 'bath-gas' here and are referred to below.) However, this method allows more flexible state preparation and can therefore measure a vast range of initial quantum states (spectroscopy permitting) which are better matched to those found in the atmosphere or combustion environments.

What Has Been Observed?

There are several comprehensive review articles on the subject of RET, specifically for open-shell species [1,43,44]. This section aims to provide an overview of RET in diatomic molecules. Examples which highlight important RET concepts for the purposes of this thesis will be addressed.

It was established early on that RET does not follow selection rules similar to spectroscopic ones, i.e. $\Delta j = 0, \pm 1$, but rather that multiple quantum 'jumps' are allowed [44]. The probability for small Δj transitions is almost universally greater than for larger Δj transitions. This decreasing cross-section as a function of Δj usually takes on an exponential form, and is well known as the exponential energy gap scaling law [45]. It comes about due to the increased spacing between adjacent rotational energy levels as the magnitude of j increases, together with an exponentially decreasing fraction of molecules with sufficient collision energy to promote such transitions.

The plots of state-to-state cross-sections *vs.* Δj are often referred to as volcano plots for this exponential dependence. However, the exponential decay may not be a smooth function. For closed-shell homonuclear diatomics these volcano plots will possess drastic even/odd alternations, whereby all Δj = odd transitions are suppressed. The explanation for this is that the nuclear spin is a spectator in the collision and thus cannot change direction (and definitely not magnitude). For this reason only ortho – ortho, or para – para transitions are allowed. When the target molecule has electronic AM, for example Li_2 ($B^1\Pi_u$), the Λ-doublets provide a route to overcome this, but for odd Δj the parity must change and for even Δj parity must be conserved [43]. Similarly, even/odd alternations in the RET propensities for heteronuclear diatomics is a reflection of the *near*-homonuclear character of the molecule; the λ = even terms in the PES expansion dominate λ = odd terms [46]. For example, these even/odd alternations are seen in the scattering of CN [47] and NO [48] in collisions with Ar. Hydrides on the other hand rarely exhibit this character. When they do it is usually a reflection that the λ = even terms are larger in the interaction potential e.g. OH ($A^2\Sigma^+$) + He [49,50]. It is not only the state-to-state RET cross-section which drop off exponentially, but also the total removal RET cross-sections for a given initial value of j. There is often a maximum in a plot of total RET *vs* rotational quantum number, j. This is because, for the lowest rotational levels, the majority of state-to-state RET processes are endoergic.

For the above reasons those molecules with smaller rotational constants will exhibit larger ranges of $|\Delta j|$. For example, Andresen and co-workers, performing CMB experiments, observed up to $\Delta j = 13$ for NO (X, $B = 1.9$ cm^{-1}) + Ar ($E_{coll} = 443$ cm^{-1}) [46], while CMB experiments for OH (X, $B = 18.91$ cm^{-1}) + Ar ($E_{coll} = 451$ cm^{-1}) failed to observe $\Delta j > 4$ [33].

The majority of RET studies of open-shell species have restricted the collision partner to simple rare gas atoms, such as He and Ar. However, there are some examples where researchers have varied the collision partner to understand what influence this may have on the observed propensities. From equation 1-9 it may be anticipated that increasing the reduced mass may result in larger RET cross-sections, as a result of the larger orbital AM available. This is indeed what seems to be observed. Caughey and Crosley found that the average change in j in S_2 ($B^3\Sigma_u^-$, $v = 4$, $j = 41$) was larger across the noble gas series He < Ne < Ar < Kr [51,52]. Xe on the other hand was weaker than Kr. This general trend has also been noted by other researchers [43]. When diatomic collision partners are used, RET cross-section sections seem to increase considerably. Many authors attribute this to the possibility of near-resonant rotation-to-rotation pathways, but it should be borne in mind that these partners have, at least, a quadrupole moment, that may significantly contribute to the interaction potential. Indeed, polyatomic collision partners which possess dipole moments have been seen to result in remarkably large cross-sections. Dagdigian and co-workers used MB methods to measure the rotational scattering of CaCl and CaBr ($X^2\Sigma^+$) in collisions with HCl (70 Å^2), HCN (180 Å^2), SO_2 (270 Å^2) and CH_3Cl (400 Å^2) [53,54]. The cross-section specified in parenthesis represents the largest observed state-to-state cross-sections, which are always for the lowest values of Δj. This indicates that RET may not be simply predicted by hard-sphere collision models, and that longer-range attractive forces may play an important role. However, the rate of RET may not scale quite as simply as strength of the interaction potential. For example ter Meulen and co-workers measured rotational state-to-state cross sections for OH ($X^2\Pi$) + N_2 and CO [55]. Despite the OH-CO surface having two van der Waals wells, and a chemically bonded well corresponding to HOCO formation, the overall behaviour of N_2 and CO are found to be very similar.

1.1.4 Vector Properties

Over the past 20 – 30 years, vector measurements have been central to understanding the ‘chemical shape’ of reactions [56,57]. These stereodynamic measurements provide a

rigorous test of the anisotropy of the PES describing the encounter. A recent review has shown that measurements of this kind can provide very detailed information of the dynamics of non-reactive molecular collisions [2]. In particular, since they measure both the magnitude and *direction* of the molecular property in question, these vector measurements are sensitive to the *full-range* of the interaction potential, including the weaker longer-range attractive forces that are often camouflaged by measuring only the scalar properties such as those introduced in section 1.1.3. Figure 1.6 draws attention to some of the vector properties amenable to experimental test. These are: the rotational AM, $\boldsymbol{j}$, and the initial relative linear momentum, represented by the wavevector, $\boldsymbol{k}$, in the centre-of-mass frame of the collision partners. $\boldsymbol{k}$ is parallel and proportional to the initial relative velocity, $\boldsymbol{v}$, and its magnitude is: $k = (2E_T/\mu)^{1/2}/\hbar$; where μ is the reduced mass of the collision pair and E_T is the relative collision energy. The orbital AM, $\boldsymbol{l}$, is the same quantity as defined in equation 1-9 and $\boldsymbol{J}$ is the total AM, which is conserved: $\boldsymbol{J} = \boldsymbol{j} + \boldsymbol{l} = \boldsymbol{j'} + \boldsymbol{l'}$. Primes indicate post-collision products.

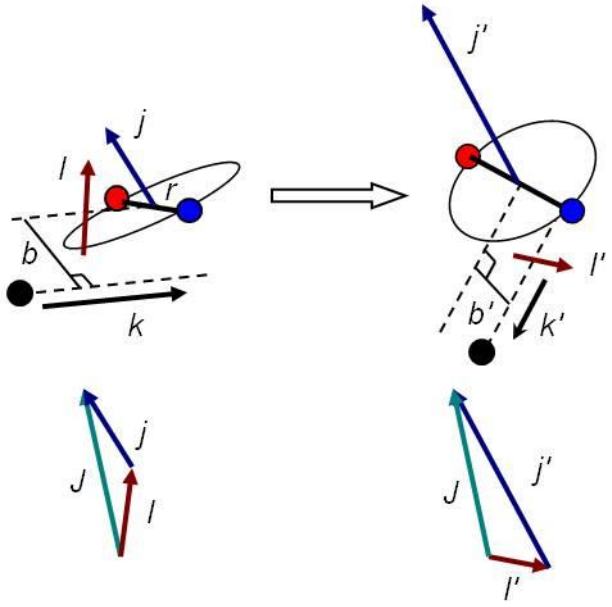

Figure 1.6: *The key vectors that describe an atom-diatom collision. Reprinted from [2].*

Differential Cross Sections (DCS)

The DCS is a measure of the $\boldsymbol{k}$-$\boldsymbol{k'}$ vector correlation. Measurement of this correlation is most easily achieved using CMB techniques. Traditionally, a rotatable TOF-MS was used to monitor the scattering probability as a function of scattering angle. However, more recently ion imaging techniques have prevailed [58], especially with the introduction of velocity-map imaging (VMI for short) [59], which can, in principle,

capture the full state-to-state DCS in one image. This technique involves state-selectively ionising the target species, usually using REMPI, and then guiding the ions to a 2-D position-sensitive detector (MCP-phosphor screen) *via* carefully controlled ion optics. Importantly, the product *velocity*, $\boldsymbol{v'}$, is mapped to a unique point on the detector independent of position in the scattering plane. Inverting the polarity of the ion optics can allow detection of photoelectrons [60-62].

A very nice example of this method is the work of Chandler and co-workers, where they measured the DSC for various rotational excitations from NO ($X^2\Pi_{1/2}$, $v = 0$, $j = ½$ *e/f*) in collisions with Ar [63,64]. They observed that the DCSs become increasingly peaked in the backward scattering direction with increasing Δj. This is a common observation and is suggestive of the physical picture that lower impact parameters, and consequently more impulsive encounters, promote larger Δj. More glancing collisions i.e. larger impact parameters result in smaller values of Δj. Chandler and co-workers also measured the degree of rotational alignment and orientation of the products through the polarisation of the probe laser in the REMPI scheme [63-65]. For the orientation measurements they observed the remarkable result that the sense of rotation of the product alternates, not only with Δj, but also with scattering angle. These general trends were well reproduced by QM scattering calculations but the power of the experiments to test the full-range of the PES led to suggested improvements in the form of the PES, particularly in the anisotropy of the repulsive core.

There have been other elegant experiments which utilise CMBs to measure vector properties of collision dynamics. Stolte and co-workers have used electrostatic hexapole fields to measure the DCS for isolated Λ-doublet levels, specifically NO ($X^2\Pi_{1/2}$, $v = 0$, $j = ½$ *f*) + He [66]. The *f* Λ-doublet for this rotational state is the low-field seeking level and can be focused through an aperture into the collision zone; the high field seeking *e* levels diverge from the MB and are not focused into the collision zone. Over and above the usual shift from forward to backward scattering as Δj increases, they observed that the DCSs were noticeably different for the different Λ-doublet states of the same final j. They realised that the shape of the DCS was the same for final states of the same space-fixed inversion parity, p ($= \varepsilon'(-1)^{j'-0.5}$), and common value of a labelling index, n ($= j' - \varepsilon\varepsilon'/2$). These observations were well reproduced by a quasi-quantum treatment (QQT) which predicted that the shape of the DCS depends on the Legendre moment of order $[j' - \varepsilon\varepsilon'/2]$.

Adding a further layer of complexity, the groups of Stolte and ter Meulen have measured the steric asymmetry of rotational excitation cross-sections, by orienting the molecular framework of the diatomic, either NO [67,68] or OH [69,70]. State-selection of Λ-doublet levels was achieved again using hexapole fields, but by incorporating a static electric field into the collision zone they were able to present either end of the diatomic molecule to the collision partner, for example, for NO, either N-end on or O-end on, simply by altering the polarity of the fields. Using LIF they were then able to measure the steric asymmetry factor, *S*, which for the example of NO + Ar is defined by:

$$S(j = 0.5 \rightarrow j', \varepsilon') = \left[\frac{(\sigma_{\mathrm{Ar-NO}}) - (\sigma_{\mathrm{Ar-ON}})}{(\sigma_{\mathrm{Ar-NO}}) + (\sigma_{\mathrm{Ar-ON}})} \right]_{j', \varepsilon'}$$

(Equation 1-16)

For OH + Ar, higher Δ*j* is observed primarily from H-end on collisions. This is not surprising from a 'ball and stick' picture: the centre-of-mass for OH is very much closer to the O atom (ball), leaving a larger torque arm between the centre-of-mass and the H atom (stick). It is therefore easier to induce large rotational excitations by striking the H atom. The values of *S* tend to be smaller in magnitude for NO, reflecting the near homonuclear nature of the diatomic. A very interesting alternation in the sign of *S* for even/odd Δ*j* was observed for both He and Ar, which means that collisions with the N-end preferentially promote Δ*j* = even and O-end collisions Δ*j* = odd.

The above examples reflect the current state-of-the art for measuring the vector properties of inelastic collision dynamics using CMBs. However, it is the ***j-j′*** correlation that is most relevant to the measurements in this thesis. Classically, this describes the tilt of rotational AM during a collision. Before discussing previous work in this area it is worthwhile introducing the concept of rotational polarisation: orientation and alignment.

Rotational Orientation and Alignment

Orientation and alignment refer to the limiting cases describing the distribution of ***j*** vectors about a quantisation axis, ***z***. Classically, the direction of ***j*** is biased towards up, *vs.* down (dipolar), for an orientation, whilst for an alignment the bias is up/down *vs.* side-to-side (quadrupolar). In terms of the rotational motion of diatomic molecules,

oriented ensembles have a preferential *sense* (clockwise or anticlockwise) of rotation, and aligned ensembles a preferential *plane* of rotation; the rotational plane being, in all cases, perpendicular to the rotational AM, ***j***.

In the high-*j* limit the distribution of the rotational angular momenta can be expressed using a set of orthonormal basis functions, for example, the modified spherical harmonics. When the system has cylindrical symmetry, often the case when using optically based techniques, the description is reduced to the following infinite weighted sum [57]:

$$N(j,\theta) = \frac{1}{4\pi}\left\{\begin{array}{l} A_0^{(0)}(j) + 3A_0^{(1)}P_1(\cos\theta) + \frac{5}{2}A_0^{(2)}P_2(\cos\theta) \\ \\ + 7A_0^{(3)}P_3(\cos\theta) + 9A_0^{(4)}P_4(\cos\theta)\ldots. \end{array}\right\}$$

(Equation 1-17)

$P_K(\cos\theta)$ are Legendre polynomials and the coefficients $A_0^{(K)}$ are the expectation values, or moments, of the distribution. They have rank K, which ranges over all integers. In general, they have component Q (spanning the space $-K \le Q \le K$), but this is zero for cylindrical symmetry. These alignment parameters describe population (K = 0), orientation (K = odd) and alignment (K = even) moments of the distribution and the first three terms have the following limits [57]:

$$A_0^{(0)}(j) = 1$$

$$A_0^{(1)}(j) = \langle P_1(\cos\theta)\rangle; \text{ range } -1 \text{ to } 1$$

$$A_0^{(2)}(j) = 2\langle P_2(\cos\theta)\rangle; \text{ range } -1 \text{ to } 2$$

(Equation 1-18)

In a QM picture it is better to describe the population distribution of the m_j-sublevels. This involves describing the density matrix (ρ) (which is a description of the m_j populations and phase relationships between them) in terms of spherical-tensor AM operators ($T_Q^{(K)}$) [57]:

$$\rho(j) = \sum_{K=0}^{2j} \sum_{Q=-K}^{+K} \rho_Q^{(K)}(j) T_Q^{(K)}$$

(Equation 1-19)

Here ρ_Q^K are the spherical-tensor moments of the expansion, which are related to the alignment parameters in equation 1-12 through the following relationship [57]:

$$A_Q^{(K)}(J) = \frac{(-1)^q C(K)}{\langle jm|\boldsymbol{J}^2|jm\rangle^{K/2}} \frac{\left(j\left\|J^{(K)}\right\|j'\right)}{\sqrt{2K+1}} \rho_{-q}^{(k)}(J) = \frac{C(K)}{\langle jm|\boldsymbol{J}^2|jm\rangle^{K/2}} \left\langle J_Q^{(K)} \right\rangle$$

(Equation 1-20)

$$\left\langle J_Q^{(K)} \right\rangle = \sum_m \rho_{mm} \langle jm|J_Q^{(K)}|jm\rangle$$

(Equation 1-21)

Here, *C(K)* is a normalisation constant [57], $\boldsymbol{J}^2$ is the total angular momentum squared and $\left(j\left\|J^{(K)}\right\|j'\right)$ is a reduced matrix element [19].

It then becomes possible to determine alignment parameters for a cylindrically symmetric system when knowing the m_j-sublevel populations (the diagonal elements, ρ_{mm}, of the density matrix, ρ) and knowing the expressions for the spherical tensor AM operators $J_Q^{(K)}$ [19]:

$$J_0^{(0)} = 1$$

$$J_0^{(1)} = J_z$$

$$J_0^{(2)} = \frac{1}{\sqrt{6}}(3J_z - \boldsymbol{J}^2)$$

(Equation 1-22)

Figure 1.7 provides examples of orientated and aligned distributions of m_j. Here an oriented ensemble is biased towards positive or negative values of m_j and an aligned

ensemble is biased toward the absolute value of m_j. An isotropic distribution has all m_j-sublevels equally populated. An oriented ensemble can possess a degree of alignment, but for an aligned sample all odd moments vanish.

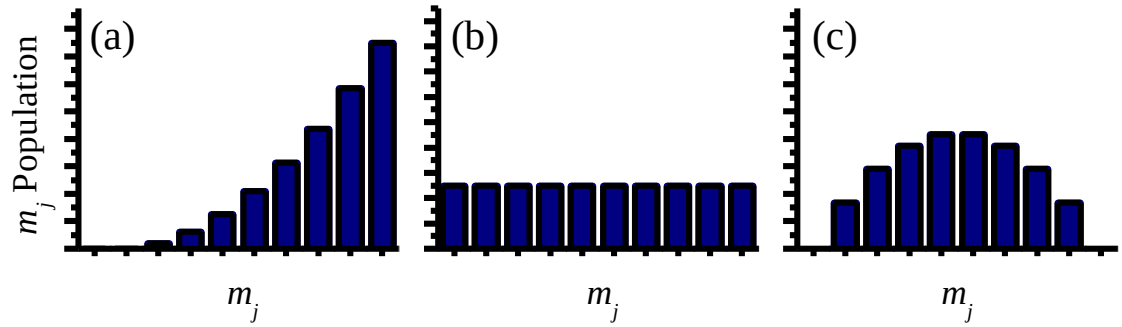

Figure 1.7: *Example m_j state distributions for j = 4.5: (a) orientation, (b) isotropic and (c) alignment. Calculated using the theoretical treatment in references [71,72] and representative of the m_j distributions created in the pump step of the PS experiment as discussed in section 1.2.2. The quantisation axis is chosen to be (a) the photon propagation direction and (c) the frame of the electric field of the pump laser.*

Optical Preparation of Alignment and Orientation

It was stated earlier that the system must depart from equilibrium to monitor the collision dynamics. So to monitor the collisional evolution of anisotropic rotational distributions an alignment or orientation must first be generated. This is achieved using the polarisation properties of laser light. The two most commonly used pure polarisation states are circular and linear. These limiting cases, and indeed all other pure polarisation states, can be constructed from linear combinations of orthogonal components of the electric field vector, $\boldsymbol{\varepsilon}$. For linear polarisation there is a multiple of $\pi/2$ phase shift between the two components and the resultant electric field oscillates sinusoidally in a plane. For circular polarisation there is a $x\pi/4$ phase shift of the two components, where x = odd. Their recombination results in $\boldsymbol{\varepsilon}$ being constant in magnitude but rotating clockwise (σ^+) or anti-clockwise (σ^-) with respect to a viewer looking against the propagation direction. (Practically, this is not a good idea!)

Circular polarisation generates rotational orientation in addition to alignment moments, i.e. K = 0, 1, 2 *etc.*, and linear polarisation will generate alignment moments only, i.e. K = even. The maximum non-zero tensor rank of the distribution is equal to twice the number of photons in this interaction. Also, triangular relations put limits on the possible non-zero moments for specific values of j. For example, j = 0, by definition, cannot show any alignment or orientation, j = 1/2 can possess orientation (K = 1), but

not alignment, and $j = 1$ is the lowest value of j that is capable of being both oriented ($K = 1$) and aligned ($K = 2$). Obviously, this can be extended to higher ranks of K, where $K_{max} = 2j$.

The generation of orientation and alignment becomes a little clearer when considering the interaction of the electric field with the transition dipole moment of the molecule, μ. The probability of interaction is related to the angle between the two vectors:

$$|\boldsymbol{\mu} \bullet \boldsymbol{\varepsilon}|^2 = |\boldsymbol{\mu}|^2 |\boldsymbol{\varepsilon}|^2 \cos^2 \theta$$

(Equation 1-23)

In the perturbative limit, polarising μ will result in ***j*** being polarised also, because ***j*** is connected to μ through the framework of the molecule (figure 1.8). It is readily apparent from figure 1.8 that Q-type rotational branches are better suited to preparing/probing rotational alignments, because μ is parallel to ***j***, and P- and R-type branches are better suited to orientation measurements, because μ is perpendicular to ***j***. The magnitude of the orientation or alignment will depend on the branch used and rotational quantum states connected by the transition.

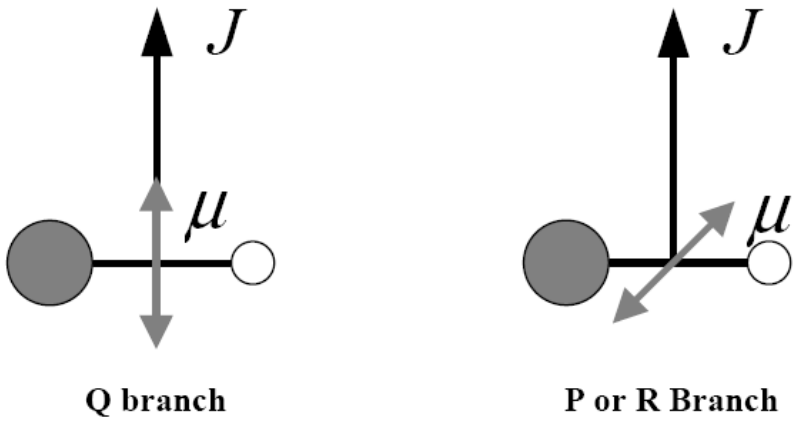

Figure 1.8: *The connection between the transition dipole moment, μ, the rotational angular momentum, J, and the internuclear axis, r (not labelled) for a diatomic molecule in the high-J limit and for a Σ ← Π transition.*

j-j' Correlations – Rotational Depolarisation

The examples of rotational AM studies provided in this sub-section can be broadly classed as m_j-changing collisions. The majority of these experiments are bath-gas type experiments which employ OODR spectroscopic schemes to first prepare a rotational

polarisation (often referred to as polarisation labelling) and then subsequently probe the rotational anisotropy as a function of collisions. This is commonly measured by recording signal intensities for two different probe laser polarisations (for example, parallel and perpendicular) relative to the polarisation of the pump (or tagging) laser. The signal may be fluorescence, or an ion count, and the degree of rotational polarisation of the probed state is related to the simple ratio, *C* (equation 1-24 for linear polarisations and 1-25 for circular polarisations). If the target molecule has been 'tagged' in an electronically excited state, the polarisation of the spontaneous fluorescence may be used to monitor the decay of rotational anisotropy. In these examples, *C* is related to signal intensities, *I*, measured from parallel and perpendicular geometries defined with respect to the pump laser polarisation and the reference axis of polarisation sensitive optics placed in-front of the detector.

$$C = \left(\frac{I_{\parallel} - I_{\perp}}{I_{\parallel} + 2I_{\perp}} \right)$$

(Equation 1-24)

$$C = \left(\frac{I_{\sigma^+} - I_{\sigma^-}}{I_{\sigma^+} + I_{\sigma^-}} \right)$$

(Equation 1-25)

Experiments of this kind (see ref. [1]) essentially measure the ability of a collision partner to redistribute the m_j-sublevel populations for elastic ($\Delta j = 0$) or inelastic ($\Delta j \neq 0$) processes, or indeed both simultaneously, which is usually the case when spontaneous fluorescence from an excited electronic state is not dispersed. With respect to figure 1.6, these experiments are a measure of the classical degree of tilt that the molecule suffers as a result of a collision; in other words, the vector correlation between ***j*** and ***j′***. Similar to the classical description of rotational AM distributions about a quantization axis, the distribution of ***j′*** about ***j*** can be written as an expansion of Legendre polynomials, when there is cylindrical symmetry:

$$P(\theta_{jj'}) = \frac{1}{2} \sum_{K} (2K+1) a^{(K)} P_K(\cos\theta_{jj'})$$

(Equation 1-26)

Here the coefficients of the expansion, $a^{(K)}$, are equivalent to the renormalized $A_Q^{(K)}$ alignment parameters defined in equation 1-18. Brouard and co-workers have provided a rigorous formalism which relates these polarisation parameters to the rate constant / cross-section for the depolarisation of an initially prepared alignment, or orientation, towards isotropy under isotropic collision conditions [29].

m_j-changing measurements have been limited in comparison to those which measure scalar properties of RET, and the majority of the m_j-changing studies are concerned with inelastic, opposed to *elastic* depolarisation. Much of this early work has been reviewed by McCaffery *et al.* [73]. It mainly involved collisions between alkali dimers or I_2 with rare gas colliders. The general conclusion from this work was that m_j is largely conserved in RET collisions. This was interpreted as support for energy-sudden models, which predict j_z-preserving propensities based on the kinematic apse model [74,75]. Here the apse is defined by the vector subtraction, $\hat{\boldsymbol{a}}_k = \left|\hat{\boldsymbol{k}}' - \hat{\boldsymbol{k}}\right|$, where $\boldsymbol{k}$ represents the collision wavevector (figure 1.4). Since the force acting in a sudden collision between an atom and a diatom acts normal to the surface of an ellipsoid which represents a diatomic molecule, i.e. parallel to $\hat{\boldsymbol{a}}_{\boldsymbol{k}}$, then the component of rotational AM in the induced plane of rotation cannot be altered. This forms the basis of the LM-AM model developed by McCaffery to explain trends in RET [21,22]. Sitz and Farrow also observed significant conservation of rotational alignment as a result of RET in self-collisions of N_2 (v = 1), but they found that a $\Delta m_j = 0$ model did not reproduce their experiments. Instead, they found better agreements with a $\Delta\theta = 0$, where θ is the classical angle between the rotational AM vectors [76,77].

However, other experiments and theoretical predictions suggest that these are isolated cases, and that the m_j conserving model is not universally applicable. Indeed, McCaffery *et al.* made the comment that "away from the sudden limit where the collision energy is comparable to the interaction well depth, knowledge of m_j processes may contain important information on the PES" [73]. Similar to the Sitz and Farrow measurements, Zacharias and co-workers used stimulated Raman pumping (SRP) to prepare rotational polarisations in the v_2 = 1, j levels of C_2H_2 (acetylene) [78-80]. LIF was used to probe the anisotropy in RET product levels. They found that alignment and orientation in the product decayed as a function of increasing Δj. In addition, their measurements were not well fitted to models where $\Delta m_j = 0$ or $\Delta\theta = 0$; their data were better modelled with exponential functions. Very recently Costen and co-workers used frequency-modulated

spectroscopy to measure the rotational alignment in products of RET in collisions between CN ($A^2\Pi$, v = 4, j) and Ar [81]. They observed product alignment of approximately 40% with respect to the alignment of the initial level. There was also a slight tendency for this ratio to reduce with increasing Δj, but the range of j probed was much less than compared to Zacharias and co-workers, primarily due to the range of Δj being small in comparison to C_2H_2 self-collisions.

Similarly, there have been very large and unexplained variations in the magnitudes of elastic depolarisation reported in the limited previous measurements. McCaffery and co-workers observed very small elastic depolarisation cross-sections (~ 0.5 Å^2) for alkali dimers in collisions with He and Ar, that are an order of magnitude or two lower than RET cross-sections [73]. Similarly, elastic depolarisation cross-sections for BaO ($A^1\Sigma^+$) in collisions with Ar were found to be < 1 Å^2 [82]. However, this increased to 8 Å^2 in collisions with CO_2. Similar to RET, it seems this may indicate that partners with higher order electrostatic terms in the interaction potential increase elastic depolarisation. This appears to be confirmed by Snow *et al.* where they measured depolarisation cross-sections for NO ($A^2\Sigma^+$) in collisions with Xe, N_2, NO, CO_2 and CHF_3 [83]. The corresponding values were < 1, < 1, (7 ± 3), (10 ± 3) and (22 ± 3) Å^2. Elastic depolarisation in CO self collisions was found to be 26 Å^2 for j = 11 [84]. Lower temperature measurements indicated that this value increases for lower values of j. However, elastic depolarisation cross-sections were also measured for H_2, HD and D_2 ($B\ ^1\Sigma_u^+$, v = 0, j = 1, m_j = 0) in collisions with atomic He, Ar and Ne, which were as large as 30 Å^2 [85]. Interestingly the cross-sections for He and Ne were larger than those for Ar. There were no obvious trends between the isotopes. It seems clear again that an m_j-preserving picture only holds true for special cases when considering elastic depolarisation.

More recently, Zacharias and co-workers extended their C_2H_2 + C_2H_2 inelastic depolarisation work to measure the elastic equivalents [86]. They found very rapid elastic depolarisation rate constants, as large as 3.21 x 10^{-10} cm^3 s^{-1} for j = 2 and decreasing to 2.35 x 10^{-10} cm^3 s^{-1} for j = 9. This is consistent with the idea of increased gyroscopic stability with an increase in the classical rotational speed. In terms of diatomics, the most recent studies have focused on NO (Brouard and co-workers) [87], CN (Costen and co-workers) [81] and OH (this work and Brouard and co-workers [88-90]). More detailed discussion of the findings from these studies will be deferred until the results of this thesis have been presented.

1.1.5 Kinetics of Elastic Depolarisation

It is the stated aim of this thesis to evaluate the collisional evolution of rotational angular momentum polarisations. The polarisation spectroscopy (PS) measurements presented in this thesis measure a phenomenological rate constant for the bulk loss of polarisation. As mentioned in the opening section of this chapter, these measurements are sensitive to both inelastic RET and elastic depolarisation. The measured rate constant, denoted $k_{PS}^{(K)}$ (where the superscript *K* represents the tensor rank of the rotational polarisation being monitored), can be decomposed into two rate constants describing the efficiency of these two processes.

$$k_{PS}^{(K)} = k_{POP} + k_{DEP}^{(K)}$$

(Equation 1-27)

Here k_{POP} and $k_{DEP}^{(K)}$ are the rate constants for inelastic population transfer out of a prepared level and its elastic depolarisation, respectively; again, *K* indicates the tensor rank of the rotational polarisation. A summary of the formal justification for equation 1-27 now follows, which was developed in parallel to the research presented here [91].

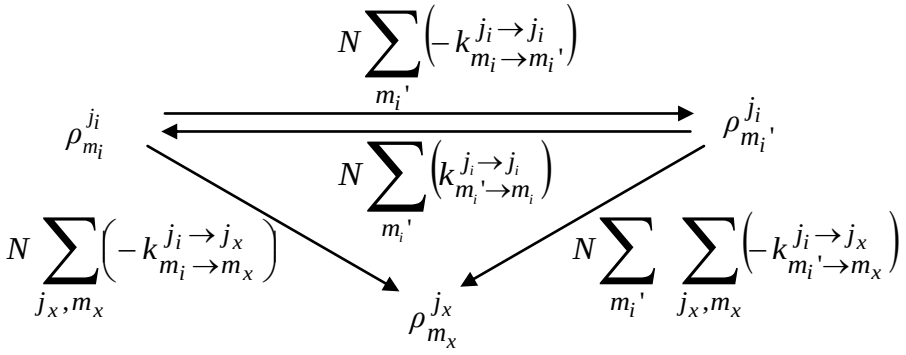

Figure 1.9: *Kinetic scheme describing the rate of collisional transfer between density matrix elements. (See text.)*

The state of the system is defined by a density matrix in the basis of $|jm\rangle$ states. The elements of the density matrix are labelled $\rho_{mm'}^{jj'}$ and the transfer between them in thermal collisions with an *isotropically* distributed, Maxwell-Boltzmann distribution of

relative velocities, *v*, has an associated rate constant: $k^{j_i \to j_p}_{m_i m_i' \to m_p m_p'}$. The PS experiments have cylindrical symmetry and so are only sensitive to the evolution of the diagonal elements describing the population of m_j levels, but not the coherences between them (which vanish when there is cylindrical symmetry). The primes are therefore dropped to give: $k^{j_i \to j_p}_{m_i \to m_p}$. A kinetic scheme (figure 1.9) can therefore be constructed for collisional transfer to and from the initial density matrix elements describing the ensemble prior to collisions, ρ^j_m. (The preparation and probing of this density matrix using PS will be summarised in section 1.2.2.) Here j_x is a product rotational level which is not equal to j_i. The differential equation for the rate of change of $\rho^{j_i}_{m_i}$ is then:

$$\frac{d\rho^{j_i}_{m_i}}{dt} = N\left(-\rho^{j_i}_{m_i}\left(\sum_{m_i'} k^{j_i \to j_i}_{m_i \to m_i'} + \sum_{j_x, m_x} k^{j_i \to j_x}_{m_i \to m_x} \right) + \sum_{M_i'} \rho^{j_i}_{m_i'}\, k^{j_i \to j_i}_{m_i' \to m_i} \right)$$

(Equation 1-28)

This can be transformed into a rate equation for the spherical tensor AM moments, $\rho^{(K)}_Q(j)$, used in the previous section to describe orientation and alignment, which are expressed in terms of ρ^j_m in equation 1-29, using the 'tensor contraction' method.

$$\rho^{(K)}_Q(j) = \sum_m (-1)^{j-m+Q} (2K+1)^{1/2} \begin{pmatrix} j & j & K \\ m & -m & -Q \end{pmatrix} \rho^j_m$$

(Equation 1-29)

The time dependence of which is the following derivative:

$$\frac{d\rho^{(K)}_Q(j)}{dt} = \sum_m (-1)^{j-m+Q} (2K+1)^{1/2} \begin{pmatrix} j & j & K \\ m & -m & -Q \end{pmatrix} \frac{d\rho^j_m}{dt}$$

(Equation 1-30)

Equation 1-28 can then be substituted in equation 1-30. The inverse of equation 1-30 can then be used to substitute the ρ_m^j terms remaining from the right hand side of equation 1-24. Asserting Q = 0 for cylindrical symmetry, and using the fact that different tensor ranks cannot interconvert under isotropic conditions [92], provides the following rate equation:

$$\frac{d\rho_0^{(K)}(j_i)}{dt} = N(2K+1)\rho_0^{(K)}(j_i) \times \left\{ \sum_{m_i,m_i'} \left[\begin{array}{l} -(-1)^{2j_i-2m_i} \begin{pmatrix} j_i & j_i & K_i \\ m_i & -m_i & 0 \end{pmatrix}^2 \left(k_{m_i \to m_i'}^{j_i \to j_i} + \sum_{j_x,m_x} k_{m_i \to m_x}^{j_i \to j_x} \right) \\ \\ +(-1)^{2j_i-m_i-m_i'} \begin{pmatrix} j_i & j_i & K \\ m_i & -m_i & 0 \end{pmatrix} \begin{pmatrix} j_i & j_i & K \\ m_i' & -m_i' & 0 \end{pmatrix} k_{m_i' \to m_i}^{j_i \to j_i} \end{array} \right] \right\}$$

(Equation 1-31)

This can be compared with a phenomenological equation for the decay of $\rho_0^{(K)}(j_i)$ in terms of distinct processes of elastic depolarisation, with rate constant $k_{DEP}^{(K)}$, and population loss, k_{POP}:

$$\frac{d\rho_0^{(K)}(j_i)}{dt} = -N\rho_0^{(K)}(j_i)\left(k_{DEP}^{(K)} + k_{POP}\right)$$

(Equation 1-32)

Comparison of equation 1-31 and 1-32 shows that the rate constant for elastic depolarisation, where the product rotational level equals the initial ($j_p = j_i$), is:

$$k_{DEP}^{(K)} = (2K+1) \sum_{m_i.m_i'} \left[\begin{array}{l} \begin{pmatrix} j_i & j_i & K \\ m_i & -m_i & 0 \end{pmatrix}^2 k_{m_i \to m_i'}^{j_i \to j_i} \\ \\ -(-1)^{2j_i-m_i-m_i'} \begin{pmatrix} j_i & j_i & K_i \\ m_i & -m_i & 0 \end{pmatrix} \begin{pmatrix} j_i & j_i & K_i \\ m_i' & -m_i' & 0 \end{pmatrix} k_{m_i' \to m_i}^{j_i \to j_i} \end{array} \right]$$

(Equation 1-33)

(where the following relationship has been invoked: $(-1)^{2j_i-2m_i} = (-1)^{2(j_i-m_i)} = 1$).

Equation 1-33 is an important result. Note that it includes, by construction, transfer both into and out of any particular $|j_i m_i\rangle$ level from and to other m_i' levels of the same j_i. This allows for the possibility that the population will, in general, be initially distributed unevenly over all the $|j_i m_i\rangle$ levels and then collisionally redistributed between them. Note also that it is compatible with there being a 'pure'-elastic rate constant, representing scattering in which only linear momentum is exchanged, because the positive and negative terms inside the square brackets cancel when $m_i' = m_i$. It should be noted that this $k_{DEP}^{(K)}$ provides the same outcome as the formalism developed by Brouard and co-workers [29] and used by Dagdigian and Alexander for extracting tensor cross-section for elastic depolarisation [93,94]:

$$\sigma^{depol,K}(j) = \sigma_{j\to j}^{K=0} - \sigma_{j\to j}^{K}$$

(Equation 1-34)

Here $\sigma_{j\to j}^{K=0}$ represents the pure elastic (i.e. including $\sigma_{m_i\to m_i}$) integral cross-section and $\sigma_{j\to j}^{K}$ is the tensor cross-section for tensor rank *K*. These are equal to the first and second terms contained in the sum of equation 1-30.

The corresponding population transfer rate constant ($j_p = j_x \neq j_i$) is

$$k_{POP} = (2K+1)\sum_{m_i}\begin{pmatrix} j_i & j_i & K \\ m_i & -m_i & 0 \end{pmatrix}^2 \sum_{j_x,m_x} k_{m_i\to m_x}^{j_i\to j_x}$$

(Equation 1-35)

The combined loss processes from some initial $|j_i m_i\rangle$ level can be summed into a single rate constant,

$$k_{m_i\to x} = \sum_{j_x,m_x} k_{m_i\to m_x}^{j_i\to j_x} = k_{j_i\to x}$$

(Equation 1-36)

Where the collisions take place in an isotropic environment, $k_{m_i \to x}$ should be the same for all m_i and so $k_{j_i \to x}$ represents rotational state changing processes for a given j_i. Note that because of the orthogonality properties of the 3-j symbols:

$$\sum_{m_i} \begin{pmatrix} j_i & j_i & K \\ m_i & -m_i & 0 \end{pmatrix}^2 = \frac{1}{2K+1}$$

(Equation 1-37)

Therefore, there is *no K*-dependence of k_{POP} (i.e. population loss is independent of whether the prepared rotational polarisation is described by $K = 1$, $K = 2$, *etc.*):

$$k_{POP} = k_{j_i \to x}$$

(Equation 1-38)

This is consistent with the physical result that any contribution to a moment is completely destroyed by transfer to the unobserved level, so all moments decay with the same rate constant and therefore no *K* label is attached to the population transfer rate constant throughout.

Obviously, according to equation 1-32, the decay of the moment $\rho_0^{(K)}(j_i)$, i.e. the time-dependence of the polarisation of the initial level, j_i, is just a simple exponential:

$$\rho_0^{(K)}(j_i) = \rho_0^{(K)}(j_i)_0 e^{-N\left(k_{j_i \to x} + k_{DEP}^{(K)}\right)t}$$

(Equation 1-39)

where $\rho_0^{(K)}(j_i)_0$ is the initial polarisation moment created before collisions take place.

So the fundamental concept of the research presented in this thesis is to optically prepare an anisotropic rotational polarisation, and then monitor that orientation or alignment as the distribution evolves back towards isotropy. In doing so, a phenomenological rate constant will be measured, which is denoted $k_{PS}^{(K)}$. This can be

decomposed, as rigorously shown above, into two distinct components: *elastic depolarisation,* $k_{DEP}^{(K)}$, and *inelastic population transfer,* k_{pop}.

1.2 Polarisation Spectroscopy

PS is the optically based technique used in this research to monitor the collisional evolution of rotational orientation and alignment in OH with various partners. PS is a 3rd order non-linear spectroscopic technique which was first developed in the 1970's as an extension to saturation spectroscopy [95]. Detecting changes in the polarisation state of a probe beam provides enhanced sensitivities over saturation spectroscopy, which detects changes in the absorption profile, by approximately a factor of 2 – 3 [96]. Because of its spectroscopic branch specificity, PS was shown to be a powerful technique for greatly simplifying complex spectra [97], particularly in environments that are prone to substantial line broadening. It was also proposed as a high resolution approach to studying relaxation rates [98].

PS is essentially a background-free spectroscopic probe, and for this reason, the vast majority of applications have been in the laser-diagnostics of luminous environments, for example, combustion [99] and plasmas [100]. PS is very closely related to other non-linear techniques such as four-wave-mixing (FWM) and coherent Anti-Stokes Raman scattering (CARS), which have also been applied to flame diagnostics. PS and FWM experiments have much greater sensitivity than CARS, and are comparable to LIF, because the laser beams are resonant with strongly allowed electric dipole transitions. However, FWM experiments are much more difficult to implement in comparison to PS since three (instead of only two) laser beams are required, and the phase-matching conditions produce signal wave-vectors that propagate in a direction related to the angles between the three input beams, instead of co-propagating with the input probe beam in PS experiments [101]. In addition, FWM techniques 'write' spatial gratings into the sample and are thus sensitive to the loss of these gratings as a result of translational motion effects. PS experiments are not sensitive to this phenomena.

PS has largely been used to measure the concentration of trace constituents in flames. Na and Ba have been detected in atomic flames with detection limits of 30 ppt and 37 ppb, respectively [102]. It has also been used to monitor the two-dimensional distributions of minor species in flames. Zizak *et al.* performed studies on Na in

acetylene/oxygen flames with a spatial resolution of 0.7 mm^3 and a sensitivity of 10 ppm [103]. As a specific example of the utility of PS in flame diagnostics, Nyholm and co-workers used PS to detect OH in acetylene/oxygen and propane/oxygen flames [104]. Using the OH $A^2\Sigma^+$ - $X^2\Pi$ (0,0) electronic band, they achieved a detection sensitivity of 10^{14} molecules cm^{-3}. They also extracted rotational temperatures in the region of 3100 – 3450 K for OH in acetylene flames and 2100 K in propane flames [105]. Extending their studies, a CCD camera was incorporated to determine the OH spatial distributions in the flame [106]. The distribution seemed to be uniform, but when the flame was deprived of oxygen the distribution was concentrated on the outer regions of the flame. They were also able to produce a temperature map of the flame. PS has been used to study a wide range of other species, which include; NO [107,108], NH [109,110], CO [109,110], CO_2 [111,112], H_2O [113], CH_4 [114], CH_3 [115], NH_3 [116], N_2 [117], atomic Hydrogen and recently CH [118].

Nyholm and co-workers suggested in their OH work that: "more quantitative measurements would require the knowledge of collisional depolarisation of the magnetic sublevels". It is therefore clear from this that knowledge of these processes, to which PS is inherently sensitive, is certainly lacking. Far fewer studies have utilised PS for the purpose of quantifying these processes, especially in controlled environments.

Dreizler *et al.* have measured relaxation times of orientated and aligned ensembles of OH radicals using pulsed picosecond laser systems [119]. Alignment relaxation times were found to be (258 ± 26) ps for j = 5 and (359 ± 62) ps for j = 10. Orientation relaxation times appear to be a factor of two longer than alignment decay times. Dreizler *et al.* reported (457 ± 106) and (701 ± 106) ps for j = 5 and 10, respectively. It seems that both orientation over alignment and higher versus lower rotational levels are more robust to loss of PS signals. Settersten *et al.* made the comparison between two-colour PS (TCPS), two-colour LIF and two-colour resonant FWM (TC – RFWM), for measuring the decay of rotational alignments in atmospheric pressure methane/air flames [120]. RET was observed with the TC – LIF, however, collision-induced signals observed in a similar way using the PS technique were weaker by factors of 100 – 1000. As the LIF signals were not sensitive to any polarisation in the sample, this suggested that retention of polarisation in the RET processes was weak. The same general conclusion was reached in a follow-up study [121].

McKendrick, Costen and co-workers have developed PS to specifically measure the rate of depolarisation of anisotropic rotational distributions under controlled conditions [71,72,122]. Prior to the research presented here, attention had focused on establishing the dependence of the PS signal on certain experimental variables, for example, laser fluence, number density and spectroscopic branch type [122]. McKendrick, Costen and co-workers began to measure the collision dynamics of OH with atomic and molecular collision partners; however, they only used single-pressure measurements [123]. It will be shown in subsequent chapters why this did not yield reliable information.

1.2.1 General Concept

Essentially PS requires two laser beams which are matched to spectroscopic transitions of the species that is being studied: a *pump* beam and a *probe* beam. In its simplest form these beams may be split from a common source. Since the frequencies will be the same, this variant is called one-colour PS (OCPS). Using two independent laser sources allows more control over the arrival time of the laser pulses, and so time-resolved pump-probe experiments can more readily be performed. This also means that two-colour PS (TCPS) experiments can be carried out. The advantages of this, as explained in more detail below, are that unique quantum states can be studied in isolation.

The pump laser propagates through the sample and produces an anisotropic m_j distribution (orientation or alignment) in both the ground and excited states connected by the transition *via* a two-photon interaction. The probe laser is also guided through the sample, crossing the pump path at an acute angle. The interaction of the probe laser with the anisotropic medium (one-photon) results in the probe laser polarisation being altered, generating an orthogonal component. This orthogonal component (fourth-photon) is the PS signal and can be resolved from the initial probe laser polarisation by placing crossed polarisers on opposite sides of the sample. The first (setting) polariser defines the initial probe polarisation and the second (analysing) polariser allows the signal to propagate, but rejects the probe beam.

Crucially, the electric field vector of the probe is geometrically off-set from the pump electric field vector (when it has linear polarisation) by 45° for maximum signal generation. This becomes clearer when considering a simplified single-molecule picture of PS signal production. Demtröder [96] provides a mathematical description of this, which will not be repeated here. The electric field vector of the probe laser, which has

linear polarisation, can be decomposed into orthogonal components. Since the resultant of these components lies at 45° relative to that of the pump laser then one of the components can be chosen to be parallel to the pump electric field and the other will be perpendicular to it. The pump laser has effectively pumped a subset of molecules to the excited state which have a particular sense, or plane, of rotation, leaving the 'unpumped' molecules (the 'hole' burned) with a mirrored rotational polarisation. Therefore, the component of the probe which is parallel to the pump will 'see' fewer molecules than the orthogonal component. The sample can therefore be treated as birefringent and dichroic, leading to a phase lag and amplitude difference between the two probe components, which is maximised when the polarisation of the pump and probe are offset by 45°. The resultant now has a degree of elliptical polarisation. It is the orthogonal component of this altered polarisation which effectively leaks through the analysing polariser as signal. Hence, if the sample does not have a rotational polarisation, then there will be no change in the probe laser polarisation and the probe laser beam will be rejected by the analysing polariser. In some respects, this is analogous to the alteration of plane polarised light incident on a sample containing chiral molecules.

Of course, this single-molecule representation is not ideal for describing molecular ensembles. A rigorous QM description is better suited.

1.2.2 Theoretical Description

Costen *et al.* developed a diagrammatic spherical-tensor treatment of OCPS [71] and TCPS [72] in the weak-field perturbative regime. This was used for the analysis of the PS data presented in the following chapters. The approach for OCPS and TCPS is essentially the same, but attention will be restricted to TCPS since most of the experiments carried out during this research project were of that nature.

The main TCPS spectroscopic schemes used to monitor the evolution of the bulk rotational angular momentum are illustrated in figure 1.10. These schemes allow the study of unique quantum states in isolation. The TCPS signal is a cooperative effect which arises from coherences between different parts of the sample. In addition, the polarisation of the system is an ensemble property, rather than of a single molecule. For these reasons, the system must be described by an ensemble average, which is achieved within the theoretical formalism of the density matrix, ρ, defined in equation 1-40.

$$\rho = \left\langle j' m_j' \middle| \rho(t) \middle| j m_j \right\rangle$$

(Equation 1-40)

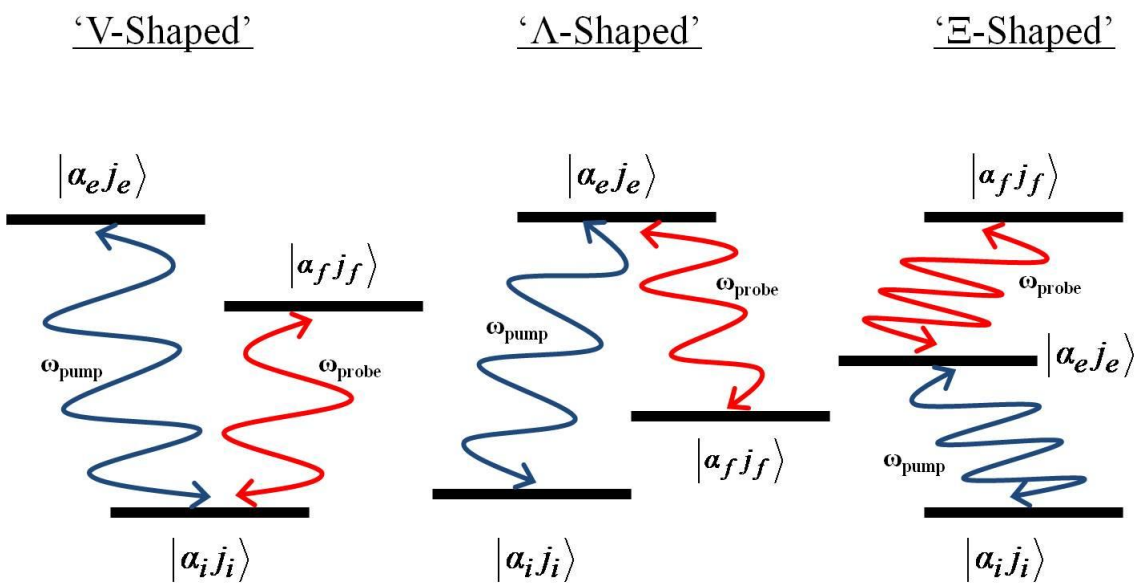

Figure 1.10: *Various TCPS spectroscopic schemes. The 'V-shaped' and 'Λ-shaped' schemes were used in the work of chapters 4/5 and 6 respectively. The kets denote definite quantum states, where α represents all other quantum labels other that the rotational quantum number, j. Subscripts represent initial (i), excited (e) and final (f) quantum states. The pump beam, of frequency ω_{pump}, connects initial and excited levels, and the probe beam, of frequency ω_{probe}, connects excited and final levels. The TCPS signal is resonant with the probe and is generated from the bulk rotational polarisation in the level common to the pump and probe.*

Here the density matrix elements span all relevant paired states j, m_j and j', m_j', which are those connected by the spectroscopic transitions in the TCPS experiment (figure 1.7). The density operator, $\rho(t)$, for time t contains all information on the molecular ensemble:

$$\rho(t) = \left| jm_j \right\rangle \left\langle j'm_j' \right|$$

(Equation 1-41)

In essence, the diagonal elements of the density matrix contains the information on populations and the off-diagonal the coherences between them.

The diagrammatic approach to non-linear optical calculations greatly simplifies the calculation of the polarisation density matrix responsible for the generation of the 3rd order non-linear signal. Feynman diagrams assist in the 'book-keeping' of the time-ordered sequence of photon interactions which operate on the density matrix. Figure 1.11 shows an example diagram for a specific set of time-ordered interactions. For each PS spectroscopic scheme (figure 1.10) there are a number of different permutations and hence set of calculations.

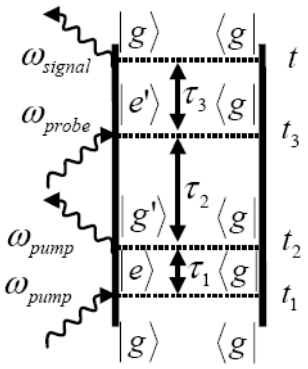

Figure 1.11: *An example of a Feynman diagram used in the calculation of PS signal (see text).*

In the Feynman diagram the two vertical lines represent the time evolution of the ket (left) and the bra (right) of the density matrix, which are shown for the states coupled by the photon interactions (wavy lines). Incoming wavy arrows represent absorption (annihilation) and the outgoing arrows represent emission (creation) of a photon. The photons are labelled as pump, probe or signal and operate on the density matrix at times t_n. During the delay between photon interactions, τ_n, the system evolves field-free. It is these periods where the state of the ensemble is subject to collisional processes. Of

particular interest is the pump-probe sequence of events, an example of which is depicted in figure 1.9. The period τ_2 is when the rotational orientation or alignment, produced by the pump, evolves in the bath of collider gas. Because this sequence has most significance for the purpose of this research it will be used as an example to describe the photon interactions.

The ensemble is initially isotropic and the density matrix is diagonal with all non-zero elements equal. The first pump photon interacts with the sample and generates a coherent superposition of states connected by the transition. The density matrix can be expanded in state multipoles and at this stage and, regardless of pump polarisation, only a single multipole of rank $K = 1$ contributes, representing an oscillating dipolar bulk polarisation. After the second pump photon interaction the density matrix spans only the ground, $|\alpha_g j_g\rangle$, or only the excited states, $|\alpha_e j_e\rangle$, states. This represents a time-invariant m_j sublevel population transfer from ground to excited states; the hole burned in the ground state m_j distribution is mirrored in the excited state (apart from the usually minor contribution from the AM of the pump photons). The density matrix may now be described by tensors of rank $K = 0$, 1 or 2 corresponding to population, orientation or alignment, respectively. As stated, it is the evolution of this that is of interest in the work presented in this thesis. The third photon, from the probe this time, interacts with the ensemble and generates a linear superposition of the ground and excited states connected by the probe laser, oscillating at the transition frequency, similar to that of t_1. The signal field associated with the third-order density matrix is then evaluated by projecting the third-order polarisation onto the desired electric field polarisation (orthogonal to the probe), and is given by the trace of the density matrix with the dipole operator. Experimentally the signal intensity that is detected will be a cycle average of the square modulus of the signal electric field strength, because the temporal profile of the ns-pulsed lasers used in this research are much longer than the optical cycle frequency.

Although it is possible to have ranks $K = 0$, 1 and 2 contributing to the second-order density matrix, which would all evolve with different rates [92], only $K = 1$ or 2 (depending on pump laser polarisation) are non-vanishing for the diagrams where the probe interaction follows the pump. This means that when the pump and probe are well separated in time, only orientation or alignment, respectively, of the bulk polarisation of the sample will be monitored and with a single representative decay rate. It should be

made clear that in the treatment being described, the quantisation axis is chosen to be the propagation direction of the laser beams, which are assumed to be co-axial. This means that both pump polarisations can be treated within a common reference frame. Other diagrams which have different sequences of photon interactions, for example, when the probe pulse interacts at t_1 or t_2, will contribute to the *magnitude* of the signal. These diagrams only contribute when the pump and probe pulses overlap in time. They will not affect the rate of decay when the pump and probe pulses are well separated. The same holds true for any collisional processes which de-cohere the oscillating dipolar polarisation generated during the field-free periods τ_1 and τ_3.

The expression for the signal electric field emitted at time t has the following form:

$$\left[\mathbf{P}^{(3)} \bullet \boldsymbol{\varepsilon}_4^*\right] = C\Phi \sum_{K_2} F(\varepsilon_1\varepsilon_2\varepsilon_3\varepsilon_4; K_2) G(j_i\, j_e\, j_f; K_2)$$

(Equation 1-42)

Expressions of the terms C, Φ, F and G are provided in equations 1-43 to 1-46 and show the dependence of the TCPS signal on a number a number of experimental and fundamental quantities (linestrengths, etc.). Specifically, the notation refers to the Feynman diagram in figure 1.10, which is for a 'V-shaped' spectroscopic scheme. The signal expression can be represented for any other with straightforward substitution.

$$C = \frac{N_{j_i}\zeta_1\zeta_2\zeta_3 \left|\left\langle \alpha_e\, j_e \mu^{(1)} \alpha_i\, j_i \right\rangle\right|^2 \left|\left\langle \alpha_i\, j_i \mu^{(1)} \alpha_f\, j_f \right\rangle\right|^2}{8i\hbar^3(2j_i+1)}$$

(Equation 1-43)

Here, N is the population of the initial rotational level and ζ_n is the magnitude of the incident electric field at t_n. The rovibronic transition line strengths are represented by the square modulus of the transition matrix elements between the initial and excited (pump) and initial and final (probe) states, respectively.

$$\Phi = e^{-i\omega_s t + i\mathbf{k}_s\cdot\mathbf{r}(t)} e^{i\tau_3(\omega_1-\omega_2+\omega_3-\omega_{j_i j_f}-\mathbf{k}_{\mathrm{probe}}\cdot\mathbf{v})} e^{i\tau_2(\omega_1-\omega_2)}$$

$$\times e^{i\tau_1(\omega_1-\omega_{j_e j_i}-\mathbf{k}_{\mathrm{pump}}\cdot\mathbf{v})} e^{-\Gamma_d^{j_e j_i}\tau_1} e^{-\Gamma_d^{j_i j_f}\tau_3}$$

(Equation 1-44)

This represents the phase-dependent terms in the signal field. Here ω_n denotes the frequencies of the photons; $\omega_{j_i j_f}\left(=\omega_{j_f}-\omega_{j_i}\right)$ is the natural transition frequency between levels j_i and j_f. This also includes the effect of Doppler motion through the scalar product of the pump and probe wave-vectors (labelled appropriately) with the velocity. Γ_d represents the dephasing rate during the field-free periods, τ_1 and τ_3.

$$F\left(\varepsilon_1\varepsilon_2\varepsilon_3\varepsilon_4;K_2\right)=\sum_{Q_1,Q_2,Q_3}(-1)Q_2\left(\varepsilon_1\right)^{(1)}_{-Q_1}\left(\varepsilon_2^*\right)^{(1)}_{Q_1-Q_2}\left(\varepsilon_3\right)^{(1)}_{Q_2-Q_3}\left(\varepsilon_4^*\right)^{(1)}_{Q_3}\left(2K_2+1\right)$$

$$\times\begin{pmatrix}1 & 1 & K_2\\ Q_1-Q_2 & -Q_1 & Q_2\end{pmatrix}\begin{pmatrix}1 & 1 & K_2\\ Q_3-Q_2 & -Q_3 & Q_2\end{pmatrix}$$

(Equation 1-45)

This term expresses the signal dependence on the polarisations of the four photons involved. The $\left(\varepsilon_n\right)^{(1)}_Q$ terms are spherical tensor components of the polarisation vector in the frame of the photon propagation direction. The 3-*j* symbols constrain the values of K_2 to 0, 1 or 2, i.e. population, orientation and alignment.

$$G\left(j_i j_e j_f;K_2\right)=(-1)^{j_i-j_f}\begin{Bmatrix}1 & 1 & K_2\\ j_e & j_e & j_i\end{Bmatrix}\begin{Bmatrix}1 & 1 & K_2\\ j_i & j_i & j_f\end{Bmatrix}e^{-\Gamma^{j_i j_i}_{K_2}\tau_2}$$

(Equation 1-46)

This final term shows the branch dependence of the TCPS signal (*via* the 6-*j* symbols) and the exponential term represents the decay during τ_2. The decay is specific to the moment K_2 and for the state of definite AM, j_i. To reiterate, this is for the situation of one sequence of photon interactions where the pump and probe are resolved in time. The exponential term is therefore the quantity of interest for the studies in this work. This exponential decay is related to equation 1-39. For a full calculation, all possible photon interactions must be considered for forward simulations or fitting of the PS data.

Equation 1-43 is required to describe the PS signal magnitude. However, there is one final consideration required for the full time-dependent (i.e. on pump-probe delay) description of the PS signal, and that is the phenomenon of nuclear hyperfine quantum beats (NHQBs).

NHQBs arise through the coupling of the prepared rotational polarisation, ***j*** to the nuclear spin, ***I***, of constituent atoms in the probed molecule. In the case of OH, H has a nuclear spin of ½, which is not acted upon by any of the laser beams and is initially isotropic. After the rotational polarisation has been created *via* the two-photon interaction of the pump, ***j*** can couple to ***I*** to form the resultant (grand) total AM, ***F***. If the energy separation of the hyperfine levels is smaller than the frequency band-width of the pump laser then these levels, $F = j \pm ½$, will be excited coherently. In a vector picture ***j*** and ***I*** precess about ***F***. This coupling therefore results in a time-dependent oscillation of the prepared polarisation of ***j*** and is represented by the following time-dependent factor [19]:

$$G^{(K)}(t) = \sum_{F',F} \cos\left[\frac{(E_{F'} - E_F)t}{\hbar}\right] \frac{(2F'+1)(2F+1)}{(2I+1)} \begin{Bmatrix} F' & F & K \\ j & j & I \end{Bmatrix}^2 .$$

(Equation 1-47)

The frequency of this oscillation is related to the energy separation of the nuclear hyperfine levels. PS experiments will observe this oscillation if the hyperfine frequency is slow compared to the temporal resolution of the pump and probe lasers. If, on the other hand, the hyperfine frequency is rapid in comparison to the probe temporal profile then the PS experiment will measure the average, effectively reducing the signal magnitude [19]:

$$\left\langle G^{(K)}(t) \right\rangle_{\text{average}} = \frac{1}{(2I+1)} \sum_{F} (2F+1)^2 \begin{Bmatrix} F & F & K \\ j & j & I \end{Bmatrix}^2 .$$

(Equation 1-48)

1.3 Scope of this Research

The work presented in this thesis demonstrates the ability of PS to measure m_j-changing processes in the dynamics of molecular collisions. The principal motivations are: to better understand these poorly understood processes from a fundamental stand-point and to test the most recent PESs which describe the interactions. A systematic study is presented for the dynamics of OH in collisions with atomic (chapters 4 and 6) and molecular colliders (chapter 5). The effect of varying the PES alone, whilst keeping the kinematics the same, is also addressed by measuring the efficiency of rotational AM depolarisation for two different electronic states: OH ($X^2\Pi$) (chapter 4) and OH ($A^2\Sigma^+$) (chapter 6). It is also shown that stray magnetic fields can adversely affect the measurement of rotational AM polarisations, and how their effect can be successfully eliminated using a simple experimental remedy (chapter 3). Chapter 2 describes in detail the PS experimental methodology employed to address the challenges in the chapters that follow.

Chapter 2

Experimental Methodology

Polarisation spectroscopy (PS) is used in work to monitor the collisional decay of rotational angular momentum moments in OH. OH was produced *in-situ* by laser photolysis of nitric acid (HNO_3) at 193 nm. Initially one-colour PS was used, but for reasons alluded to in the preceding chapter the two-colour variant was favoured. To aid the description of the experimental method, specific details, for example, spectroscopic schemes used, will be addressed in the relevant chapters. This chapter will therefore only describe the apparatus common to all experiments.

Other than the generation of the chosen diatomic free-radical, the main requirements for this experiment include: state-specific preparation of rotational orientation and alignment moments *via* optical pumping; significant discrimination between probe and signal photons; and independent control over the admission of the precursor and collision partner, to examine the pseudo-first order kinetics of the collisional decay. The following sections will discuss each aspect of the experimental set-up in detail. For reference, figure 2.1 provides a schematic representation of the experimental set-up. The design and construction of this set-up was largely the work of two previous post-graduate students [123,124] and laboratory technicians at Heriot-Watt University. Only slight modifications have been implemented during this research project.

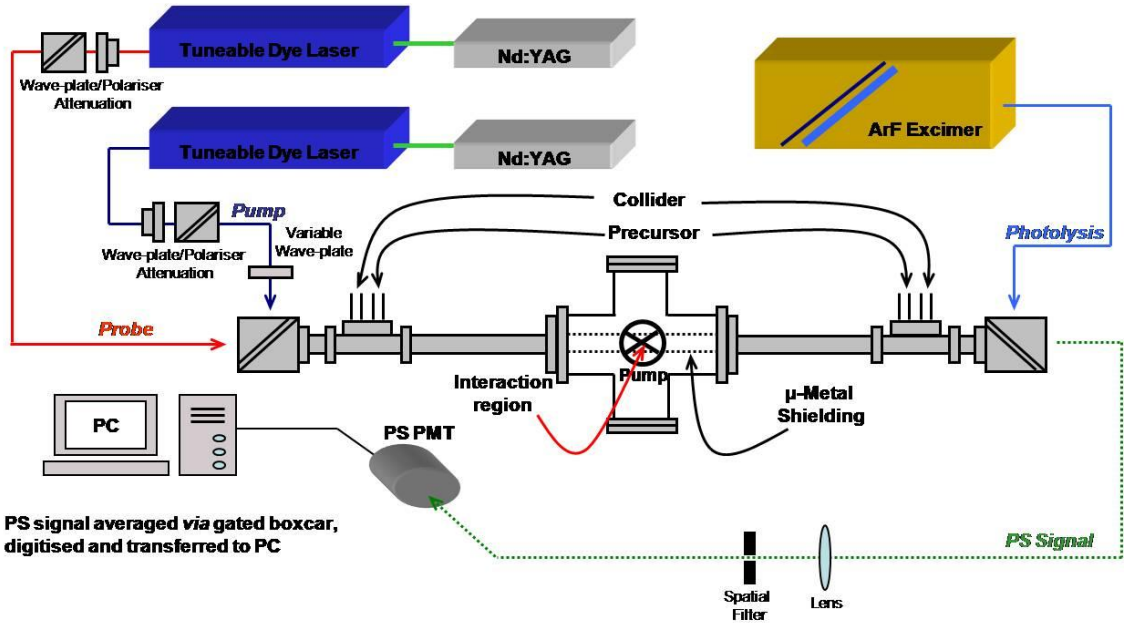

Figure 2.1: *Experimental schematic*

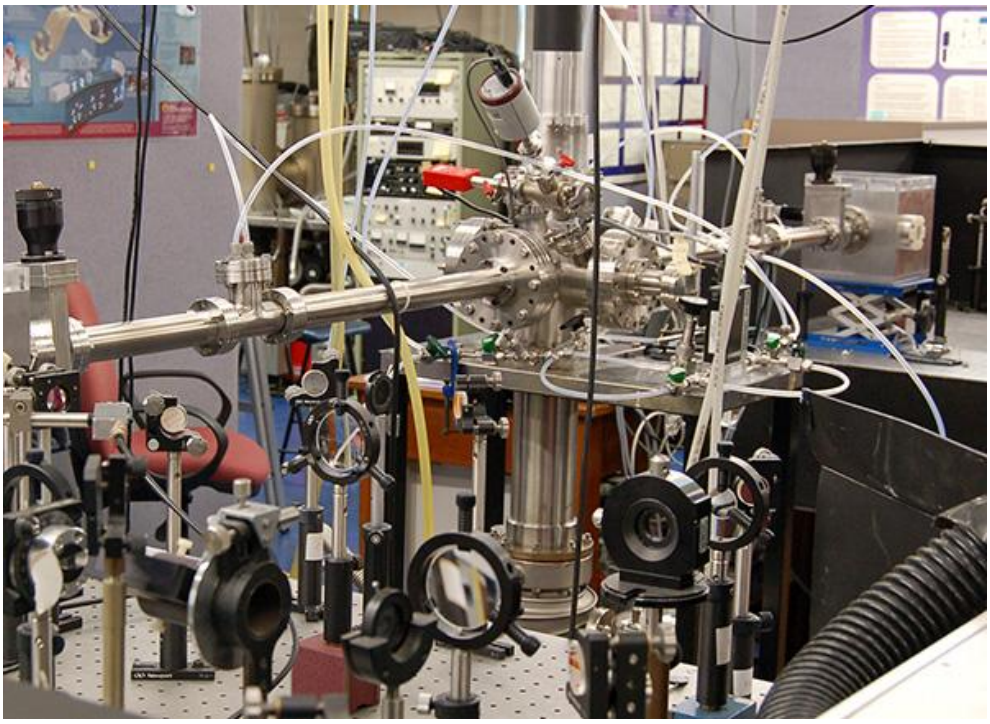

Figure 2.2: *Photograph of the vacuum chamber represented schematically in figure* ***2****.1.*

2.1 Vacuum Systems and Gas Handling

At the heart of all experiments was a stainless steel vacuum chamber (Vacuum Components), which had a six-way-cross at the centre (6 x 150 mm ports) and arms extending from opposite ports. These arms were approximately 1 m in length, had an internal diameter of 38 mm, and connected cubical polariser housings to the six-way-cross. The line of sight through the chamber arms defined the main axis of the chamber. Details of the polariser housings will be addressed in section 2.1.3 below. Incorporated into the length of the arms were T-junctions which allowed the admission of gases. In total, the capacity of the vacuum chamber was estimated to be 11 – 12 L. During operation this volume was evacuated by a diffusion pump (Edwards diffstak 100M), mounted on the lower 150 mm port, which in-turn was backed by a mechanical rotary pump (Edwards, E2M8). A base pressure of 10^{-5} mbar was typically achieved, and was monitored by a Penning pressure gauge (Edwards). (Note: this pressure gauge was subsequently removed as a source of magnetic fields as discussed in chapter 3.) Overnight, and when the experiment was not running, the chamber was roughed by a second mechanical rotary pump, maintaining a pressure of 10^{-2} mbar. A tube of μ-metal shielding was inserted into the chamber spanning the length between the two T-pieces. This isolated the centre of the chamber from any stray magnetic fields, including the Earth's own geomagnetic field. Chapter 3 will provide a more detailed demonstration of how magnetic fields can affect the PS measurements. A gated photomultiplier tube (PMT 1, EMI, 9813QB) was also attached directly to the chamber *via* the upper 150 mm port, which facilitated the identification of spectroscopic lines *via* laser-induced fluorescence (LIF). The PMT was contained in a darkened housing with μ-metal shielding. The two remaining 150 mm ports were sealed with blank CF flanges.

All gases were admitted *via* the T-pieces into the vacuum chamber. These included the collider gases (He, Ar, Xe, N_2 and O_2: 99.9 % purity, BOC Ltd.) and the HNO_3 (69% w/v, Aldrich) precursor for the OH experiments, which was contained in a custom-made glass bubbler vessel (see figure 2.3).

Figure 2.3: *Photograph of the bubbler unit used to contain the HNO_3 liquid. It consists of two separate bulbs, which were sealed using vacuum grease when running experiments. A partial flow of the collider gas was guided through the precursor via a glass tube with a sintered tip. The graduation mark in the lower bulb was approximately 50 ml and equalled the capacity of the upper bulb. This safety measure prevented any unwanted upstream back-flows.*

All collider gases were fed directly from their cylinders *via* Teflon tubing. A mass flow controller (MFC1, MKS, 1000 s.c.c.m.) was used to control the partial pressure of the collision partner in the chamber by adjusting the flow rate at constant pumping speed, which was maintained by throttling the diffusion pump. The specification of the MFC allowed the tuning of the partial pressure over the range required for the experiments for all collision partners, which was typically in the range 200 – 2000 mTorr. Upstream of MFC1, a partial flow of the collision partner was fed into the bubbler unit *via* a second MFC (MFC2, MKS, 10 s.c.c.m.). The precursor was entrained in this partial flow as it passed into the chamber. Typically, the partial pressure of the precursor mixture was set to 5 – 10 mTorr prior to introduction of the collision partner.

2.2 Laser Systems

The experiment employed three laser systems in total, all operating at 10 Hz. A *photolysis* laser was required to photodissociate the HNO_3 precursor; a *pump* laser was

used to polarise the diatomic radicals (state specifically), generating an orientation or alignment; and a *probe* laser was used to interrogate the prepared anisotropy remaining after a given pump-probe delay time. Because the laser systems had ns temporal resolution it was crucial that the pump and probe beams were generated from two independent systems to ensure the delay times were substantially larger than the pulse lengths to allow faithful measurements of the collisional evolution of the prepared rotational anisotropy. In all measurements the pump and probe beams counter-propagated the photolysis beam, but co-propagated with each other along the main axis of the vacuum chamber.

2.2.1 Photolysis Laser

An excimer laser (Lambda Physik, Compex 102) served as the photolysis source. The optically active gas mixture was Ar and F_2 which produced 193 nm laser light upon dissociation of the ArF* exciplex. The gas mixture also contained He and Ne, which acted as inert and buffer gases, respectively. Initially the F_2 was provided by a dedicated solid-state source but this was latterly replaced with an F_2 gas cylinder (5% F_2 in He). The output laser beam had a rectangular cross-section, approximately 30 mm in height and 10 mm wide. The maximum energy per pulse was approximately 180 – 200 mJ, which was achieved after maintaining the optics of the laser cavity. When running the experiments, the excimer was operated on *energy constant* mode which maintained a user defined output energy by altering the discharge voltage (typically 25 – 30 kV) accross the laser cavity. Usually this was set between 60 and 120 mJ. However, the energy of the UV beam which entered the vacuum chamber was substantially lower than this due to loss at each reflective face of optics and also the absorption by the laboratory atmosphere. Absorption of the UV by O_2 in the atmosphere results in approximately an 80% reduction in the 193 nm intensity over an approximate path length of 3 – 4 m ($\sigma_{O_2}^{193} \approx 2\times10^{-21}$ cm^2 molecule^{-1}) [125].

The main photodissociation pathway of HNO_3 at 193 nm is:

$$HNO_3 \rightarrow OH\ (X^2\Pi) + NO_2, \qquad \lambda < 602 \text{ nm},$$

but other dissociation pathways produce the following products in various stoicheometric proportions: HONO, O(^{1}D)/O(^{3}P), NO_3, H (^{2}S), NO, NO_2, and O_2 [126,127]. The absorption cross-section is approximately 1.3 x 10^{-17} cm^2 and the

quantum yield of OH ($X^2\Pi$) is in the region of 0.47 ± 0.07 [128]. Approximately 86% of the available energy remaining after photodissociation ($E_{available}$ = 35569 cm^{-1}) is deposited into internal energy of the NO_2 [128]. There is therefore no formation of OH ($A^2\Sigma^+$) and only 5% of the OH ($X^2\Pi$) is formed in v = 1 [129]. The OH photofragments are, however, translationally hot, with $<E_{trans}>$ estimated to be 2332 cm^{-1}, and have a statistical rotational distribution with a temperature of approximately 1000 K [128].

2.2.2 Pump Laser

The pump laser beam was produced by a Nd:YAG-pumped tuneable dye laser system. The second harmonic (532 nm) of the Nd:YAG (Surelite II-10, Continuum Ltd.) laser, which provided 230 mJ $pulse^{-1}$ of s-polarised light (vertical in the lab), was used to pump the dye laser. A separating unit positioned after the main laser output reduced or eliminated the residual fundamental (1064 nm) before entering the dye laser.

The dye laser (Cobra-Stretch, Sirah) had two dye cuvettes; an oscillator and a main amplifier. Both of these were continuously refreshed with dye solution by a mechanical pump and transversely pumped by the incoming radiation provided by the Nd:YAG. The stimulated emission from the oscillator cuvette irradiated a single grating (2400 grooves mm^{-1}) and reflecting mirror, which were used for wavelength selection. The laser beam created from this resonator leaked from an output coupler, through 3 Brewster's-angle plates and was guided by a 180° prism back into the oscillator cuvette, but through a different volume element from the oscillator path. This served as pre-amplification before the laser beam passed through the main amplifier cuvette. Typically the main amplifier provided a factor of 5 – 10 amplification. All laser dyes used in this work produced visible laser light and required frequency conversion to produce the ultraviolet (UV) wavelengths suitable for electronic excitation of OH.

The frequency conversion unit (FCU) was bolted to the output port of the dye laser for second harmonic generation (SHG). This contained a doubling crystal (KD*P), a quartz compensator to compensate for the altered beam alignment, and a Pellin-Broca assembly which functioned as a separating unit. To achieve phase matching conditions for SHG, the doubling crystal was rotated on a stage to effectively alter the laser beam incidence angle on the crystal face. This crystal position was calibrated to the fundamental wavelength for maximum conversion. The compensator was, in-turn, geared to the motor position of the doubling crystal to minimise 'walking' of the laser

beam. The final output was always horizontally polarised (>98%) in the laboratory frame and usually yielded 1 – 5 mJ of UV, which was more than ample for the PS measurements. The bandwidth was determined to be ≤ 0.3 cm^{-1} by scanning over a known OH spectroscopic transition, using LIF for detection.

2.2.3 Probe Laser

The probe laser system was essentially identical to the pump laser system in concept, so only the differences between them will be highlighted. The Nd:YAG laser (Spectra Laser Systems, SL800) produced approximately 200 mJ $pulse^{-1}$ of 532 nm. The only substantial difference between the dye lasers was the grating. This laser had a dual, instead of a single, grating system, each with a groove density of 2400 grooves mm^{-1}. The laser system produced approximately 1 – 3 mJ $pulse^{-1}$ of UV and was horizontally polarised in the lab. In a similar fashion to the pump beam, the probe bandwidth was determined to be ≤ 0.15 cm^{-1}. This is still a factor of ~ 3 greater than specification despite considerable effort to reduce it. The reduced bandwidth in comparison to the pump is primarily because of the dual grating, but it is also sensitive to the oscillator dye cell alignment and pulse shape of the pump beam.

The temporal profiles of both the pump and probe UV pulses are shown in figure 2.4. Both waveforms were recorded using a fast photodiode (EOT, ET200, risetime: < 200 ps) and an oscilloscope (LeCroy waverunner 44xi, 10 GS/s) and are representative of ~ 308 nm by frequency doubling. Full width at half maximum (FWHM) pulse widths were determined to be ~6 ns and ~15 ns for the pump and probe respectively.

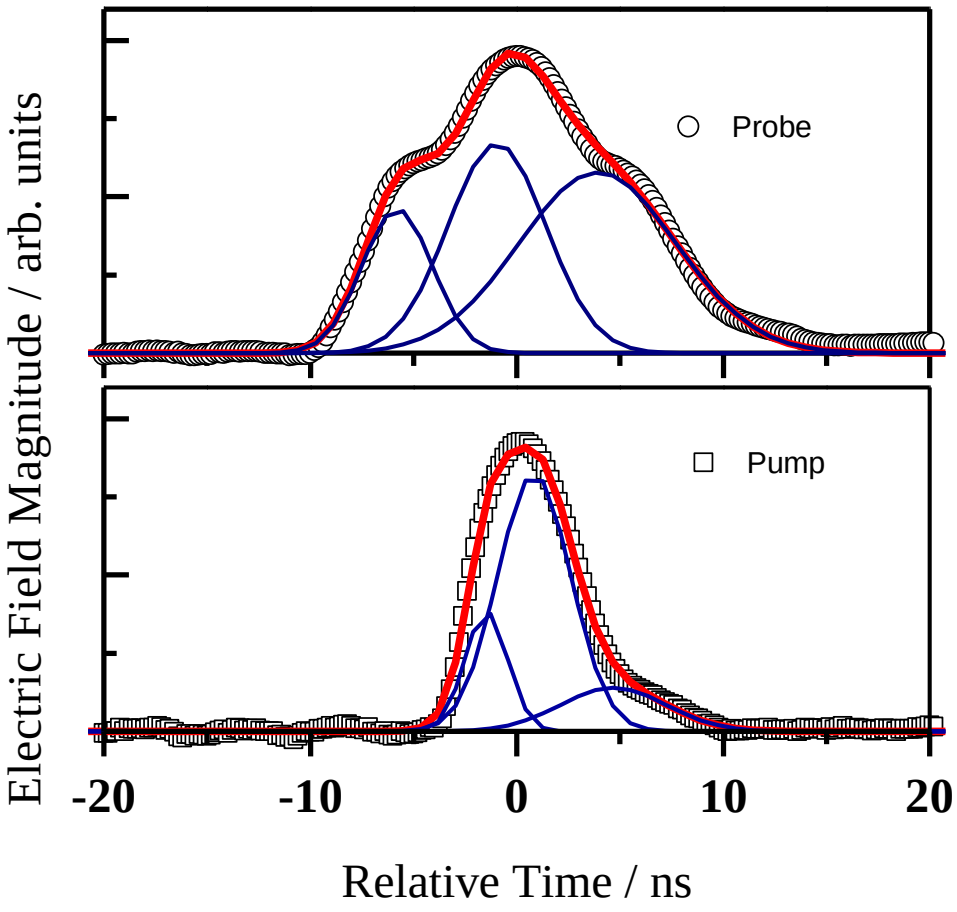

Figure 2.4: *Temporal profiles of (a) probe and (b) pump laser pulses. The waveforms were fit best using a sum of three Gaussian functions (red). The decompositions of the fits are also shown (navy). The peak centres, peak amplitudes and the standard deviations were used to fit the experimental data.*

2.3 Polariser Housings

The polariser housings were milled from aluminium blocks and each contained high extinction ratio polarisers (10^{-6}, Glan-Taylor α-BBO, CASIX, Inc.), which were held in precision rotation stages and secured to vacuum compatible mounts (figures 2.5 and 2.6). Having the polarisers *within* the vacuum system ensures that changes to the polarisation state of the probe beam, caused by stress-induced birefringence in the windows, were eliminated. Each polariser housing had two entrance windows, one in line with the main axis of the chamber and the other on a perpendicular face (side window). Both polarisers were mounted on the vacuum side of the chamber next to the

windows in-line with the main axis. The first polariser was contained in the *setting polariser housing* and was employed to define the linear polarisation of the probe beam, which was geometrically offset by 45° with respect to the pump beam polarisation. The second, 'analysing polariser', was crossed with respect to the setting polariser (orthogonal to the input probe polarisation) and resolved the signal and probe beams. In practice there was usually a small amount of probe 'leak-through'. Each polariser had coarse adjustment and a fine control feature covering a range of ± 2°. A feed-through connected to the fine adjustment on one of these polarisers and allowed user control under vacuum. This was necessary when stress on the vacuum fittings, induced by mechanical pumping, slightly perturbed the position of the polariser mounts. A schematic of the polariser housings is provided in figure 2.5.

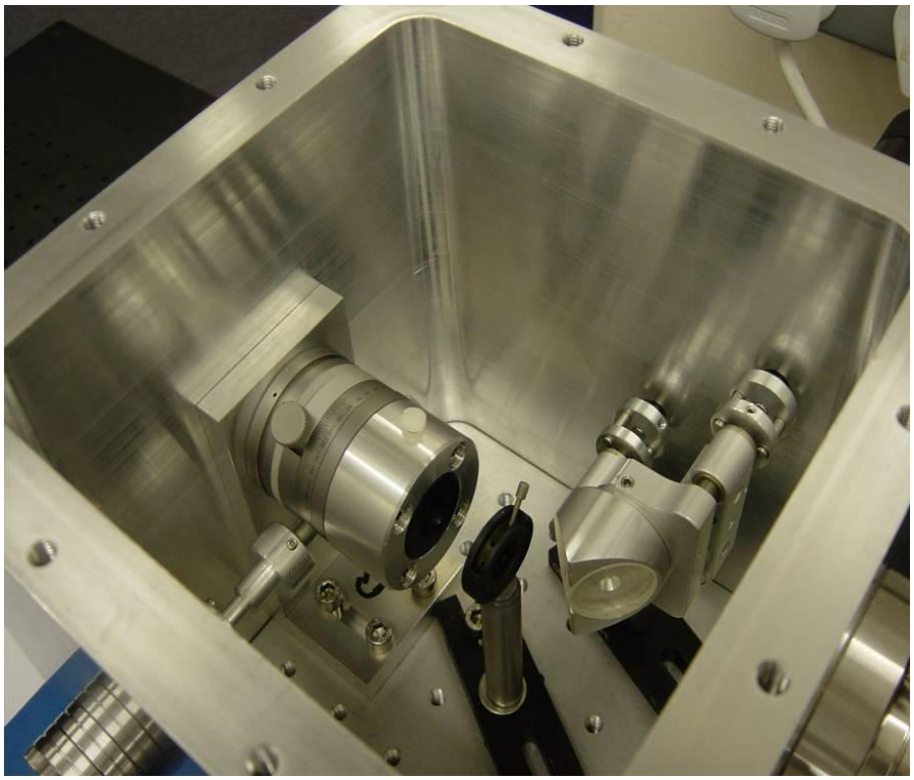

Figure 2.5: *Photograph of the analysing polariser housing. When the chamber is sealed this is covered with a Perspex lid. This shows the polariser in the rotation stage and a turning mirror, which is used to guide the photolysis laser through the chamber. An iris is positioned before the polariser to assist in alignment of the probe beam, but also to block the pump laser beam and reduce pump scatter.*

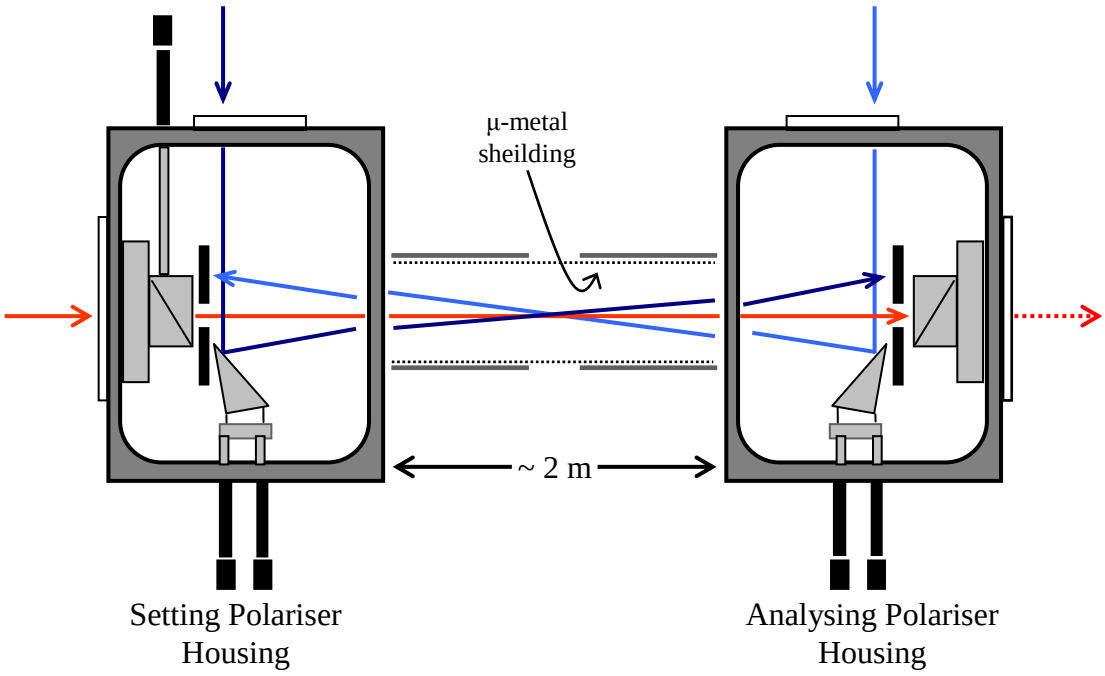

Figure 2.6: *Schematic diagram of the polariser housings. The photolysis (light blue), probe (red), and pump (dark blue) laser beam alignments are shown. The signal beam is represented by the broken red line leaking from the analysing polariser.*

The side windows of the setting and analysing polariser housings allowed the entrance of the pump and photolysis beams, respectively. Both beams were guided down the length of the chamber by highly reflective 25.4 mm diameter turning mirrors, which were secured in vacuum compatible mounts near the opposite face from the window. These turning mirrors were connected to 'feed-throughs' enabling the user to have control of the beam alignment under vacuum. The excimer beam illuminated a column through the chamber arms and the pump beam crossed the path of the pump at an acute angle (~0.3°). All laser beams crossed at the centre of the six-way-cross and provided an overlapping path length of approximately 1 m.

2.4 Laser Beam Alignment

After the photolysis beam exited the excimer laser it was necessary to collimate it due to its large spatial profile. This was achieved by passing the beam through a pair of cylindrical lenses (Laser Components) which reduced the beam cross-section to approximately 1 cm^2. Highly reflective mirrors (> 98%, Laser Components) were used

to steer the beam through this lens assembly and then into the chamber. Before entering the side window of the analysing polariser housing, an iris selected a section of the beam which was ~ 1 cm in diameter.

Both the pump and the probe UV outputs were beam expanded using a standard telescope set-up. The central portions of the beams, roughly 3 – 4 mm in diameter, were selected using irises. Each beam was guided through an attenuation assembly before entering the chamber. In the pump path this was a double Fresnel rhomb and polariser combination. The polariser was set to transmit vertically polarised light in the laboratory frame. Turning the Fresnel rhomb around its axis altered the polarisation state of the pump beam and hence resulted in an increase or decrease of the intensity of light after the polariser. A similar attenuation scheme was used in the probe beam path, but a Babinet-Soleil compensator was used in place of the Fresnel rhomb. Highly reflective turning mirrors suitable for the particular wavelengths were used to guide the beams through the appropriate optics and into the chamber *via* the designated entrance ports described in the previous section.

For orientation measurements, the pump beam propagated through a Berek's compensator variable wave-plate directly before entering the side window of the setting polariser housing. This was used to provide the required circular polarisation. The key to this, however, was not to have circular polarisation going *into* the chamber, but rather, to have circular polarisation *throughout* the length of the chamber after passing through the side-window and being reflected by the turning mirror in the setting polariser housing. To achieve this, the Babinet-Soleil componsator was first set to be a λ/4-waveplate and was positioned after the analysing polariser, outside the vacuum chamber. The analysing polariser was removed from the chamber, mounted in a suitable rotation stage and positioned after the Babinet-Soleil λ/4-waveplate. The pump laser beam was then directed through this optical set-up i.e. through the Berek's compensator prior to the side window of the setting polariser housing, along the length of the chamber and through the Babinet-Soleil compensator and polariser. Altering the orientation and retardance of the Berek's compensator converted the linear polarisation to some form of elliptical polarisation. When the pump laser beam had circular polarisation throughout the length of the chamber a null would be observed after the polariser positioned after the Babinet-Soleil. The optics and laser beams were then re-configured for experiments.

The signal beam generated during the experiment from the interaction of the pump and probe beams was transmitted through the analysing polariser and was guided approximately 3 m, using high reflective turning mirrors, to a side-on PMT contained in a darkened housing (PMT 2, R166UH, Hammatsu). This distance, together with a spatial filter, helped reduce or eliminate scattered pump radiation.

2.5 Timing and Data Acquisition

For the majority of experiments all operations were controlled with a dedicated experimental PC, which communicated with timing and data acquisition modules *via* a CAMAC (Computer Automated Measurement and Control) interface, using custom designed LabVIEW programmes. A pulse generator provided trigger pulses at 10 Hz for two LeCroy delay generators (4222 PDG) simultaneously, which in-turn produced +5 V TTL pulses at user-defined delays with respect to the input trigger pulse. A custom designed line driver was used to manipulate the voltage and polarity of these pulses to meet the requirements of individual laser systems.

The PS signal was collected with PMT 2 and transferred to a gated integrator and boxcar averager (Stanford Research Systems SR240), which integrated the signal over a given time-gate. This information was digitised using an A/D converter (Hytec, ADC520) and passed to the PC over the CAMAC interface.

The delay between the photolysis and pump lasers was fixed at ~10 μs for all of the OH experiments, to allow for sufficient translational thermalisation. It is crucial that the experiments were performed under isotropic and thermal collision energy conditions. The LabVIEW programme then scanned the pump-probe delay in a pseudo-random fashion with a precision of 1 ns, to counter the effects of any systematic drifts in experimental conditions. Typically, 5 signal shots were acquired at a chosen pump-probe dime delay and the average of these was recorded before another pseudo-random delay was chosen. The probe leakthrough, acquired prior to running the delay scan, was subtracted from each of these averaged data points. A user defined total number of points were recorded such that reliable statistics were acquired for each time delay; usually this was approximately 25 – 35 shots per point. This meant that each specific time delay was chosen, on average, 5 – 7 times. The user also had control over the time resolution of each delay scan (time interval), and also the span of the time-base. This enabled more efficient running of the experiment and avoided the collection of

superfluous information when there was already sufficient signal-to-noise, or if the decay of the PS signal was rapid. When the delay scan was complete all data points at a given time delay were averaged and a sorted (with respect to pump-probe delay time) spreadsheet was saved. This decay trace was then used in the subsequent data analysis. If there was any significant pump laser scatter, then a high S/N pump background would be collected separately, but using the same routine as above. This produced a profile which reflected the pump scatter contribution to the decay curve. Crucially, it only contributed to the ~ 20 – 50 ns interval between the signal gates. The length of the signal gate was not representative of the laser pulse lengths; it was specifically set to assist in the subtraction of the pump-scatter background trace from the raw PS decay trace.

2.6 Data Analysis

All PS data were fitted using the previously derived theoretical descriptions of one-colour and two-colour PS [71,72]. A custom-written programme (FORTRAN) essentially forward simulated the PS decay trace by computing the signal electric field for each experimental pump-probe delay and assuming an initial trial decay rate. The temporal pulse profiles of the lasers were accounted for by Monte-Carlo selection from a weighted sum of three Gaussian functions, matching those determined experimentally (figure 2.4). Nuclear hyperfine quantum beats (NHQBs) were also included; the energetic splitting of the hyperfine levels and hence the frequencies of the quantum beats were determined from literature data [130]. The calculated PS decay trace was then normalised to the experimental data by requiring them to share a common area. A one-dimensional golden-search algorithm was then used to adjust the calculated PS decay rate to minimise the χ^2 deviation between experiment and simulation until a user-defined tolerance was satisfied. Typically 15 – 20 iterations were required. An example input file for this fitting routine is provided below (table 2-1). Figure 2.7 illustrates the quality of the fit to a typical PS decay trace. The returned decay rate is given the following symbol: $\Gamma_{PS}^{(K)}$. Here *K* denotes the spherical tensor rank describing the density matrix that is produced by the interaction of the OH ensemble with the pump photons and detected by the probe. $K = 1$ describes orientation and $K = 2$ describes alignment (see sections 1.1.4 and 1.2.2).

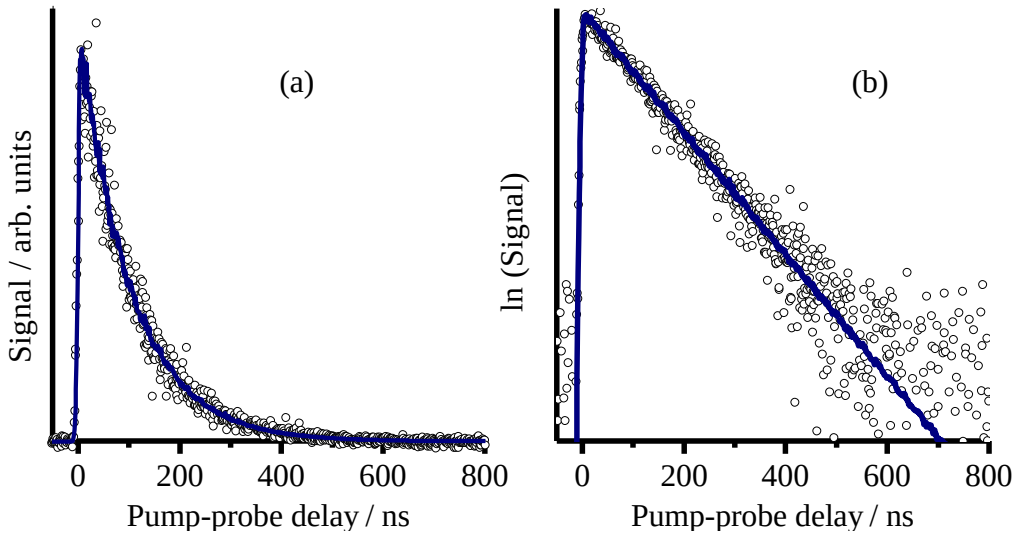

Figure 2.7: *(a) Example PS decay trace. Averaged data points (open circles) are presented together with the fit (solid line) using the previously developed theoretical model. This specific example is for OH($X^2\Pi$, v = 0, j = 5.5) + Ar (300 mTorr), recorded with linear pump polarisation. (b) Same decay trace represented on a semi-log plot. This highlights the excellent single-exponential fit to the data.*

Table 2-1: *Example input file for fitting the experimental PS data.*

32390.9			Wavenumber of probe laser
35377.8			Wavenumber of pump laser
-105.0e-9			Start time of probe laser / s
-0.3592	0.9127	5.357	Centres of pump gaussians / ns
1.56	1.855	3.725	s.d. of pump gaussians / ns
2.847	1.885	0.983	Amplitudes of pump gaussians
-4.443	-1.232	2.787	Centres of probe gaussians / ns
1.5075	1.72	4.01	s.d. of probe gaussians / ns
0.415	1.749	4.618	Amplitudes of probe gaussians
400			No. of time steps
1.5			Initial state J
0.5			Excited state J
0.5			Final state J
1			Initial state spin manifold
1			Excited state spin manifold
1			Final state spin manifold
L			Pump Polarisation (L / C)
53.171e6			Ground state hf splitting / Hz
298			Temperature of System
0.017			Molar Mass
1e-02			Tolerance for fit (>1e-07)
123474389			Seed random number
20000			No. of Monte Carlo iterations
2111200701.sub			Input data filename
2111200701.fit			Output fit filename
2111200701.txt			Output rate filename

Chapter 3

Influence of Stray Magnetic Fields

The effect of magnetic fields on PS measurements was first highlighted by G. Richmond [123] in the latter stages of his PhD research project; however, no conclusive demonstration was achieved at that time. This chapter provides an overview of the influence of magnetic fields on diatomic rotational polarisation, focusing on the consequences for PS studies. A qualitative demonstration of a simple experimental cure is also provided, which is used in all subsequent studies discussed in this thesis. The measurements discussed in this chapter were published as a communication [131].

3.1 Introduction

The interaction of external magnetic fields with molecular species is, of course, well known as the Zeeman effect. This forms the basis of many microwave spectroscopic techniques used to determine molecular and spectroscopic constants [11], and is also the underlying principle of nuclear magnetic resonance (NMR). For the scope of this chapter though, attention will be focused on *electronic*, rather than nuclear, responses to the magnetic field. The resulting magnetic dipole moment of a molecule, formed through the coupling of various electronic angular momenta (Hund's cases), interacts with external magnetic fields. The Hamiltonian of the perturbation is described by the following dot product:

$$H' = -\boldsymbol{\mu}^{(m)} \bullet \boldsymbol{B}$$

(Equation 3- 1)

where the tensors, $\boldsymbol{\mu}^{(m)}$ and $\boldsymbol{B}$ are the magnetic dipole operator and the magnetic field, respectively. For diatomic molecules this perturbation will remove the degeneracy of the m_J sub-levels (hence their designation as *magnetic* sub-levels), resulting in $(2J + 1)$ equally spaced energy levels, with separations directly proportional to the magnetic dipole moment of the molecular quantum state and the strength of the magnetic field [92,132]. In general, if the magnetic field is uniform then the bulk rotational polarisation, produced by the pump laser beam in PS experiments, will precess about the external field direction, $\boldsymbol{B}$, at the Larmor frequency, ω_L. This classical precession frequency is related to the energy separation, ΔE, of the projection quantum states [19]*:*

$$\frac{\Delta E}{hc} = \frac{\omega_L}{2\pi} = \frac{g_J \mu_B B}{h}$$

(Equation 3- 2)

Here μ_B is the Bohr magneton$\left(\frac{e\hbar}{2m_e} = 9.274 \times 10^{-24}\ \mathrm{J\,T^{-1}} \right)$ and g_J is the Landé *g*-factor for the rotational quantum state.

At a quantum level, the projection quantum levels are excited coherently (because the energy separation is smaller than the spectral bandwidth of the lasers used) and the states of different energy have definite phase relationships. Consequently, phase accumulation will result in oscillations in measurements which are sensitive to the sub-elements of the density matrix. In the time-domain this gives rise to Zeeman quantum beats (ZQBs), analogous to the nuclear hyperfine quantum beats (NHQBs) discussed in section 1.2.2. Similar to the NHQBs, they do not result in true depolarisation i.e. tendency towards an isotropic rotational distribution. In fact, experiments designed to measure these ZQBs, under conditions of known applied magnetic fields, have been widely used to determine excited state Landé *g*-factors [133], and more recently to study the collisional evolution of rotational alignment [134].

However, stray magnetic fields accidentally present in a typical experimental apparatus are likely to be *inhomogeneous* across the interaction region. These result in a range of precession frequencies that may combine to give a net phenomenological depolarisation. For an experiment measuring angular momentum polarisation kinetics, this will result in non-exponential behaviour, and for a product polarisation study under ‘single-collision’ conditions it provides a mechanism, even in the absence of secondary

collisional depolarisation, which can potentially destroy orientation or alignment. Inhomogeneous magnetic fields can therefore significantly corrupt experimental results of the type that the work of subsequent chapters aims to address.

3.2 Experimental

A consequence of magnetic fields interacting with rotational polarisations in the PS measurements is to destroy the spatial symmetry imposed by the interaction of the pump laser with the ensemble of diatomic radicals. Therefore, a comparison of two different experimental geometries (figure 3.1) should reveal any effect which breaks the spatial symmetry. Both of these geometries involve linear pump laser polarisation and, as always, linear probe laser polarisation. In the experimental apparatus, the pump polarisation can be aligned either horizontally or vertically in the laboratory frame, with the probe at 45° to the pump for maximum signal-to-noise. As long as the external magnetic field does not accidentally happen to lie parallel to the electric field of the probe laser, $\boldsymbol{\varepsilon_{probe}}$, then measurements with vertical and horizontal pump polarisation should demonstrate if the spatial symmetry of the experiment has been destroyed.

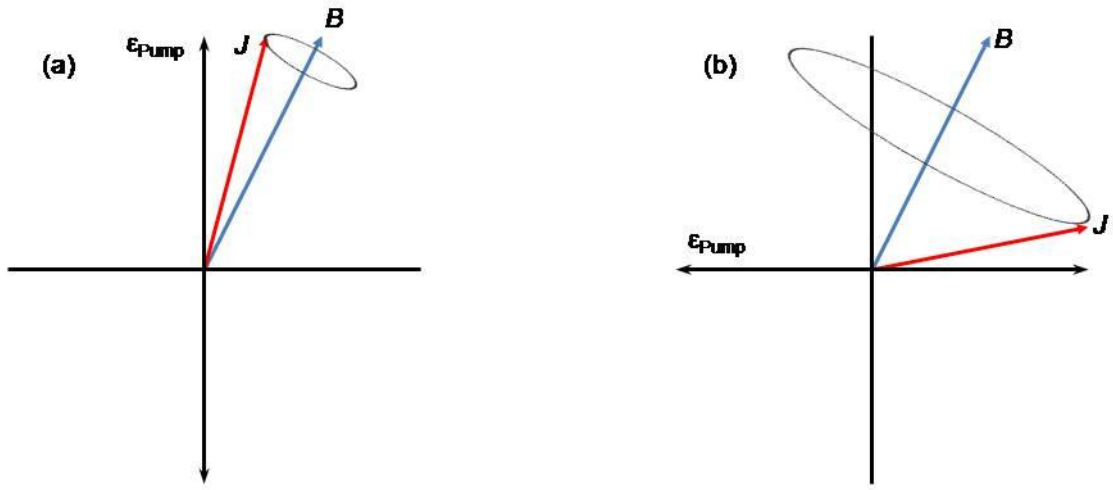

Figure 3.1: *Simple vector representation of Larmor precession of a rotational angular momentum vector, J, about an external magnetic field, B. The pump laser polarisation is (a) horizontal and (b) vertical in the laboratory frame. This illustrates how a fixed magnetic field can affect the same rotational polarisation prepared in two different reference frames.*

PS pump-probe delay traces for OH (X) + He were recorded using the two experimental geometries outlined in figure 3.1. In addition, experiments were performed with and without 'mu-metal' magnetic shielding (Magnetic Shields Ltd). Mu-metal is a high-permeability Ni / Fe / Mo alloy, making it an efficient screen for magnetic fields (figure 3.2). To shield the interaction region formed by the overlap of the three laser beams, whilst still allowing diffusion of the gas mixture, the mu-metal sheet (thickness 0.35 mm) was formed into a loosely coiled cylinder of two layers, with a gap between the layers greater than the thickness of the metal. The inner diameter of this cylinder was ≈ 3.3 cm, enabling the laser beams to pass unhindered. The length was ≈ 1 m, completely enclosing the interaction region.

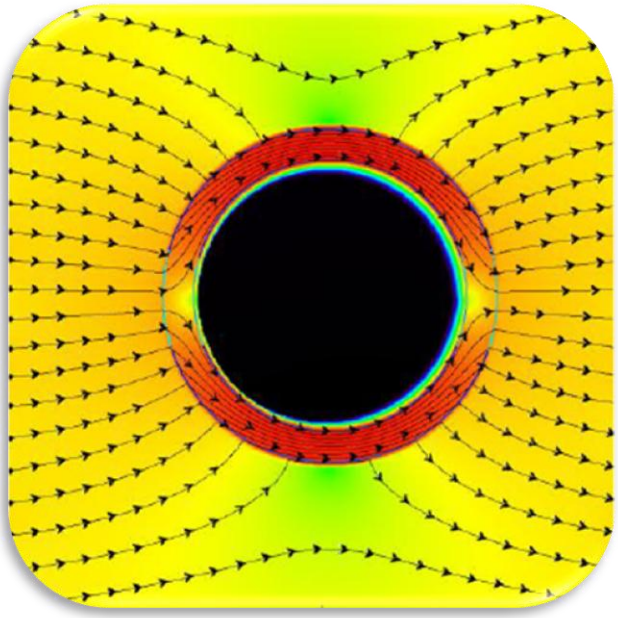

Figure 3.2: *Schematic field diagram illustrating how a hollow cylinder of mu-metal can isolate the centre of the cylinder from magnetic fields [135].*

All the measurements here were made using OCPS with linearly polarised pump and probe light centred on the OH A $^2\Sigma^+ \leftarrow$ X $^2\Pi$ (0,0) $P_1(2.5)$ spectroscopic transition at 308.64 nm. The results of the previously published theoretical work were used to fit the experimental data as discussed in section 2.6. At low-*j*, the OCPS signal from P-branch transitions is much more sensitive to bulk polarisation created in the electronic ground state than in the excited state. The effects of NHQBs were included using mathematical descriptions of the temporal profiles of both the pump and probe laser pulses (see section 2.2).

3.3 Results

Initially experiments were performed without any special precautions to reduce magnetic-field effects, such as magnetic shielding, but also without any conscious attempt to introduce strong fields. Figure 3.3 shows PS signals for a He collider pressure of 280 mTorr, together with the best fit to the theoretical model, with the linear pump polarisation defined as either horizontal or vertical in the laboratory frame. The oscillations with a period of ≈ 70 ns are the result of NHQBs, and are fully accounted for in the theoretical model. In figure 3.3(a) the results are displayed in a linear plot, clearly showing that the signal for horizontal pump polarisation decays faster than that for vertical polarisation. In figure 3.3(b) the same results are plotted on a semi-$\log_{10}$ scale, which shows that the deviation between pump polarisations is the result of the horizontal pump polarisation data decaying in a non-exponential fashion, contrary to the theoretical model. Consequently these data are not well described by the fits to the theoretical model, most notably at longer times, unlike the vertical pump polarisation data.

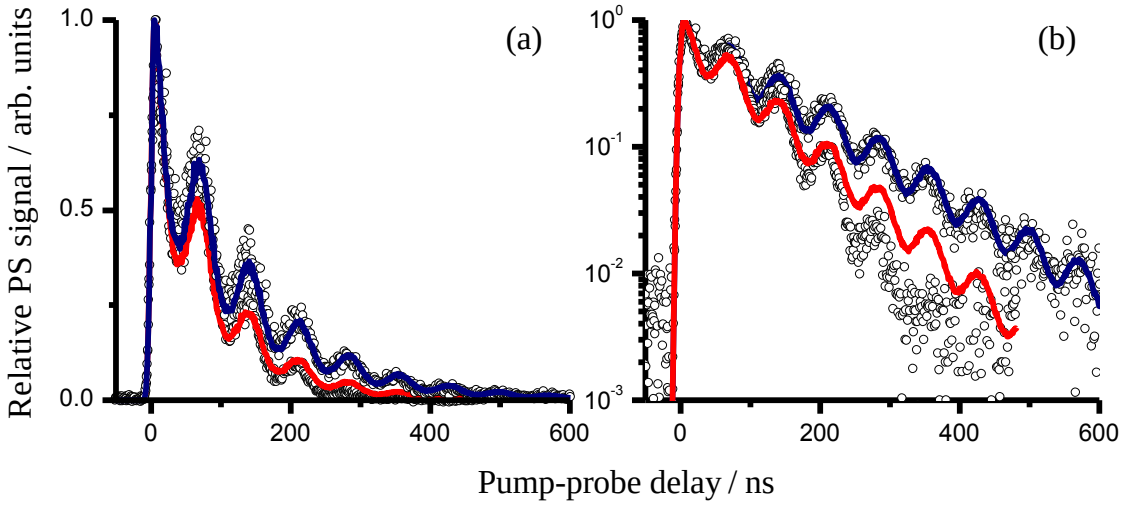

***Figure 3.3**: PS signals as a function of pump-probe delay for OH $A^2\Sigma^+$ - $X^2\Pi$ (0, 0) $P_1(2.5)$ using linear pump polarisation, without magnetic shielding of the interaction region. (a) linear y-axis scale (b) log10 y-axis scale. Open circles represent the raw data points and the solid lines represent the fit to the data for horizontal pump polarisation (red) and vertical pump polarisation (blue).*

A dependence of the signal decay rate on the direction of the pump polarisation can clearly only arise if there is an external effect breaking the spatial symmetry of the experiment, as discussed above. Measurements with a Gaussmeter (Redcliffe Magnetronics Ltd.) in the centre of the vacuum chamber showed that magnetic fields of order 50 – 100 μT were present, similar to, or slightly larger than, the geomagnetic field in Edinburgh. The phenomenological decay rates, resulting from fits to the pump-probe delay scans at a range of collider pressures (250 – 1500 mTorr) with both pump polarisations, are shown in figure 3.4, together with linear fits to extract second-order depolarisation rate constants, $k^{(2)}_{OCPS}$. As can be seen from figure 3.2, the plots for the two pump polarisations have similar slopes, $k^{(2)}_{OCPS}$ = 1.9 ± 0.2 x 10^{-10} cm^3 s^{-1} and $k^{(2)}_{OCPS}$ = 1.6 ± 0.1 x 10^{-10} cm^3 s^{-1} for vertical and horizontal, respectively. Quoted uncertainties represent 95% confidence limits obtained through the linear regression fit. However, a marked vertical displacement of the horizontal pump polarisation line above that for vertical pump polarisation is seen, representing different zero collider-pressure intercept rates, $\Gamma^{(2)}_{Intercept}$ = 2.3 ± 0.4 x 10^6 s^{-1} and $\Gamma^{(2)}_{Intercept}$ = 3.8 ± 0.4 x 10^6 s^{-1} for vertical and horizontal, respectively. The intercept rate is expected to have a contribution from collisions with the precursor HNO_3/H_2O (≈ 30 mTorr pressure), which on the basis of literature rate constants is estimated to be ≈ 2 x 10^6 s^{-1} [136,137] (see also chapter 4). This is consistent with the vertical pump polarisation results, but it seems clear that the horizontal pump polarisation intercept has been increased significantly by a non-collisional process.

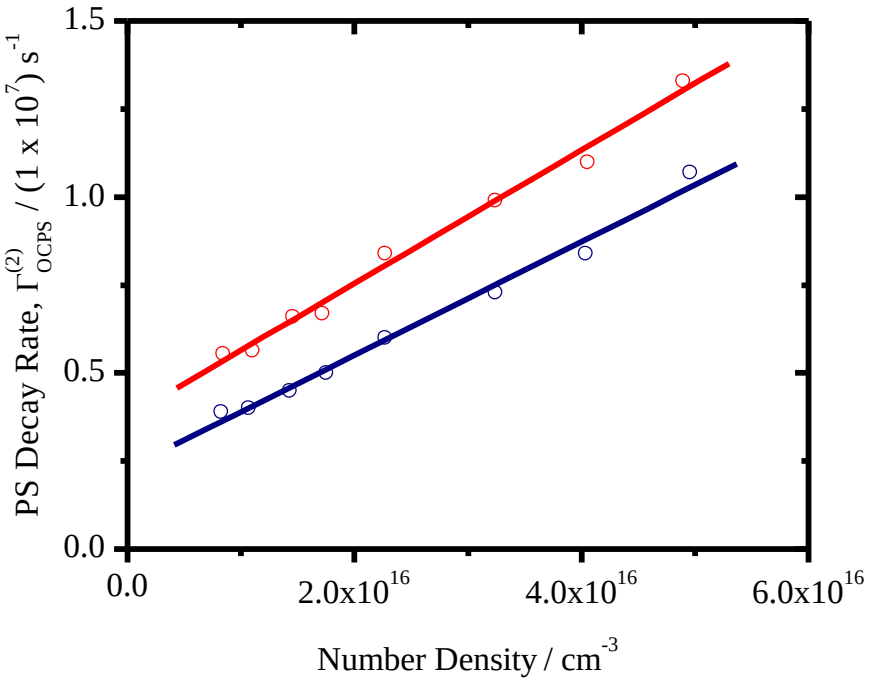

Figure 3.4: *Pseudo first-order rates,* $\Gamma^{(2)}_{OCPS}$*, for the removal of OCPS signal versus collider number density without mu-metal shielding. Filled and open circles represent horizontal and vertical pump laser polarisation respectively. The solid lines represent the corresponding fits to the data to yield the second-order PS signal loss rate constant,* $k^{(2)}_{OCPS}$ *.*

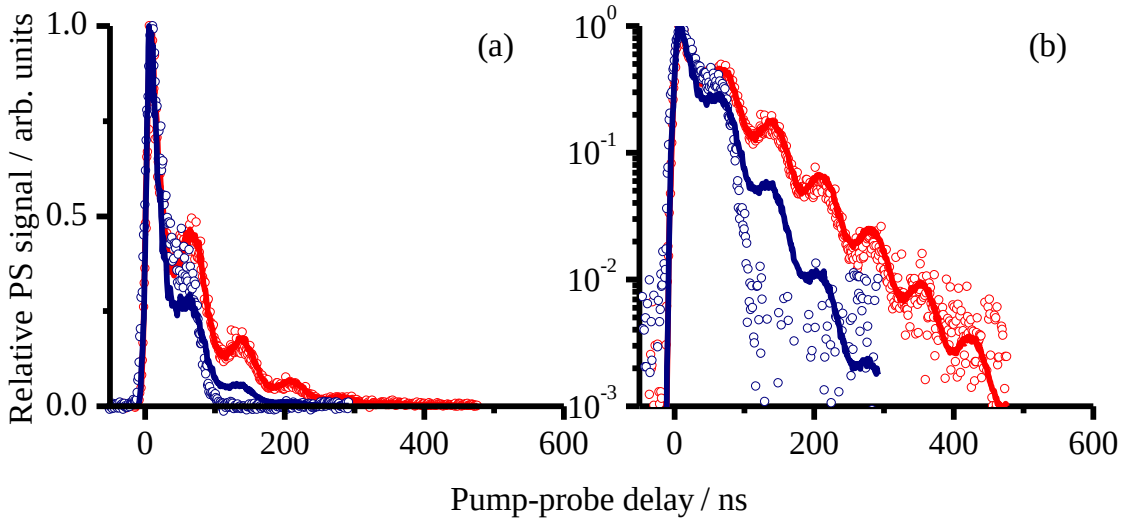

Figure 3.5*: PS signals as a function of pump-probe delay for OH* $A^2\Sigma^+$*-* $X^2\Pi$ *(0, 0)* $P_1(2.5)$ *using linear pump polarisation, with an applied magnetic field. (a) linear y-axis scale (b)* log_{10} *y-axis scale. Open circles represent the raw data points for horizontal pump polarisation (red) and vertical pump polarisation (blue), the solid lines represent the fit to the data.*

To test empirically whether the observed behaviour was indeed consistent with the presence of external magnetic fields, a strong permanent magnet (an optical mount base), was introduced external to the chamber but as close as possible to the centre of the six-way cross. This resulted in an inhomogeneous field across the interaction region which varied between 1 – 3 mT, with the major field axis horizontal in the laboratory. Figure 3.5 shows the results of PS pump-probe delay scans with both pump polarisations at a He collider pressure of 350 mTorr. These reveal a much faster and clearly non-exponential decay, which in this case is faster for vertical than horizontal pump polarisation, such that the theoretical model noticeably fails to reproduce the observed decay.

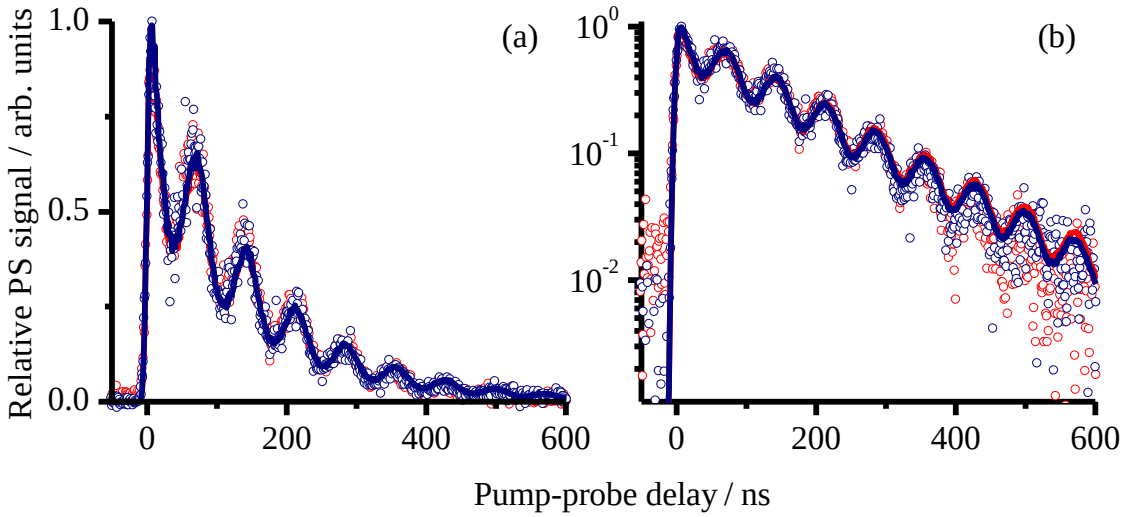

Figure 3.6: *PS signals as a function of pump-probe delay for OH $A^2\Sigma^+$ - $X^2\Pi$ (0, 0) $P_1(2.5)$ using linearly polarised pump radiation, with magnetic field sources minimized and mu-metal shielding introduced. (a) linear y-axis scale (b) log10 y-axis scale. Open circles represent the raw data points for horizontal pump polarisation (red) and vertical pump polarisation (blue), the solid lines represent the fit to the data.*

Subsequently the permanent magnet was removed, together with any other obvious sources of significant magnetic fields. With the aid of the Gaussmeter several other, less obvious, sources of local magnetic fields, such as small ferrous-metal bolts were traced. Finally, the magnetic shielding was introduced, after which the magnetic field in the chamber was essentially immeasurable within the sensitivity of the Gaussmeter (< 10 μT). The horizontal and vertical pump polarisation scans were then repeated again at 280 mTorr He collider pressure, and are shown in figure 3.6. Significantly, they are indistinguishable within the experimental signal-to-noise on both linear and $\log_{10}$ scales.

As can be seen from figure 3.6, the model now accurately reproduces the experimental data, and both experimental data sets decay in a purely exponential fashion.

3.4 Discussion

Clear evidence has been provided to show that external magnetic fields are capable of depolarising the prepared alignment of low-*J* ground state OH radicals on an experimental timescale of a few hundred ns, even when no particularly obvious source of a magnetic field was present. These results can be rationalised by considering more closely the time evolution of rotational polarisations in the presence of a homogeneous external field.

Perturbation of the rotational alignment by an external magnetic field is a weak interaction and can be neglected during the instantaneous interaction with the pump laser. Following the PS formalism introduced in section 1.2.2, the bulk rotational polarisation at this time, t_2, can be described by the following second-order density matrix:

$$\rho^{(2)}(t_2) = \sum_{K,Q} \rho_Q^{(K)} T_Q^{(K)}$$

(Equation 3-3)

The ensemble then couples to the magnetic field and propagates in time during the period τ_2. To assess what influence this has on the measurement, the density matrix must first be rotated into the frame of the magnetic field. The field then lifts the degeneracy of the magnetic sub-levels and the density matrix elements evolve by factors of ω_L relative to one another. This ensemble then needs to be rotated into the frame where the measurement is made, which coincides with the quantisation frame at t_2. The second-order density matrix at t_3 (prior to interaction with the probe) therefore has the following form:

$$\rho^{(2)}(t_3) = \sum_{K,q} \rho_q^{(K)} T_q^{(K)}$$

(Equation 3-4)

where the tensor moments in the measurement frame, indicated by lower case projection numbers (the tensor *ranks* are not mixed and so upper case notation remains), are linear combinations of the tensor moments at time t_2 multiplied by a time-dependent Green's function [92]:

$$\rho_q^K(t_3) = \sum_Q \rho_Q^K(t_2) G(t)_K^{Qq}$$

where,

$$G_{(K)}^{Qq}(t) = \sum_{Q'} \exp(-i\omega_L Q' t) D_{Q'Q}^{(K)}(0,\theta,\chi) D_{Qq}^{(K)*}$$

(Equation 3-5)

Here the angles $(0,\theta,\chi)$ are the usual Euler angles specifying the rotation relating the laboratory experimental frame and the applied magnetic field axis, Q' is the projections in the magnetic field frame and the rotation matrix elements have a standard form [19]:

Equation 3-3 indicates that for a tensor rank, $K = 2$ (alignment), there will be a time independent component ($Q' = 0$), a component oscillating at the Larmor frequency ($Q' = 1$) and a component oscillating at twice that ($Q' = 2$), the exact relative magnitudes of which will depend on the angle between the experimental and magnetic field frames.

However, if the field is sufficiently *inhomogeneous* across the volume where the PS signal is generated, the net effect will be an apparent collective decay without a visible recurrence on the observable timescale on which the PS signal is lost through other processes. Even if the field is homogeneous, and the precession timescale is similar to the field-free signal decay time, then the apparent behaviour of the signal will be a faster, non-exponential decay, rather than a clear oscillation and recurrence. Although with higher field strengths, the ZQBs can be rapid in comparison to collisional decay. This is the principal foundation of Zeeman Quantum Beat Spectroscopy (ZQBS) experiments employed by Brouard and co-workers to monitor the collisional relaxation or rotational polarisations [134].

This treatment rationalises the observed variation in apparent PS signal removal rates when the pump polarisation was varied between horizontal and vertical in the experiments presented here. In figure 3.3 the external magnetic field clearly happened to

be closer to vertical than horizontal in the laboratory frame, resulting in a slower apparent depolarisation for the vertical polarisation. When the strong permanent magnet was introduced in figure 3.4 the large applied field was in the horizontal plane, resulting in the more rapid depolarisation for the vertical pump polarisation. The geomagnetic field might be presumed to be the major source when no obvious artificial magnetic field sources are present. At the latitude and longitude of Edinburgh the geomagnetic field has a total strength of 49.7 μT, with the field axis inclined at 69.5º to the horizontal, broadly consistent with the magnetic fields measured in the apparatus when no significant known artificial sources were present [138]. The gyromagnetic ratios for the low-*j* states of OH $X^2\Pi$ (v'' = 0, F_1) have been measured [139], and result, for j = 2.5, e at 50 μT, in a predicted Larmor frequency, ω_L = 2.12 MHz. This is broadly consistent with the timescale of the observed non-exponential behaviour in the measurements shown in figure 3.3, when the magnetic shielding was absent.

The effects of stray magnetic fields on prepared or collisionally generated alignments have not been considered widely in the literature. Meyer [140] and Wade *et al.* [63] have discussed the influence of the geomagnetic field as a source of depolarisation in their measurements of NO alignment resulting from NO + Ar/He inelastic scattering. Wade *et al.* concluded that magnetic fields may have been responsible for some, but not all of the observed discrepancy between experimentally measured and theoretically predicted alignments. Crossed-beam scattering experiments such as these, where the alignment is created at a range of relatively long (μs) times before the probe step are clearly most at risk of magnetic field depolarisation. However, the results presented here show that even laser pump-probe experiments working on a sub-μs timescale can suffer from the presence of stray magnetic fields. This is particularly the case if care has not been taken to remove sources of strong permanent fields, such as magnetic optical mounts, Penning gauges, and even minor ferrous-metal components, which are often significantly magnetised. It has been demonstrated conclusively here that the removal of these sources and the implementation of a simple magnetic shielding design can eliminate this problem.

Chapter 4

OH ($X^2\Pi$) + Atomic Partners

Presented in this chapter is a comprehensive dynamical study of OH ($X^2\Pi$, $v = 0$, j) with atomic collision partners from the noble gas series, namely: He, Ar and Xe. The main objective was to measure absolute rate constants for the collisional removal of bulk rotational orientation and alignment for a number of rotational quantum states. Rigorous quantum scattering calculations on state-of-the-art *ab initio* potential energy surfaces (PESs) were performed in conjunction with polarisation spectroscopy (PS) measurements to evaluate new *elastic depolarisation* rate constants. In addition, it will be shown that the comparison of experimental results to the scattering calculations provides a powerful test of these most recent PESs. It should be made clear from the outset that the quantum scattering calculations were performed by Dr Sarandis Marinakis during his time as a post-doctoral research assistant at Heriot-Watt University. However, because the following discussion is strongly linked to the computational results, details of the calculations and an overview of the results will be given in their own right. The work discussed in this chapter has already been published in four journal articles [18,141-143]. It should be noted also that the OH ($X^2\Pi$, $v = 0$)-Ar PES, constructed in collaboration with the work presented here, was initially calculated in a slightly distorted frame [18]. Subsequent to its publication this issue has been resolved [144] and all discussion in this chapter will be with respect to the correctly revised PES and calculations performed on it.

4.1 Previous work

The emphasis in this sub-section is strictly on the title systems. It is repeated for convenience that the PS measurements discussed in this chapter are sensitive to two main collisional processes which result in the collective decay of PS signals. These are:

inelastic, or quantum-state-changing processes which removes population from the level being probed; and *elastic depolarisation*, which destroys the m_j-sublevel anisotropy (orientation or alignment). The phenomenological bimolecular rate constant measured using PS has the familiar form introduced in chapter one:

$$k_{PS}^{(K)} = k_{POP} + k_{DEP}^{(K)}$$

(Equation 4-1)

The rate constant for population removal can be further decomposed into a component reflecting the efficiency of pure Λ-doublet transfer and a rate constant reflecting the efficiency of all other rotationally inelastic processes excluding pure Λ-doublet transfer:

$$k_{POP} = k_{\Lambda} + k_{RET}$$

(Equation 4-2)

The following review will primarily focus on the current state-of-the-art with respect to experimental measurement of k_{POP} and k_{DEP} , the PESs which describe the OH-Rg systems, and the scattering calculation performed on them.

Theoretical Work

Much of the theoretical work on these OH-Rg systems has been inspired by the substantial spectroscopic investigations of van der Waals complexes belonging to this family [145-152]. Because they are relatively simple three-atom systems they are theoretically tractable at an *ab initio* level calculation. One of the first *ab initio* PESs for OH ($X^2\Pi$)-Ar (^1S) was constructed by Esposti and Werner using the coupled electron pair approximation (CEPA) [16]. The global minimum on the average surface, V_{SUM}, was approximately 100 cm^{-1} in the linear Ar-H-O geometry, and at a separation, *R*, of 3.8 Å. The same authors later performed quantum scattering calculations on this potential [15] and showed that the close-coupled (CC) calculations and calculations using the coupled states (CS) approximation yielded essentially the same cross-sections for rotationally inelastic processes. Using the computationally cheaper CS method they went on to show the vibrational level dependence of the interaction potential by computing vibrationally averaged PESs using three internuclear separations, r_{OH}, in the range between 0.85 and 1.22 Å. Scattering calculations on v = 0 and v = 2 PESs demonstrated that the two quanta of vibrational energy increased the magnitude of

rotationally inelastic scattering cross-sections by approximately 20%. In addition, Esposti *et al.* computed thermal rate constants for OH ($X^2\Pi$, $v = 2$) by integrating their cross-sections, evaluated at thirteen collision energies, over a Boltzmann distribution at 300 K [15]. Unfortunately, thermal rate constants were not calculated for $v = 0$ that would be relevant here. In 2000, Kłos *et al.* published a new PES using "supermolecular unrestricted fourth-order Møller-Plesset perturbation theory and a large correlation consistent basis set, supplemented with bond functions" (UMP4 for short) [153]. The global minimum of V_{SUM} was again found at the Ar-O-H linear geometry, but the depth was now found to be 141 cm^{-1} at a separation of 3.75 Å, in better agreement with previous spectroscopic measurements of the bound complex [154,155]. The Ar-O-H 'T-shaped' ($\theta = 90°$) geometry corresponds to a saddle point which is elevated 51.8 cm^{-1} from the global minimum at an intermolecular separation of 3.55 Å. Endo and co-workers recently reported a PES for bound regions of the Ar-OH (X) complex, obtained by optimising an initial *ab initio* trial PES by fitting the available spectroscopic data for transitions between bound levels [156]. The most recent OH (X)-Ar PES was calculated in parallel to the work of this thesis and will be described in section 4.4.1

Because He is less polarisable than Ar, the interaction with OH (X) is much weaker, and there has therefore been less computational effort; confirmation of the existence of a bound van der Waals dimer has only recently been published by Han and Heaven [157]. Esposti and Werner reported an *ab initio* PES using the CEPA approach and were able to locate a global minimum in the linear He-H-O geometry, similar to that found for OH-Ar, which was approximately 30 cm^{-1} deep [15]. This result was in contrast to the previous view that the surface was entirely repulsive [158]. Scattering calculations were also performed [15], which show some interesting RET propensities in comparison to Ar. These are summarised below alongside experimental work. Lee *et al.* later calculated a restricted open-shell coupled cluster potential with single and double excitations and with non-iterative perturbational treatment of triple excitations [RCCSD(T)] [159] (see figure 4.1). The global minimum for this was found at 68° with essentially the same magnitude as the CEPA potential. Local minima exist at 0° and 180° with magnitudes of 27 cm^{-1} and 21 cm^{-1} respectively. It is this PES which was used in the OH(X) + He QM scattering calculations discussed in section 4.4.2.

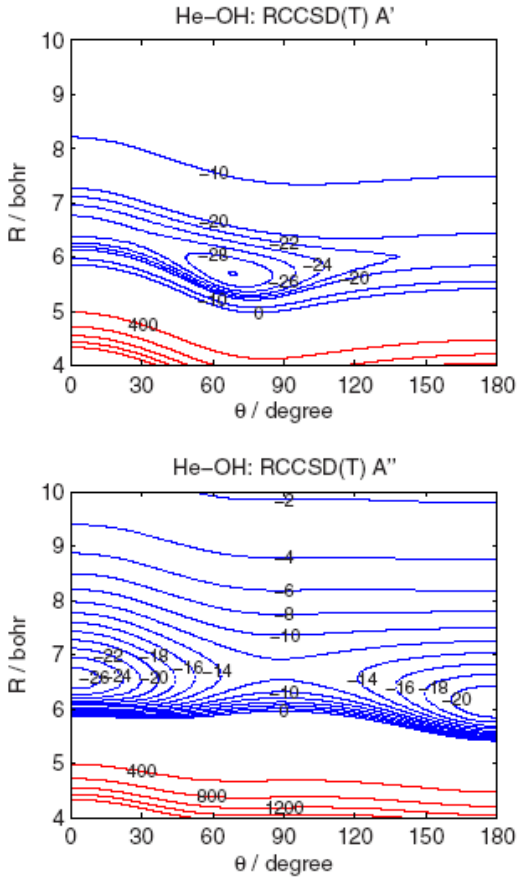

Figure 4.1: *OH (X)-He 2A' and 2A'' PESs. Reprinted from [18]*

In terms of OH(X)-Xe, elementary arguments predict that the magnitude of the global minimum on the surface should follow the trend: He < Ar < Xe. This was indeed confirmed in a very recent *ab initio* calculation using the RCCSD(T) methodology [40]. The global minimum in this case was for a T-shaped geometry (θ = 90°) and was reported to be 224 cm^{-1} with $R \approx 3.5$ Å (see figure 4.2). This is therefore over 50% deeper than the OH(X)-Ar PESs referenced above and an order of magnitude more attractive than that for He. This PES was used in the QM scattering calculations discussed in section 4.4.2.

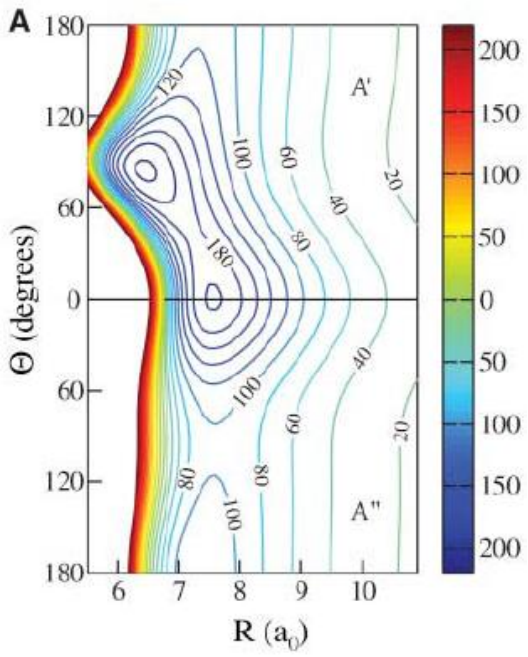

Figure 4.2: *OH (X)-Xe $^2A'$ and $^2A''$ PESs. Reprinted from [40]*

Experimental Work

The PESs above have been tested through a number of independent experimental studies. As highlighted in the introduction there are generally two distinct approaches to measure rotationally inelastic scattering. First, there are crossed-beam experiments which are capable of measuring *relative* state-to-state cross-sections with well defined collision velocities and energies, and second there are bath-gas studies, which are capable of measuring *absolute* thermal rate constants for an energy transfer process. The latter are of most relevance to the studies in this thesis.

Ter Meulen and co-workers have been pioneers in the crossed molecular-beam scattering studies on OH + Rg systems [33,69,70,160,161]. Their challenging experiments employ hexapole state selection of specific Λ-doublet levels, which avoids averaging of rotational scattering over the two nearly degenerate parity states *e* and *f*. OH ($X^2\Pi_{3/2}$, j = 1.5, *e/f*) were initially prepared in a supersonic expansion from the photodissociation of H_2O_2 and the scattered products from collisions with He (E_{coll} = 394 cm^{-1}) and with Ar (E_{coll} = 451 cm^{-1}) were monitored using LIF [33]. Several interesting observations were made which were previously predicted with QM scattering calculations by Esposti and Werner [15,16]. Ter Meulen and co-workers found that Λ-doublet transfer is the dominant process in Ar scattering and that rotational excitation to product states of the same spin-orbit manifold is preferred by an order of magnitude, as opposed to spin-orbit changing transitions. This is in contrast to He,

where the probability for spin-orbit changing transitions are almost equal to spin-orbit conserving transitions and Λ-doublet transfer is surprisingly weak; $\Delta j = +1$ $f \rightarrow e$ is found to be more likely by a factor of greater than four. In spite of these differences, He and Ar exhibit similar parity propensities, which were again broadly predicted by quantum scattering calculations. There appears to be a tendency to populate levels of opposite Λ-doublet symmetry label for both spin-orbit conserving and changing transitions. Complementing this study, ter Meulen and co-workers performed OH(X) + Ar scattering at a higher collision energy, E_{coll} = 746 cm^{-1} [160]. All previous propensities were confirmed, but the major effect of the increased collision energy was to reduce the cross-section for the most probable channel – Λ-doublet transfer. However, all other scattering cross-sections were found to increase with the most profound change in the spin-orbit changing scattering. Arguments based on competing components in the PES were made, but discussion of this will be postponed in anticipation of the PS results presented here.

The molecular beam experiments which are closest to the studies in this chapter are the steric asymmetry measurements by ter Meulen and co-workers that were mentioned in the introduction (section 1.1.4) [69,70]. By changing the polarity of a static quadrupole electric field, positioned after the hexapole state selector in the collision zone, they were able to alter the (framework) orientation of the OH in a way that they measured the scattering of OH + Ar (H-end on) or HO + Ar (O-end on) processes [69]. Using this set-up they demonstrated that smaller Δj transitions progressed *via* O-end collisions and larger Δj transitions *via* H-end collisions. Although this can be explained using the simple physical model of torque arms and linear momentum to angular momentum transfer, the authors struggled to explain their observation that *f* product states are favoured by H-end collisions. Using the control over orientation and the stark shifted electronic transition they went on to measure m_j changing collisions [70]. They showed that $\Delta m_j = 1$ transitions had a cross-section of around 25 $Å^2$ and that the probability decreased with increasing Δm_j. This was based on the assumption that purely elastic, velocity changing collisions had a cross-section of 189 $Å^2$ and all $|\Delta m_j|$ transition were assumed to be equally likely.

Currently there is only one study of RET in collisions between OH(X, $v = 0$, $j = 1.5$ *f*) and Xe. This was carried out using a novel MB approach developed by Meijer and co-workers [40]. By passing the OH MB through a stark decelerator they were able to measure the probabilities for rotational excitation as a function of collision energy in the

range 50 – 400 cm^{-1}. Consequently they were capable of measuring the near-threshold onset of RET, which was shown to be well predicted by the new OH(X)-Xe PES [40]. Very recently they demonstrated this for the OH (X) + Ar system [162].

There have been several attempts to measure the rate constant for removal of a prepared rotational level in the presence of a chosen buffer gas for OH (X). Crosley and co-workers used an IR-UV double resonance scheme to measure RET rate constants for OH ($X^2\Pi_{3/2}$, v = 2) + He and found the same propensity rules that were highlighted above [163]. Farrow and co-workers monitored the rotational relaxation of a 'hot' OH (X, v = 0) rotational distribution from photodissociation of H_2O_2 in the presence of Ar [42]. They showed that relaxation rates are significantly faster for lower j than for higher j in accord with energy gap scaling laws. One of their conclusions was that RET is a significant source of pressure broadening in OH microwave transitions and also contributes to broadening of the UV spectrum. This idea will be returned to in chapter 6.

However, most directly related to the present experiments is the work of Smith and co-workers [137,164]. An IR-UV double resonance scheme was used to prepare and probe total RET rate constants for OH ($X^2\Pi_{3/2}$, v = 1, j e) + Ar/He for j = 1.5 and 3.5 – 6.5 [136]. They also measured Λ-doublet transfer for j_i = 3.5 and 6.5 [137]. The principal finding here was that RET removal rate constants for He and Ar were found to be very similar. Across the range of j, k_{RET}, for He and Ar, was found to be within the range 0.8 – 2.0 x 10^{-10} cm^3 s^{-1}. Λ-doublet transfer is found to be much more pronounced for Ar, with k_Λ = 0.5 and 0.3 x 10^{-10} cm^3 s^{-1} for j = 3.5 and 6.5 respectively in comparison to k_Λ = 0.1 x 10^{-10} cm^3 s^{-1} for He, j = 3.5. These absolute rate constants, albeit for a different vibrational level, will be re-considered in the discussion of the PS measurements in the subsequent sections.

4.2 One-Colour Polarisation Spectroscopy

Initially, the experimentally simpler one-colour approach was used with two separate laser systems for the pump and probe beams. Both lasers were resonant with the A $^2\Sigma^+$ ← X $^2\Pi$ (0,0) $P_1(j)$ electronic transitions, where j ranged between 1.5 and 6.5. OCPS delay profiles were collected with He and Ar as collision partners. The spectroscopic scheme employed is illustrated in figure 4.3. In all cases a rotational polarisation is created by the pump in both the ground and excited rovibronic states connected by the electronic transition. OCPS signals are generated from both these quantum states because the probe is also tuned to the same transition. For the specific example in figure 4.3, signal is generated from both OH (X, v = 0, j = 4.5 e) and OH (A, v = 0, N = 3 f_1). However, at low-j the signal generated is strongly branch dependent, and for the $P_1(j)$ lines used here, signal is predominately generated from OH (X) (see section 1.2.1). This branch sensitivity is linked to the pump laser polarisation, so only linear pump polarisation (vertical in the laboratory frame) was used for this work, and consequently these experiments are sensitive only to the K = 2 alignment moments. The $P_1(j)$ transitions used were all fully resolved from neighbouring transitions for the bandwidths of the pump and probe lasers used. Typical values for the pump and probe laser fluences were 150 μJ cm^{-2} and 60 μJ cm^{-2} respectively, to avoid optical saturation.

Representative decay traces for each transition used are provided for OH + Ar in figures 4.4 and 4.5. They show the high signal-to-noise ratio achievable with this technique, and also that the signals fall to less than 5% of their initial intensity on a sub-microsecond timescale with the lowest collision partner pressures used; typically 250 – 350 mTorr. A noticeable feature of these traces is the oscillations superimposed on the exponential decay. These are nuclear hyperfine quantum beats (NHQBs) that arise from the coupling of the total rotational angular momentum, j, and the nuclear spin of the hydrogen atom (I = 1/2), to form the grand total angular momentum, F. The two hyperfine levels formed are not resolved by the pump or probe lasers and are therefore excited and probed coherently. The result is an oscillation in the prepared laboratory frame alignment with a period related to the energy separation of the nuclear hyperfine levels (see section 1.2.2); analogous to the Larmor precession introduced in chapter 3. The corresponding frequencies for each spectroscopic line are provided in table 4-1. The time-dependence of the OCPS decay traces are not complicated by oscillations originating from the splitting of the excited state hyperfine levels, because the stronger

coupling in the A state results in an oscillation too fast (several hundred MHz) to be resolved by the temporal profiles of the laser pulses [165].

Table 4-1: *Energy splitting and corresponding oscillation periods for all J_g levels used in this work. Obtained from [130].*

Transition	j_g	Δm_F / MHz	2π Oscillation Period / ns
$P_1(1.5)$	1.5	53.171	18.8
$P_1(2.5)$	2.5	13.997	71.4
$P_1(3.5)$	3.5	7.4765	134.8
$P_1(4.5)$	4.5	21.321	46.9
$P_1(5.5)$	5.5	30.95	32.3
$P_1(6.5)$	6.5		

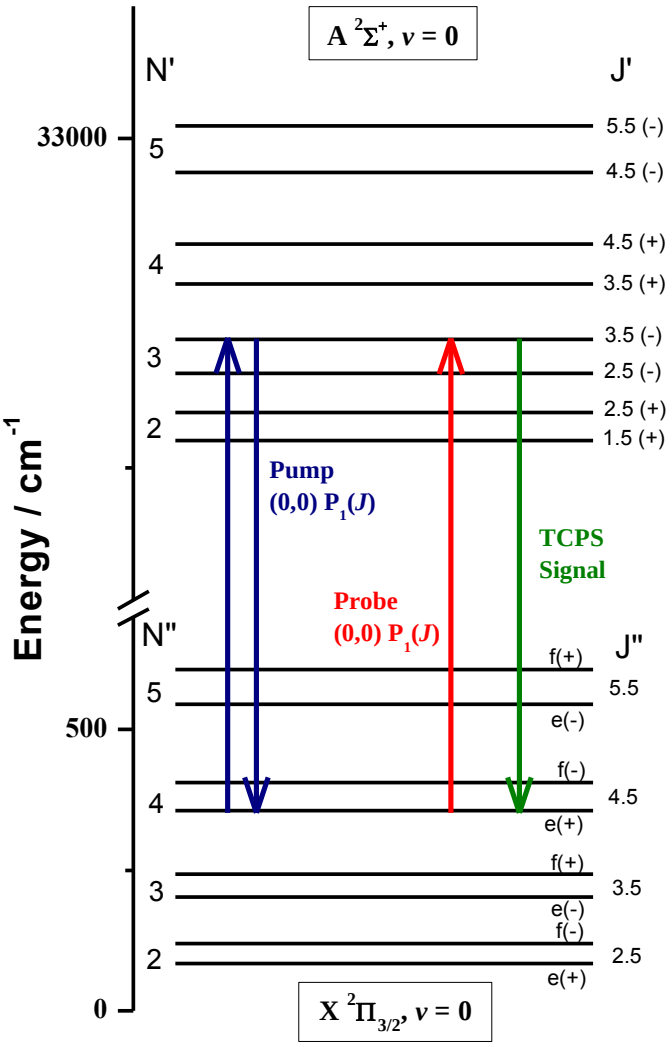

***Figure 4.3**: Schematic diagram of rotational energy levels for OH $X^2\Pi$ $v = 0$ and $A^2\Sigma^+$ $v = 0$ relevant to OCPS signal generation. For clarity, energy-level splittings are not shown to scale: the Λ-doublet splitting in $X^2\Pi_{3/2}$ and the spin-rotation splitting in $A^2\Sigma^+$ are both considerably exaggerated. The upper F_2 ($X^2\Pi_{3/2}$) spin-orbit manifold has been omitted. Example TCPS transitions, specific to this work, are indicated; the pump (navy) and probe (red) beam are both resonant with the diagonal (0,0) $P_1(j)$ branch. This example would result in signal generation (Green) from the OH ($X^2\Pi_{3/2}$, $v = 0$, $j = 4.5e$) and OH ($A^2\Sigma^+$, $v = 0$, $N = 3$ f_1: $j = 3.5$).*

The NHQBs are most pronounced, i.e. have the greatest modulation depth, for the lowest *j* (figure 4.4(a)) studied, and the depths of the modulations become progressively smaller as *j* becomes proportionately larger with respect to *F*. These are fully accounted for in the PS fitting routine [71] and the collected data are well fit by the known hyperfine frequencies in table 4-1.

Figure 4.6 presents a selection of decay traces for representative spectroscopic transitions with He as a collision partner. Again the NHQBs are superimposed on the exponential decays and are well fit using the previously published theoretical treatment for OCPS [71]. The quantum beats are independent of collision partner and are therefore identical in comparison to the OH + Ar equivalents. The change in collision partner can however change the rate at which the OCPS signal is removed. Making the appropriate comparisons between figure 4.6 and figures 4.4 and 4.5 it is evident that Ar removes the OCPS signal more rapidly. Another variable in figures 4.4 to 4.6 is, of course, the spectroscopic line used, but from first observations there does not seem to be a clear *j* dependence on the decay rate for OH + Ar or OH + He. It should be noted though that these decay traces were recorded with a single (and in some cases slightly different) collision partner pressure. The purpose of presenting them here is largely illustrative. To reveal the true influence of the two variables (collider gas and rotational level), and to measure absolute rate constants for the removal of bulk alignment, it is essential to monitor the pressure dependence of OCPS signal decay rate.

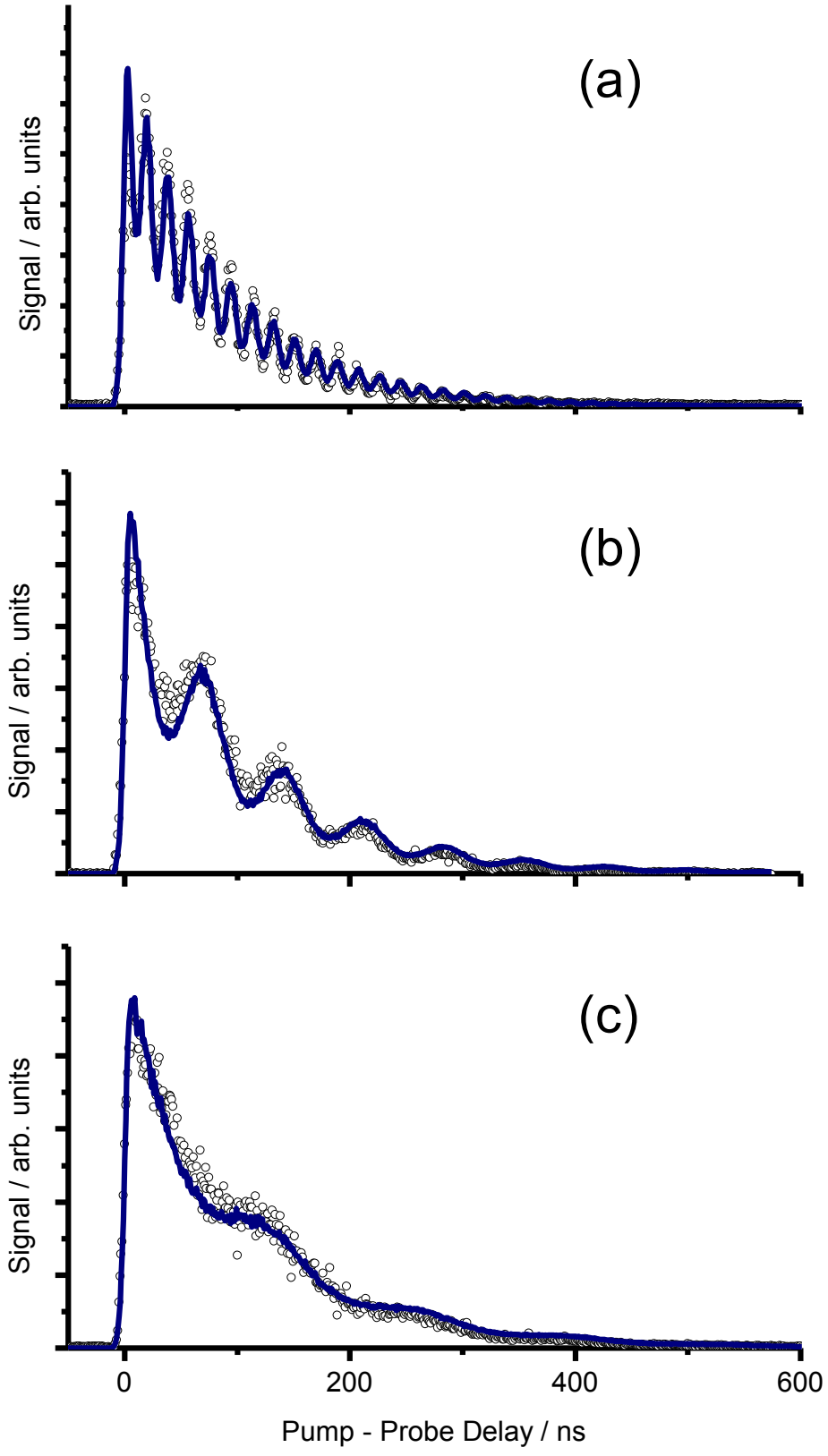

Figure 4.4: *OCPS signal as a function of pump-probe delay for OH (X) + Ar linear pump polarisation. Representative decay traces with both pump and probe centred on (a) $P_1(1.5)$, (b) $P_1(2.5)$ and (c) $P_1(3.5)$. Ar collider gas pressures range from 250 – 350 mTorr. Open circles are the collected data points and the solid line represents the fit using the OCPS theoretical treatment [71].*

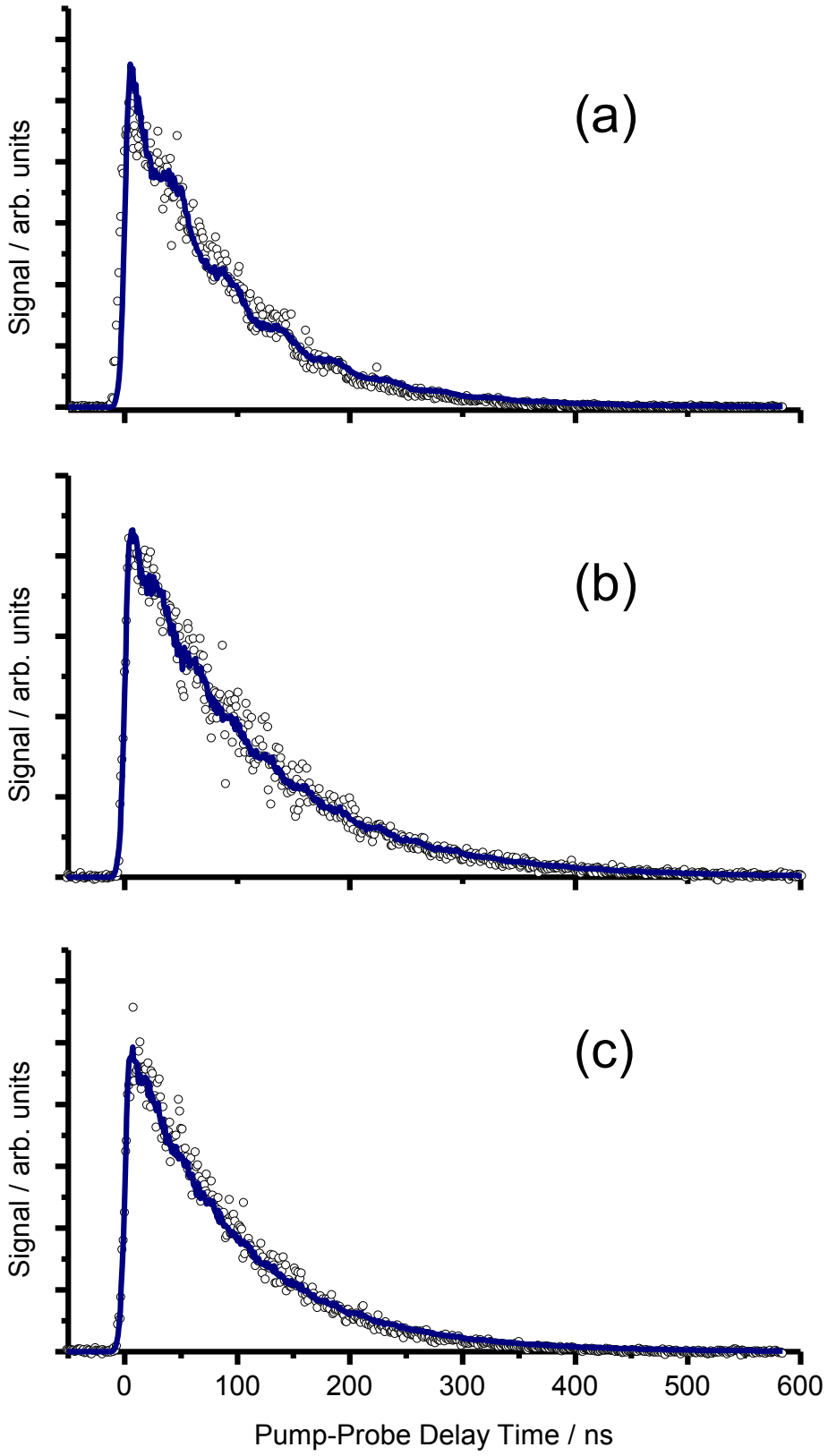

Figure 4.5: *OCPS signal as a function of pump-probe delay for OH (X) + Ar using linear pump polarisation. Representative decay traces with both pump and probe centred on (a) P_1(4.5), (b) P_1(5.5) and (c) P_1(6.5). Ar collider gas pressures range from 250 – 350 mTorr. Open circles are the collected data points and the solid line represents the fit using the OCPS theoretical treatment [71].*

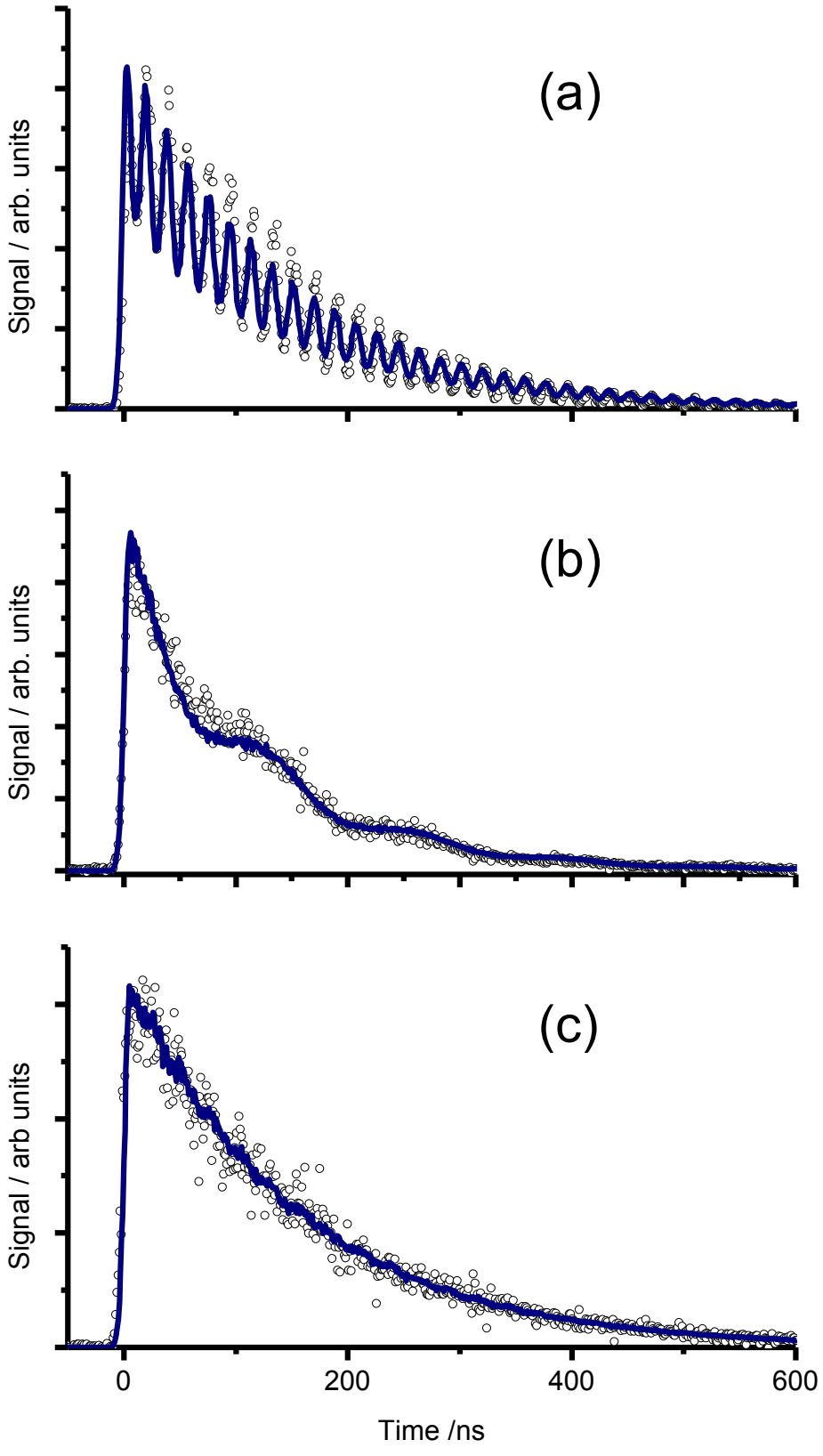

Figure 4.6: *OCPS signal as a function of pump-probe delay for OH(X) + He using linear pump polarisation. Representative decay traces with both pump and probe centred on (a) P_1(1.5), (b) P_1(3.5) and (c) P_1(6.5). He collider gas pressures range from 250 – 350 mTorr. Open circles are the collected data points and the solid line represents the fit using the OCPS theoretical treatment [71].*

4.2.1 Pressure Dependence

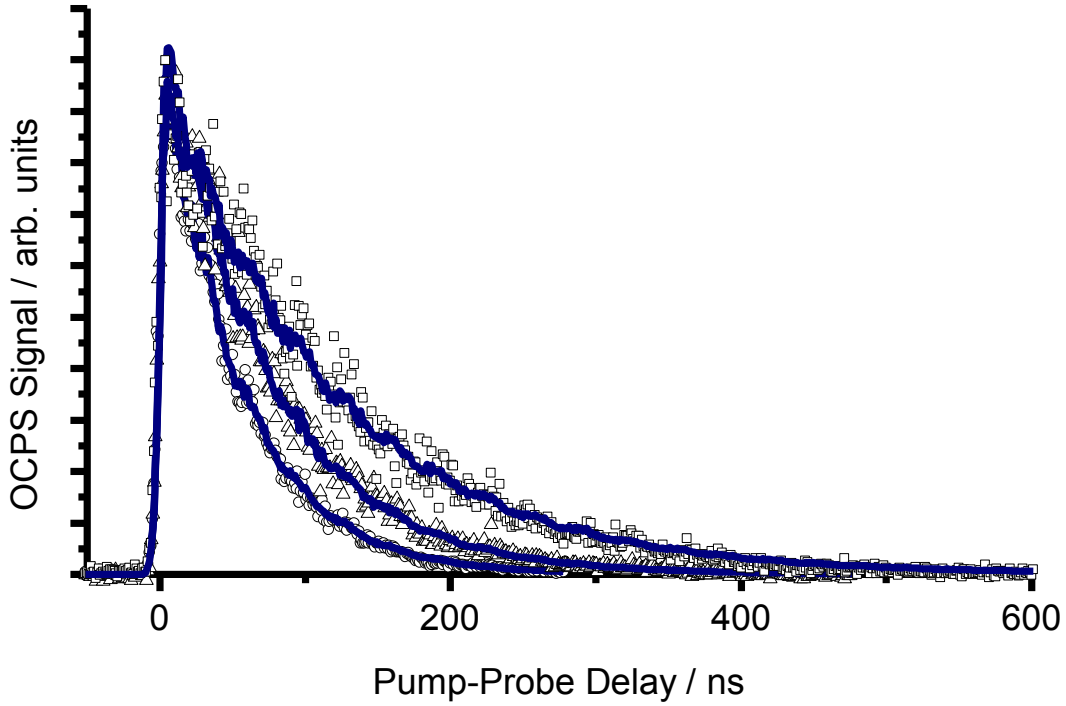

Figure 4.7: *OCPS signals a function of pump-probe delay time for OH + He with the pump and probe laser centred on the P_1(5.5) line. Shown are decay traces for three different collider gas pressures: 255 mTorr (open squares), 770 mTorr (open triangles) and 1430 mTorr (open circles).*

OCPS decay traces were acquired for a variety of collision partner pressures, keeping the precursor pressure constant, over the range 200 – 1600 mTorr. The example in figure 4.7 clearly shows the expected pressure dependence of the OCPS signal. This is representative of OH + He for *P_1(5.5)*, but the same trend is observed in all other cases. To evaluate the 2nd order bimolecular rate constant, $k_{OCPS}^{(2)}$, the returned decay rate from the fitting routine, $\Gamma_{OCPS}^{(K)}$, was plotted against the collision partner number density, [*M*].

$$\Gamma_{OCPS}^{(K)} = \Gamma_{Intercept}^{(K)} + k_{OCPS}^{(K)}[M]$$

(Equation 4-3)

Figure 4.8 is a collection of all these plots for all transitions investigated. The fit through the data points is a standard linear regression with no weighting to uncertainties of any individual decay rates. Any uncertainties in the decay traces are assumed to be outweighed by minor systematic variations in experimental conditions, for example, the

partial pressure of the precursor. The slopes of these lines are equal to $k_{OCPS}^{(2)}$ and these values are tabulated in table 4-2 alongside the equivalent thermally averaged cross sections, which accounts for the difference in collision frequency for He and Ar. The quoted errors represent 95% confidence limits from the linear fits. It is clear here that the primary observation made earlier, that Ar removes the OCPS signal more rapidly than He, is observed again here.

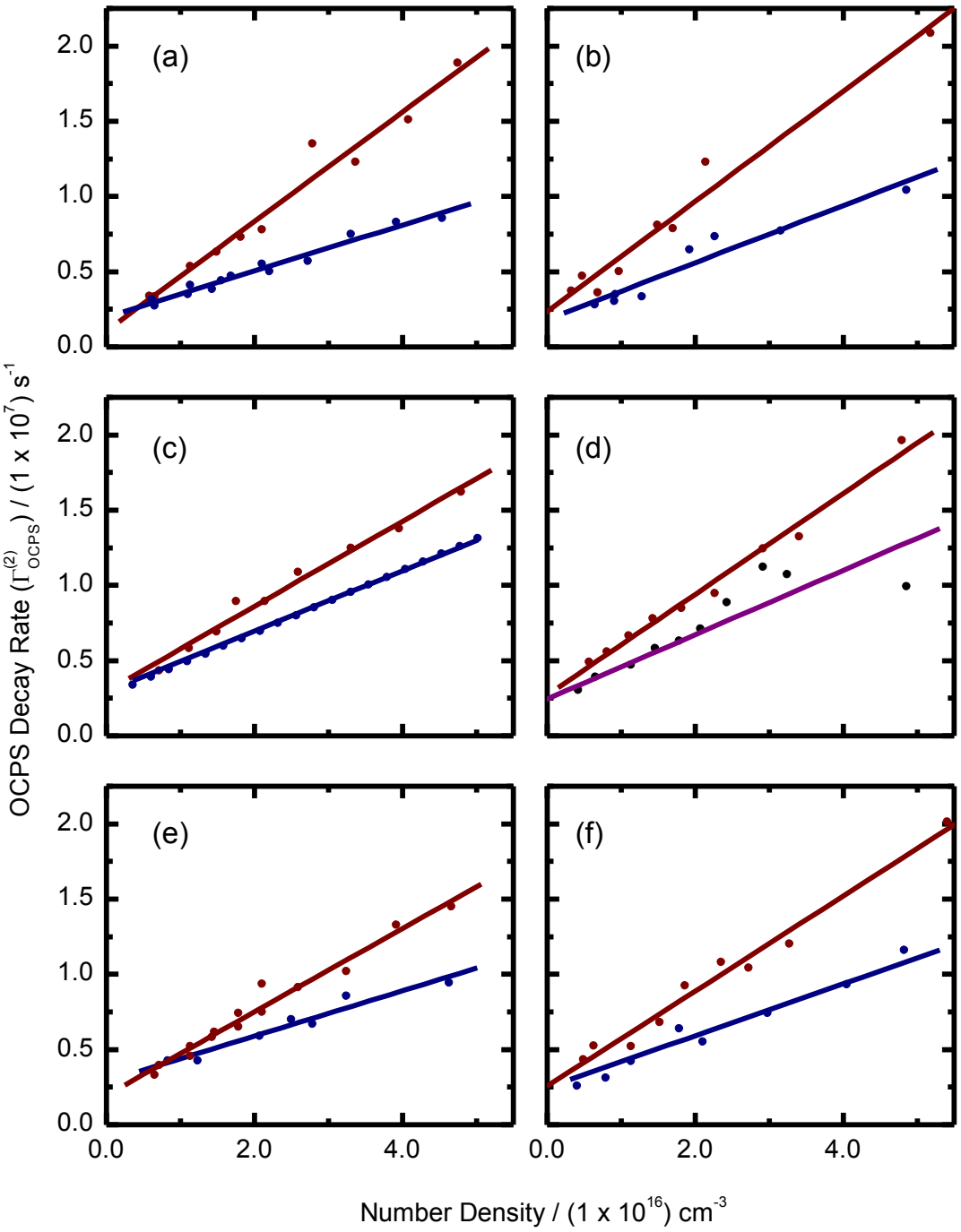

Figure 4.8: *OCPS decay rates as a function of collision partner number density: He (Navy) and Ar (Red). The filled circles represent the measured decay rates for a given collision partner number density and the colour-coordinated solid lines are linear regression fits to the data. The slope of these fits yields the bimolecular rate constant,* $k^{(2)}_{OCPS}$*, where the superscript denotes K = 2 for alignment. Plots are shown for* j_g *= (a) 1.5, (b) 2.5, (c) 3.5, (d) 4.5, (e) 5.5 and (f) 6.5.*

Table 4-2: *OCPS rate constants (1 x 10^{-10} cm^3 s^{-1}) and thermally averaged cross-sections ($Å^2$).*

		J = 1.5e	***J = 2.5e***	***J = 3.5e***	***J = 4.5e***	***J = 5.5e***	***J = 6.5e***
He	$k^{(2)}_{OCPS}$	*1.5 ± 0.2*	*1.9 ± 0.2*	*2.0 ± 0.3*	*2.1 ± 0.2*	*1.5 ± 0.3*	*1.7 ± 0.2*
	$\left\langle \sigma^{(2)}_{OCPS} \right\rangle$	11 ± *1.4*	14 ± *1.4*	14 ± *2.0*	15 ± *1.4*	11 ± *2.0*	12 ± *1.4*
Ar	$k^{(2)}_{OCPS}$	*3.6 ± 0.4*	*3.7 ± 0.6*	*2.8 ± 0.3*	*3.4 ± 0.3*	*2.8 ± 0.3*	*3.2 ± 0.4*
	$\left\langle \sigma^{(2)}_{OCPS} \right\rangle$	*49 ± 6.0*	*51 ± 8.0*	*38 ± 4.0*	*47 ± 4.0*	*38 ± 4.0*	*44 ± 6.0*

Table 4-2 shows that $k^{(2)}_{OCPS}$ values lie within the range 1.5 – 2.1 x 10^{-10} cm^3 s^{-1} for He and are significantly larger for Ar (2.8 – 3.7 x 10^{-10} cm^3 s^{-1}). This difference is considerably amplified when comparing the thermally averaged cross-sections, $\left\langle \sigma^{(2)}_{OCPS} \right\rangle$.

An additional observation from figure 4.8 is that there is an appreciable non-zero intercept, $\Gamma^{(2)}_{OCPS}$, on the second-order plots. By definition this intercept is representative of a significantly positive decay rate in the absence of collider gas. There are a number of possible physical explanations for this, which include effective depolarisation from stray magnetic fields, but it is assumed that this effect has been successfully eliminated (see chapter 3). Another possible contribution to the non-zero intercept is 'fly-out' of OH from the detection zone. Using the mean speed of OH at 298 K (609 m s^{-1}) and a laser beam diameter of approximately 3 mm the estimated loss rate from this process is 1 – 2 x 10^5 s^{-1}; an order of magnitude lower than the ~ 2 x 10^6 s^{-1} intercept observed. A more obvious source of this phenomenon is collisions with the OH precursor, which is the following mixture: HNO_3/H_2O/buffer gas. Smith and co-workers used HNO_3 as a precursor in their RET and Λ-doublet measurements of OH (X, v = 1, j) [137,164] and were therefore able to measure its k_{RET}. For OH (X) + HNO_3 they obtained k_{RET} = 2.9 – 5.4 x 10^{-10} cm^3 s^{-1} for the range j = 1.5 – 5.5. They did not measure k_{Λ} for all rotational states used in this work, but they did obtain values of 24 x 10^{-10} cm^3 s^{-1} and 7.5 x 10^{-10} cm^3 s^{-1} for j = 3.5 and 6.5 respectively. This provides a total removal rate constant k_{POP} ≈ 1 – 2 x 10^{-9} cm^3 s^{-1}, consistent with the ~ 30 mTorr precursor pressure used in the experiments and an observed intercept of ~ 2.5 x 10^6 s^{-1}. It should be noted however that OCPS would also be sensitive to elastic depolarisation of OH with HNO_3, which in-turn

would contribute to the intercept. There are no previous measurements of this kind to compare to these initial results.

4.3 Two-Colour Polarisation Spectroscopy

The primary motivation for the two-colour approach was to measure the evolution of OH (X) rotational polarisations for *isolated* rotational quantum states; removing any contamination from other contributing levels. A 'V-shaped' scheme was used where the pump and probe were resonant with different spectroscopic transitions. Specifically, the pump was resonant with the off-diagonal A – X (1,0) band (282 – 284 nm) and the probe with the diagonal A – X (0,0) band (308 – 310 nm). In both cases the $P_1(j)$ branches were used. Figure 4.9 illustrates this scheme, providing a specific example where signal is generated *only* from OH (X, v = 0, j = 4.5 e). This time TCPS decay traces were acquired for He, Ar and Xe, using both linear and circular pump polarisations, to prepare and monitor the decay of orientation (K = 1) and alignment (K = 2) moments, respectively.

An additional advantage of the two-colour approach was to reduce/eliminate residual pump laser scatter from reaching the PS PMT. By placing an interference filter (centred at 308 nm, FWHM = 10 nm) prior to the PMT it was possible to transmit only the probe wavelength, and hence the signal, and to block the pump scatter. In concept it is possible therefore to increase the effective experimental path length by reducing the crossing angle of the pump and probe beams, but in practice this was restricted by the design of the apparatus.

Representative TCPS decay traces are shown for OH (X) + Ar in figures 4.10 – 4.12 below. Figures 4.10 and 4.11 are representative of alignment decay and figures 4.12 and 4.13 of orientation decay. The general form of these traces is very similar to the examples shown in section 4.2, including the observation of NHQBs, that are again successfully fitted by the fitting routine [72]. There is, however, a striking difference in the NHQBs observed for orientation and alignment decay traces for a common rotational level. For orientation the modulation depth of the NHQBs is suppressed in comparison to the alignment equivalents, which is most notable at low-j where the largest modulation depths are observed. This can be easily explained using a simple classical picture: a rotation of $\boldsymbol{j}$ by π is required to destroy an orientation, whereas a $\pi/2$

rotation is sufficient to destroy an alignment. This concept will be important later in comparative discussion of the results for collisional decay of orientation and alignment.

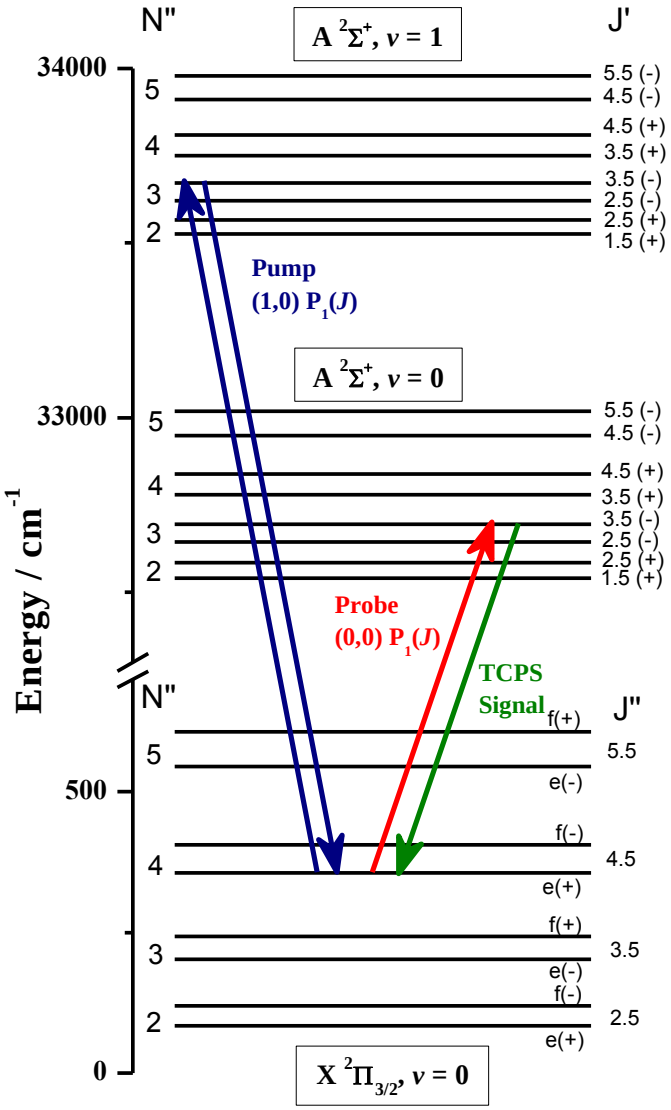

Figure 4.9: *Schematic diagram of rotational energy levels for OH $X^2\Pi$ v = 0 and $A^2\Sigma^+$ v = 0 and 1 relevant to TCPS signal generation. For clarity, energy-level splittings are not shown to scale: the Λ-doublet splitting in $X^2\Pi_{3/2}$ and the spin-rotation splitting in $A^2\Sigma^+$ are both considerably exaggerated; the vibrational spacing in $A^2\Sigma^+$ is reduced. The upper F_2 ($X^2\Pi_{3/2}$) spin-orbit manifold has been omitted. Example TCPS transitions, specific to this work, are indicated; the pump beam (navy) is resonant with the off-diagonal (1,0) $P_1(j)$ branch and the probe (red) is resonant with the diagonal (0,0) $P_1(j)$ branch. This example would result in signal generation (green) from only the OH ($X^2\Pi_{3/2}$, v = 0, j = 4.5e) level.*

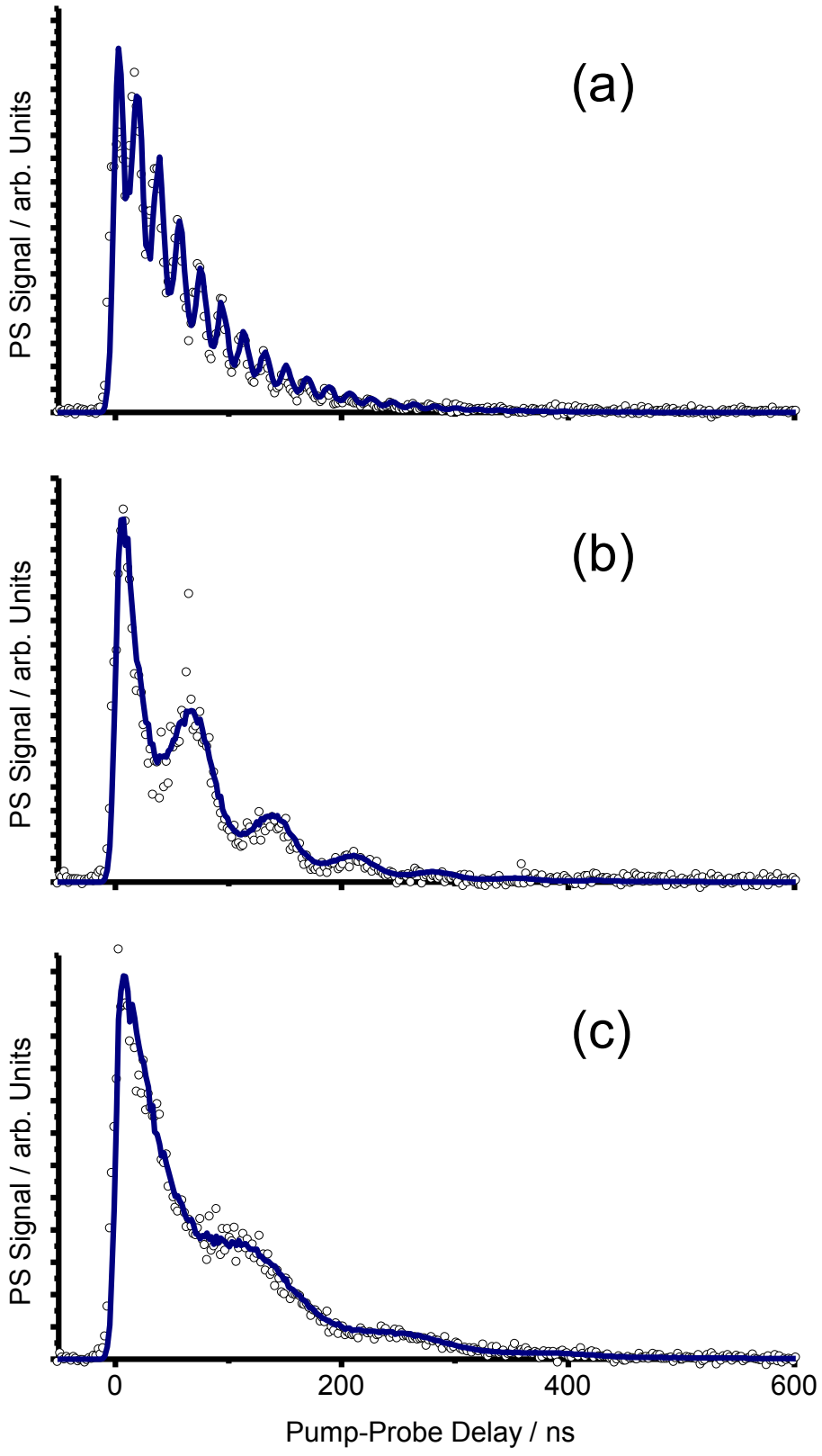

Figure 4.10: *TCPS signal as a function of pump-probe delay for OH (X) + Ar linear pump polarisation. Decay traces representative of (a) j = 1.5 (b) j = 2.5 and (c) j = 3.5. Ar collider gas pressures range from 250 – 350 mTorr. The open circles are the recorded data points for a given pump-probe delay time and the solid lines are fits using the previously reported theoretical treatment [72].*

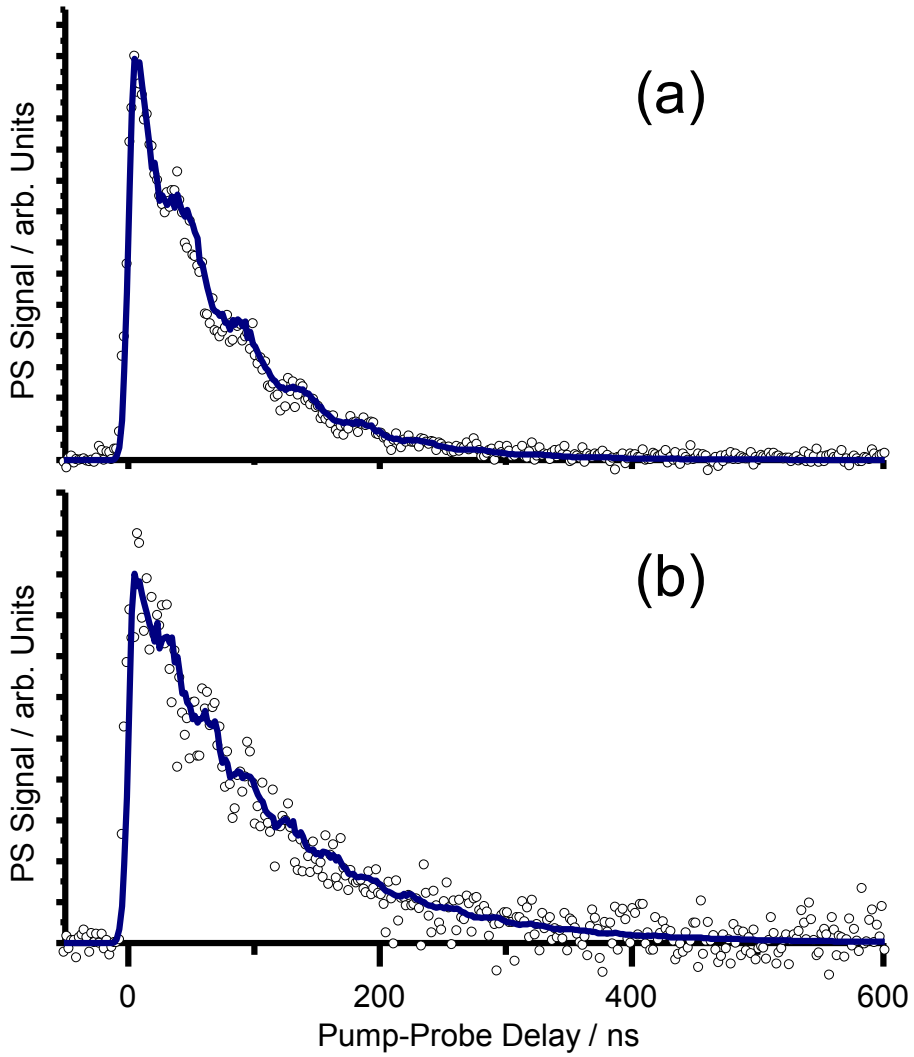

Figure 4.11: *TCPS signal as a function of pump-probe delay for OH(X) + Ar with linear pump polarisation. Decay traces representative of (a) j = 4.5 and (b) j = 5.5 Ar collider gas pressures range from 250 – 350 mTorr. The open circles are the recorded data points for a given pump-probe delay time and the solid lines are fits using the previously reported theoretical treatment [72].*

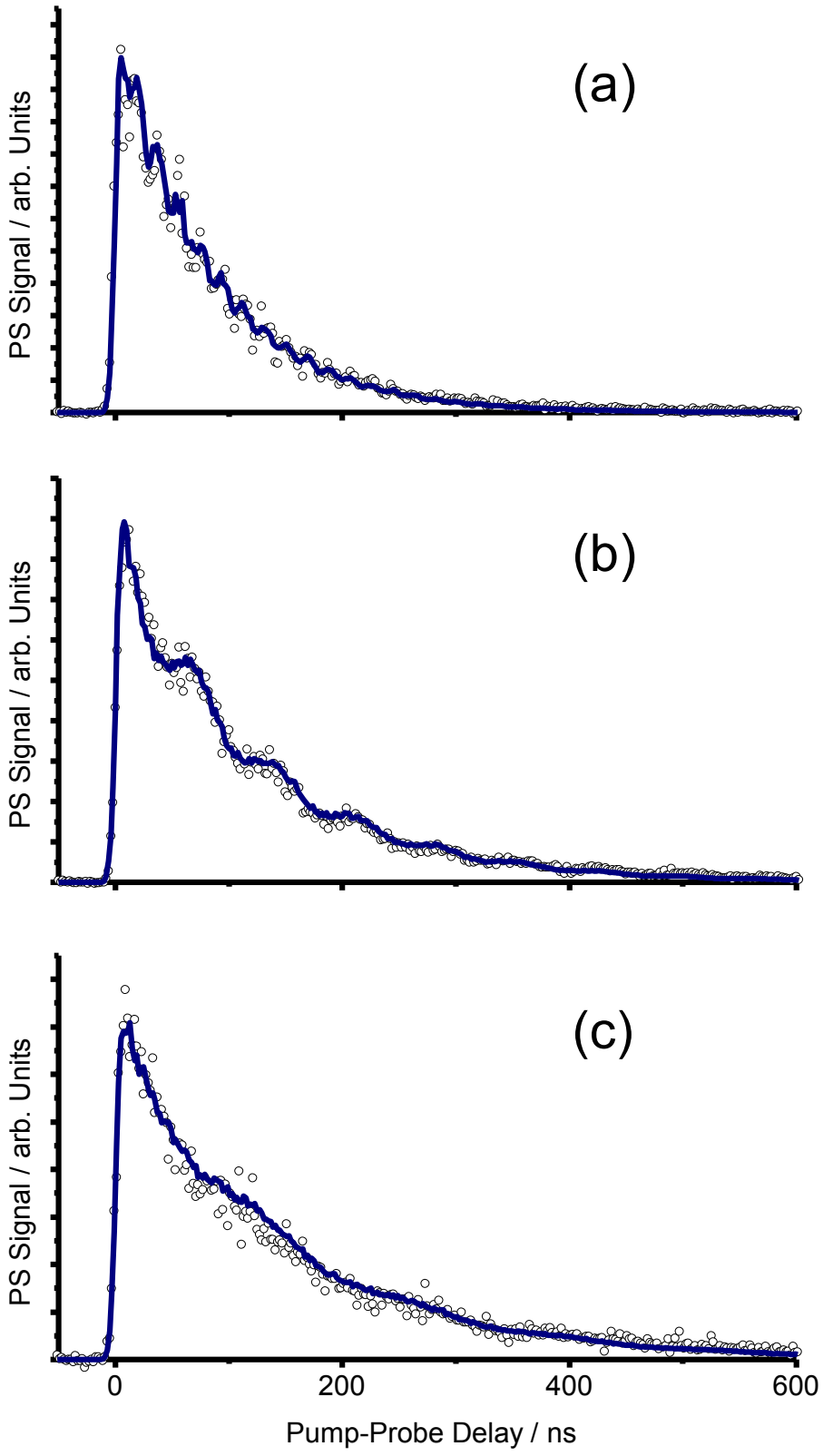

Figure 4.12: *TCPS signal as a function of pump-probe delay for OH (X) + Ar with circular pump polarisation. Decay traces representative of (a) j = 1.5 (b) j = 2.5 and (c) j = 3.5. Ar collider gas pressures range from 250 – 350 mTorr. The open circles are the recorded data points for a given pump-probe delay time and the solid lines are fits using the previously reported theoretical treatment [72].*

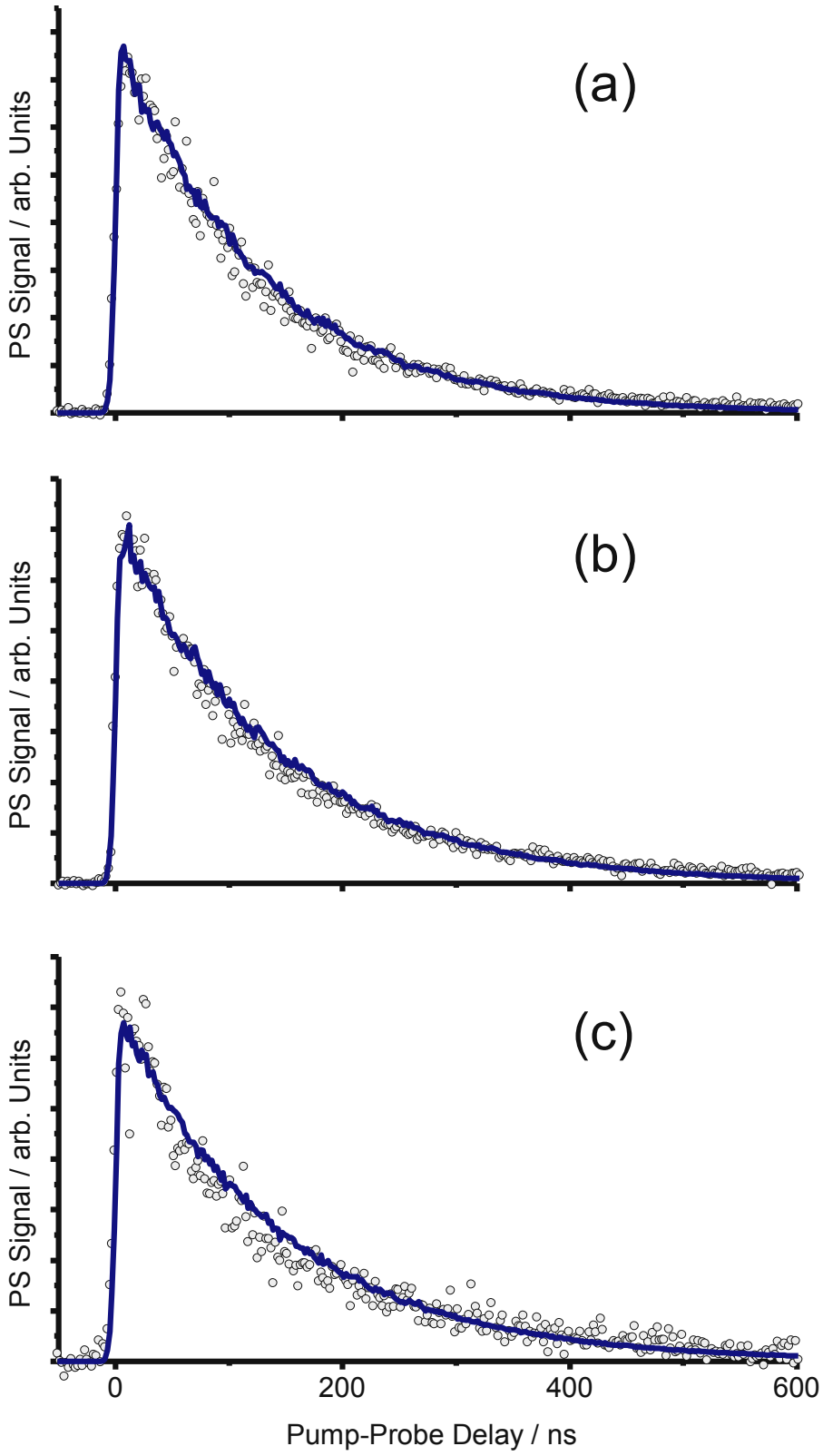

Figure 4.13: *TCPS signal as a function of pump-probe delay for OH (X) + Ar with circular pump polarisation. Decay traces representative of (a) j = 4.5 (b) j = 5.5 and (c) j = 6.5. Ar collider gas pressures range from 250 – 350 mTorr. The open circles are the recorded data points for a given pump-probe delay time and the solid lines are fits using the previously reported theoretical treatment [72].*

Aside from the differences of the NHQBs between orientation and alignment, it is also noted upon close inspection that the decay rate for orientation is slower than that for alignment when comparing similar *j* and with comparable collision partner number densities. Although not shown here the trends for OH (X) + He are very similar; all that alters is the absolute rate of the overall decay for a given pressure.

For OH (X) + Xe, measurements were made on a more restricted set of rotational levels, namely j = 1.5 and 4.5, with both circular and linear pump polarisations. Example decay traces for these measurements are provided in figure 4.15. Again the same trends are observed as before. For economic consumption of the more expensive rare gas (hence only selected rotational levels) these measurements were collected using different flow rates compared to their He and Ar counterparts. Figure 4.14 illustrates a collider-flow-rate test for OH (X, j= 1.5) + Ar.

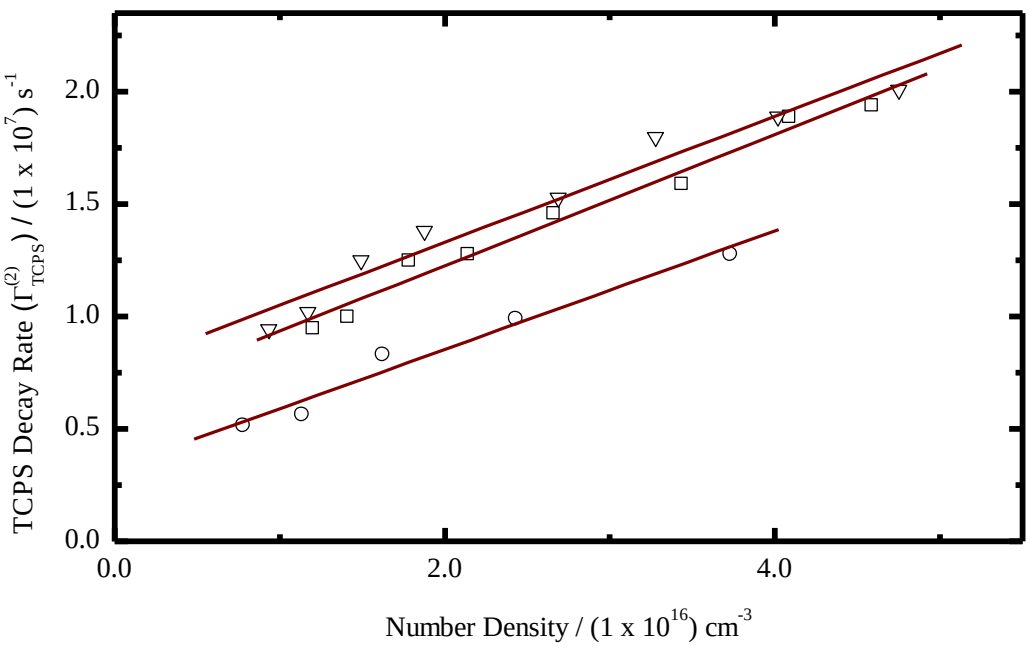

Figure 4.14: *TCPS decay rates versus collision partner number density for OH (X) + Ar and for J = 1.5e. The three traces correspond to three different flow rates for a collision partner pressure of 800 mTorr: 76 s.c.c.m. (circles), 56 s.c.c.m. (squares) and 37 s.c.c.m. (triangles).*

In this flow-rate test a specific mass flow controller setting was chosen to maintain a particular flow rate. The diffusion pump was throttled to achieve a desired pressure, which was chosen to be 800 mTorr, approximately the median of the pressures used to acquire a rate constant. The flow rate was then altered to record pressure-dependent decay rates. The traces in figure 4.14 correspond to different initial flow rates used to

obtain the same selected pressure of 800 mTorr. Lower flow rates require more throttling and *vice versa*. Consequently the precursor partial pressure, which was set first, increases at lower flow-rates. This is the principal reason behind the increase of the intercept from 3.26 x 10^6 s^{-1} to 7.69 x 10^6 s^{-1}, in broad agreement with the decrease in flow rate by a factor of 2; although the relationship between flow rate of collider, pumping speed and precursor pressure may not be exactly linear. However, the main point here is that the slopes were measured to be 2.81 ± 0.47, 2.92 ± 0.36, and 2.64 ± 0.53 10^{-10} cm^3 s^{-1}; all equivalent within the experimental 2σ uncertainties. Incidentally, this provides further confidence for the earlier statement that the intercept is largely the result of collisions with the precursor.

A more rigorous measure of any dependence on the variables, i.e. *j*, orientation and alignment, or collision partner, as stated in the previous section, is to measure the phenomenological bimolecular rate constant, $k_{TCPS}^{(K)}$. *K* distinguishes between orientation and alignment, as usual. The observed TCPS decays, and their dependence on collider pressure, were very similar to those previously shown in figure 4.7, and so are not presented here. Figures 4.16 and 4.17 show representative plots of TCPS decay rate, $\Gamma_{TCPS}^{(K)}$, as a function of collision partner number density for all rotational levels studied and with all colliders used. The slopes provide $k_{TCPS}^{(K)}$. The extracted rate constants and the associated thermally averaged cross sections are provided in table 4-3. The primary observation from these results is that measured rate constants are progressively larger in magnitude in the series: Xe > Ar > He. As noted above, this trend is even more pronounced in terms of $\sigma_{TCPS}^{(K)}$. In all cases, the rate constants for orientation are smaller than for alignment, and the only collider gas which shows any significant *j* dependence for the levels probed is Ar; $k_{TCPS}^{(2)}$ decreases from 3.4 to 1.9 x 10^{-10} cm^3 s^{-1} and $k_{TCPS}^{(1)}$ decreases monotonically from 2.7 to 1.5 x 10^{-10} cm^3 s^{-1}. Further discussion of all of these results is deferred until sections 4.5 and onwards.

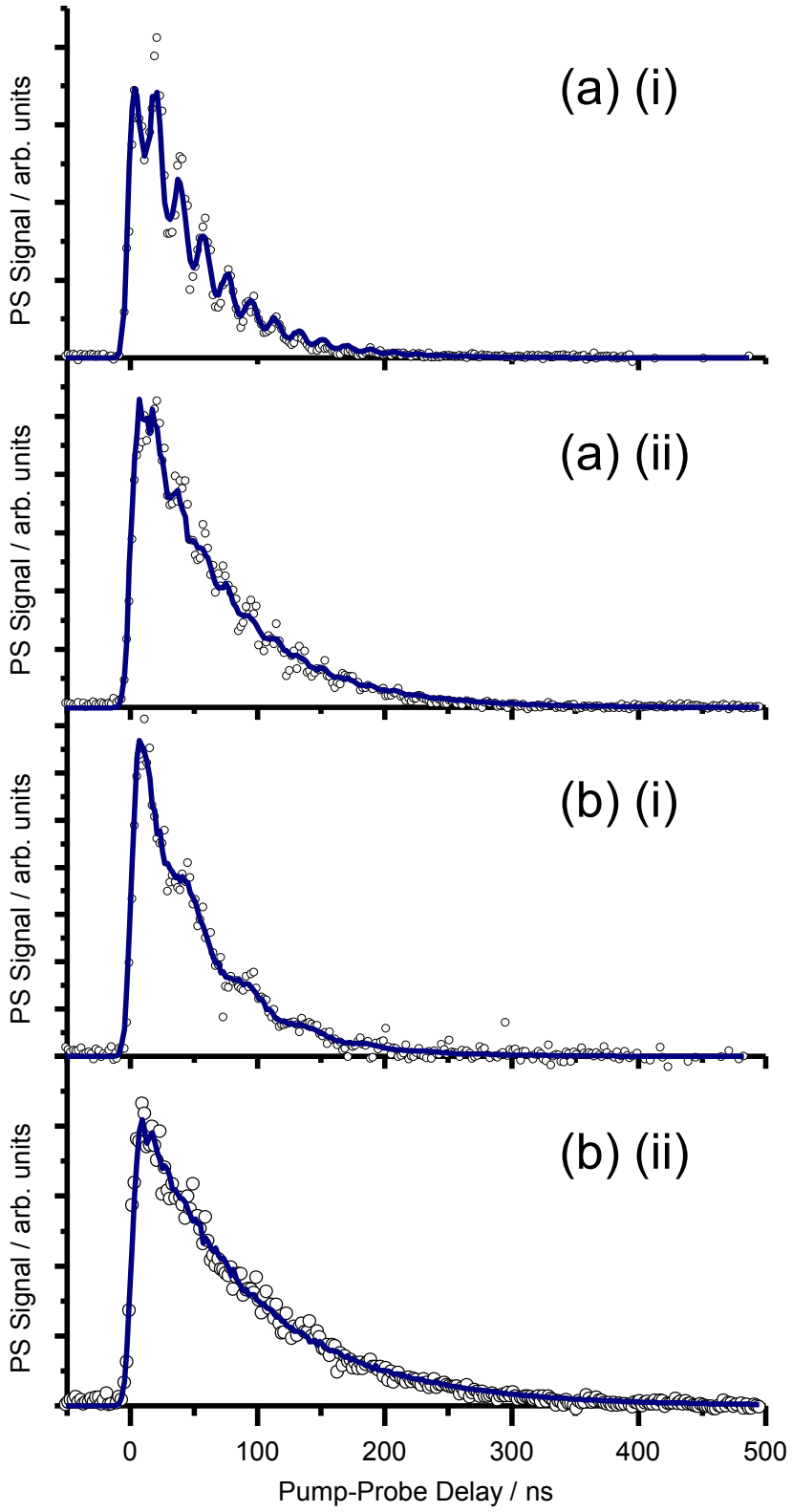

Figure 4.15: *TCPS signal as a function of pump-probe delay for OH (X) + Xe. Decay traces representative of (a) j = 1.5 and (b) j = 4.5 with (i) linear and (ii) circular pump polarisation. Xe collider gas pressures range from 250 – 350 mTorr. The open circles are the recorded data points for a given pump-probe delay time and the solid lines are fits using the previously reported theoretical treatment [72].*

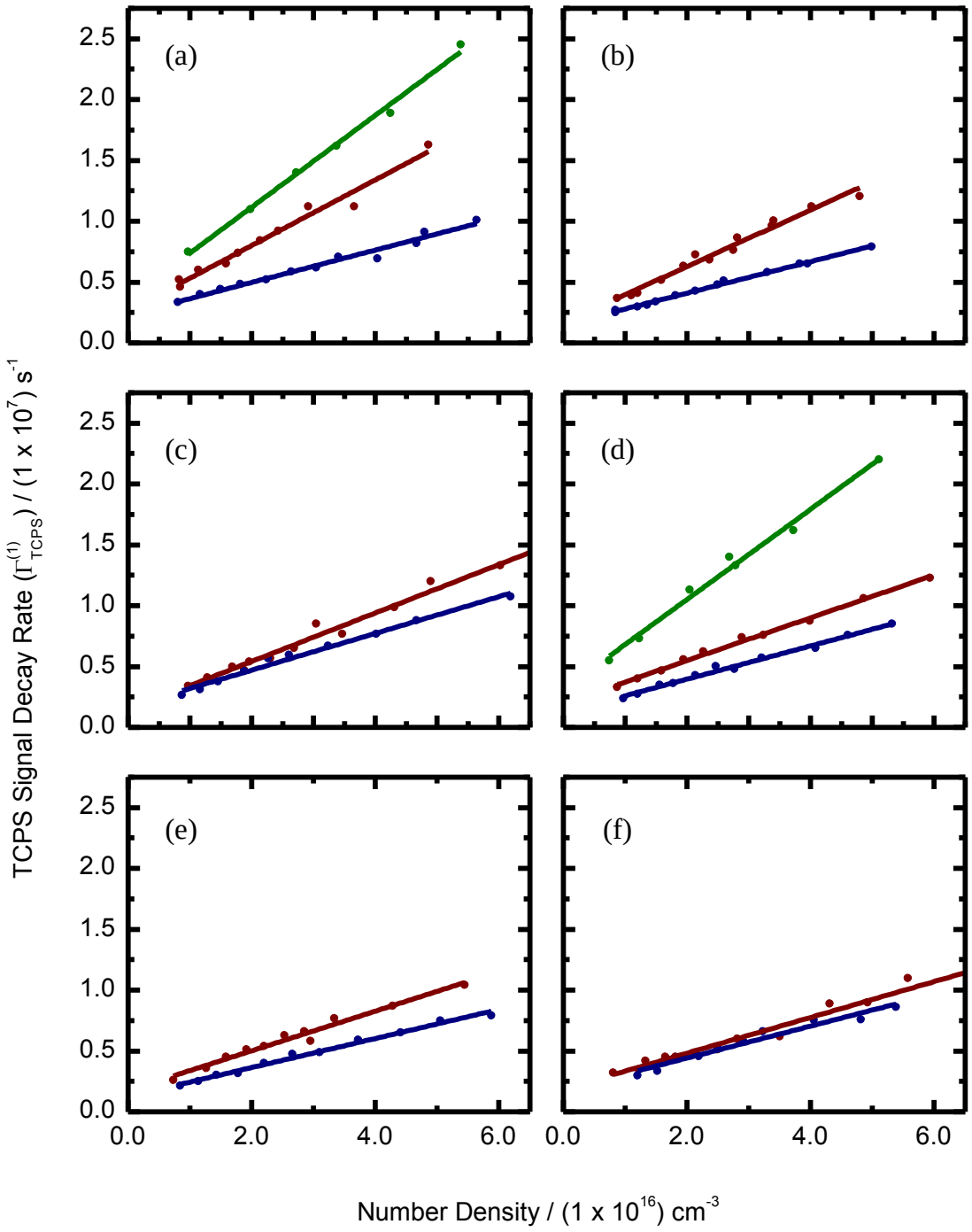

Figure 4.16: *(Orientation, K = 1) TCPS decay rates as a function of collision partner number density: He (navy), Ar (Red) and Xe (green). The filled circles represent the measured decay rates for a given collision partner number density and the colour coordinated solid lines are linear regression fits to the data points. The slope of these fits yields the bimolecular rate constant,* $k^{(1)}_{TCPS}$ *. Plots are shown for (a) j = 1.5, (b) j = 2.5, (c) j = 3.5, (d) j = 4 5, (e) j = 5.5 and (f) j = 6.5.*

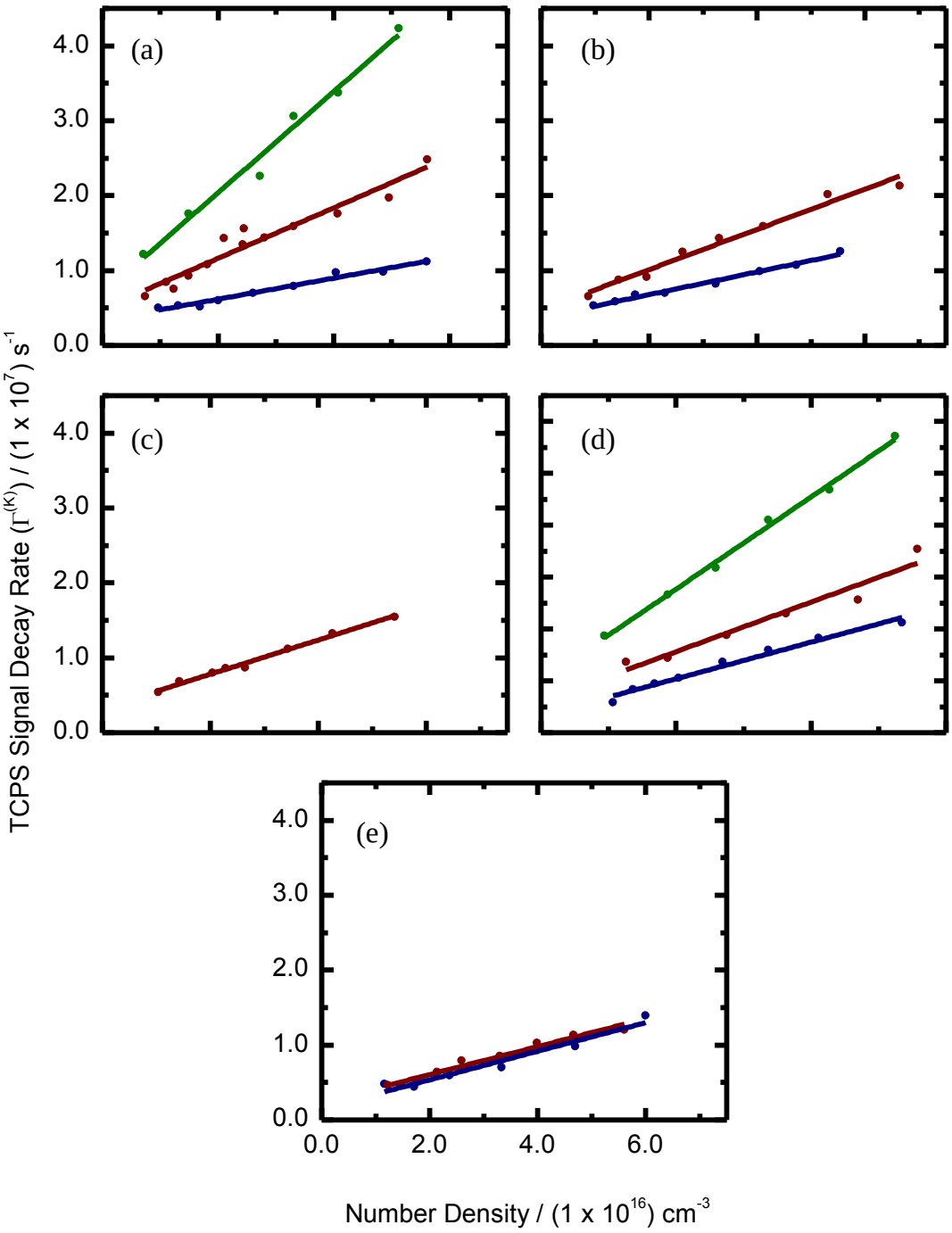

Figure 4.17: *(Alignment, K = 2) TCPS decay rates as a function of collision partner number density: He (navy), Ar (Red) and Xe (green). The filled circles represent the measured decay rates for a given collision partner number density and the colour coordinated solid lines are linear regression fits to the data points. The slope of these fits yields the bimolecular rate constant,* $k_{TCPS}^{(2)}$ *. Plots are shown for (a) j = 1.5, (b) j = 2.5, (c) j = 3.5, (d) j = 4 and (e) j = 5.5.*

***Table 4-3**: TCPS and OCPS rate constants (in units of 1 x 10^{-10} cm^3 s^{-1}) and thermally averaged cross-sections (in units of $Å^2$).*

		j = 1.5e	*j = 2.5e*	*j = 3.5e*	*j = 4.5e*	*j = 5.5e*	*j = 6.5e*
He	$k^{(1)}_{TCPS}$	*1.3 ± 0.1*	*1.3 ± 0.1*	*1.4 ± 0.1*	*1.4 ± 0.1*	*1.2 ± 0.1*	*1.3 ± 0.1*
	$\langle\sigma^{(1)}_{TCPS}\rangle$	*9.28 ± 0.7*	*9.28 ± 0.7*	*10.0 ± 0.7*	*10.0 ± 0.7*	*8.57 ± 0.7*	*9.28 ± 0.7*
	$k^{(2)}_{TCPS}$	*1.4 ± 0.2*	*1.5 ± 0.2*	*1.5 ± 0.1*	*1.8 ± 0.2*	*1.9 ± 0.2*	
	$\langle\sigma^{(2)}_{TCPS}\rangle$	*10.0 ± 1.4*	*10.7 ± 1.4*	*10.7 ± 0.7*	*12.9 ± 0.7*	*13.6 ± 1.4*	
Ar	$k^{(1)}_{TCPS}$	*2.7 ± 0.3*	*2.3 ± 0.2*	*2.0 ± 0.1*	*1.8 ± 0.1*	*1.6 ± 0.2*	*1.5 ± 0.1*
	$\langle\sigma^{(1)}_{TCPS}\rangle$	*36.9 ± 4.1*	*31.5 ± 2.7*	*27.4 ± 1.4*	*24.6 ± 1.4*	*21.9 ± 2.7*	*20.5 ± 1.4*
	$k^{(2)}_{TCPS}$	*3.4 ± 0.5*	*2.7 ± 0.4*	*2.3 ± 0.2*	*2.4 ± 0.6*	*1.9 ± 0.5*	
	$\langle\sigma^{(2)}_{TCPS}\rangle$	*46.5 ± 6.8*	*36.9 ± 5.4*	*31.5 ± 2.7*	*32.8 ± 8.2*	*26.0 ± 6.8*	
Xe	$k^{(1)}_{TCPS}$	*3.8 ± 0.5*	-	-	*3.8 ± 0.3*	-	-
	$\langle\sigma^{(1)}_{TCPS}\rangle$	*58.6 ± 7.7*			*58.6 ±4.6*		
	$k^{(2)}_{TCPS}$	*4.2 ± 0.5*	-	-	*4.4 ± 0.3*	-	-
	$\langle\sigma^{(2)}_{TCPS}\rangle$	*64.8 ± 7.7*			*67.8± 4.6*		

4.4 OH(X)-Rg Calculations

This section will outline the methodology behind the quantum scattering calculations performed on the most recent *ab initio* PESs for OH (X)-He (Lee *et al.* [159]), OH (X)-Ar (section 4.4.1) and OH (X)-Xe (Gilijamse *et al.* [40]) . The OH (X)-Ar PES presented in section 4.4.1 below was constructed by R. Tobola and J. A. Klos from the University of Maryland, USA [18,144]. The details of this surface are provided first before introducing the scattering calculations.

4.4.1 OH (X)-Ar Potential Energy Surface

The description of the triatomic system follows the discussion in section 1.1.2. The OH bond length was set to the equilibrium value r = 0.9122 Å. The [RCCSD(T)] level of theory was used. The calculations for the A' and A'' adiabatic PESs employed the

augmented correlation-consistent quadruple zeta (aug-cc-pVQZ) basis set of Dunning and co-workers [166,167] with an additional (3s3p2d2f1g) set of bond functions centred in the mid-point of the ***R*** vector, commonly denoted as avtz+(33221). The interaction energies were corrected for the basis set superposition error according to a procedure equivalent to the counterpoise method of Boys and Bernardi [168]. In particular, the interaction energy was obtained as the numerical difference between the energies of the dimer and the monomers. All calculations were performed using the MOLPRO 2006.1 package [169]. Energies of the *A*' and *A*" states were calculated in the range for *R* from 3.75 to 16 bohr, at angles θ = 0°, 20°, 40°, 60°, 80°, 90°, 100°, 120°, 140°, 160°, and 180°. In total, 320 energies for the *A*' and *A*" states were calculated. The results for $V_{A'}$, $V_{A''}$, V_{SUM} and V_{DIFF} were fitted according to the expressions described by Kłos *et al.* [153]. Additional points were calculated at 30° and 70° for the purpose of testing the quality of the fit, but were not used later for the main calculations.

Figure 4.18 below shows contour plots of the computed *A*' and *A*" surfaces alongside the average, V_{SUM}, and half-difference, V_{DIFF}, of the two adiabatic surfaces. It is the diabatic linear combinations that are used in the scattering calculations below. V_{DIFF} is entirely repulsive and V_{SUM} is attractive when $R > \sim 6\ a_0$ with a repulsive core at shorter separations. A global minimum of 140.4 cm^{-1} exists for the linear O-H-Ar geometry (θ = 0°), R = 6.98 a_0 and a local minimum of 91.8 cm^{-1} lies at θ = 180°, the opposite linear arrangement, with a separation of R = 6.71 a_0. There are subtle differences between these surfaces and those constructed by Esposti *et al*. Those reported here are less repulsive for low *R* and slightly less attractive for larger *R* over the range θ = 0 – 90°, with the opposite being true at θ = 180°. The PESs are, however, calculated to a higher level of theory and with a larger basis set present and so might reasonably be expected to be more reliable.

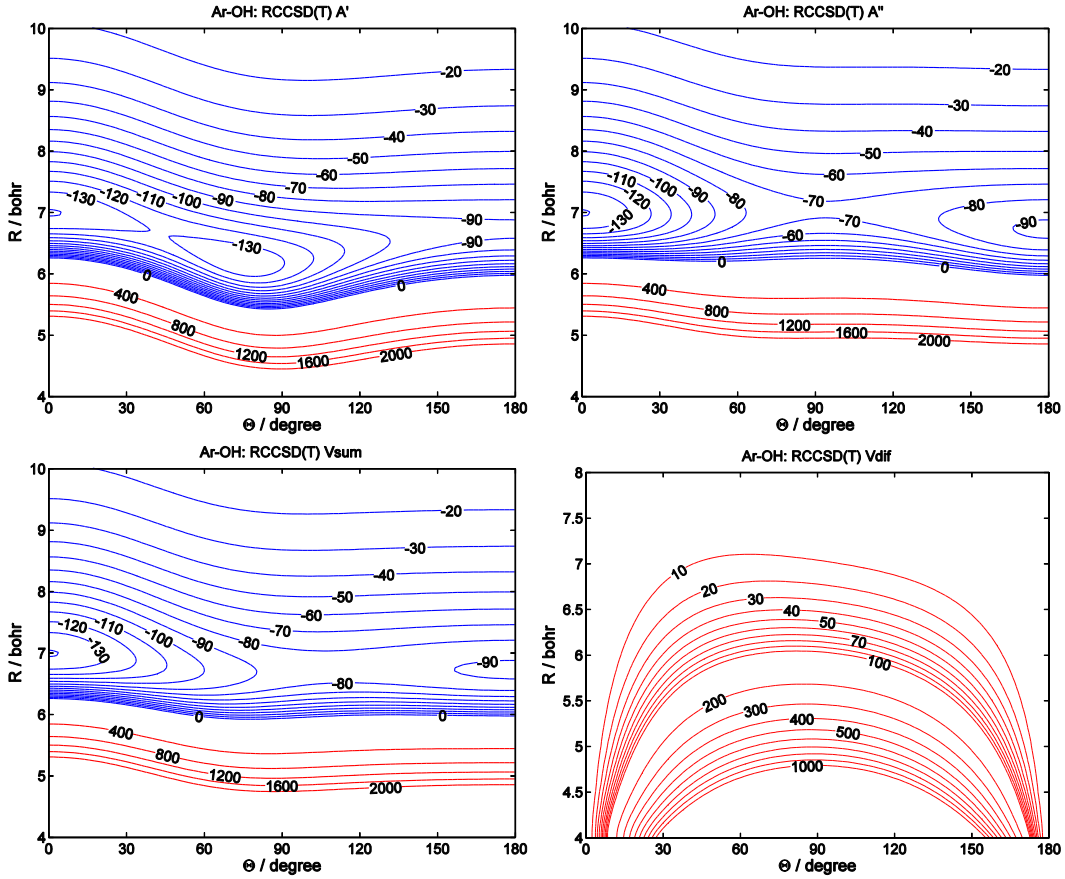

Figure 4.18: *Contour plots of the OH (X)-Ar PESs in Jacobi coordinates (see section 1.1.2). Plots are shown for the A' (upper left) and A" (upper right) surfaces as well as the linear combinations, V_{SUM} (lower left), and V_{DIFF} (lower right). Red and blue contours represent positive and negative interaction energies, respectively. The labels indicate the interaction energy of the contour lines. [18,144]*

4.4.2 Quantum Scattering Calculations

The motivation for performing these calculations was to predict thermal rate constants for the process outlined in equation 4-4. Previous theoretical rate constants had only been evaluated for $v = 2$ [15]. In addition there have been no measurements of RET for $v = 0$ for direct comparison to the PS measurements in sections 4.2 and 4.3.

$$\mathrm{OH}(\mathrm{X}^2\Pi_\Omega, v = 0, j, \varepsilon) + \mathrm{Ar} \rightarrow \mathrm{OH}(\mathrm{X}^2\Pi_{\Omega'}, v = 0, j', \varepsilon')$$

(Equation 4-4)

Exact CC calculations without any dynamical approximations were performed using the OH (X)-Ar PESs presented in section 4.1 and 4.4.1, taking account of the open-shell electronic structure of the OH molecule. The internuclear distance of OH (X) was set to its equilibrium value: r_e = 0.9122 Å. The HIBRIDON suite of codes was used to execute the quantum scattering calculations [27], which uses the Log-Derivative propagator by Manolopoulos [170]. The cross-sections were calculated on a grid of > 3000 total energies ranging from 0.1 to 2500 cm^{-1}. The grid covered the lowest energies from 0 to 200 cm^{-1} with a step of 0.1 cm^{-1}. For energies between 200 and 500 cm^{-1} the step was increased to 0.5 cm^{-1}. For total energies above 500 cm^{-1}, successively increasing steps of 1, 5, 10 and 25 cm^{-1} were used, with the largest step covering the upper energy region between 2000 and 2500 cm^{-1}. To converge the integral cross sections at the highest total energies, a maximum value of the total angular momentum, J^{tot} = 250, and a maximum value of the rotational quantum number of the OH molecule, j_{max} = 14.5 were required. The cross sections calculated in this way were then spline-interpolated and thermal rate constants at 298.15 K were obtained by integration over a Boltzmann distribution of relative translational energies:

$$k_{if}(F, j, \varepsilon \rightarrow F', j', \varepsilon'; T) = \sqrt{\frac{8}{\pi\mu}}(kT)^{-3/2} \times \int_0^\infty \sigma_{if}\left(F, j, \varepsilon \rightarrow F', j', \varepsilon'; E_k\right)\exp\left(-\frac{E_k}{kT}\right)E_k \; dE_k$$

(Equation 4-5)

Details of the state to state cross-sections at 300 cm^{-1} can be found elsewhere [18]. For OH (X) + He the individual state-to-state rate constants are systematically larger by approximately 15% than the work of Esposti *et al* [15]. However, the PESs were different, which differ by 23% in the global minimum alone, and also the methods of calculation were different; these here being exact CC and the previous study using the CS approximation. For OH (X) + Ar the calculated rate constants are very similar to those of Esposti *et al.* despite being calculated for different vibrational levels (v = 2 vs. v = 0). However, similar to the OH (X) + He case, the calculations were performed on two different surfaces and using different levels of scattering calculations, so the agreement may simply be accidental. There are no equivalent comparisons for OH (X) + Xe. It appears that these calculations are the first predictions of thermal RET rate constants for any vibrational level on this recent surface.

All relevant state-to-state rate constants obtained are collected in tables 4-4 – 4-6 below. The values of interest for the PS measurements are highlighted in bold, which include k_{Λ}, k_{RET} and their sum, k_{POP}. For convenience these important quantities are summarised together in figure 4.19. It is clear that for all colliders the efficiency of Λ-doublet transfer decreases monotonically as a function of increasing j. The j-dependence of total RET removal rate constants has a maximum for all j, which occurs at j = 2.5 for Ar and 3.5 for He and Xe, before falling monotonically as the initial j becomes larger. This is well understood in terms of energy gap scaling laws and degeneracy factors introduced in chapter 1.

Table 4-4: *Calculated state-to-state population transfer rate constants (in 10^{-12} cm^3 s^{-1}) for OH ($X^2\Pi_{3/2}$, v = 0, j, e/f) + He collisions at 298 K.*

Initial state $^2\Pi_{3/2}$ (F_1)		*j=1.5 e(-)*	*j=1.5 f(+)*	*j=2.5 e(+)*	*j=2.5 f(-)*	*j=3.5 e(-)*	*j=3.5 f(+)*	*j=4.5 e(+)*	*j=4.5 f(-)*	*j=5.5 e(-)*	*j=5.5 f(+)*	*j=6.5 e(+)*	*j=6.5 f(-)*
Final state $^2\Pi_{3/2}$ (F_1)													
j=1.5	*e(-)*		***12.46***	*13.89*	*8.06*	*16.49*	*1.52*	*4.83*	*0.82*	*2.17*	*0.14*	*1.11*	*0.04*
j=1.5	*f(+)*	***12.46***		*55.81*	*6.57*	*7.34*	*3.20*	*5.43*	*0.50*	*2.11*	*0.18*	*0.98*	*0.06*
j=2.5	*e(+)*	*13.90*	*55.89*		***9.89***	*17.98*	*8.03*	*12.32*	*0.98*	*5.42*	*0.34*	*1.51*	*0.11*
j=2.5	*f(-)*	*8.06*	*6.57*	***9.88***		*46.18*	*7.59*	*7.21*	*1.80*	*3.61*	*0.45*	*1.91*	*0.13*
j=3.5	*e(-)*	*12.43*	*5.53*	*13.54*	*34.80*		***7.99***	*21.98*	*11.96*	*8.55*	*0.66*	*4.89*	*0.15*
j=3.5	*f(+)*	*1.14*	*2.41*	*6.03*	*5.71*	***7.97***		*31.92*	*9.28*	*6.35*	*1.72*	*2.31*	*0.27*
j=4.5	*e(+)*	*2.17*	*2.44*	*5.52*	*3.24*	*13.09*	*19.05*		***6.03***	*24.10*	*15.89*	*6.28*	*0.70*
j=4.5	*f(-)*	*0.37*	*0.23*	*0.44*	*0.80*	*7.10*	*5.52*	***6.01***		*21.52*	*10.48*	*5.39*	*1.80*
j=5.5	*e(-)*	*0.47*	*0.46*	*1.17*	*0.78*	*2.45*	*1.82*	*11.60*	*10.40*		***4.58***	*24.51*	*18.74*
j=5.5	*f(+)*	*0.03*	*0.04*	*0.07*	*0.10*	*0.19*	*0.49*	*7.60*	*5.03*	***4.55***		*15.40*	*10.94*
j=6.5	*e(+)*	*0.09*	*0.08*	*0.13*	*0.16*	*0.55*	*0.26*	*1.19*	*1.02*	*9.63*	*6.09*		***3.53***
j=6.5	*f(-)*	*0.00*	*0.01*	*0.01*	*0.01*	*0.02*	*0.03*	*0.13*	*0.34*	*7.30*	*4.29*	***3.50***	
Final state $^2\Pi_{1/2}$ (F_2)													
j=0.5	*e(+)*	*0.15*	*32.64*	*9.03*	*0.82*	*1.28*	*1.34*	*1.18*	*0.52*	*0.66*	*0.17*	*0.22*	*0.07*
j=0.5	*f(-)*	*23.76*	*0.22*	*1.10*	*16.38*	*3.07*	*1.01*	*1.03*	*0.22*	*0.45*	*0.19*	*0.23*	*0.06*
j=1.5	*e(-)*	*14.20*	*0.62*	*0.31*	*39.12*	*9.82*	*2.41*	*2.11*	*2.06*	*0.99*	*0.53*	*0.72*	*0.16*
j=1.5	*f(+)*	*1.04*	*16.99*	*19.24*	*1.06*	*2.93*	*24.61*	*2.27*	*1.67*	*0.94*	*0.29*	*0.45*	*0.20*
j=2.5	*e(+)*	*0.20*	*1.36*	*13.65*	*1.28*	*0.38*	*43.42*	*8.50*	*2.95*	*2.23*	*1.96*	*0.74*	*0.50*
j=2.5	*f(-)*	*5.00*	*1.11*	*2.27*	*11.42*	*18.06*	*1.18*	*3.10*	*22.86*	*1.52*	*1.83*	*0.67*	*0.28*
j=3.5	*e(-)*	*0.16*	*0.11*	*0.22*	*0.87*	*11.04*	*1.14*	*0.42*	*43.80*	*6.46*	*2.94*	*1.91*	*1.53*
j=3.5	*f(+)*	*0.64*	*1.03*	*2.47*	*1.20*	*1.90*	*6.71*	*18.39*	*1.05*	*2.73*	*18.31*	*0.97*	*1.60*
j=4.5	*e(+)*	*0.03*	*0.02*	*0.06*	*0.04*	*0.15*	*0.48*	*8.22*	*0.89*	*0.40*	*41.82*	*4.73*	*2.56*
j=4.5	*f(-)*	*0.20*	*0.24*	*0.29*	*0.37*	*1.14*	*0.84*	*1.40*	*3.79*	*18.42*	*0.84*	*2.20*	*14.19*
j=5.5	*e(-)*	*0.00*	*0.00*	*0.01*	*0.01*	*0.02*	*0.02*	*0.08*	*0.24*	*5.88*	*0.63*	*0.34*	*38.80*
j=5.5	*f(+)*	*0.05*	*0.04*	*0.06*	*0.08*	*0.12*	*0.13*	*0.50*	*0.50*	*0.97*	*2.20*	*17.78*	*0.66*
j=6.5	*e(+)*	*0.00*	*0.00*	*0.00*	*0.00*	*0.00*	*0.00*	*0.01*	*0.01*	*0.04*	*0.11*	*4.11*	*0.43*
j=6.5	*f(-)*	*0.01*	*0.01*	*0.01*	*0.01*	*0.02*	*0.03*	*0.05*	*0.05*	*0.22*	*0.27*	*0.65*	*1.32*
k_{RET}		***84.1***	***128.1***	***145.3***	***132.9***	***161.3***	***130.8***	***151.4***	***122.8***	***132.6***	***112.4***	***99.99***	***95.29***
k_{POP}		***96.56***	***140.5***	***155.2***	***142.8***	***169.3***	***138.8***	***157.5***	***128.8***	***137.2***	***116.9***	***103.5***	***98.79***

Table 4-5: *Calculated state-to-state population transfer rate constants (in 10^{-12} cm^3 s^{-1}) for OH ($X^2\Pi_{3/2}$, v = 0, j, e/f) + Ar collisions at 298 K.*

Initial state $^2\Pi_{3/2}$ (F_1)		*j=1.5 e(-)*	*j=1.5 f(+)*	*j=2.5 e(+)*	*j=2.5 f(-)*	*j=3.5 e(-)*	*j=3.5 f(+)*	*j=4.5 e(+)*	*j=4.5 f(-)*	*j=5.5 e(-)*	*j=5.5 f(+)*	*j=6.5 e(+)*	*j=6.5 f(-)*
Final state $^2\Pi_{3/2}$ (F_1)													
j=1.5	*e(-)*		***139.12***	*15.66*	*26.74*	*22.48*	*1.54*	*7.24*	*0.27*	*2.26*	*0.08*	*0.80*	*0.03*
j=1.5	*f(+)*	***139.08***		*82.96*	*15.47*	*10.64*	*3.08*	*4.13*	*0.31*	*2.22*	*0.07*	*0.92*	*0.03*
j=2.5	*e(+)*	*15.68*	*83.08*		***66.40***	*26.12*	*30.20*	*8.79*	*1.20*	*4.09*	*0.28*	*1.29*	*0.07*
j=2.5	*f(-)*	*26.75*	*15.48*	***66.34***		*35.22*	*5.20*	*7.93*	*1.96*	*1.92*	*0.29*	*0.83*	*0.07*
j=3.5	*e(-)*	*16.95*	*8.02*	*19.67*	*26.55*		***44.12***	*29.80*	*25.67*	*6.36*	*1.09*	*2.56*	*0.21*
j=3.5	*f(+)*	*1.16*	*2.32*	*22.69*	*3.91*	***44.02***		*12.90*	*7.12*	*4.22*	*1.56*	*1.36*	*0.25*
j=4.5	*e(+)*	*3.25*	*1.85*	*3.94*	*3.56*	*17.75*	*7.70*		***29.76***	*25.88*	*22.76*	*5.16*	*0.98*
j=4.5	*f(-)*	*0.12*	*0.14*	*0.54*	*0.88*	*15.23*	*4.23*	***29.64***		*9.82*	*7.75*	*3.64*	*1.13*
j=5.5	*e(-)*	*0.49*	*0.48*	*0.88*	*0.41*	*1.82*	*1.21*	*12.45*	*4.75*		***21.81***	*19.27*	*20.58*
j=5.5	*f(+)*	*0.02*	*0.02*	*0.06*	*0.06*	*0.31*	*0.45*	*10.89*	*3.72*	***21.68***		*9.06*	*6.17*
j=6.5	*e(+)*	*0.07*	*0.08*	*0.11*	*0.07*	*0.29*	*0.15*	*0.98*	*0.69*	*7.57*	*3.58*		***16.51***
j=6.5	*f(-)*	*0.00*	*0.00*	*0.01*	*0.01*	*0.02*	*0.03*	*0.18*	*0.21*	*8.02*	*2.42*	***16.37***	
Final state $^2\Pi_{1/2}$ (F_2)													
j=0.5	*e(+)*	*0.75*	*11.99*	*7.23*	*8.31*	*2.52*	*2.91*	*0.93*	*1.24*	*0.50*	*0.41*	*0.16*	*0.11*
j=0.5	*f(-)*	*6.75*	*1.24*	*3.97*	*24.52*	*3.94*	*5.11*	*1.09*	*1.00*	*0.18*	*0.40*	*0.09*	*0.15*
j=1.5	*e(-)*	*3.74*	*1.94*	*2.19*	*17.78*	*8.64*	*6.07*	*3.68*	*2.75*	*0.95*	*0.64*	*0.38*	*0.18*
j=1.5	*f(+)*	*2.40*	*4.39*	*8.90*	*6.41*	*9.44*	*66.56*	*2.89*	*6.54*	*0.57*	*0.93*	*0.22*	*0.21*
j=2.5	*e(+)*	*0.39*	*0.52*	*4.62*	*1.81*	*2.43*	*24.34*	*13.77*	*4.69*	*4.39*	*1.66*	*1.09*	*0.37*
j=2.5	*f(-)*	*1.00*	*1.56*	*3.54*	*4.54*	*13.45*	*6.68*	*13.55*	*53.53*	*2.82*	*3.97*	*0.45*	*0.58*
j=3.5	*e(-)*	*0.10*	*0.08*	*0.24*	*0.27*	*3.98*	*1.43*	*3.15*	*35.21*	*13.15*	*3.95*	*3.79*	*0.90*
j=3.5	*f(+)*	*0.60*	*0.33*	*0.60*	*1.21*	*4.71*	*3.37*	*25.06*	*4.43*	*11.09*	*42.17*	*2.29*	*2.08*
j=4.5	*e(+)*	*0.02*	*0.02*	*0.03*	*0.03*	*0.09*	*0.14*	*3.28*	*1.19*	*3.00*	*49.04*	*10.79*	*3.17*
j=4.5	*f(-)*	*0.13*	*0.13*	*0.18*	*0.17*	*0.65*	*0.80*	*3.97*	*2.37*	*37.29*	*3.42*	*8.03*	*34.10*
j=5.5	*e(-)*	*0.00*	*0.00*	*0.00*	*0.00*	*0.01*	*0.01*	*0.04*	*0.08*	*2.66*	*0.91*	*2.53*	*61.95*
j=5.5	*f(+)*	*0.02*	*0.03*	*0.04*	*0.03*	*0.08*	*0.10*	*0.42*	*0.46*	*2.78*	*1.65*	*47.35*	*2.66*
j=6.5	*e(+)*	*0.00*	*0.00*	*0.00*	*0.00*	*0.00*	*0.00*	*0.00*	*0.00*	*0.02*	*0.04*	*2.13*	*0.58*
j=6.5	*f(-)*	*0.00*	*0.00*	*0.01*	*0.01*	*0.01*	*0.01*	*0.04*	*0.05*	*0.22*	*0.23*	*1.71*	*1.15*
k_{RET}		***80.40***	***133.69***	***178.08***	***142.74***	***179.86***	***171.33***	***167.28***	***159.52***	***152.59***	***149.84***	***136.61***	***141.95***
k_{POP}		***219.48***	***272.81***	***244.41***	***209.14***	***223.88***	***215.44***	***196.92***	***189.28***	***174.27***	***171.65***	***152.98***	***158.46***

Table 4-6: *Calculated state-to-state population transfer rate constants (in 10^{-12} cm3 s^{-1}) for OH ($X^2\Pi_{3/2}$, v = 0, j, e/f) + Xe collisions at 298 K.*

Initial state $^2\Pi_{3/2}$ (F_1)		*j=1.5 e(-)*	*j=1.5 f(+)*	*j=2.5 e(+)*	*j=2.5 f(-)*	*j=3.5 e(-)*	*j=3.5 f(+)*	*j=4.5 e(+)*	*j=4.5 f(-)*	*j=5.5 e(-)*	*j=5.5 f(+)*	*j=6.5 e(+)*	*j=6.5 f(-)*
Final state $^2\Pi_{3/2}$ (F_1)													
j=1.5	*e(-)*		***208.80***	*25.75*	*45.19*	*16.05*	*2.58*	*8.64*	*1.24*	*2.85*	*0.20*	*1.07*	*0.06*
j=1.5	*f(+)*	***208.80***		*72.06*	*26.18*	*12.89*	*9.06*	*5.41*	*0.80*	*2.53*	*0.22*	*1.05*	*0.06*
j=2.5	*e(+)*	*25.84*	*72.34*		***148.00***	*38.40*	*45.67*	*11.01*	*2.16*	*4.65*	*0.67*	*1.43*	*0.13*
j=2.5	*f(-)*	*45.29*	*26.28*	***147.80***		*34.67*	*17.27*	*5.84*	*4.58*	*1.55*	*0.58*	*0.71*	*0.12*
j=3.5	*e(-)*	*12.16*	*9.77*	*29.03*	*26.20*		***105.70***	*38.61*	*52.68*	*9.98*	*1.91*	*3.42*	*0.41*
j=3.5	*f(+)*	*1.95*	*6.85*	*34.42*	*13.01*	***105.40***		*13.41*	*14.77*	*3.34*	*2.28*	*1.03*	*0.29*
j=4.5	*e(+)*	*3.91*	*2.44*	*4.96*	*2.63*	*23.08*	*8.01*		***76.06***	*30.19*	*50.19*	*7.11*	*1.30*
j=4.5	*f(-)*	*0.55*	*0.36*	*0.97*	*2.05*	*31.25*	*8.80*	***75.64***		*13.78*	*9.55*	*4.24*	*1.09*
j=5.5	*e(-)*	*0.62*	*0.55*	*1.01*	*0.34*	*2.88*	*0.97*	*14.61*	*6.69*		***59.25***	*19.75*	*44.21*
j=5.5	*f(+)*	*0.04*	*0.05*	*0.14*	*0.13*	*0.55*	*0.65*	*24.16*	*4.63*	***58.93***		*12.61*	*5.91*
j=6.5	*e(+)*	*0.09*	*0.09*	*0.12*	*0.06*	*0.39*	*0.12*	*1.36*	*0.81*	*7.85*	*5.04*		***47.47***
j=6.5	*f(-)*	*0.00*	*0.00*	*0.01*	*0.01*	*0.05*	*0.03*	*0.24*	*0.21*	*17.44*	*2.34*	***47.07***	
Final state $^2\Pi_{1/2}$ (F_2)													
j=0.5	*e(+)*	*2.33*	*7.60*	*9.13*	*15.07*	*3.38*	*4.59*	*1.34*	*1.51*	*0.53*	*0.64*	*0.15*	*0.20*
j=0.5	*f(-)*	*7.08*	*2.55*	*6.21*	*16.57*	*6.32*	*9.92*	*1.30*	*2.98*	*0.27*	*0.88*	*0.12*	*0.27*
j=1.5	*e(-)*	*2.58*	*3.48*	*3.97*	*16.43*	*13.39*	*12.83*	*6.98*	*3.55*	*1.75*	*0.78*	*0.50*	*0.21*
j=1.5	*f(+)*	*2.39*	*4.79*	*7.95*	*7.25*	*15.84*	*71.36*	*5.10*	*9.46*	*1.14*	*1.74*	*0.28*	*0.40*
j=2.5	*e(+)*	*0.56*	*1.22*	*5.58*	*3.06*	*6.15*	*26.54*	*22.95*	*10.41*	*7.20*	*2.05*	*1.60*	*0.43*
j=2.5	*f(-)*	*1.91*	*1.90*	*1.82*	*5.01*	*17.59*	*12.04*	*20.09*	*53.92*	*3.25*	*5.42*	*0.64*	*0.86*
j=3.5	*e(-)*	*0.19*	*0.13*	*0.36*	*0.55*	*7.16*	*3.14*	*7.77*	*45.45*	*26.00*	*8.44*	*6.28*	*1.27*
j=3.5	*f(+)*	*0.68*	*0.50*	*0.70*	*1.40*	*2.99*	*4.79*	*33.64*	*10.22*	*14.92*	*44.56*	*2.19*	*2.89*
j=4.5	*e(+)*	*0.03*	*0.02*	*0.06*	*0.05*	*0.17*	*0.33*	*6.99*	*2.77*	*7.33*	*70.17*	*24.98*	*6.09*
j=4.5	*f(-)*	*0.16*	*0.16*	*0.19*	*0.23*	*0.62*	*1.01*	*3.12*	*3.14*	*52.09*	*9.08*	*11.07*	*36.39*
j=5.5	*e(-)*	*0.00*	*0.00*	*0.00*	*0.00*	*0.01*	*0.02*	*0.07*	*0.18*	*6.13*	*1.89*	*7.08*	*96.53*
j=5.5	*f(+)*	*0.03*	*0.03*	*0.03*	*0.03*	*0.09*	*0.13*	*0.40*	*0.52*	*2.75*	*2.29*	*71.13*	*7.59*
j=6.5	*e(+)*	*0.00*	*0.00*	*0.00*	*0.00*	*0.00*	*0.00*	*0.00*	*0.01*	*0.03*	*0.07*	*5.07*	*1.06*
j=6.5	*f(-)*	*0.00*	*0.00*	*0.00*	*0.00*	*0.01*	*0.01*	*0.04*	*0.05*	*0.21*	*0.27*	*1.99*	*1.92*
k_{RET}		***108.4***	***141.1***	***204.5***	***181.4***	***234.0***	***239.9***	***233.2***	***232.8***	***218.5***	***221.9***	***202.4***	***214.9***
k_{POP}		***317.2***	***349.9***	***352.3***	***329.4***	***339.4***	***345.6***	***308.9***	***308.9***	***277.4***	***281.2***	***249.5***	***262.4***

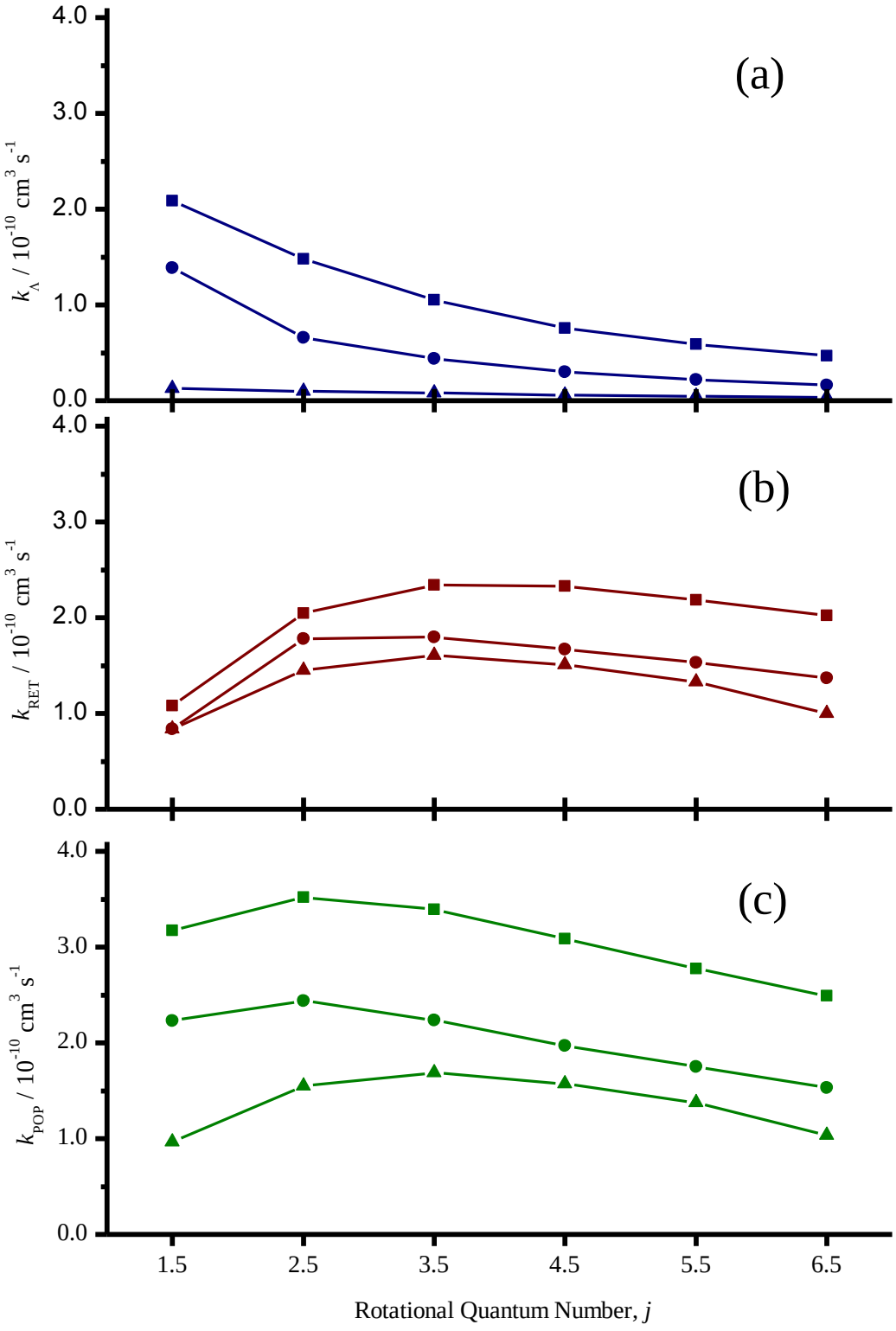

Figure 4.19: *Comparison of CC QM rate constants for collisions of OH ($X^2\Pi_{3/2}$, v = 0, j, e) with Xe (squares), Ar (circles) and He (triangles). (a) k_Λ, Λ-doublet transfer only; (b) k_{RET}, all inelastic processes, excluding Λ-doublet transfer and (c) k_{POP}, the sum of k_{RET} and k_Λ .*

4.5 Discussion

4.5.1 Comparison of TCPS with OCPS

First, the experimental measurements of $k_{PS}^{(K)}$ will be discussed in their own right, beginning with the initial OCPS studies. From the data in table 4-2 it is clearly seen that the rate constants are larger for Ar than for He, with Ar being, on average, 85% larger. From the computed k_{POP} values obtained from the calculations in section 4.4.2, there is a predicted increase of 63% from He to Ar, suggesting that there is an additional process that is more efficient for Ar than He. The OCPS measurements are also sensitive to elastic depolarisation, so perhaps this is the first indication that depolarisation is a significant process and that Ar is more efficient than He. However, this is a bold statement when only considering the OCPS measurements, which are, by construction, at least partially sensitive to OH (A) as well as the desired OH (X) quantum states connected by the spectroscopic transitions used. It also relies on the accuracy of the predicted rate constants.

As emphasised above, the TCPS measurements are sensitive to *only* the rotational quantum state that is common between the pump and probe transitions; in this case OH (X, v = 0, j). TCPS signal can only be generated from OH (A), in the 'V-shaped' scheme used, through population transfer *with retention of rotational polarisation* to the OH (A) rovibronic level resonant with the probe transition. Crosley and co-workers have measured rate constants for vibrational energy transfer (VET) from v' = 1 to v' = 0 in OH (A) for various colliders [171,172]. They reported a total VET rate constant of (4.1 ± 0.3) x 10^{-12} cm^3 s^{-1} for Ar with a thermal (300 K) OH v = 1 rotational distribution, and of (1.3 ± 0.4) x 10^{-12} cm^3 s^{-1} for He interpolated for OH (A, v = 1, N = 2) [173]. They also noted that, in general, the product v' = 0 distribution tends to be broad and non-thermal, populating high j'. Since the measurements in this chapter focus on low rotational levels, and the measured $k_{TCPS}^{(K)}$ values are approximately two orders of magnitude larger than the total VET rate constants, it is reasonable to assume that VET from v = 1 to v = 0 is not a contributing factor to the TCPS signal.

Figure 4.20 shows a direct comparison between the OCPS and TCPS measurements made using linear pump polarisation. Appropriate thermally averaged cross-sections are plotted as a function of OH (X) rotational level for both Ar and He.

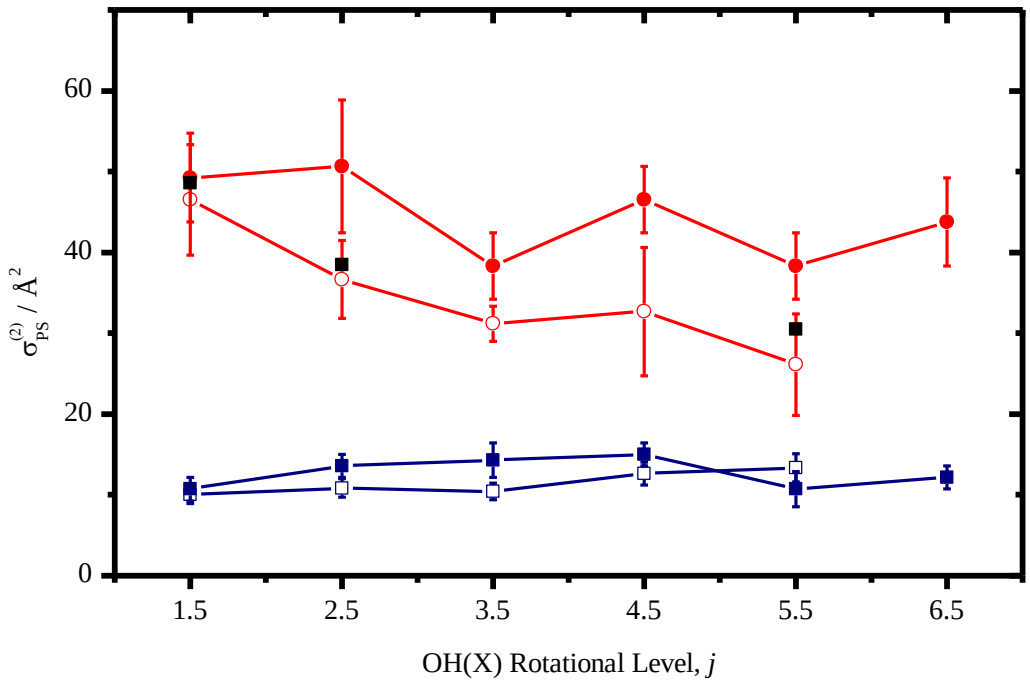

Figure 4.20: *Thermally averaged cross-sections as a function of OH (X) rotational level. Comparison of* $\langle \sigma^{(2)}_{OCPS} \rangle$ *(filled symbols) and* $\langle \sigma^{(2)}_{TCPS} \rangle$ *(open symbols) for both Ar (red) and He (navy). The error bars represent 2σ uncertainties. As described in the text, the filled squares represent simulated OCPS cross-sections for OH + Ar, using measured cross-sections for OH (X) and OH (A).*

For OH + Ar, the magnitude of $\langle \sigma^{(2)}_{TCPS} \rangle$ declines more rapidly than $\langle \sigma^{(2)}_{OCPS} \rangle$ does as a function of j and consequently the measured cross-sections deviate significantly more (by up to ~40%) at higher j. For OH + He there is much less of a deviation, but nonetheless, the numerical value of the OCPS measurements are larger than the TCPS equivalents, with the exception of j = 5.5. Interestingly, the values obtained for j = 1.5 for both OCPS and TCPS are essentially the same within the experimental errors. The upper level for the OCPS measurements, in this example, is OH (A, v = 0, N = 0, f_1), which, by definition, cannot possess any degree of alignment. Moreover, there will be no orientation moments generated because the polarisation of the pump laser was linear. As a result, for the lowest j there can be no contribution to the OCPS signal from OH (A). It is therefore no accident that the TC and OCPS values are the same and provides some confidence in the measured rate constants/cross-sections acquired completely independent of one another.

In attempt to rationalise the deviation for the other rotational levels, OCPS simulations were run for OH + Ar (j = 2.5 and j = 5.5). These simulations include $k_{TCPS}^{(2)}$ values for OH (X) and OH (A) (which are fortunately known – see chapter 6) and the measured intercepts. This produced a synthetic OCPS pump-probe decay trace for a given pressure, which was subsequently fitted using the OCPS fitting routine, used to analyse all OCPS measurements, to provide a decay rate, $\Gamma_{OCPS}^{(2)}$. This was evaluated for a range of pressures similar to the OCPS measurements to give $k_{OCPS}^{(2)}(sim.)$. Figure 4.20 shows the results of these simulations. The $k_{OCPS}^{(2)}(sim.)$ values fall short of those measured experimentally, but at least the correction is in the right direction. This OCPS *vs.* TCPS comparison does, however, highlight the need for uncontaminated TCPS measurements for robust assessment of elastic depolarisation. These will be more reliable for comparison to calculations and previous experiments of RET, which are not a convolution of multiple quantum states. In addition, TCPS allows the reliable measurement of orientation decay, which would be heavily contaminated by OH (A) in OCPS measurements. Hence, all further discussion will refer only to the TCPS study.

4.5.2 Orientation *vs.* Alignment

All results from the TCPS study are summarised in figure 4.21 using the thermally averaged cross-sections. This takes into consideration the more frequent collisions for the lighter collision partners. The empirical observation made in the previous section that $k_{TCPS}^{(K)}$ values for loss of alignment are always larger than those for orientation becomes easier to see. This observation demonstrates directly, without appealing either to theory or other measurements, that there must be significant elastic depolarisation of OH (X) by Ar and Xe, where the difference is largest. The only way such a difference can arise is if depolarising collisions do contribute. Otherwise, the measured $k_{TCPS}^{(K)}$ would be entirely made up of inelastic transfer, with values that are independent of K (see section 1.1.5). Moreover, the depolarising collisions must lead to an incomplete scrambling of m_j values. If not, the depolarisation contribution to $k_{TCPS}^{(K)}$, although finite, would be the same for both orientation and alignment. The greater robustness of orientation over alignment is characteristic of processes in which $|\Delta m_J|$ is restricted. This

comes from the same basis used to rationalise the reduction in the NHQBs for orientation *vs.* alignment (see section 4.3).

For He, although k_{PS} is again numerically larger for alignment than for orientation for most j values, the statistical significance of the differences is marginal. The most likely implication is that inelastic transfer is dominant, with elastic depolarisation being a less important process for He, than for Ar or Xe.

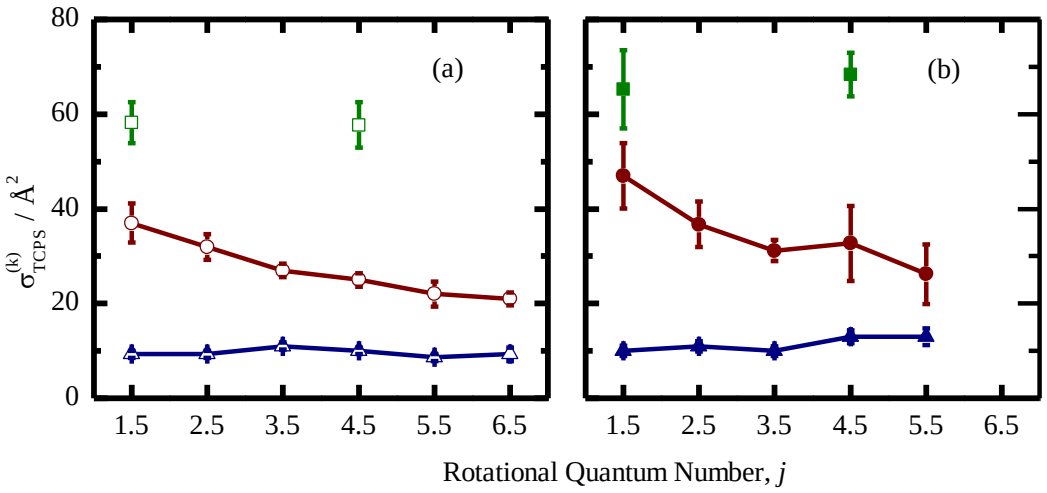

Figure 4.21: *Thermally averaged PS removal cross-sections for collisions of OH ($X^2\Pi_{3/2}$, v = 0, j, e) with Xe (squares), Ar (circles) and He (triangles), with associated 2σ uncertainties. (a) K = 1 (orientation) (b) K = 2 (alignment).*

This difference between orientation and alignment can serve as an indicator for the magnitude of elastic depolarisation amongst these collision partners for OH (X, v = 0). Taking cross-sections for the lowest rotational level measured, j = 1.5, this provides estimates for the magnitudes of elastic depolarisation, σ_{DEP}, to be: < 1 Å^2 (He), 9.6 Å^2 (Ar) and 6 Å^2 (Xe). Although, these values must be related to elastic depolarisation they do not necessarily provide absolute magnitudes for $\sigma^{(K)}_{DEP}$. Despite this, it does confirm the conclusion that depolarisation for He is modest and OH (X) + Ar and Xe results in significant depolarisation.

For OH (X) + Ar, there is clearly a systematic trend for $\sigma^{(K)}_{TCPS}$ to decrease with increasing rotational quantum number, for both orientation and alignment. However, $\sigma^{(K)}_{TCPS}$ is a combination of inelastic population transfer and elastic depolarisation. Therefore, further comment on j-dependent trends for collisional depolarisation will be postponed until consideration of the inelastic contributions to $\sigma^{(K)}_{TCPS}$ has been made.

Regardless of this, there seems to be little, if any, significant j dependence of $\sigma_{TCPS}^{(K)}$ for OH (X) + He and Xe for either orientation or alignment.

4.5.3 Magnitude of Elastic Depolarisation and testing the PES

This section will quantitatively assess the role of elastic depolarisation that has been inferred qualitatively above from the clear difference between $k_{TCPS}^{(K)}$ for orientation and alignment. To do so, a value for k (or, $\sigma)_{POP}$ needs to be evaluated (see equation 4-2). It is then possible to deduce by difference the rate constants (cross-sections), $k(\sigma)_{DEP} = k(\sigma)_{TCPS} - k(\sigma)_{POP}$, for those rotationally elastic collisions which only destroy the prepared orientation or alignment. This can be done in two ways: either taking k_{POP} from the previous experiments of Smith and co-workers or from the scattering calculations reported in this thesis or elsewhere.

Using the experimental data from Smith and co-workers [136,137] k_{POP} can be evaluated for only two rotational quantum states where measurements of k_A were made, namely j = 3.5 and 6.5. For j = 3.5, Smith and co-workers found k_{POP} = 2.5 x 10^{-10} cm^3 s^{-1}. Since the corresponding $k_{TCPS}^{(K)}$ values for j = 3.5 are 2.2 x 10^{-10} cm^3 s^{-1} for K = 1 and 2.3 x 10^{-10} cm^3 s^{-1} for K = 2, this would imply the seemingly unphysical result that k_{POP} *exceeds* $k_{TCPS}^{(K)}$: it can, of course, at most equal it, although the observed differences between $k_{TCPS}^{(K)}$ for orientation and alignment (which are larger on average than for this particular j) require it to be definitely lower in practice. There is a similar apparent problem for j = 6.5, for which $k_{TCPS}^{(K)}$ for orientation is equal, at 1.5 x 10^{-10} cm^3 s^{-1}, to k_{POP}. A simple conclusion from this is that the reported values of k_{POP} for OH (v = 1) + Ar measurably overestimate the values for v = 0 implied by the $k_{TCPS}^{(K)}$ results reported here. Other than unknown systematic errors affecting either or both experiments, a possible fundamental explanation lies in the anticipated vibrational-level dependence of the removal rate constants with Ar, as discussed in sections 4.1 and 4.4.2.

For He, the data are even more limited, with only a single value (j = 6.5) for which Smith and co-workers measured both k_{RET} and k_A, giving k_{POP} = (1.2 ± 0.1) x 10^{-10} cm^3 s^{-1}. This is once more very similar to the measured $k_{TCPS}^{(1)}$ value of (1.3 ± 0.2) x 10^{-10} cm^3 s^{-1} for j = 6.5 in v = 0, although the small difference is at least on the physically

plausible side, consistent with at most a minor contribution from elastic depolarisation for He.

The alternative, for a more complete comparison across all rotational levels measured, is to take the quantum scattering calculations as the source of k_{RET} and k_{Λ}. The calculations performed in conjunction with the experimental results of this thesis provide these values (section 4.4.2). The original comparisons were carried out by subtracting the calculated k_{POP} values from the $k_{TCPS}^{(K)}$ values to provide $k_{DEP}^{(K)}$ [18]. Stimulated by the publication of this work, on which this chapter is based, Dagdigian and Alexander have published theoretical predictions of $k_{DEP}^{(K)}$ for OH (X) + He [93] and OH (X) + Ar [94,174] on the same PESs used in the scattering calculations presented in section 4.4.2. Together with calculated k_{POP} values this provides a full prediction of the measured values in this thesis; a predicted $k_{TCPS}^{(K)}$ $\left(\sigma_{TCPS}^{(K)}\right)$. The scattering calculations performed on the OH (X) + Xe system also evaluated these so-called tensor cross-section, but for only one collision energy of 300 cm^{-1}. First, comparison will be made between these full predictions and the corresponding measurements.

Figures 4.22 – 4.24 summarise this comparison. The total height of the coloured bars represents the calculated thermally averaged cross sections, $\sigma_{TCPS}^{(K)}$, which are decomposed into their constituent parts that the experiments are sensitive to.

For OH (X) + He the calculations are seen to over-predict the absolute magnitude of $\sigma_{TCPS}^{(K)}$ for the majority of rotational levels where a comparison can be made. The calculations show a *j*-dependent trend which seems to be influenced by the variation of the dominant RET component as a function of *j*, with a rise to a maximum at $j = 3.5$ and a slow decline at higher rotational levels. However, this rise and fall is rather modest and is in reasonable agreement with the relatively *j*-independent trend that is measured, given the experimental uncertainty.

For Ar all calculations of $\sigma_{TCPS}^{(K)}$ are larger than the measurements where full comparisons can be made. This disagreement is about 35% in the worst case at $j = 1.5$ and for $K = 2$, with increasing agreement at higher values of *j*, falling within the experimental uncertainty for $j = 4.5$ and 5.5. The measured *j*-dependent trend of $\sigma_{TCPS}^{(K)}$ is also qualitatively predicted by the calculations, which smoothly declines from $j = 1.5$

– 6.5. This is largely explained by the combined decline of the calculated $\sigma_{DEP}^{(K)}$ and σ_{Λ} values, which are dominant at low *j*.

For Xe, the same large discrepancy between calculated and measured $\sigma_{TCPS}^{(K)}$ values is at low-*j*. As for Ar, the agreement is better for the measurement at the higher rotational level, j = 4.5, where the absolute value of the measurement is larger than that of the calculation. Although the calculations predict a similar *j*-dependence to that of Ar, the experiments do not reveal this. Any *j*-dependent conclusions based on this small data set would however be somewhat speculative.

So it seems as though the calculated values of $\sigma_{TCPS}^{(K)}$, by and large, overestimate those found experimentally using TCPS and quite considerably at low-*j*. This poses the question, what component(s) of the calculations (i.e. k_{Λ}, k_{RET} or $k_{DEP}^{(K)}$) are being predicted incorrectly? To attempt to answer this it is useful to discuss the comparison of $\sigma_{TCPS}^{(K)}$ with the calculated values of σ_{POP}.

A considerable number of measured $\sigma_{TCPS}^{(K)}$ values for OH (X) + He are lower than the predicted cross-sections for σ_{POP} alone. Using the same subtraction used above in the comparison to the work of Smith and co-workers, this would result in a similar (unphysical) negative elastic depolarisation rate constant/cross-section for many of the rotational levels studied. But it is at least qualitatively consistent with σ_{DEP} being small, requiring particularly accurate values for both $\sigma_{TCPS}^{(K)}$ and σ_{POP} to reveal $\sigma_{DEP}^{(K)}$ correctly. Assuming confidence in the measurements and the scattering calculation methodology, for example, treatment of the OH vibrational motion, then the source of overestimating the TCPS measurements must lie with the construction of the PES. A similar situation is observed for Ar. In this case, calculated σ_{POP} values are larger than the $\sigma_{TCPS}^{(1)}$ values for the rotational levels j = 2.5 – 6.5. This suggests that the conclusion about the PES overestimating the inelastic contribution for He is likely to be true for Ar also. The alignment measurements, $\sigma_{TCPS}^{(2)}$, are however larger than all σ_{POP} (calc.), providing a positive contribution from elastic depolarisation, expected from the empirical experimental observation that alignment is, in all cases, larger than orientation. Evaluating $\sigma_{DEP}^{(2)}$ based on subtraction of σ_{POP} (calc.) from $\sigma_{TCPS}^{(2)}$ would be a lower-

bound limit due to the conclusion that σ_{POP} (calc.) should be finitely lower in practice. It is more difficult to assess whether σ_{POP} (calc.) is incorrect for Xe since all measured $\sigma_{TCPS}^{(K)}$ values are numerically larger. It is also not possible to make any judgements on the accuracy of the inelastic components, σ_{RET} and σ_{Λ}.

We return now to the component of the TCPS measurements that is of most interest, $\sigma_{DEP}^{(K)}$. All calculations of $\sigma_{DEP}^{(K)}$ show that it is largest for the lowest rotational level, j = 1.5, and declines monotonically as j increases. From a classical point-of-view this makes physical sense: it is harder to tilt a faster rotating body than a slower rotating one (gyroscopic effect). It is not too surprising therefore that for this lowest rotational level the measured $\sigma_{TCPS}^{(K)}$ values are larger than σ_{POP} (calc.) for all three colliders. Another interesting observation from the results of the calculated $\sigma_{DEP}^{(K)}$ values is that, on average, $\sigma_{DEP}^{(2)} \approx 2\sigma_{DEP}^{(1)}$. This suggests that the difference between orientation and alignment measurements should be roughly equal to $\sigma_{DEP}^{(1)}$.

Focusing on Ar, the only rotational level where $\sigma_{TCPS}^{(1)}$ and $\sigma_{TCPS}^{(2)}$ are both larger than σ_{POP} is j = 1.5. Using the conventional subtraction $\left(\sigma_{DEP}^{(K)} = \sigma_{TCPS}^{(K)} - \sigma_{POP}\right)$, $\sigma_{DEP}^{(1)}$ and $\sigma_{DEP}^{(2)}$ would be ≈ 7 and 16 Å^2, respectively. (It is interesting to note that there is also an approximate factor of 2 observed between these numbers.) This is in general agreement with the observed difference between orientation and alignment of 9.6 Å^2, implying that for Ar, $\sigma_{DEP}^{(2)}$ could range up to 20 Å^2, comparable in magnitude to competing inelastic processes. These values are however still considerably less than those values calculated for low-j, which are, on their own, as large as the total cross-section measured using TCPS. This is indicative that the PES is also incapable of reproducing the elastic depolarisation component.

One might expect that $\sigma_{DEP}^{(K)}$ for Xe would be larger than Ar from a simple projection based on the fact that He displays little elastic depolarisation, yet Ar provides significant elastic depolarisation. This is indeed the outcome of the scattering calculations. However, the TCPS experiments seem to contradict this line of thought. Because all values of $\sigma_{TCPS}^{(K)}$ are larger than the calculated inelastic cross-sections, then

this provides a significantly positive contribution from $\sigma_{DEP}^{(K)}$ inferred by subtraction. These are evaluated to be ~ 9 Å^2 for orientation and ~ 16 – 20 Å^2 for alignment; the factor of two between orientation and alignment is now becoming increasingly familiar. The magnitude of these inferred cross-sections are consistent with the difference between $\sigma_{TCPS}^{(2)}$ and $\sigma_{TCPS}^{(1)}$ being 6.2 Å^2 and 9.2 Å^2 for j = 1.5 and 4.5 respectively. In comparison to Ar, elastic depolarisation for Xe appears to be relatively similar.

Unfortunately the j-dependent decrease of $\sigma_{DEP}^{(K)}$ (calc.) cannot be seen convincingly from the measurements due to their precision, but overall the difference between orientation and alignment does decease from ~ 10 Å^2 to ~ 4 Å^2 over the range j = 1.5 – 5.5 for OH (X) + Ar. This would be indicative of $\sigma_{DEP}^{(K)}$ decreasing with increasing j. It is not possible to comment on this j-dependence for OH (X) + He/Xe.

Despite the calculations being unsuccessful in quantitatively reproducing the TCPS measurements, one thing the calculations do predict quite well is the *proportional* increase in the value of $\sigma_{TCPS}^{(K)}$ across the series of collider gases studied. Using j = 1.5 as an example, $\sigma_{TCPS}^{(2)}$ is seen to increase by a factor of 4.6 from He to Ar and then by a factor of 1.5 from Ar to Xe. The respective multiplication factors taken from the scattering calculations are 5.1 and 1.5. So perhaps the form of the PES is to some extent reproducing this general trend across colliders, but still fails to reproduce the absolute magnitude of the TCPS measurements.

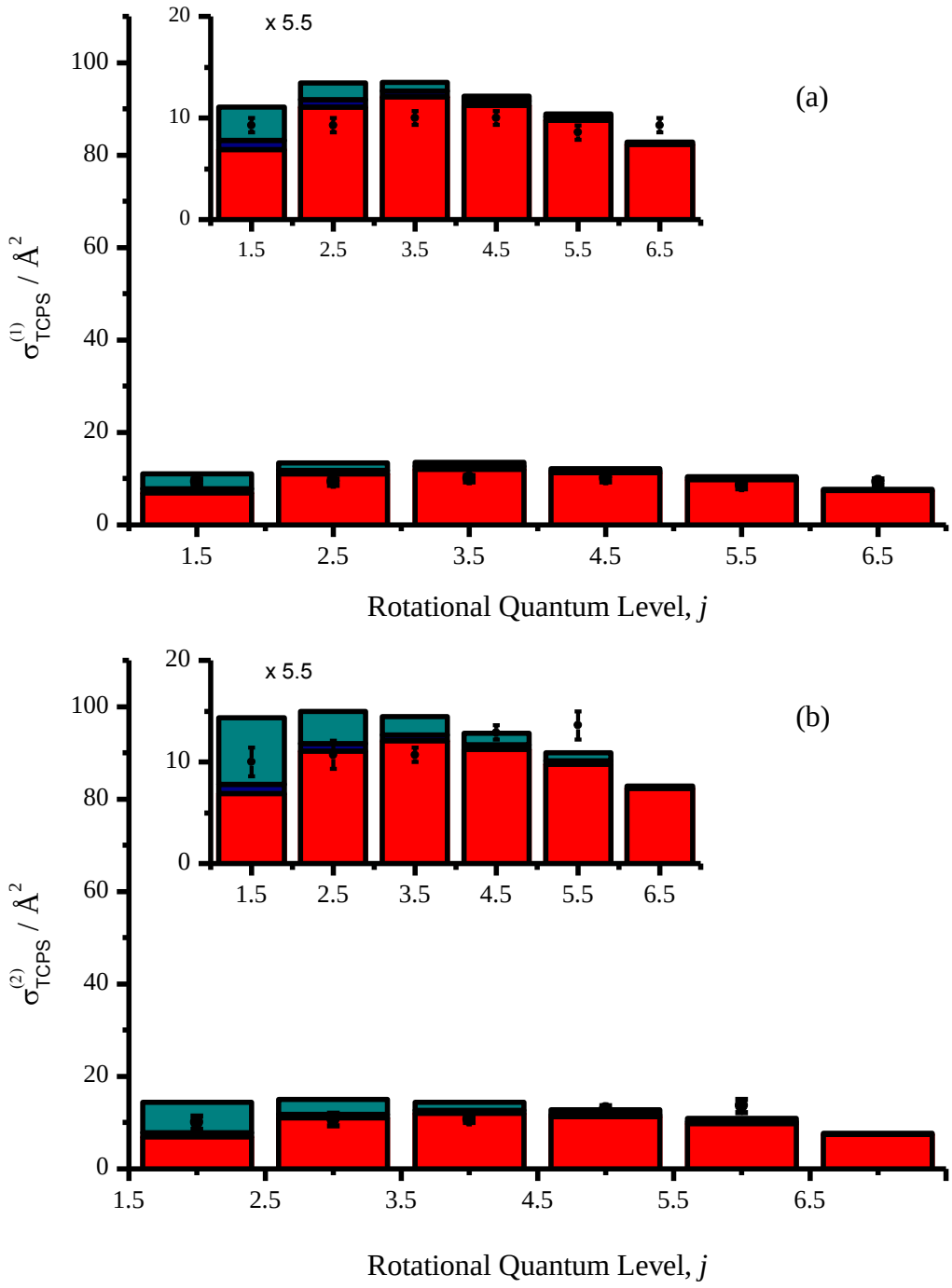

Figure 4.22: *Thermally averaged cross sections from TCPS measurements (data points with associated 2σ uncertainties) and quantum scattering calculations (stacked bars) for OH (X) + He. The total height of the stacked bars represents a predicted* $\sigma^{(K)}_{TCPS}$ *for (a) orientation (K=1) and (b) alignment (K=2). The predicted cross-sections have been decomposed into RET (red), Λ-doublet transfer (navy) and elastic depolarisation (cyan). RET and Λ-doublet transfer (which are the same in both (a) and (b)) are from this work and elastic depolarisation is from [175]. The insets show the same data on expanded vertical scales so that the main figure can be shown on the same vertical scale as figures 4.24 and 4.25.*

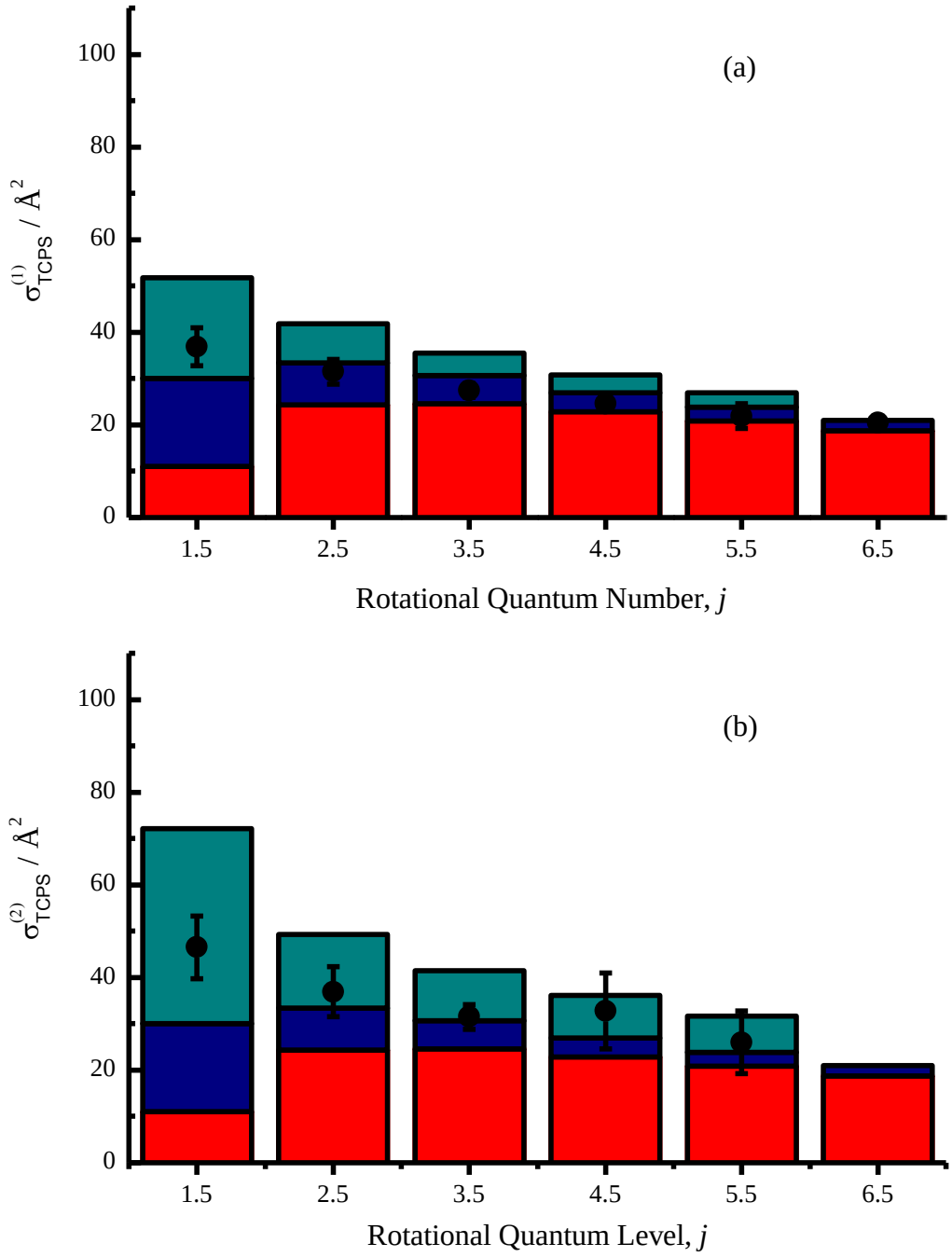

Figure 4.23: *Thermally averaged cross sections from TCPS measurements (data points with associated 2σ uncertainties) and quantum scattering calculations (stacked bars) for OH(X) + Ar. The total height of the stacked bars represents a predicted* $\sigma^{(K)}_{TCPS}$ *for (a) orientation (K=1) and (b) alignment (K=2). The predicted cross-sections have been decomposed into RET (red), Λ-doublet transfer (navy) and elastic depolarisation (cyan). RET and Λ-doublet transfer (which are the same in both (a) and (b)) are from this work and elastic depolarisation is from [94,174].*

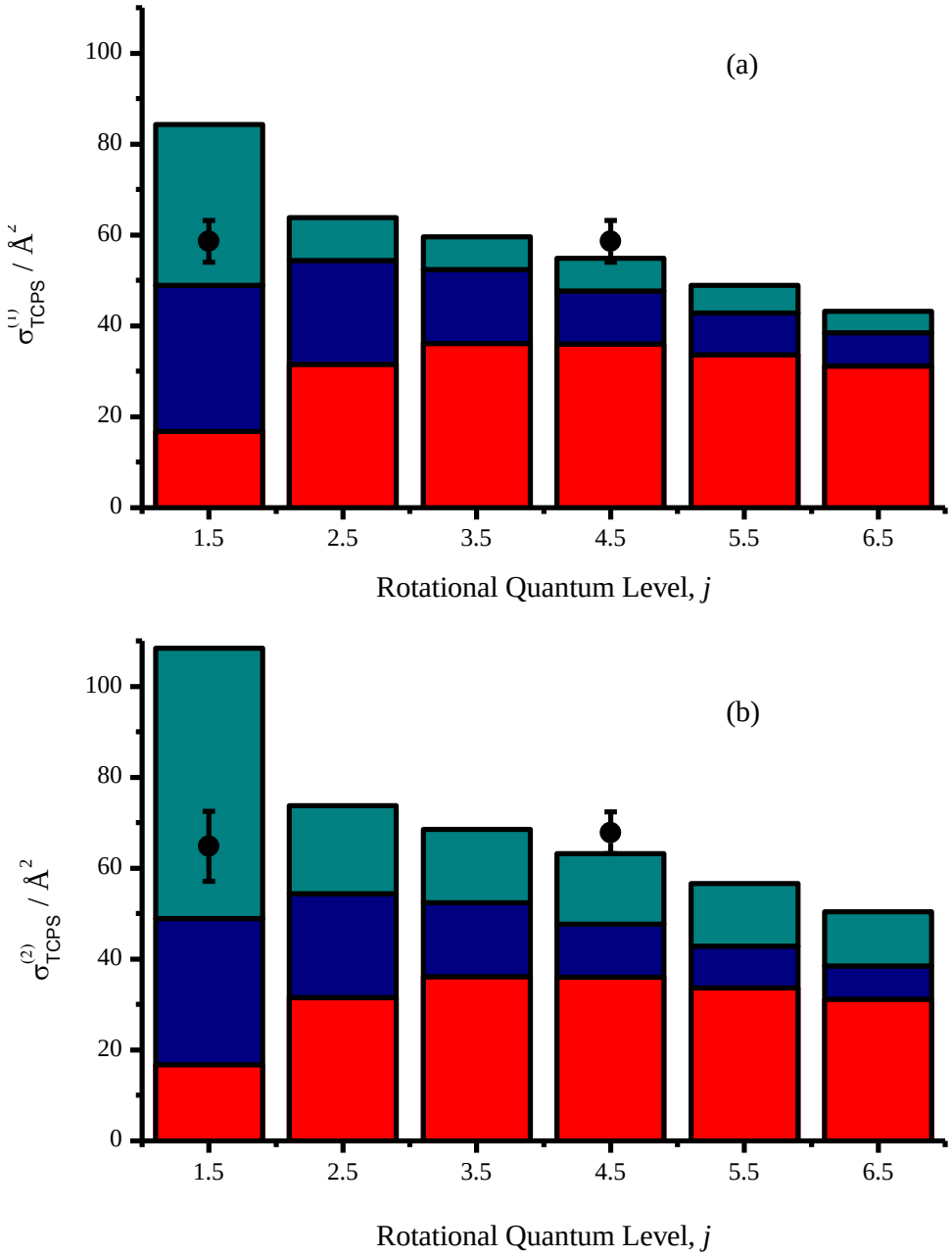

Figure 4.24: *Cross sections from TCPS measurements (data points with associated 2σ uncertainties) and quantum scattering calculations (stacked bars) for OH(X) + Xe. The total height of the stacked bars represents a predicted* $\sigma^{(K)}_{TCPS}$ *for (a) orientation (K=1) and (b) alignment (K=2). The predicted cross-sections have been decomposed into RET (red), Λ-doublet transfer (navy) and elastic depolarisation (cyan). RET, Λ-doublet transfer (which are the same in both (a) and (b)) and elastic depolarisation are from this work. The cross-sections for elastic depolarisation were calculated at a single energy (300 cm^{-1}), while all others are thermally averaged cross-sections from the standard Thermal-average relationship to the rate-constant.*

4.5.4 Possible Experimental Artefacts

The above conclusions that the PESs may to some extent overestimate the TCPS measurements does rely on having confidence that there are no experimental artefacts which would under-measure the true values of $\sigma_{TCPS}^{(K)}$. This sub-section will take time to consider some possibilities.

One of the conclusions reached in section 4.5.3 was that the PESs used in the scattering calculations overestimated the inelastic contribution alone. The TCPS measurements should in principle measure this process as a minimum requirement, if there is no elastic depolarisation. Because TCPS is sensitive to the overall population in the unique rotational level being studied, then a physical process which reduces the true decay rate for population removal from this level will cause $k_{POP}(\sigma_{POP})$ to be under-measured and hence similarly $k_{TCPS}^{(K)}(\sigma_{TCPS}^{(K)})$. A possible source of this would be secondary collisions which return population back to the initial level. The probability, or fraction, of returning molecules can be estimated using the state-to-state rate constants presented in tables 4-4 and 4-6 above. Division of the state-to-state rate constant for $j_i \rightarrow j_p$, k_{ip}, by the total removal rate constant for j_i, represents the probability that molecules that have undergone an inelastic collision populate a product rotational level, j_p. By a similar process it is possible to establish the probability that the initial level is repopulated after a second collision. Applying this stochastic treatment reveals that for He, the fraction of returning molecules in 2 collisions is 16% for j = 1.5, 16% for j = 3.5 and 6% for j = 6.5. The corresponding values for Ar are 5%, 12%, and 17%, respectively. However, it should be stressed that for the TCPS experiment to underestimate the 'real' rate constants by this amount, population must be transferred with *retention* of the rotational polarisation in *two* subsequent collisions. Otherwise, the returning molecules cannot contribute to the PS signal. Moreover, this would result in a noticeable deviation from a single exponential decay of the TCPS signal that is not observed in the present experiments. Figure 4.26 illustrates this by simulating the collisional repopulation of the initial level being probed using Poisson statistics.

The probability distribution for a given event (collisions), r, is related to the incidence (or frequency of event), μ, by the following equation:

$$P(r) = \frac{e^{-\mu}\mu^{r}}{r!}$$

(Equation 4-6)

The deviation from exponential decay as a result of collisional re-population of the initial level can therefore be simulated by evaluating [*P(0)* + (*f*$^{(2)}$*P(2))*], where *f*$^{(2)}$ represents the fraction of returning molecules, and plotting this against the incidence. The exponential agreement can be tested by fitting this to a standard single exponential decay, e^{-kt}. Figure 4.25 demonstrates that when the fraction of returning molecules is 0.2 the deviation from exponential behaviour is pronounced. It seems, therefore, that the measurements of this thesis should be capable of reproducing the true inelastic component of $k_{TCPS}^{(K)}(\sigma_{TCPS}^{(K)})$.

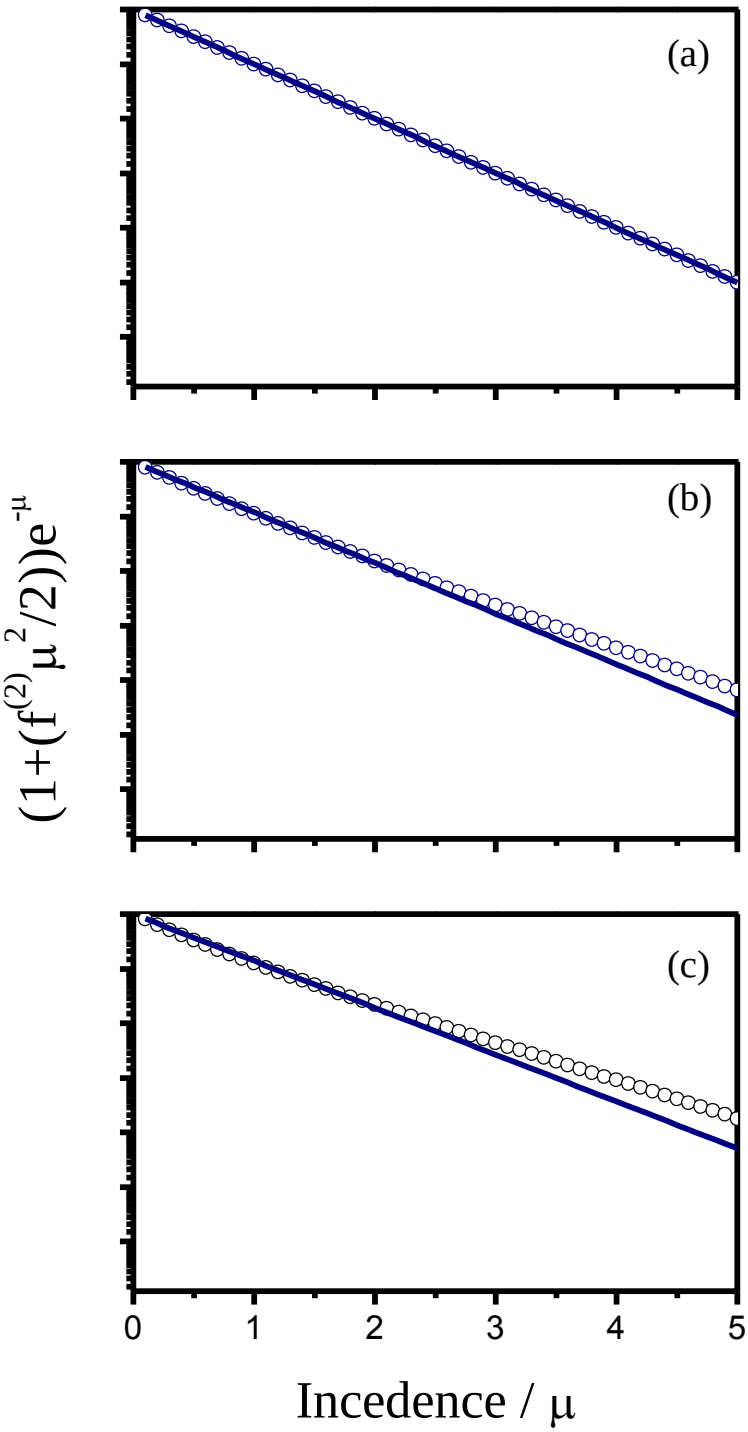

Figure 4.25: *Plots of P(0) + P(2) vs incidence, which is related to the average number of collisions. The deviation from single exponential behaviour is shown for various fractions of returning molecules that have suffered two collisions, $f^{(2)}$: (a) 0%, (b) 10% and (c) 20%.*

It is more difficult to visualise a physical process that will under-measure the elastic depolarisation contribution. However, the recent work of Rakitzis and co-workers could point to one possibility [176-178]. They have demonstrated through the time-dependent photodissociation of rotationally oriented hydrogen halides, in particular HCl, that it is possible to produce highly spin polarised H atoms. The foundations of this are angular momentum conservation and the inherent nuclear hyperfine interactions which occur when one of the nuclei has spin greater than zero. Of course, this interaction is well known and is treated fully in the fitting of all PS measurements, but what influence may this phenomenon have on the accurate measurement of $k_{TCPS}^{(K)}$? The OH rotational orientation or alignment generated by the pump laser will oscillate as a function of time as it couples to the nuclear spin of the hydrogen (I = 1/2). From Rakitzis' observations this coupling leads to a mirrored oscillation of the nuclear spin: photodissociation of the HCl diatomic at the right pump-photolysis time delay results in the preparation of spin polarised hydrogen, which would have been un-polarised (isotropic) prior to the pump interaction. In terms of collision dynamics, no elastic depolarisation could take place when the rotational polarisation is effectively 'hidden' in the polarisation of the nuclear spin, due to the very weak intermolecular interaction with the nuclear spin (hence, the timescale of the NHQBs in the PS experiments). The knock-on effect would be that the magnitude of elastic depolarisation would be damped. The exact scale of such an effect has not been evaluated quantitatively at the time of writing this thesis. But, qualitatively, the degree of 'damping' should be related to the relative magnitudes of I and j. This means that the effect would be most pronounced for low rotational levels and for the alignment measurements, where the depths of the NHQBs are largest.

4.5.5 Role of the PES

A quantitative comparison of the TCPS measurements was made with the results of the quantum scattering calculations in section 4.5.3. Following this, it is of interest to establish, qualitatively, what parts of the PES, i.e. what Legendre components, are responsible for the different collisional processes that the TCPS measurements are sensitive to. To start with it is useful to simply compare the magnitudes of the TCPS cross-sections to the range of the potentials directly, by converting the measured cross-sections into collision radiuses, r_{coll}. Figure 4.26 presents the OH (X)-He, OH (X)-Ar and OH (X)-Xe V_{SUM} PESs expanded in a Legendre series (see equation 1-1 and 1-3). Using the largest values for alignment obtained here, r_{coll} = 2.1 Å (~ 4 a_0) for He, which

fits well within the repulsive core. Indeed, it also matches quite well the classical turning point for the average collision energy of 300 cm^{-1}, supportive of RET being the dominant process, often assumed with classical models to be predominately caused by the repulsive wall of the PES. In contrast, r_{coll} for Ar extends to considerably longer range (3.9 Å; 7.3 a_0), well outside the repulsive core and coinciding with the attractive minimum. Similarly, this is also true for Xe where r_{coll} = 4.7 Å (8.8 a_0). Given these observations, and the fact that the well-depth in the interaction potential is progressively more attractive in the series He < Ar < Xe, then a reasonable conclusion is that attractive forces play an important role in elastic depolarisation. However this does not entirely explain why there is no marked increase in the inferred elastic depolarisation from Ar to Xe. To answer this question it is useful to make reference to the PESs shown in figure 4.26.

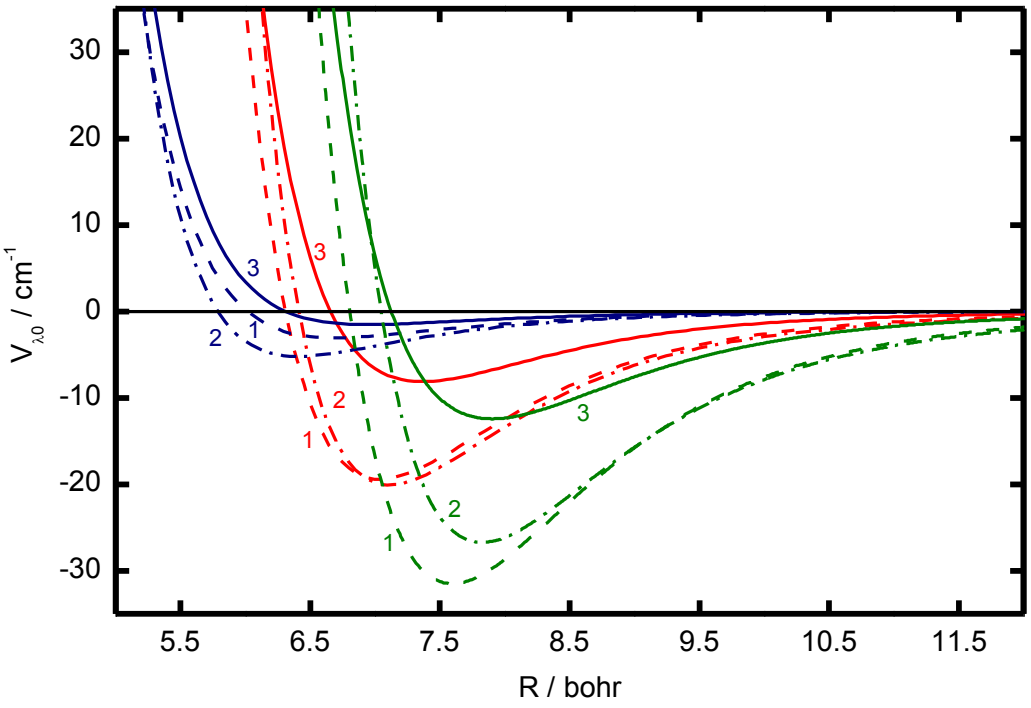

Figure 4.26: *Legendre components of order λ, as indicated, of the intermolecular potentials V_{l0} between OH ($X^2\Pi$, v = 0) and He [159] (navy), Ar [18,144] (red), Xe [40] (green). The isotropic terms V_{00} have been omitted for clarity.*

It was established in the opening chapter (section 1.1.3) that, from the original analysis of Alexander [24], collisional transfer propensities are governed by direct coupling between the initial and final quantum states and the scattering probability is proportional to the magnitude of the relevant coupling terms $V_{\lambda m}$ of the decomposed average and half-difference PESs. In the limit of Hund's coupling case (a) $V_{\lambda 0}$ terms are

responsible for coupling initial and final levels *within* the same spin-orbit manifold and $V_{\lambda 2}$ terms for coupling *between* spin-orbit manifolds. One other important result of Alexander's formalism is that odd-λ components are responsible for parity changing transitions and even-λ components for parity conserving. OH (X) conforms to an intermediate coupling scheme, but in the low-j levels studied here it does not depart very much from case (a). This means that all $\lambda > 0$ terms contribute to RET processes. However, transfer between the Λ-doublet levels is entirely controlled by the lowest odd term ($\lambda = 1$), because it is purely a parity changing event. The j-conserving elastic depolarisation processes are mediated by the even $\lambda = 2$ term. The isotropic V_{00} components cannot alter the magnitude or orientation of angular momentum and therefore only cause pure elastic scattering (i.e. alteration only of the collision partner trajectories). This much larger term is therefore not relevant to this discussion and hence omitted from figure 4.26.

The forms of the relevant potential terms for He and Ar have already been inspected and their effects on population transfer propensities discussed by Esposti *et al* [15] and Schreel *et al.* [33]. Alongside their work on QM predictions of $\sigma_{DEP}^{(K)}$, Dagdigian and Alexander also analysed the behaviour for He and Ar in terms of the Legendre-decomposition of the potentials [93,94]. A summary of this analysis is relevant.

For He [93], as can be seen from figure 4.27, the attractive limbs for all λ are very weak relative to thermal energies and Dagdigian and Alexander find that RET correspondingly has a positive energy dependence, consistent with dominant repulsive interactions. Pure Λ-doublet changing was predicted to be very inefficient. By decomposing the total cross-section into J^{tot}-dependent contributions (analogous to the impact parameter of classical trajectory simulations) for a thermal-average collision energy of 300 cm^{-1}, Dagdigian and Alexander showed that Λ-doublet changing for OH (X) + He is mostly the result of relatively low-J^{tot} collisions. However, there is notably also a small but finite contribution from higher J^{tot} corresponding to classical impact parameters, b, of *ca.* 6-7 a_0, well into the weakly attractive region of the potential. Other than at very low collision energies, the Λ-doublet-changing cross sections varied only slowly with collision energy. Elastic depolarisation was predicted to make a more important contribution than Λ-doublet changing for low rotational levels, but decline rapidly with J. Depolarisation shows a positive collision-energy dependence in the region of thermal energies, again consistent with a process mediated by the repulsive

wall of the potential. Significant contributions to the partial cross sections for elastic depolarisation are restricted to relatively low J^{tot}, implying $b < 5\ a_0$. This corresponds to the region of the repulsive wall, confined to shorter range than for Λ-doublet changing and much less so than for completely elastic (non-depolarising) collisions.

In contrast, Dagdigian and Alexander find that for Ar [94] both Λ-doublet changing and elastic depolarisation show strong negative collision-energy dependences across the full range of thermal energies. This is consistent with the dominant influence of attractive forces. Elastic depolarisation is predicted to be considerably more efficient than for He, in at least qualitative agreement with the TCPS experimental conclusions of section 4.5.3 .The analysis of J^{tot}-dependent partial cross sections indicates a dominant contribution from impact parameters < ~8 a_0, with a peak in the region of the OH-Ar attractive minimum. There is a negligible contribution to depolarisation from more weakly attractive forces at longer ranges. The Λ-doublet-changing cross sections for Ar are predicted to be much larger than for He, for which there is also independent experimental support [33]. Very interestingly, the Λ-doublet-changing partial cross sections are rather sharply peaked around J^{tot} corresponding to $b \sim 8\ a_0$. The contributing impact parameters for Ar lie significantly outside those for elastic depolarisation, well into the attractive regions of the $\lambda = 1$ and 3 potentials (see figure 4.26) that can induce pure Λ-doublet changes. Dagdigian and Alexander have argued that the ordering of the even- and odd-λ terms may explain the predominance of Λ-doublet changing over elastic depolarisation at longer ranges. However, it appears from the expanded view in figure 4.26 that the even $\lambda = 2$ term for Ar is only slightly more attractive over the majority of the relevant region in comparison to $\lambda = 1$. The $\lambda = 3$ component is considerably weaker.

In their original analysis, Esposti, Berning and Werner [15] had also noted that there did not seem to be a simple correlation between the magnitudes of the various λ-dependent terms and the relative abilities of He and Ar to induce Λ-doublet changes. They demonstrated, by artificially varying the masses, that there was also a significant kinematic contribution to this effect. This could presumably also be a factor in elastic depolarisation.

For Xe there is unfortunately no analysis of the J^{tot}–dependent partial cross sections. Nevertheless, given that the OH + Xe kinematics are relatively similar to those for OH + Ar, it may perhaps be more possible to predict successfully the progression from Ar to

Xe purely on potential-energy grounds. Inspection of figure 4.26 reveals that compared to Ar, the dominant odd-λ potential, $\lambda = 1$, for Xe becomes relatively deeper, and shifts more to longer range than does $\lambda = 2$. It might therefore reasonably be anticipated that the greatest change from Ar to Xe would be in the odd-λ-induced Λ-doublet changing efficiency, over even-λ-induced depolarisation with which it is in competition at long range. This is appealing because it is at least qualitatively consistent with the observations in section 4.5.3. It is clear from figures 4.22 – 4.24 that there is indeed a substantial increase in the calculated rate constants for Λ-doublet changing for Xe over Ar, whereas the inferred experimental elastic depolarisation cross-sections from comparison of $\sigma_{TCPS}^{(K)}$ and calculated σ_{POP} are relatively more similar. So it seems that elastic depolarisation and Λ-doublet transfer are in competition with one another and which is the dominant process is related to the magnitude of the even and odd terms in the PES.

It is worth mentioning, however, that the above comparisons may not reveal the complete picture. Dagdigian and Alexander very recently tried to better understand the dependence of elastic depolarisation on the potential [179]. To help do so, they artificially modified the OH (X)-Ar potential by effectively switching off V_{DIFF}. QM scattering calculations on this modified PES surprisingly revealed that the $\sigma_{DEP}^{(K)}$ values reported in figure 4.23 were considerably reduced (by up to a factor of 8). This implies that the V_{DIFF} potential plays an important role in elastic depolarisation, which Dagdigian and Alexander propose is because the V_{22} expansion coefficient is larger in magnitude than the V_{20} term for a given separation, R. The basis of this claim lies in the authors comparison to similar calculations performed on NO(X)-Ar where the V_{22} term is smaller in magnitude than V_{20} for a given R and correspondingly elastic depolarisation is less affected by V_{DIFF} being switched off. It should also be noted that V_{DIFF} has opposite signs in OH (positive) and NO (negative). It may be the case that interference between V_{SUM} and V_{DIFF} may play an important role in elastic depolarisation. Clearly, the routes of elastic depolarisation, at least for OH (X), are still not completely certain and it is perhaps more complex than originally thought. Any future attempts to rationalise elastic depolarisation should take into consideration the true intermediate coupling scheme of OH ($X^2\Pi$) and not presume that V_{DIFF} is not important based on assuming Hund's case (a) scattering formalism.

4.5.6 Comparison to other systems

Finally the above observations are put in context of previous measurements and models of related systems. The literature on collisional depolarisation is sparse in general. The majority of those reports that have appeared are concerned with the polarisation changes that accompany inelastic processes [73]. This discussion though, will be restricted primarily to the even fewer studies of pure m_j-changing processes ($\Delta j = 0$, $\Delta m_j \neq 0$), of direct relevance to the results of this chapter. Perhaps the closest example is the work of ter Meulen's group, introduced in section 4.1, on reorientation for OH (X) + Ar, at higher mean collision energies of around 750 cm^{-1}[70]. As noted, they found that the reorientation cross sections ($\Delta j = 0$, $\Delta(m_j,\Omega) \neq 0$) were significant, and comparable to those for RET. Assuming a simple model in which all collision–induced transitions corresponding to equal reorientation have equal probability, their results were best reproduced if the cross sections for $\Delta m_j = 0$, 1, 2 and 3 transitions, suitably scaled to a purely elastic collision cross-section of 189 $Å^2$ [70], were 164, 25, 12 and 13 $Å^2$, respectively. Although they are not exactly comparable quantities, these $\Delta m_j \neq 0$ values are reassuringly of similar magnitude to the thermally averaged $\sigma_{DEP}^{(K)}$ values from this work: 9 $Å^2$ (K = 1) and 16 $Å^2$ (K = 2) for j = 1.5, inferred from subtracting σ_{POP}(calc) (see table 4-5) from $\sigma_{TCPS}^{(K)}$ (see table 4-3). It is also interesting that $\Delta m_j > 1$ transitions are approximately a factor of two less probable than $\Delta m_j = 1$. Any such gradation in the m_J-resolved cross-sections implies that the rate of decay for an orientation will be slower than that of an alignment, as observed in the PS measurements here.

The remaining previous studies of OH (X) depolarisation have been carried out in the distinctly different environment of flames. Settersten and co-workers used picosecond IR-UV TCPS to measure loss of orientation and alignment of OH ($X^2\Pi_{3/2}$, v = 1) in atmospheric-pressure methane-air flames [120]. They were able to access a broader range of j (expressed in terms of N = 1 – 12) than in our thermal measurements. They observed that the alignment relaxation *time* was relatively constant for low N, but increased significantly beyond N > 4. They ascribed this to the dominant role of inelastic population transfer in the measured TCPS decay, based on the correspondence with energy gap scaling laws for RET. It is therefore perhaps not surprising that they found very similar relaxation times for orientation and alignment (confirming a later [180], but not earlier [119], report from Dreier's group using OCPS and the related

resonant four-wave mixing technique), because elastic depolarisation is presumed to make at most a minor contribution under their conditions. This observed difference from this work could be due in part both to the much higher collision energies in the flame environment, reducing the sensitivity to the attractive parts of the PES, and the contrasts between Ar and H_2O, believed by Settersten and co-workers to be the partner principally responsible for OH inelastic collisions in the flame.

Beyond OH, distinct behaviour has also been observed for at least one other system, even under thermal conditions similar to this work. Zacharias and co-workers used polarised stimulated Raman pumping in combination with a polarised LIF probe to study the depolarisation of vibrationally excited acetylene in self-collisions with a thermal bath of C_2H_2 [86]. Using a master-equation analysis they were able to extract rate constants for orientation decay due to rotationally elastic collisions. Most interestingly, they observe no difference between orientation and their own earlier alignment decay rate constants, which range from $3 - 1 \times 10^{-10}$ cm^3 s^{-1} across the rotational levels measured: $j = 1 - 15$. These values are somewhat larger, by about a factor of 2 – 6, in comparison to OH (X) + Ar, and are contrary to the differences between orientation and alignment observed in the TCPS measurements. The origin of this contrast in behaviour between C_2H_2 self-collisions and OH (X) + Ar is therefore an intriguing question. It should be noted that, in addition to obvious kinematic differences, acetylene has a closed-shell electronic structure, which could conceivably contribute to the different behaviour. Zacharias and co-workers did not explore the possible role of the attractive potential for C_2H_2 + C_2H_2, introducing an interesting alternative argument based on impulsive interactions in different collision geometries. They argue that the complete randomization of the prepared m_j distribution implied in rotationally *elastic* self-collisions would be explained if they occur preferentially perpendicular to the plane of rotation of the polarised C_2H_2 rotor. This conclusion was based in part on the contrast with their own previous studies of rotationally *inelastic* collisions, which were found to be accompanied by a significant *retention* of either alignment or orientation, which they correspondingly associated with collisions that occur in the plane of rotation.

These RET and depolarisation mechanisms are supported by a classical trajectory study of RET on model N_2 + Ar PESs with and without attractive wells, and with varying locations of the attractive wells [181]. Mayne and Keil presented results for the classical polarisation angle, χ (projection of j on the initial collision direction), as a function of initial orientation of the diatomic, for a PES with attractive minima at linear

configurations similar to that for OH(X) + Ar. For collisions at large impact parameter, near the radius of the minima, several different classes of trajectory were found. If the diatomic is initially oriented in the xz collision plane there is a strong probability of substantial RET with χ near 90°. This is the result of a mechanism in which the molecule tends to 'follow' the atom as it passes. Very different results are found for initial orientations tilted out of the collision plane. These collisions result in small or no RET, with the product χ either near 90°, or crucially, close to zero, arising from 'tumbling' of the molecular axis. Although the kinematics of OH (X)+Ar are very different from those of N_2 + Ar these calculations do provide a model of elastic depolarisation consistent with our observation of elastic depolarisation that is slower than, but of the same order of magnitude as, RET on a moderately attractive PES. Mayne and Keil also predict much greater depolarisation for collisions on surfaces with 'T-shaped' attractive minima, for example OH (X) + Xe, resulting from tumbling about the 'doughnut-shaped' minimum. However, the OH (X) + Xe results in this thesis do not support such an argument.

There are a number of other elastic depolarisation studies that are perhaps comparable to the experiments discussed in this chapter, such as the work of Brouard and co-workers on OH (A) + Ar [29,88,89] and NO (A) + Ar [87], and also of other $^2\Pi$ molecules, for example CN (A) + Ar [81]. However, a more involved comparison between these systems will be delayed until the TCPS studies of OH (A) + Ar in chapter 7 have been introduced.

4.6 Summary

The key conclusions from this chapter are summarised below:

i. TCPS provides a more rigorous method for measuring the collisional depolarisation of rotational angular momentum polarisations compared to OCPS.
ii. TCPS rate constants (or cross-sections) are consistently larger for alignment than orientation for all colliders studied – elastic depolarisation must be a contributing component to the decay of TCPS signals and the m_J distribution is not scrambled in a single collision.
iii. The total removal of TCPS signal increases across the series He < Ar < Xe in line with the PESs becoming progressively more anisotropic to longer range.
iv. The efficiency of elastic depolarisation for Ar and Xe appears to be relatively similar and thermally averaged cross-sections for alignment depolarisation can range up to ~ 20 $Å^2$. Both are significantly more efficient than He.
v. There is good evidence that $\sigma_{DEP}^{(2)} \approx 2\sigma_{DEP}^{(1)}$.
vi. Comparison of the TCPS measurements and the quantum scattering calculations reveal that the PESs overestimate both elastic depolarisation and RET with the largest discrepancy at low-j.
vii. There is strong evidence which supports the role of attractive forces in elastic depolarisation.
viii. Elastic depolarisation and Λ-doublet transfer, which both seem to be influenced by the long-range part of the potential, appear to be in competition. This may be explained qualitatively through the odd and even moments in the PESs decomposed in a Legendre series.
ix. For an intermediate Hund's case (a)/(b) system V_{DIFF} is predicted to play an important role in elastic depolarisation, making simple predictions based purely on the V_{SUM} potential unreliable.

Chapter 5

OH ($X^2\Pi$) + Molecular Partners

The work presented in this chapter serves as an extension to the model rare gas systems presented in chapter 4 towards systems of real interest in, for example, the atmosphere and combustion. Consequently the molecular partners chosen were the atmospherically relevant diatomics, N_2 and O_2. Because of their abundance in the atmosphere and the importance of OH in its chemistry, there have been recent attempts to characterise the interaction between these partners. Addressing this was the focus of a plenary lecture at the International Symposium on Gas Kinetics (Manchester, 2008), delivered by Professor Marsha Lester. It was this presentation that provided the inspiration for the experiments discussed in this chapter the results of which have subsequently been published [182].

5.1 Introduction

Studies of rotational energy transfer (RET) with OH and molecular partners are quite rare in comparison to those experiments which measure RET rates for OH + atomic partners. The majority of energy transfer measurements with N_2 and O_2 have focused on EET [183-186] and VET [171,173,187-194]. In terms of RET these systems are more complex due to the availability of rotation-rotation transfer. This extra degree of freedom means they are less theoretically tractable, both in terms of constructing full-dimensional *ab initio* PESs, and also in the treatment of scattering calculations. The molecular partners also introduce extra electrostatic terms into the interaction, namely the dipole-quadrupole term. How these kinematically similar colliders affect the decay of rotational polarisations is therefore an interesting question.

Lester and co-workers have investigated the van der Waals complexes of both OH-N_2 [195-197] and OH-O_2 [198-202] using infrared action spectroscopy in an attempt to measure their binding energies. The main motivation behind this is the importance of the HO_3 adduct in OH formation and destruction pathways in the atmosphere. Their spectroscopic information and a thermodynamic model suggested that 66% of atmospheric OH may be converted to HO_3 in the troposphere [199]. This estimate was based on an upper limit of the HO-O_2 binding energy of 2140 cm^{-1} (later revised to 1856 cm^{-1} [201]) relative to the OH (X) + O_2 asymptote, in the *trans* OH-OO planar geometry. Calculations run on restricted points of an analytical surface have confirmed this rather deep minimum [203,204]. However, very recent work, which is discussed below in light of the TCPS results, seems to contradict this argument [205,206]. For HO-N_2, Lester and co-workers measured a binding energy for of 277 cm^{-1} [196], which is more attractive than that for OH (X)-Ar[18,144].

Most of the published rotationally inelastic scattering experiments involving OH(X) + molecular partners have been carried out by ter Meulen and co-workers [55,207-211]. Initially they measured relative state-to-state scattering cross-sections, with Λ-doublet resolution of the initial state, in collisions with ortho- and para-H_2 [212], which is of both fundamental and astrophysical interest. The poor efficiency of 'cold' ortho-H_2 (j = 0 primarily) to promote OH (X, v = 0, j = 1.5f) → OH (X, v = 0, j = 1.5e), led them to the conclusion that collisional processes were not the primary reason for the OH population inversion in interstellar dust clouds, and the resulting OH maser emission. Interestingly, they did observe efficient Λ-doublet transfer with 'warm' para-H_2 (j = 1 primarily, plus j = 3). They attribute this Λ-doublet changing efficiency, which is larger than that for OH + He, to the dipole-quadrupole electrostatic term, not present for H_2 (j = 0). They then later performed similar experiments for OH (X) + N_2, CO and CO_2 [55]. Surprisingly, the relative cross-sections for total removal from j = 1.5e/f were similar for all colliders. There was however a slight increase of cross-section which correlated with increasing physical size of the collision partner target. It was found that Λ-doublet transfer for N_2 was very efficient for this lowest rotational level, accounting for approximately 60% of the total removal cross-section. The fraction of Λ-doublet transfer with respect to all population removal processes is found to increase proportionately with heavier partners. More recently ter Meulen and co-workers have measured rotational excitation cross-sections using diatoms from the series HX (where

X = Cl, Br and I) [207-211]. To date there have been no attempts to measure the rotational excitation of OH(X) with O_2 using crossed beam methods.

Smith and co-workers, in parallel to measuring total removal and Λ-doublet transfer rate constants for OH(X, v = 0, j) in collisions with He and Ar, also measured the same properties for N_2, but not for O_2 [136,137]. Unfortunately they did not measure both k_{RET} and k_{Λ} for all rotational levels, and so k_{POP} was only determined for j = 3.5 and 6.5, which were 5.9 (2.1) and 3.3 (1.1) x 10^{-10} cm^3 s^{-1}, respectively (the values in parenthesis represents the partial contribution from pure Λ-doublet transfer). The fraction of Λ-doublet transfer closely matches the fraction observed by ter Meulen and co-workers for j = 1.5f.

Rotational *relaxation* rates have however been measured for both N_2 and O_2 [42]. Kliner and Farrow used LIF to monitor the rotational thermalisation of OH following photodissociation of H_2O_2 at 266 nm, producing OH (X, v = 0, N = 1 – 12). They used an exponential-energy-gap-scaling-law to model average RET rate constants, which were found to be 0.4 and 0.79 x 10^{-10} cm^3 s^{-1}, for O_2 and N_2 respectively, over the range OH (X, N = 1 – 5), directly relevant to the rotational levels studied here. For Ar they obtained an average RET rate constant of 0.23 x 10^{-10} cm^3 s^{-1}. This increased efficiency of N_2 over O_2 has also been observed in pressure broadening measurements, which are inherently sensitive to inelastic population transfer rates [213-216]. Nesbitt and co-workers [216] associated this with different leading terms in the electrostatic interaction; N_2 has a larger quadrupole moment than does O_2. As will be discussed later these specific IR pressure broadening measurements are not the only examples where this trend is observed. The experiments described below will evaluate the interesting question of whether the decay of TCPS signal will be influenced by the more attractive well in the global PES for OH + O_2 or the dominant longer-range quadrupole term for OH + N_2.

5.2 Experimental

The experimental approach is essentially identical to that described in section 5.3. A 'V-shaped' two-colour polarisation spectroscopy (TCPS) scheme was employed, allowing the collisional evolution of a prepared rotational orientation or alignment, in a selected unique spectroscopic state of OH ($X^2\Pi$, v = 0), to be monitored. The OH(X) was produced by 193 nm (ArF Excimer, Lambda Physik) laser photolysis of a constant low

pressure of HNO_3/H_2O precursor. The collision partners, O_2 (BOC Gases) and N_2 (BOC Gases), were admitted to the vacuum chamber via an independent mass flow controller. Measurements were made in the total pressure range 200 – 1600 mTorr.

The pump laser was tuned to either the $P_1(1.5)$ or $P_1(4.5)$ line, respectively, in the $A^2\Sigma^+$-$X^2\Pi$ (1,0) band. Circular and linear pump polarisations were used. These create an orientation or alignment, respectively, in both the upper and lower states. The probe laser was tuned to the corresponding P_1 branch line in the $A^2\Sigma^+$-$X^2\Pi$ (0,0) band. This ensures that the bulk polarisation of *only* the lower, OH ($X^2\Pi$, $v = 0$, $j = 1.5$ or 4.5, F_1 e) state, is detected. The decay of the rotational orientation or alignment as a function of the pump-probe delay was fitted to the existing theoretical treatment of TCPS signals, discussed in section 1.2.2.

5.3 Results

Example PS decay traces for $j = 1.5e$ for each of the pump polarisations and with N_2 and O_2 as collision partners are shown in figure 5.1, along with the fits to the data. The high frequency oscillations are the familiar result of nuclear hyperfine depolarisation due to the nuclear spin of the H atom ($I = ½$). They are included fully in our treatment of the signals. Of more interest here are the overall rates of decay. It is clear that for both collision partners, this is more rapid for alignment than for orientation. Furthermore, N_2 is a more effective partner than O_2, particularly for orientation. The corresponding traces for $j = 4.5e$, and those at other total pressures, were all qualitatively similar other than variations in the absolute decay rates and the expected smaller amplitudes of the hyperfine beats at higher j (see section 4.3).

The phenomenological bimolecular rate constants for decay of the PS signal were extracted from the slopes of plots of pseudo-1st order decay rates against number density of the collision partner. The same $k_{\mathrm{TCPS}}^{(K)}$ (and $\sigma_{\mathrm{TCPS}}^{(K)}$) notation introduced previously is used to distinguish the rank, $K = 1$ or 2, of the spherical tensor moment interrogated using circularly or linearly polarised pump radiation, respectively. The $k_{\mathrm{TCPS}}^{(2)}$ data for decay of alignment of $j = 1.5e$ for N_2 and O_2 (figure 5.2) emphasise the clear collision-partner dependence, with N_2 again seen to be markedly more effective than O_2. The non-zero intercept is, as previously noted, effectively independent of collision partner and is mostly attributable to collisions with the HNO_3/H_2O precursor.

The extracted $k_{\mathrm{TCPS}}^{(K)}$ values for N_2 and O_2 are listed in Table 5.1 along with the associated thermally averaged cross-sections, $\sigma_{\mathrm{TCPS}}^{(K)}$, for use in the discussion that follows. The results quantify the clear contrasts in effectiveness between these two collision partners noted above, with N_2 exceeding O_2 for both rotational levels and both polarisations. Any *j*-dependence for either partner is weak, other than an apparent decline with *j* for orientation with O_2. For N_2, there is a consistent but modestly more rapid loss of alignment than orientation. For O_2, the trends are less clear, with an apparent considerably larger difference between $k_{\mathrm{TCPS}}^{(1)}$ and $k_{\mathrm{TCPS}}^{(2)}$ for $j = 4.5e$ than for $j = 1.5e$.

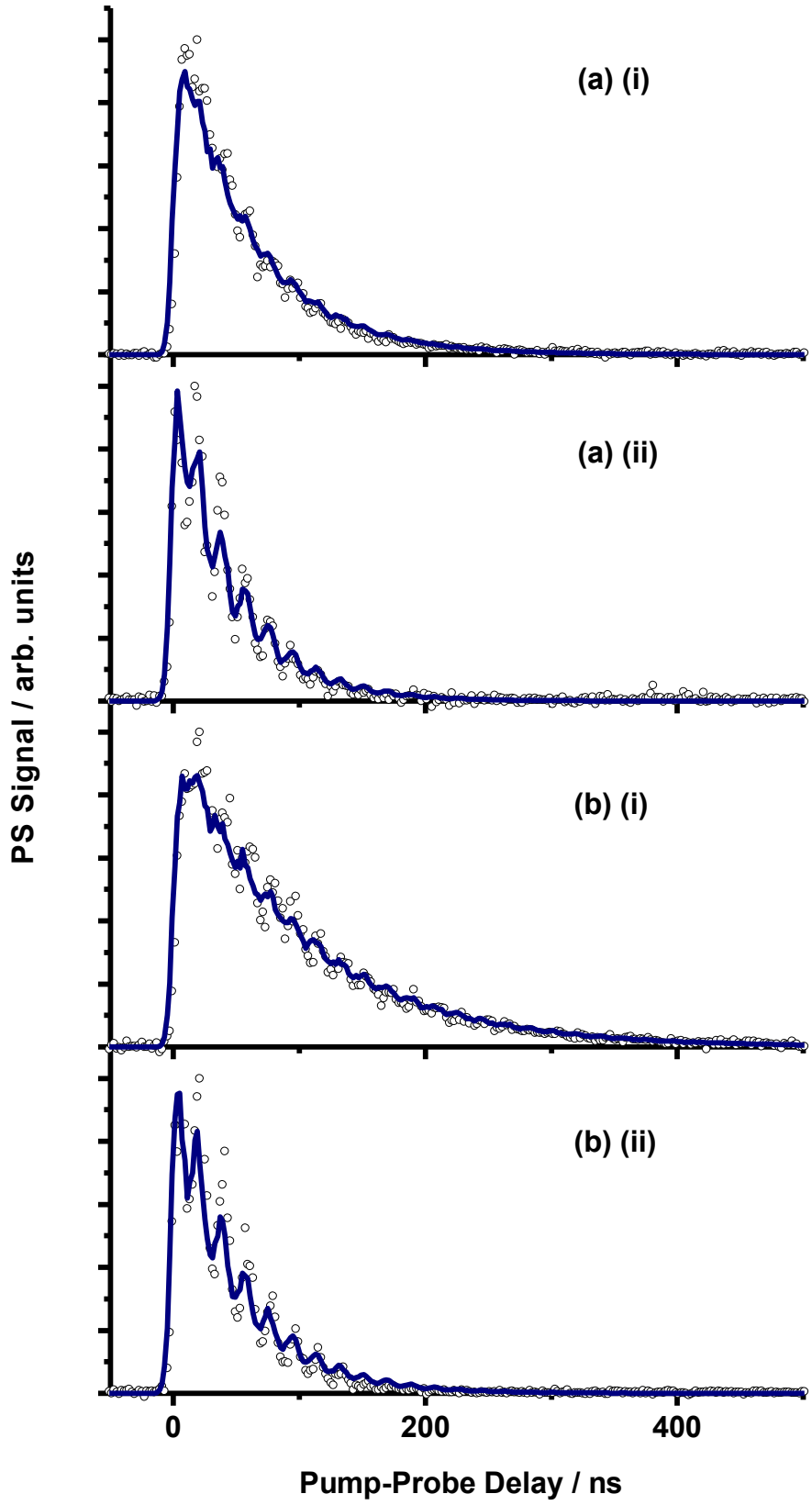

Figure 5.1: *TCPS signals as a function of pump-probe delay. Decay traces are shown for loss of both (i) orientation (K = 1) and (ii) alignment (K = 2) with (a) N_2 and (b) O_2 as collision partners. The total pressure (precursor + buffer gas) is approximately 300 mTorr.*

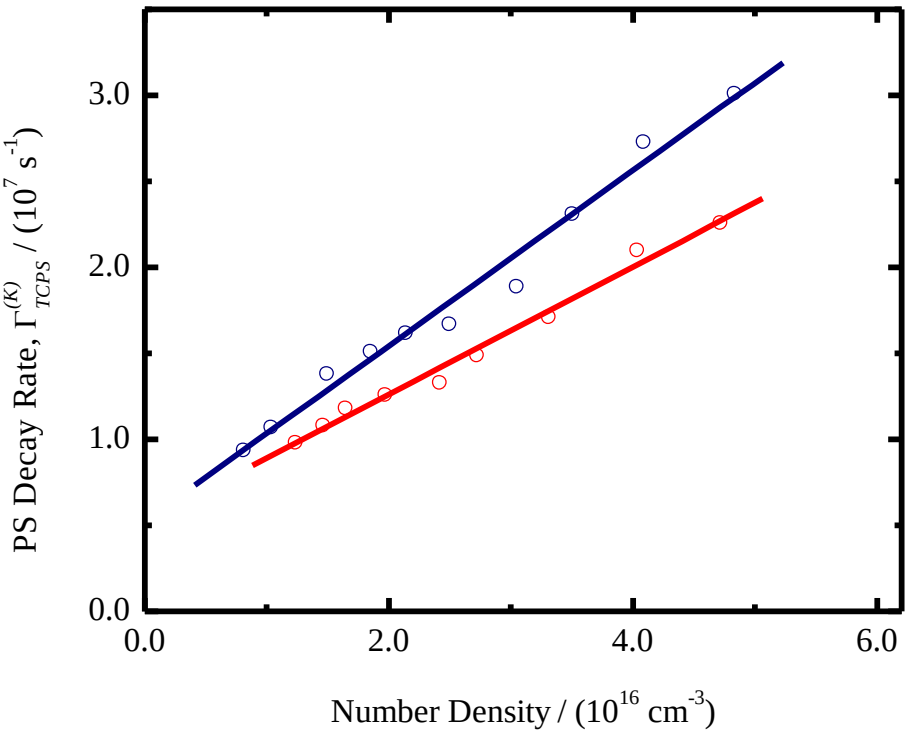

Figure 5.2: *Pseudo first-order rates for the decay of OH(X, v = 0, j = 1.5e) TCPS signals against collision-partner number density. Linear pump polarisation, hence a prepared alignment. Collision partners N_2 (navy circles) and O_2 (red circles). The slopes of the linear fits yield the phenomenological bimolecular rate constants, $k^{(2)}_{\mathrm{TCPS}}$.*

Table 5.1: *TCPS decay rate constants, $k^{(K)}_{TCPS}$ (in 10^{-10} cm^3 s^{-1}), and thermally averaged cross-sections, $\sigma^{(K)}_{TCPS}$ (in $Å^2$,) for loss of orientation (K =1) and of alignment, (K = 2) with associated 2σ statistical uncertainties. N_2 and O_2 collision partners at room temperature (nominally 298 K).*

	j* = 1.5*e		***j* = 4.5*e***	
	$k^{(K)}_{\mathrm{TCPS}}$	$\sigma^{(K)}_{\mathrm{TCPS}}$	$k^{(K)}_{\mathrm{TCPS}}$	$\sigma^{(K)}_{\mathrm{TCPS}}$
N_2				
K = 1 *(Orientation)*	*4.72 ± 0.28*	*61.1 ± 3.6*	*4.00 ± 0.43*	*51.8 ± 5.6*
K = 2 *(Alignment)*	*5.10 ± 0.50*	*66.1 ± 6.5*	*4.49 ± 0.22*	*58.2 ± 2.9*
O_2				
K = 1 *(Orientation)*	*3.49 ± 0.33*	*46.3 ± 4.4*	*2.27 ± 0.12*	*30.1 ± 1.6*
K = 2 *(Alignment)*	*3.71 ± 0.31*	*49.2 ± 4.1*	*4.00 ± 0.40*	*53.1 ± 5.3*

5.4 Discussion

The basic core observation (table 5.1 and figure 5.2) is that N_2 is a more efficient partner than O_2 for the collisional destruction of PS signals from OH (X). There may be several reasons for this outcome, the most plausible of which will be explored below.

5.4.1 Correlation with Attractive Forces

It was inferred in the previous chapter that the longer-range attractive forces in the interaction potential played an important role in the removal of rotational polarisations in the TCPS experiments. The relationship between the removal rate constant or cross-section and the degree of attractive forces between the collision partners can be represented approximately through a Parmenter-Seaver correlation plot [217,218]. This has been used previously to demonstrate the role of attractive forces in electronic state deactivation, and also rotational and vibrational relaxation in polyatomic and diatomic species. The following Arrhenius-type relation was drawn from the original analysis:

$$\ln \sigma_Q = \ln C + \left(\frac{\varepsilon_{MQ}}{k_B T} \right)$$

(Equation 5-1)

Here σ_Q is the total removal, or quenching cross-section, ε_{MQ} is the well depth between colliding partners (where M = probed molecule and Q = quencher or collision partner), k_B is Boltzmann's constant and C is a variable scaling parameter. To avoid having to have prior knowledge of ε_{MQ}, the dependence of removal rate may be expressed in terms of ε_{QQ}, the well depth for collision partner self-interactions, for which information is more widely available:

$$\ln \sigma_Q = \ln C + \beta \left(\frac{\varepsilon_{QQ}}{k_B} \right)^{1/2}$$

$$\beta = \left(\frac{\varepsilon_{MM}}{k_B T^2} \right)^{1/2}$$

(Equation 5-2)

This assumes that the following geometric combination relationship holds:

$$\varepsilon_{MQ} = \sqrt{\varepsilon_{MM}\varepsilon_{QQ}}$$

(Equation 5-3)

A linear relationship between ln σ_Q and $\sqrt{\varepsilon_{QQ}/k_B}$ therefore implies that the attractive well plays an important part in the quenching or collisional process.

As figure 5.3 shows, the correlation for the noble gases is plausibly linear for both the *j* values under consideration here. In comparison, O_2 lies on average marginally higher, but in general fits closely into the established trend of increasing PS cross sections with stronger attractive forces. In contrast, N_2, which actually has a lower well depth for self-interaction than O_2, shows a more positive displacement. As briefly alluded to earlier the well depths for the noble gases arise, by definition, exclusively from the dispersion interaction. For the homonuclear diatomics N_2 and O_2, the lowest-order additional electrostatic term is the quadrupole-quadrupole interaction. However, OH (X) has a significant dipole moment. This suggests that one possible explanation for the slight deviations from the lines in figure 5.3 may be a larger contribution from long-range dipole-quadrupole interactions for OH-N_2 than for OH-O_2.

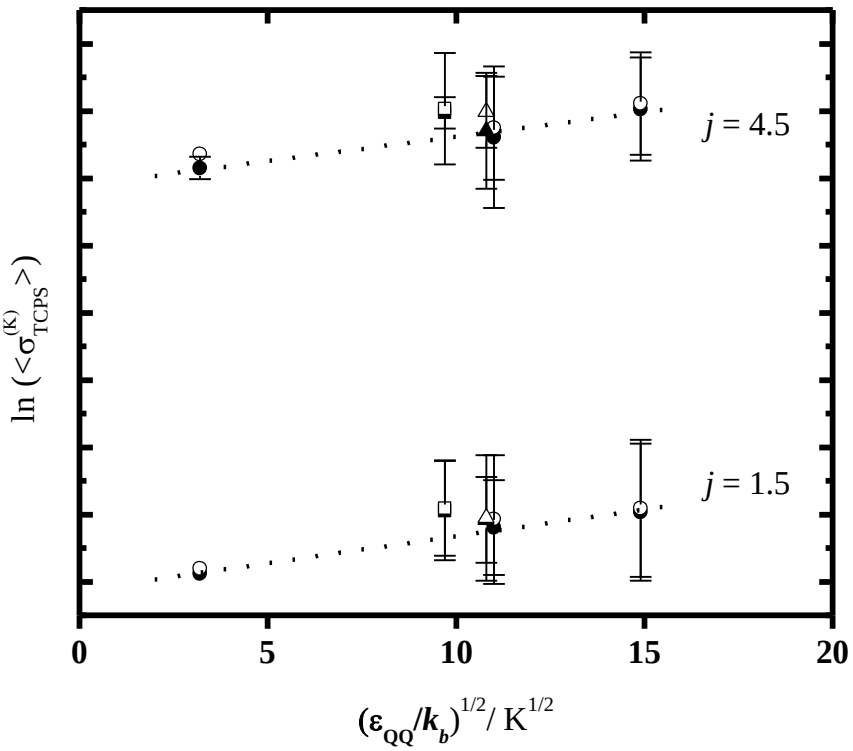

Figure 5.3: *Parmenter-Seaver correlation plot of relative OH(X, v = 0, j, e) TCPS thermally averaged cross sections,* $\sigma^{(1)}_{\mathrm{TCPS}}$ *(filled symbols) and* $\sigma^{(2)}_{\mathrm{TCPS}}$ *(open symbols) for the noble gases He, Ar and Xe (circles, as indicated) and molecular colliders* O_2 *(triangles) and* N_2 *(squares).* ε_{QQ} *is the well depth for pairs of the collision partner, taken from reference [218]. The data for j = 1.5e and 4.5e have been offset vertically for purposes of presentation.*

5.4.2 Elastic Depolarisation

For N_2, the behaviour is quite regular and relatively familiar from the measurements on the noble gases. There is at most a modest decline in either $k^{(K)}_{\mathrm{TCPS}}$ from j = 1.5 to 4.5 and the polarisation-dependence is straightforwardly explained, with $k^{(2)}_{\mathrm{TCPS}}$ consistently larger than $k^{(1)}_{\mathrm{TCPS}}$. As is known from the previous chapter, this is the expected behaviour when there is an elastic depolarisation contribution to the PS decay, and the $m_j \rightarrow m_j'$ propensities are constrained to decline in some way with $|\Delta m_j|$. The difference between orientation and alignment measurements reflects the degree of elastic depolarisation. For the two rotational levels studied here, this places an estimate of $\sigma^{(1)}_{\mathrm{TCPS}}$ at ~ 10 Å^2 for N_2, comparable but slightly lower in magnitude than Ar. Proportionately, therefore, the total removal cross-section for N_2 is dominated by inelastic population transfer.

In contrast, for O_2, any such patterns are much less obvious. There is a very small difference, in the expected direction, between $k^{(2)}_{\mathrm{TCPS}}$ and $k^{(1)}_{\mathrm{TCPS}}$ for j = 1.5, but it is much larger for j = 4.5. Note in particular, that the absence of a difference between $k^{(2)}_{\mathrm{TCPS}}$ and $k^{(1)}_{\mathrm{TCPS}}$ does not necessarily mean that there is no elastic depolarisation, only that any such depolarisation destroys orientation and alignment equally. The individual decay plots for O_2 are not in any way remarkable, compared to those for N_2 or the noble gases, and the bimolecular plots are comparably linear, as shown in figure 5.2 and reflected by the error bars in Table 5-1. Therefore, there is no objective reason for suspecting any errors in the O_2 measurements. Although it may be possible to construct explanations for the unusual trends in O_2 based on distinct sets of $\left|j,m_j\right\rangle \rightarrow \left|j',m_j'\right\rangle$ propensities for j = 1.5 and 4.5, the large difference between orientation and alignment (23 Å^2) for the latter, based on the usual subtraction ($k^{(K)}_{\mathrm{TCPS}} - k_{POP}$), would imply a surprising and unrealistically low cross-section for inelastic population transfer (~ 7 Å^2). However, this would be highly speculative on the basis of only two j values.

It is not possible in the case of either N_2 or O_2 to carry out the kind of systematic subtraction carried out for the noble gases to evaluate the elastic depolarisation contributions, $k^{(K)}_{\mathrm{DEP}}$, from the experimental $k^{(K)}_{\mathrm{TCPS}}$ results. The necessary k_{POP} data are either incomplete or entirely lacking. There have been no corresponding quantum scattering calculations on *ab initio* potentials. For N_2, the nearest experimental measurements are those of Smith and co-workers mentioned in the section 5.1 [136,137], in-which k_{POP} is only available for j = 3.5 and 6.5. However, their results for He and Ar tend to slightly overestimate k_{POP} either from QM scattering calculations on OH (X, v = 0), or the upper limits inferred from our experimental $k^{(K)}_{\mathrm{TCPS}}$ values. However, there may be good reasons for this based on the vibrational-level dependence of the anisotropy in the potentials. This may therefore presumably also apply to N_2.

There are no reliable absolute rate constants for O_2. As mentioned in section 5.1, Kliner and Farrow [42] carried out a master-equation analysis of the collisional relaxation of rotationally hot OH distributions produced by photolysis. However, Smith and co-workers [136] have already noted the poor agreement of Kliner and Farrow's inferred absolute rate constants for Ar and N_2 with their state-specific values of k_{RET}. Furthermore, Kliner and Farrow made, in the absence of other information, what are

now seen to be the rather extreme assumptions that k_Λ was independent of both collider and j. Nevertheless, their results did establish some of the qualitative trends, particularly the fact that N_2 induces RET in OH considerably more efficiently than O_2, similar to the behaviour of $k_{TCPS}^{(K)}$ values presented here, which probably have a substantial RET component.

5.4.3 Comparison to Pressure Broadening Measurements

In the absence of absolute rate constants to compare the measured $k_{TCPS}^{(K)}$ values for N_2 and O_2 with directly, a slightly more indirect comparison can be made with pressure broadening measurements. Like the TCPS measurements, these are a measure of the phenomenological rate constant associated with a number of collisional processes.

It may help to be clear what fundamental concepts are behind measurements of this kind, and the collisional processes to which they are sensitive. All spectroscopic transitions have an inherent and fixed *natural line-width*, which essentially stems from the uncertainty principle and the fact that molecular or atomic quantum states have a finite lifetime; the shorter the lifetime the broader the line-width. Assuming the lifetime is dominated by radiative loss then this is related to the Einstein A-coefficient and is therefore proportional to the frequency of the transition cubed. Translational motion of the probed species (more specifically the velocity projection onto the probe laser propagation vector) leads to *Doppler broadening*. Collisional processes lead to the remainder of spectral-line broadening and they can be sub-divided into three categories: inelastic energy transfer, m_j-changing events and pure elastic collisions. These are all sensitive to the number density of the collision partner and are collectively referred to as *pressure broadening*. Inelastic processes physically remove population from quantum states resonant with the probing transition and thus reduce their lifetime. Elastic collisions may result in de-coherence of the macroscopic polarisation written into the sample.

Measuring the incremental change of the full-width at half maximum for spectroscopic transitions as a function of collision partner number density will therefore measure the efficiency of the collisional process(es) which result in the broadening of the spectroscopic line. The measured quantity is the pressure broadening coefficient, labelled here by γ_{fi}, which has dimentions of frequency per unit number density, and

where the subscripts represent the initial (*i*) and final (*f*) levels connected by the transition.

Figure 5.4 provides a summary of all the information available on absolute rate constants relevant here. This includes $k^{(1)}_{\mathrm{TCPS}}$ and $k^{(2)}_{\mathrm{TCPS}}$ values for N_2 and O_2 obtained from the work of this chapter. Those for He and Ar from chapter 4 are also included for the purposes of comparison and to allow a more general assessment of the significance of those for N_2 and O_2 (Xe is excluded because the author is not aware of any relevant data beyond the new measurements and calculations presented in chapter 5). Various rate constants for population transfer are also collated, either from independent experiments or scattering calculations. Finally, the available collisional line-broadening measurements have been included. Rate constants, k_{PB}, have been obtained from the pressure broadening coefficients, γ_{fi}, using the expression [96,216]:

$$k_{\mathrm{PB}} = \pi\gamma_{fi}$$

(Equation 5-4)

Note that k_{PB} is an average over the initial (*i*) and final (*f*) states connected by the relevant spectroscopic transition. Therefore, for those derived from pure rotational, rovibrational, or electronic transitions, the results are plotted at the (integer) value of *j* that is the mean of the upper and lower states.

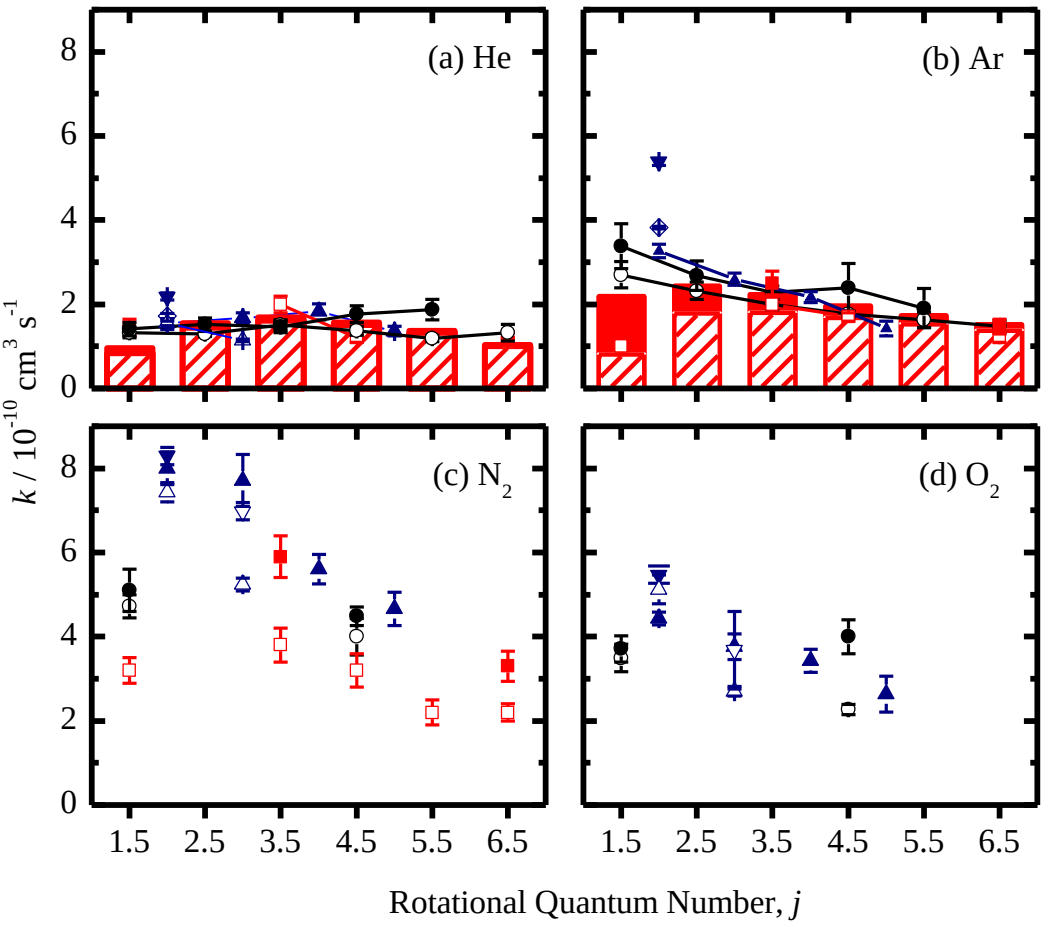

Figure 5.4: *Collected rate constants for OH collisional processes with (a) He, (b) Ar, (c) N_2 and (d) O_2. In all cases circles represent OH ($X^2\Pi_{3/2}$, v = 0, j, e) TCPS decay rate constants (this work) for orientation, $k^{(1)}_{TCPS}$ (open circles) and alignment, $k^{(2)}_{TCPS}$ (filled circles).For the atomic partners (frames (a) and (b)) the columns represent a QM-prediction of the population transfer, decomposed into purely Λ-doublet transfer, k_Λ (filled portion) and all other RET processes, k_{RET} (hashed portion). The height of these stacked components is equal to the total population transfer rate constant, $k_{POP} = (k_{RET} + k_\Lambda)$. The calculated data are those of section 4.4.2. The squares represent corresponding experimental measurements of k_{RET} (open squares) and $k_{POP} = k_{RET} + k_\Lambda$ (filled squares) from Smith and co-workers; refs [136,137]. All remaining symbols are collisional line-broadening measurements: open symbols from pure rotational spectra OH($X^2\Pi_{3/2}$, v = 0, j) of Park et al. (up triangles) refs [214,215], Chance et al. (down triangles) ref. [213], Burrows et al. (diamonds) ref.[219]; filled symbols from OH ($X^2\Pi_{3/2}$, v = 1-0) rotation–vibration spectra of Schiffman and Nesbitt (up triangles) ref. [216]and OH $A^2\Sigma^+ \leftarrow X^2\Pi_{3/2}$ (0,0) electronic spectra of Shirinzadeh et al. (down triangles) ref.[220].*

For He, virtually all of these various measurements or calculations are in rather good agreement. This suggests that population transfer dominates not only the TCPS decays, as was concluded earlier, but also line-broadening, for which elastic depolarisation and pure dephasing collisions are implied to make at most a minor contribution. Perhaps the only exception may be the one available measurement of broadening of the OH (*A*-*X*) electronic transition by He, which lies slightly above the other data. Interestingly, Zare and co-workers also inferred that there must be a substantial pure-dephasing contribution to the OH (*A*-*X*) line-widths for He in their FWM studies in flames [221]. The degenerate nature of their measurements again means that there were contributions from both ground and excited states, which were assumed equal in their analysis. Furthermore, they deduced significant elastic depolarisation contributions (assumed equal for ranks $K = 1$ and 2) for the lower j states, being negligible for $j = 8.5$, but 40% of the population transfer rate for $j = 3.5$ and reaching 100% for $j = 1.5$. The origin of the contrast with the TCPS results on OH (X), where, as can be seen from figure 5.4(a) the depolarisation contributions are definitely more modest, could again conceivably lie with significantly more efficient elastic depolarisation of lower-j OH (A). As will be discussed in detail in chapter 6, this may not be a sound assumption. However, the more attractive isotropic term in the OH (A)-He surface in comparison to OH (X)-He could lead to more velocity changing collisions which contribute to dephasing processes that affect the FWM measurements, but not the TCPS measurements. It should also be borne in mind that the temperature regimes of the two measurements are very different.

The discrepancy between line-broadening of the OH (A-X) electronic transition and the other collected measures is amplified for Ar, for which the directly measured line-broadening [220] is now a clear outlier in figure 5.4 (b). Otherwise, the line-broadening data are in very good agreement with the TCPS measurements, particularly the systematic rovibrational data of Schiffman and Nesbitt [216], which match both the absolute values and j-dependent trends of $k^{(2)}_{\mathrm{TCPS}}$. Setting aside the possibility that the departure from k_{POP} for Ar is the result of enhanced RET in $v = 1$, this would suggest that (despite what Schiffman and Nesbitt thought at the time) there is a significant elastic contribution to Schiffman and Nesbitt's collisional broadening data that is comparable to the elastic depolarisation component we have deduced for $k^{(2)}_{\mathrm{TCPS}}$.

The data for He and Ar illustrate the degree of correspondence that can be observed in some cases between line-broadening of rotational or rovibrational transitions confined

to the OH (X) state and TCPS measurements on this state. Comparing this with the main focus of the current chapter, N_2 and O_2, it is found that the $k^{(1)}_{\mathrm{TCPS}}$ and $k^{(2)}_{\mathrm{TCPS}}$ values for N_2 do, as would be expected, exceed the absolute k_{RET} data of Smith and co-workers [136]. Unfortunately, k_Λ is only available for two different states, j = 3.5 and 6.5 [137], than the two, j = 1.5 and 4.5, for which we have measured $k^{(K)}_{\mathrm{TCPS}}$. As can be seen from figure 5.4(c), an interpolation between Smith and co-workers' k_{POP} points probably implies a result for j = 4.5 that exceeds our $k^{(K)}_{\mathrm{TCPS}}$ values. As noted above though, a similar discrepancy was found for Ar. Regardless of this, it is interesting that the collisional broadening data tend to be significantly larger than $k^{(K)}_{\mathrm{TCPS}}$, particularly at low-j. Again neglecting any strong vibrational-level dependence, this would suggest a contribution to line-broadening that does not result in either population transfer or elastic depolarisation, corresponding to pure elastic dephasing with no change in m_j. For clarity, such pure elastic dephasing would affect only the absolute magnitude of PS signals as a function of pressure. It has no effect on the PS signal decay as a function of pump-probe delay and therefore does not contribute to $k^{(K)}_{\mathrm{TCPS}}$ [71,122,124].

In contrast, for O_2, $k^{(K)}_{\mathrm{TCPS}}$ values straddle the line-broadening measurements. Both sets of results have significantly lower values than for N_2. One possible logical conclusion from this is that O_2 is missing the 'extra', pure-elastic-dephasing, contribution to line-broadening inferred for N_2. This may also reflect enhanced long-range interactions for N_2 over those in O_2, which is considered in section 5.4.5 below.

5.4.4 Rotation-Rotation Transfer

It was briefly mentioned earlier that the diatom collision partners also have rotational degrees of freedom and as a result there exists the possibility of transfer of energy between near-resonant rotational levels in the colliding partners. Perhaps this provides an explanation for N_2 being more efficient than O_2 at removing the rotational anisotropy in TCPS experiments and, in general, the ability of N_2 to promote RET in comparison to O_2. The rotational ladders for $^{14}N_2$ and $^{16}O_2$ are quite different because they conform to different electronic terms in their ground electronic state: $^1\Sigma_g^+$ and $^3\Sigma_g^-$ respectively. Because ^{16}O has no nuclear spin, the nuclei are indistinguishable, resulting in all odd j-levels of positive parity being non-existent. Each level however is triply degenerate due

to the spin-rotation coupling. For ^{14}N, $I = 1$, and so all rotational levels in $^{14}N_2$ (even and odd) exist, but with the statistical weight of 2:3 in the favour of even levels with negative parity. The density of states for levels where a comparison can be made is no different between N_2 and O_2. However N_2 does not necessarily have more favourable Δj changing capabilities than O_2 because Δj = odd, which corresponds to ortho - para rotational transitions, are expected to be vanishingly weak. So it seems from this assessment that N_2 and O_2 should in principle be equally good at rotation-to-rotation transfer. In addition, their rotational constants are of similar magnitude. If rotation-to-rotation transfer was efficient then O_2 would be more efficient at removing TCPS signals than Ar, where rotation-to-translation is the only energy exchange pathway, over and above translation-to-translation. This is contrary to the experimental observations. Rotation-rotation transfer should also manifest in a larger range of Δj in OH observed in RET state-to-state measurements, because the rotational energy of the diatomic collider would effectively add to the available collision energy. For OH (X) the range of Δj observed is essentially equal for Ar and N_2 [55,160]. Similar situations are found for CH [23,124] and CN [222,223], supporting the conclusion that rotation-to-rotation transfer does not significantly enhance RET when polyatomic collision partners are used.

5.4.5 Interaction potential

Without any sound arguments based on density of states or resonant pathways leading to more efficient destruction of TCPS signals for N_2 as opposed to O_2, then it seems that the answer must lie exclusively in the differences of the interaction potentials, with the assumption that the small differences in kinematics can be neglected. The independently known differences in the interaction potentials for N_2 and O_2 have been established experimentally by Lester and co-workers. The clear conclusion is that there is a relatively deep minimum for OH-O_2 at the *trans* HO-OO geometry, presumably due to some incipient O-O chemical bonding. In contrast, OH-N_2 is found experimentally to be around an order of magnitude less strongly bound than OH-O_2. It is therefore quite striking that the observed rate constants in figure 5.4 (c) and (d), for both the $k_{\mathrm{TCPS}}^{(K)}$ results reported here, and the previous line-broadening measurements, clearly show that O_2 is a *less* effective collision partner than N_2! The anti-correlation between the depth of the attractive potential and the various collision cross sections is, at least at first sight, surprising. Its resolution could conceivably lie with a tight steric constraint to access the

strongly attractive shorter-range minimum in OH-O_2. In addition, it could also be the result of the respective *ranges* of the two attractive potentials.

Interestingly, more recent experimental and theoretical activity on this problem (subsequent to the publication [182] of the results presented here) has revised the binding energy of the OH-O_2 dimer to a substantially lower value of < 1000 cm^{-1} [205]. The origin of this revision was due to Stanton and co-workers identifying a barrier to the dissociation (see figure 5.5). Such a barrier would be 'invisible' to the experiments of Lester and co-workers, in which the internal energy of the OH fragments from unimolecular dissociation was measured. Subtraction of this from the photon energy used for excitation of the van der Waals dimer provides an *upper* limit to the dissociation energy. However, an exit barrier would reduce the true binding energy relative to the asymptotic dissociation limit. From figure 5.5 it is clearly predicted that this barrier is significant; reaching ~ 700 cm^{-1} at the turning point. This would severely restrict access to the deep attractive well under thermal conditions. In light of this, it may be more effective to assess the ranges of the outer regions of the interaction potential in comparison to the measured TCPS cross-sections.

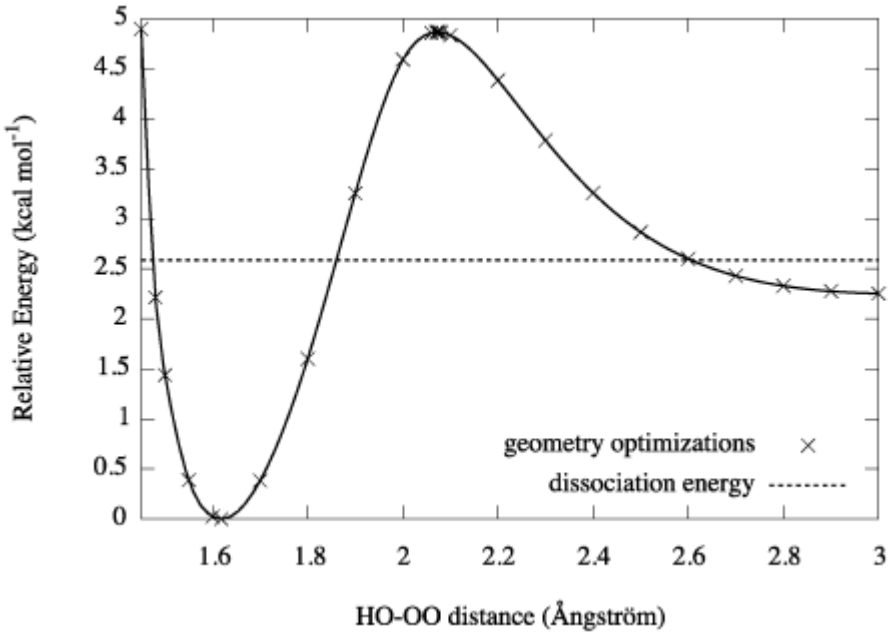

Figure 5.5: *The EOMIP-CCSD*/cc-pVQZ (fc) minimum energy path for dissociation of trans-HOOO to OH + O_2. The broken line represents the asymptotic limit corresponding to OH + O_2. At a central O-O distance of 3 Å there exists a van der Waals minimum; by 10 Å the interaction energy has converged to the dissociation limit. Reprinted from [205].*

Lester and co-workers' rotationally resolved trans-HO-OO spectra are best-fit by an inner O-O distance of around 1.69 Å, in good agreement with earlier microwave measurements [224] and the theoretical work of Stanton and co-workers (figure 5.5) [205]. This corresponds to an HO-O_2 centre-of-mass separation of only around 2.3 Å. In contrast, Lester and co-workers most recently infer a centre-of-mass separation of 3.9 Å for OD-N_2, with a 270 cm^{-1} well depth and binding energy of 208 cm^{-1}, which is reduced to 174 cm^{-1} for OH-N_2. The strength of the attraction is reproduced well by their own model electrostatic potentials for OH-N_2, based originally on the OH dipole - N_2 quadrupole interaction, and more recently including also the by-no-means negligible OH quadrupole - N_2 quadrupole term [197]. The OH-N_2 minimum clearly lies to significantly longer range than the more strongly bound HO-OO minimum. It is more compatible with the collision radii of *ca.* 4.0 - 4.5 Å inferred from the experimental cross sections for TCPS decay for N_2.

It is well established that the N_2 quadrupole moment is substantially larger than that for O_2, with typical recommended values of -1.12 and -0.23 ea_0^2, respectively [225]. It would therefore certainly be expected qualitatively that the longer range interactions would be weaker in OH-O_2. Indeed, the enhanced dipole-quadrupole interaction has been the conventional explanation for the observed differences in efficiency of

collisional line-broadening for OH [216,226]. If this was also taken to be the explanation for the OH RET rate constants being larger for N_2 than for O_2, as observed by Kliner and Farrow [42], this would imply that RET is not dominated exclusively by short-range impulsive interactions, as is sometimes conventionally assumed. However, this qualitative analysis based on quadrupole moments does not seem to be supported by those rigorous calculations currently available on OH-O_2 [203,227]. These predict that there is also a long-range van der Waals minimum in the OH-OO geometry, with a well depth of 364 cm^{-1} and a binding energy of 232 cm^{-1} at a centre-of-mass separation of 4.11 Å. These parameters are comparable to the van der Waals minimum at the HO-O_2 geometry (figure 5.5), which is similar to those properties of OH-N_2.

The inability to arrive at any clear explanation to account for the differences in collisional measurements for N_2 and O_2 with OH based on potential surface arguments remains to be resolved. Clearly, this warrants further experimental (particularly state-to-state measurements, which reveal scattering propensities), and theoretical investigation, especially when such differences between N_2 and O_2 are not exclusive to OH. They are also found in pressure-broadening measurements of other simple dipoles, such as HF and HCl [228]. Similarly the surprising behaviour of N_2 *versus* O_2 is not confined to collisional broadening, applying also to RET in related diatomic radicals, including, for example, CN ($A^2\Pi$) [229] and NO ($A^2\Sigma^+$) [230].

5.5 Summary

i. N_2 is a more effective partner than O_2 at removing the rotational anisotropy in OH in the TCPS experiments.

ii. N_2 stands out more clearly than O_2 from the general trend of total TCPS cross-sections among the noble gases based on attractive dispersion forces.

iii. Comparison with existing OH line-broadening data establishes a basis of close agreement between PS and collisional broadening rate constants for He, Ar and O_2.

iv. For N_2, the line-broadening rate constants are larger than those for PS decay.

v. Perhaps pure elastic dephasing provides an additional contribution to collisional broadening for N_2.

vi. It is not yet possible to decompose the total PS decay rate constants for N_2 and O_2 into population transfer and elastic depolarisation components.

vii. The comparison of Ar, N_2 and O_2 reveals that rotation-to-rotation transfer is not an important factor in explaining the efficiencies of molecular partners.

viii. Access to the deep attractive well for HO-OO seems to be prevented by a substantial barrier and so does not outweigh other factors that favour N_2 for the destruction of polarisation in OH(X).

ix. Presumably the stronger dipole-quadrupole interaction of OH-N_2 is the explanation behind the larger TCPS cross-sections in comparison to O_2, but this proposal is not supported by the existing rigorous theory.

Chapter 6

OH ($A^2\Sigma^+$) + Atomic Partners

Presented in this chapter is a comprehensive dynamical study of OH ($A^2\Sigma^+$, v = 1, N) with two noble gas collision partners, He and Ar, using TCPS. It was inferred in chapter 5 that elastic depolarising collisions were mediated by the attractive limbs of the potential energy surface (PES) and that perhaps specific Legendre components of the decomposed surface were primarily responsible. The limited work on OH(X) + Xe suggested, however, that increasing the potential well depth had at most a modest effect on the magnitude of elastic depolarisation. The primary motivation for the work presented in this chapter was to pursue this concept further by investigating systems with *identical* kinematics to those discussed in chapter 4, but with PESs that have drastically different topologies. To strengthen the analysis of this work, a detailed comparison was made with experimental and theoretical work carried out in parallel by Brouard and co-workers at the University of Oxford. Consequently a summary of this independent work will be provided as a platform for discussion of the results herein. All work presented here has been published [90].

6.1 Previous Work

Similar to the results contained in chapter 4, the measurements shown in this chapter are sensitive to two main collisional processes: elastic depolarisation and inelastic population removal. On this occasion there are additional processes which may contribute to k_{POP}. These include electronic energy transfer (quenching) and vibrational energy transfer (VET). It is only natural therefore to consider previous investigations of these processes as well as RET before commencing with discussion of the TCPS results. It should also be noted that the TCPS measurements will also be sensitive an additional non-collisional process, that is spontaneous fluorescence. For OH (A, v = 1) the

fluorescence lifetime is approximately 700 ns [9] and so in a plot of TCPS decay rate *versus* collision partner number density the contribution from this process alone be ~ 0.3 x 10^6 s^{-1}. Below is a summary of previous theoretical and experimental work on OH (A) + collider now follows.

6.1.1 Theoretical work

Starting with OH (A)-Ar, there are essentially two main versions of the PES that will be relevant for future discussion. One was constructed by Esposti and Werner (E&W) [16] and the other, very recently, by Kłos *et al.* [17]. The $^2\Sigma^+$ electronic state is non-degenerate with respect to an approaching spherical (^{1}S) partner and consequently there is only one PES describing the system, in contrast to OH (X)-Ar. E&W employed the CEPA method similar to that used for their development of the OH (X)-He and Ar PESs. The topology of the surface shows rather deep minima in both linear geometries, HO-Ar and OH-Ar. These have well depths of 1000 and 1100 cm^{-1}, respectively, at separations from the OH centre-of-mass of 2.9 and 2.2 Å, respectively. At θ = 90° (T-shaped geometry) there exists a saddle point 1000 cm^{-1} above the global minimum. This very anisotropic PES was used in QM scattering calculations to predict OH (A, v = 0, N) + Ar rotational state-to-state cross-sections (at 300 cm^{-1}) and thermally averaged state-to-state rate constants from calculations run with differing collision energies and weighted by a Boltzmann factor at 300 K [16,49]. The summation of these state-to-state rate constants, including the transfer between the closely spaced spin-rotation (SR) levels (note the change in nomenclature in comparison to $^2\Pi$ electronic structure), are the values most relevant here. SR changing transitions are defined by: $\Delta N = 0$, $\Delta j = \pm 1$. E&W computed thermal rate constants which decline smoothly as a function of initial rotational level, N, and are in the range 2.46 – 1.68 x 10^{-10} cm^3 s^{-1} (34 – 23 $Å^2$). It should be noted that transfer between the SR levels is generally more probable than other inelastic processes. This is an important point in the discussion that follows.

Kłos *et al*. [17] used the more rigorous [RCCSD(T)] approach to calculate their *ab initio* PES for OH (A)-Ar. They found the landscape to be considerably more anisotropic than that of E&W with a global minimum of 1720 cm^{-1} in the HO-Ar linear geometry and a local minimum of 1220 cm^{-1} at the opposite linear geometry. The saddle point at the T-shaped geometry almost reaches -50 cm^{-1}. This surface is drastically different from the OH (X) equivalent, as shown in figure 6.1.

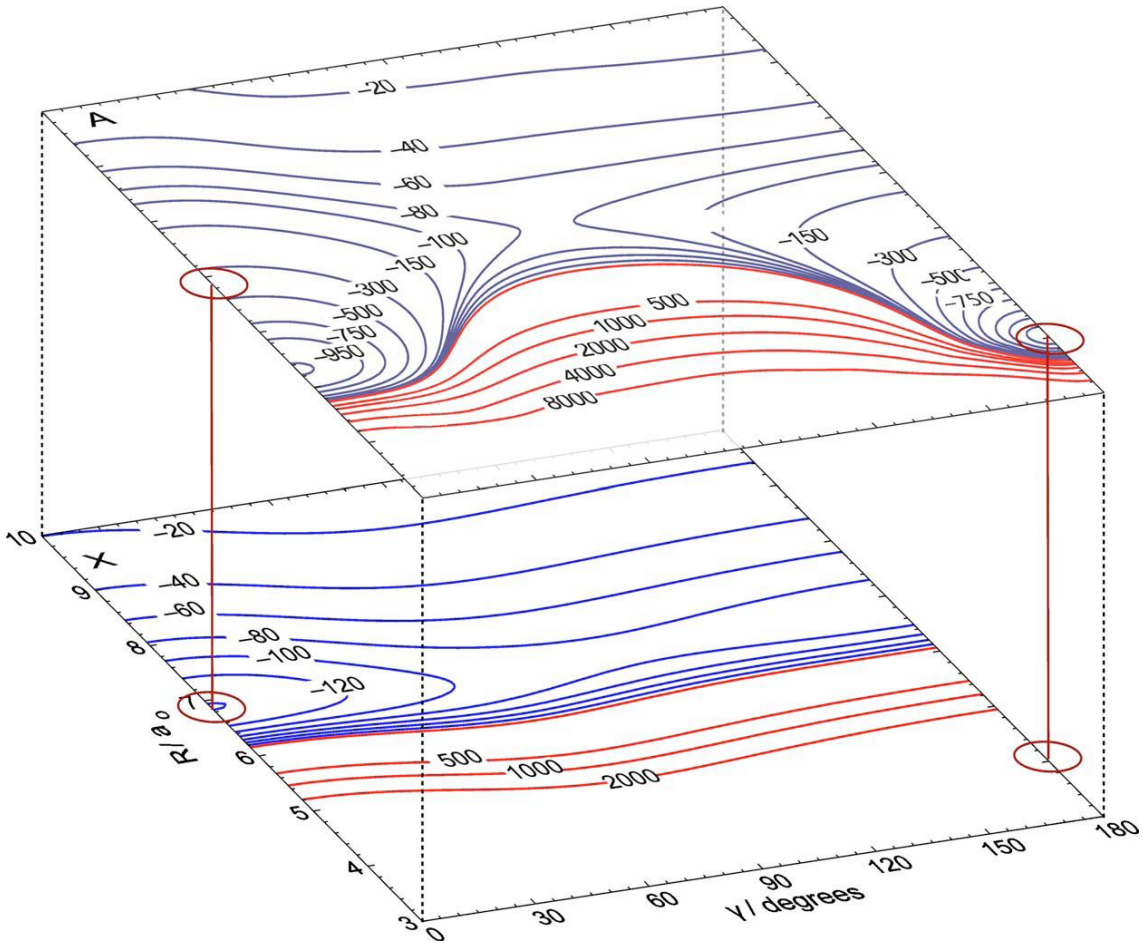

Figure 6.1: *(Upper sheet) Contour plot of the RCCSD(T) PES for the OH (A)–Ar complex calculated at the OH (A) equilibrium internuclear distance, ref. [17]. Energy is in wavenumbers. The largest negative energy contours, which are not labelled due to lack of space, are −950, −1200, −1400, and −1600 cm^{-1}. (Lower sheet) Contour plot of the average, V_{SUM}, refs. [18] and [144] of the OH (X)-Ar PES's of A′ and A″ symmetry. The two vertical green lines, and accompanying circles, indicate that at 0° vertical excitation from the collinear minimum on the OH (X)-Ar PES accesses the outer limb of the OH (A)–Ar well and that at 180° the HO (A)–Ar well corresponds to geometries high on the repulsive wall of the HO (X)–Ar PES. Reprinted from Ref [17].*

Kłos *et al.* performed preliminary closed-shell (c-s) and open-shell (o-s) QM and QCT calculations [17]. A (c-s) QM calculation treats the OH artificially as a $^1\Sigma^+$ diatomic and an (o-s) QCT calculation is made possible using the spin-spectator model discussed in section 1.1.3. For the QM calculations they used both CC and CS methods. Comparisons were made between these methods and those results obtained from other PESs including that of E&W for rotational scattering out of OH (A, $v = 0$, $N = 0$, f_1). In general, the c-s and o-s QM calculations yield cross-sections within a few percent of one another once summed over all final states. The QCT calculations are in good

agreement with QM calculations and there is no more than 5% deviation with respect to the total inelastic cross-section when comparing them to scattering calculations performed on previous surfaces. In a subsequent paper, Brouard and co-workers extended this work to cover more initial rotational levels, and also provided classical and QM theoretical formalisms for extracting polarisation information [29,89]. The results of this work are directly linked to the work presented here, so discussion is deferred until section 6.3.1.

For OH (A)-He the most recent *ab initio* PES is that of Jorg, Esposti and Werner (JEW) [49]. They employed the same CEPA method used for OH (A)-Ar. Understandably, the interaction is less attractive, with a global minimum of 107 cm^{-1} at the OH-He linear geometry and a local minimum of 37 cm^{-1} for HO-He. Again, the saddle point is located at the T-shaped geometry. The global minimum for OH (A)-He is therefore a factor of approximately 16 shallower than OH (A)-Ar, in contrast to only a factor of 5 weaker for OH (X). There are two reasons why OH-He is expected to be more weakly bound than OH-Ar. First, Ar is obviously more polarisable than He. Second, it is suspected that an incipient chemical bond exists in OH-Ar from the interaction between the singly occupied OH 3σ molecular orbital with a 2*p* atomic orbital from Ar; obviously this is not accessible for He. JEW went on to provide QM scattering calculations for rotational inelastic processes in OH (A) + He collisions [49]. Similar to OH (A) + Ar they obtained state-to-state rate constants which, when summed over all final levels, resulted in thermal RET total removal rate constants that will be useful for comparison to TCPS measurements. For initial levels OH (A, v = 0, N, f_1), where N ranged from 0 – 5, rate constants declined smoothly from 2.50 – 0.39 x 10^{-10} cm^3 s^{-1} (18 – 3 $Å^2$). SR changing events appear to be a dominant state-to-state process again, but for some initial levels the rate constants for $|\Delta J| = |\Delta N| = 2$ transitions are comparable in magnitude. In general, even quantum jumps are preferred with retention of SR label. A comparison of the most recent OH (A)-He/Ar PESs, expanded as a Legendre series, is provided in figure 6.2, together with the OH (X) counterparts. As was seen in chapter 4, this information will be useful for discussion of the results.

6.1.2 Experimental Work

Experiments measuring the efficiencies of VET and electronic quenching are summarised first. Williams and Crosley [191] optically prepared OH (A, v = 1, N), from OH (X) formed *via* reaction of NO_2 with H atoms, and the time-resolved fluorescence

was monitored to measure state-to-state VET. They used a number of collision partners including: N_2, O_2, H_2O and Ar. They found that N_2 was the most efficient collision partner, with a VET cross-section ($v' = 1 \rightarrow v' = 0$) of 30 $Å^2$, and surprisingly O_2 was found to be relatively inefficient, with $\sigma = 3$ $Å^2$. Even less efficient was the atomic collision partner, Ar, with $\sigma = 0.56$ $Å^2$. They also observed that the efficiency of vibration-to-rotation transfer was strongest for those weakest at VET: O_2 and Ar. This is supportive of a mechanism of VET occurring through collinear collision geometries (i.e. internuclear axis and collision vector parallel). Crosley later demonstrated that there was a negative temperature dependence on the measured rate constant of VET, which is indicative of attractive forces playing an important role [193]. It has been noted that He is also extremely inefficient at VET [192].

Paul *et al.* [183] measured electronic quenching of OH (A) with several collision partners. They found that OH (A) + HNO_3 had the largest quenching cross-section of 81 $Å^2$. Using H_2O as a collision partner resulted in electronic quenching being an order of magnitude weaker in comparison to HNO_3 (8 $Å^2$). Xe had the same cross-section as H_2O and Ar was found to be very inefficient (0.06 $Å^2$).

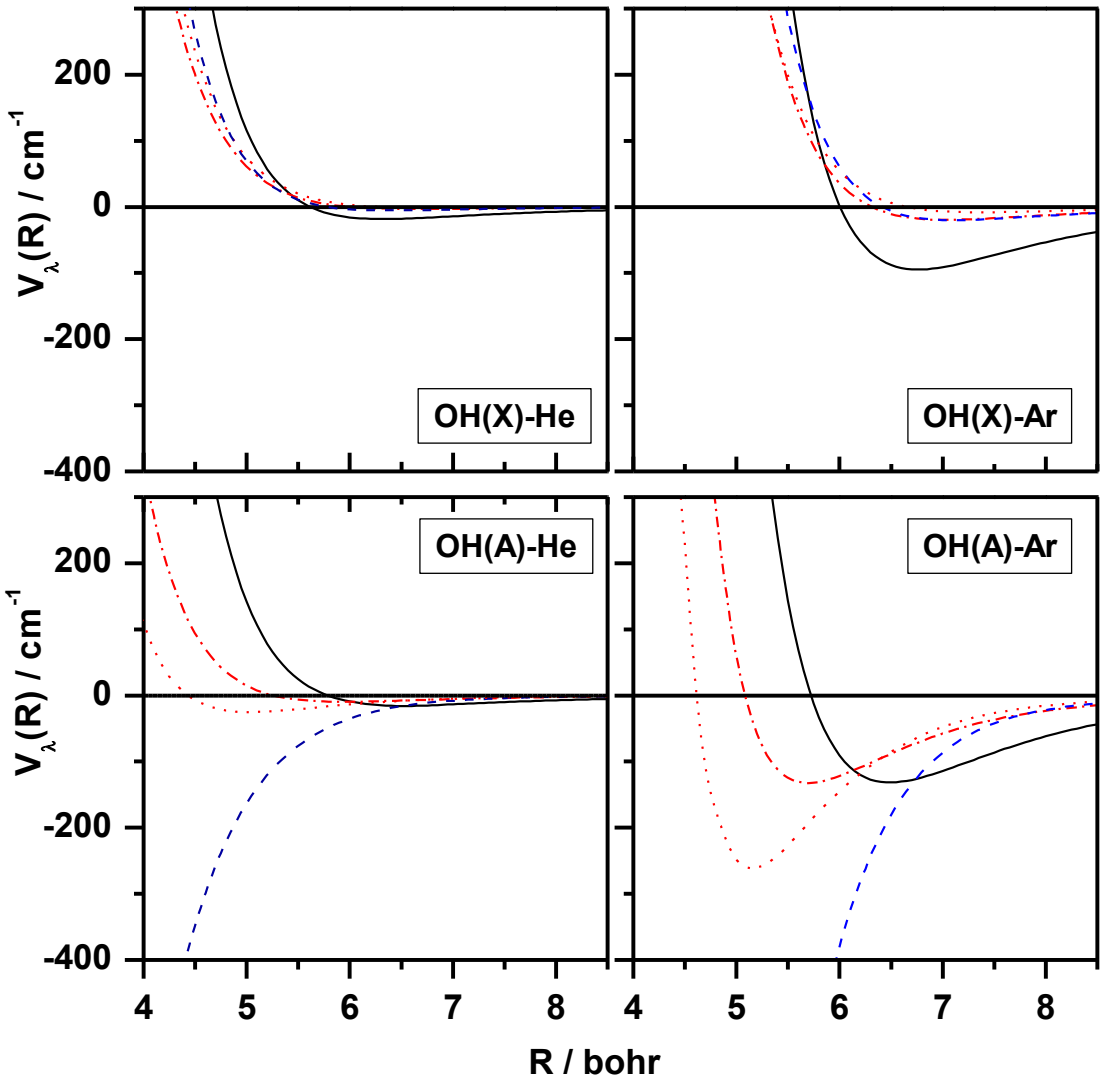

Figure 6.2: *Ab initio PESs decomposed into Legendre components [$P_\lambda(\cos\theta)$] of order λ = 1-3. Plots for OH-He/Ar are shown for both OH (X) and OH (A), as indicated. The OH (X)-He data are taken from ref [159], the OH(X)-Ar data are from ref [18,144], OH(A)-He are from ref [16], and the OH(A)-Ar data are taken from ref [17]. Curves are for λ = 0 (black), λ = 1 (dashed-dotted red), λ = 2 (dashed blue), λ = 3 (dotted red).*

Comparing the measured VET and electronic quenching cross-sections to the rate constants/cross-sections for RET, taken from the scattering calculations mentioned in section 6.1.1, it is clear that RET is the dominant process. From this point onward it will therefore be assumed that the contribution to the TCPS measurements from VET and electronic quenching is negligible.

There have been a few experimental RET studies for the OH (A) + He and Ar systems. Accompanying their VET work, Lengel and Crosley used LIF to monitor rotational state changing collisions [34]. They were able to establish the total removal cross-sections (by summing over all measured final levels) for Ar, from two initial rotational

levels: N = 1 (f_1) and N = 4 (f_1) and within the lowest vibrational level, to be 20 and 18 Å^2 respectively. These values are about a factor of 2 smaller than the equivalent rate constants predicted by E&W. Jorg *et al.* [36] later used a more direct method to determine the state-to-state rate constants for OH (A) + Ar and OH (A) + He. From the two rotational levels measured, N = 4 (f_2) and N = 5 (f_2), good agreement was observed with the predictions of JEW, as well as confirming the predicted state-to-state propensities mentioned in the previous sub-section (6.1.1). Away from these controlled thermal conditions, Stepowski and Cottereau measured RET cross-sections for OH (A) + Ar in low pressure flames (1300 – 2000 K) [30]. At these elevated temperatures they found a total removal cross-section of 18 Å^2 for N = 7 (f_1). This is similar to the measurement of Jorg *et al.* for N = 5 (f_2), and suggests that there is little influence of increased temperature on the RET cross-sections. This may be expected from the energy-dependent cross-sections calculated by E&W, which show a positive energy dependence between threshold energy and thermal energies and a plateau (slightly declining) towards higher energies. This is evidence of repulsive interactions dominating RET processes, as is commonly accepted, particularly when collision energies exceed the well depth.

The most recent collisional studies of OH (A), which are directly relevant to the experimental results of this chapter, are those of Brouard and co-workers [89]. In their work, Zeeman quantum beat spectroscopy (ZQBS) was used to measure the decay of rotational anisotropy from optically pumped OH (A) in the presence of a chosen collision partner. A description of this experimental approach is outlined in section 6.3.1. Initially they measured unresolved rotational depolarisation cross-sections for OH (A) + H_2O of 83 – 14 Å^2 under superthermal collision conditions (mean OH speed = 3490 m s^{-1}) over the range N = 5 – 14 (f_2 for N = 8 and 14; f_1 for N = 5). They went on to investigate the depolarisation of rotational AM in OH (A) + Ar under thermal conditions [89]. After taking a dephasing contribution into account, that arises from collisions populating final rotational levels which have different Landé g-factors, they find depolarisation cross-sections which decrease from 80 – 23 Å^2 across the range N = 2 – 14 (all f_1) [89]. It would not be valid to draw comparisons between H_2O and Ar due to the extremely different collision environments. For OH (A) +Ar, they compared their results to QCT calculations using the PES of Kłos *et al.* [17] and found that the calculations fall short of the ZQBS experimental results, by up to 20% in the worst case. One advantage of the ZQBS technique is its ability to measure RET separately,

providing a unique route to resolving the components measured jointly using TCPS. In parallel with the work presented in this chapter, Brouard and co-workers extended their measurements to extract *elastic* depolarisation and the RET cross-section for OH (A) + Ar. The following sections present a comparative study of OH (A) + Ar and He by TCPS, and also OH (A) + Ar by TCPS and ZQBS.

6.2 Two-Colour Polarisation Spectroscopy

6.2.1 Experimental

For the OH (A) experiments a 'Λ-shaped' spectroscopic scheme was used, illustrated in figure 6.3. The pump laser was resonant with a rovibronic transition in the $A - X$ (1,0) (~ 282 nm) band and the probe was resonant with the diagonal (1,1) (~ 314 nm) band. Consequently, the TCPS measurements were sensitive to unique rotational levels in OH (A, $v = 1$, N). Although it is possible in principle to access $v' = 0$, this would require probing on the weak off-diagonal (0,1) electronic band. The difference in transition probabilities [9] cannot be gained back by increasing the probe intensity, because this has a linear relationship with the probe 'leak-through'. Circular and linear pump polarisations were used to generate bulk polarisations characterized by non-zero spherical tensor moments with $K = 1$ and $K = 2$, respectively. For the orientation measurements, $P_1(j)$ spectroscopic lines were used for the pump and probe steps, and for the alignment studies $Q_1(j)$ lines were used. The reasoning behind this lies in the branch sensitivity of the TCPS signal, which ultimately is determined by the squared 6-j symbol in the signal electric field expression (see section 1.2.2, equation 1-46). These experiments were therefore sensitive to the f_1 SR levels. It should be noted that the main Q-type branch has a neighbouring satellite branch, namely ${}^{Q}P_{21}(j)$, separated spectroscopically by ~0.3 cm^{-1}, similar to the pump laser bandwidth. Potentially this could introduce a contribution from f_2 levels into the alignment measurements. However, because of the non-linear nature of the TCPS experiments, the polarisation generated depends on the square of the pump fluence and also the transition linestrength, hence that prepared in the wing of the pump pulse is negligible. Scanning the probe laser, which has a narrower bandwidth (~ 0.15 cm^{-1}), while the pump was centred on the corresponding ${}^{Q}Q_{11}(j)$ line indicated that there was no contribution from the f_2 level to the TCPS alignment measurements. In principle, a further experimental artefact could arise from spontaneous fluorescence from the pumped $A^2\Sigma^+$ level which

populates OH ($X^2\Pi$, v = 1) with some degree of polarisation. If so, this would produce a contribution to the TCPS signal from the lower electronic state with which the probe is resonant. However, given the relatively long time scales for fluorescence (radiative lifetime ~ 700 ns) and the dilution over rotational quantum levels in the lower state, this contribution is likely to be negligible.

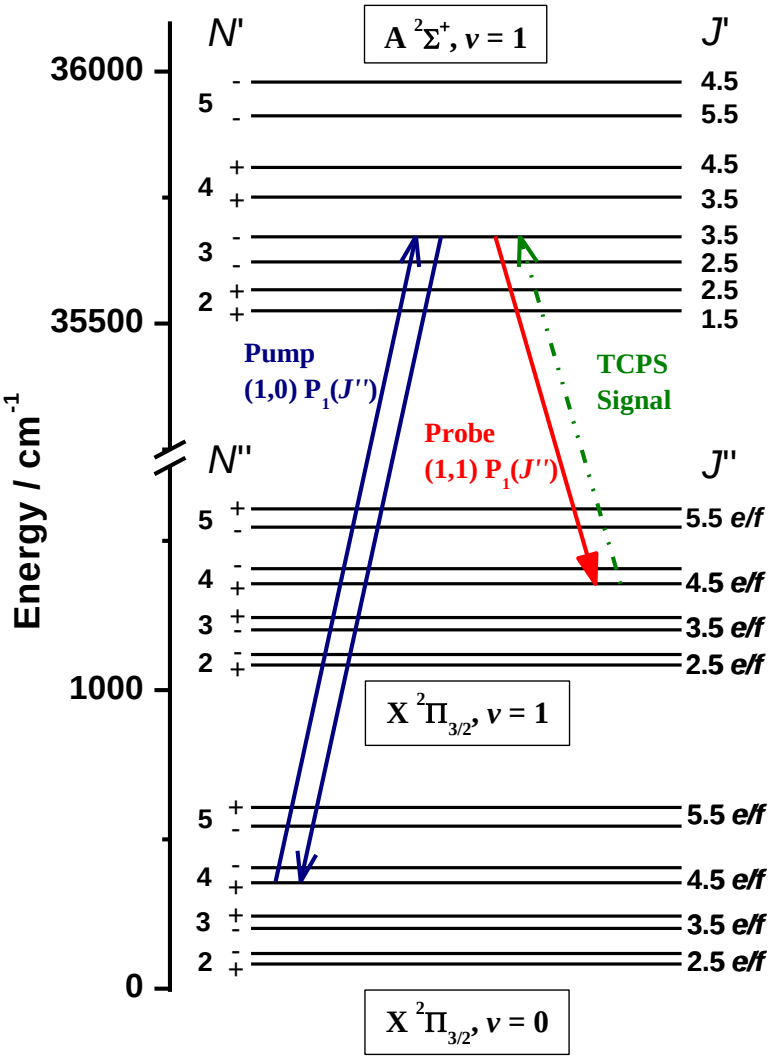

Figure 6.3: *Schematic diagram of rotational energy levels for OH ($X^2\Pi$, v = 0, 1) and OH ($A^2\Sigma^+$, v = 1) relevant to TCPS signal generation. For clarity, energy-level splittings are not shown to scale. The Λ-doublet splitting in OH ($X^2\Pi_{3/2}$) and the spin-rotation splitting in OH ($A^2\Sigma^+$) are both considerably exaggerated; the vibrational spacing in OH $X^2\Pi$) is reduced. The upper $X^2\Pi_{1/2}$ spin-orbit manifold (f_2) has also been omitted for clarity. Example TCPS transitions, specific to this work, are indicated; the pump beam is resonant with the off-diagonal (1,0) P_{11} (j) branch and the probe is resonant with the diagonal (1,1) P_{11}(j) branch. This example would result in signal generation (broken arrow) from only the OH ($A^2\Sigma^+$, v = 1, N = 3, f_1) level*

6.2.2 Results

TCPS decay traces were collected for a number of rotational levels, *N*, over the range *N* = 0 – 5 (all f_1 SR levels, where this denotes rotational levels with $j = N + 1/2$). Circular and linear pump polarisations were used to measure rotational orientation and alignment respectively, in the presence of either He or Ar. Example decay traces are provided in figure 6.4. In all cases it is observed that Ar is more efficient than He, as perhaps expected from the results of chapter 4. A second observation is that there are no visible NHQBs superimposed on the exponential decays on the timescale of the experiment. This does not mean that they are not physically present, but rather the temporal profile of the probe laser (~ 15 ns) is incapable of resolving the rapid oscillations (> 100 MHz) [89]. As a result, the TCPS measurements probe the average of the hyperfine induced oscillation of the rotational orientation/alignment produced by the pump photons (see section 1.2.2).

These decay traces were acquired for various pressures of collision partner, over the range 100 – 2800 mTorr, to measure the second-order bimolecular rate constant, $k_{TCPS}^{(K)}$. Examples of these plots are provided in figure 6.5. As expected, a significantly positive intercept, $\Gamma_{intercept}^{(K)}$, is observed, which is primarily the result of collisions with the OH precursor (HNO_3/H_2O), but also includes a small component from spontaneous fluorescence and fly-out. The intercept in all cases is larger for alignment than for orientation, which is suggestive of elastic depolarisation between OH and HNO_3 or H_2O. Because the error in the intercept is relatively high, most likely due to precursor pressure fluctuations, and also the uncertainty of the precursor partial pressures, this contribution is not assessed any further. However it is clear from figure 6.5 that $k_{TCPS}^{(K)}$, the slope, is larger for Ar than for He. In addition, for this specific rotational level, alignment is destroyed more efficiently than orientation for Ar but not for He.

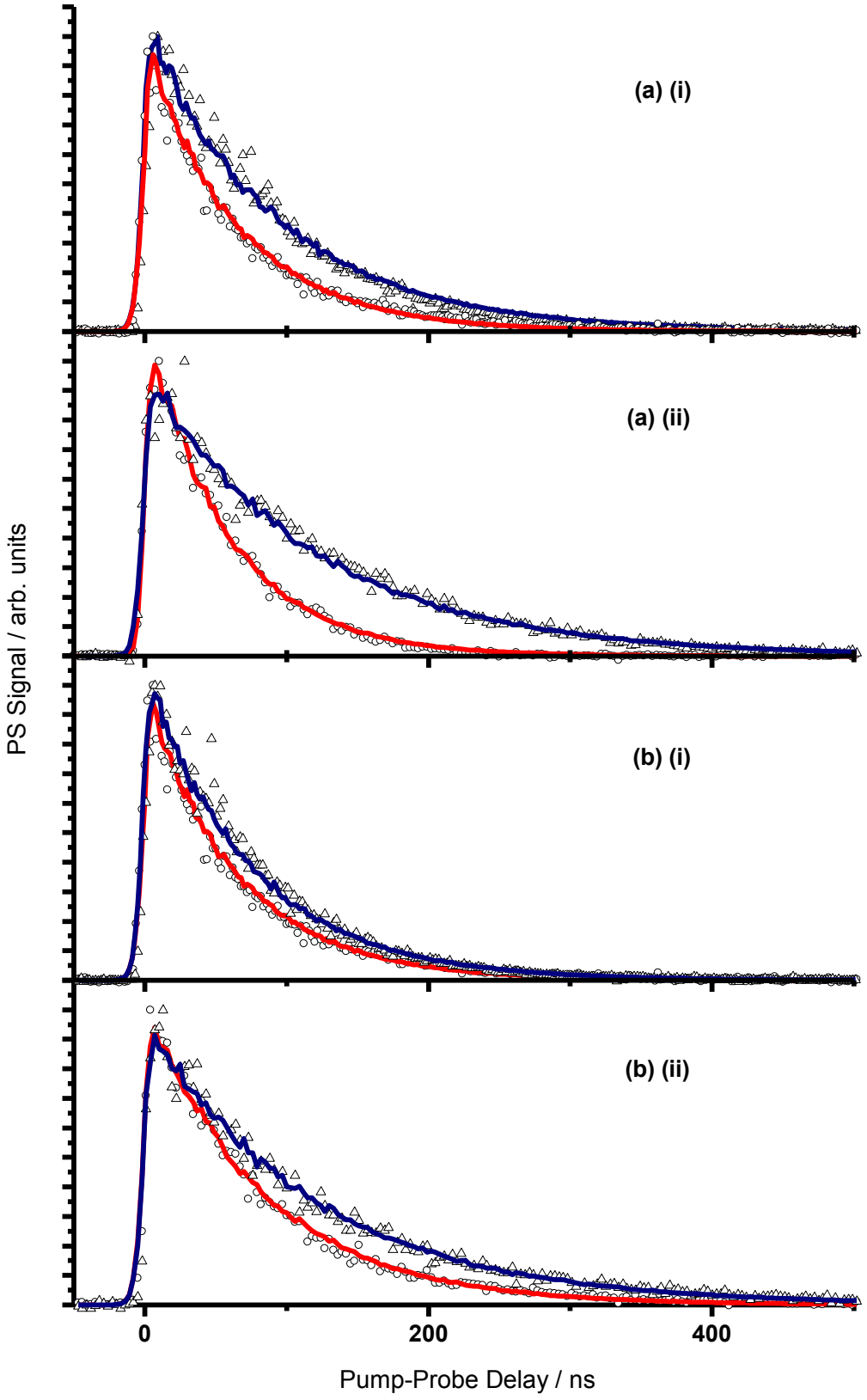

Figure 6.4: *Example OH (A, v = 1) TCPS signals as a function of pump-probe delay. (a) K = 1 and (b) K = 2 for (i) N = 1 and N = 4 (f_1 spin-rotation levels). All decay traces were recorded with approximately 300 mTorr of collision partner: Ar (red) or He (blue). The solid lines represent fits to the data using the TCPS theoretical treatment [72].*

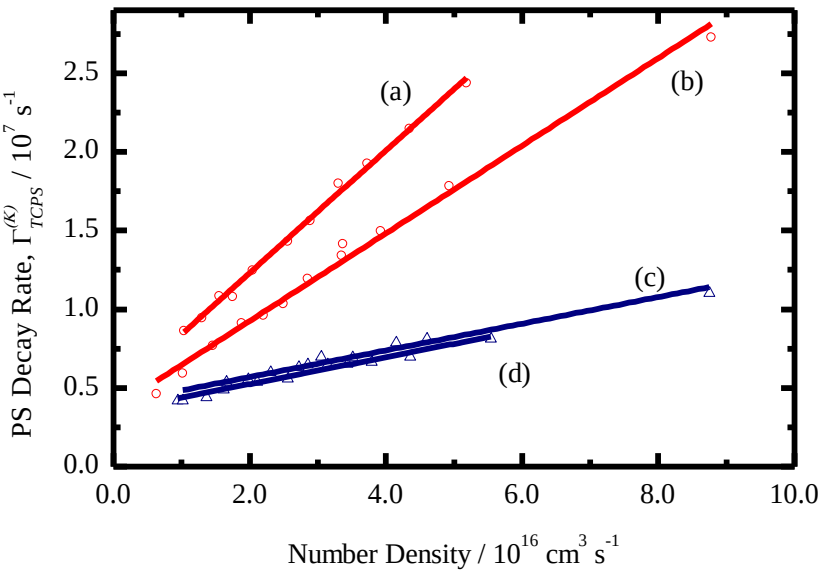

Figure 6.5: *Representative plots of the measured TCPS decay rate as a function of collision partner number density. All data are for OH (A, v = 1) N = 4 (f_1 spin-rotation level). (a) Ar, K = 1; (b) Ar, K = 2; (c) He, K = 1; (d) He, K = 2.*

Table 6.1: *TCPS rate constants (in 10^{-10} cm^3 s^{-1}) and thermally averaged cross-sections (in $Å^2$) for collisional removal of OH (A, v = 1) TCPS signal.*

		N = 0 F_1	***N = 1 F_1***	***N = 2 F_1***	***N = 3 F_1***	***N = 4 F_1***	***N = 5 F_1***
He	$k_{TCPS}^{(1)}$	*2.64 ± 0.28*	*2.31 ± 0.20*	*1.65 ± 0.20*	*1.58 ± 0.27*	*0.81 ± 0.11*	*1.11 ± 0.20*
	$\langle\sigma_{TCPS}^{(1)}\rangle$	*18.9 ± 2.0*	*16.5 ± 1.4*	*11.8 ± 1.4*	*11.3 ± 1.9*	*5.8 ± 0.8*	*7.9 ± 1.4*
	$k_{TCPS}^{(2)}$		*2.72 ± 0.28*	*1.61 ± 0.13*	*1.20 ± 0.10*	*0.85 ± 0.14*	*0.69 ± 0.15*
	$\langle\sigma_{TCPS}^{(2)}\rangle$		*19.4± 2.0*	*11.5 ± 0.9*	*8.6 ± 0.7*	*6.1 ± 1.0*	*4.9 ± 1.1*
Ar	$k_{TCPS}^{(1)}$	*2.45 ± 0.24*	*3.04 ± 0.40*	*2.38 ± 0.29*	*2.91 ± 0.36*	*3.10 ± 0.17*	*2.92 ± 0.30*
	$\langle\sigma_{TCPS}^{(1)}\rangle$	*33.5± 3.3*	*41.7 ± 5.5*	*32.6 ± 4.0*	*39.8 ± 4.9*	*42.4 ± 2.3*	*40.0 ± 4.1*
	$k_{TCPS}^{(2)}$		*3.20 ± 0.35*	*3.89 ± 0.33*	*3.50 ± 0.28*	*3.86 ± 0.35*	*3.10 ± 0.25*
	$\langle\sigma_{TCPS}^{(2)}\rangle$		*43.8 ± 4.8*	*53.2 ± 4.5*	*47.9 ± 3.8*	*52.8 ± 4.8*	*42.4 ± 3.4*

Reported in the table 6.1 are the phenomenological rate constants and corresponding thermally averaged cross-sections extracted from the slopes of the bimolecular plots. It is clear that for He $k_{TCPS}^{(K)}$ declines smoothly as a function of N for both $K = 1$ and $K = 2$. As an example $k_{TCPS}^{(2)}$ is a maximum for $N = 1$ (2.64 x 10^{-10} cm^3 s^{-1}) and falls monotonically by a factor of ~ 4 at $N = 5$ (0.69 x 10^{-10} cm^3 s^{-1}). It should be noted here that the spherical tensor moment for $K = 2$ is necessarily zero for $N = 0$ f_1 with $J = ½$; this state cannot be aligned and so no alignment decay rate constant for this state is reported. The values for $k_{TCPS}^{(1)}$ are broadly similar to those for $k_{TCPS}^{(2)}$ values and for several rotational levels ($N = 2$, 3 and 5) they are numerically larger. This is most likely due to experimental uncertainty. Overall, the data are consistent with at most a minor contribution from elastic depolarisation.

In contrast to He, Ar has rate constants that are less sensitive to N with $k_{TCPS}^{(1)}$ and $k_{TCPS}^{(2)}$ nearly constant over the range investigated. The values in table 6.1 show pronounced differences between orientation and alignment, implying unambiguously that there must be a significant contribution from elastic depolarisation.

6.3 Independent Experimental and Theoretical Work

6.3.1 Zeeman Quantum Beat Spectroscopy

As stated in the introduction, Brouard and co-workers at the University of Oxford performed complementary experiments in collaboration to measure elastic depolarisation in collisions between OH (A, $v = 0$, N) and Ar. It is therefore appropriate to present these results jointly for the discussion that follows. OH (X, $v = 0$) was produced photolytically from a 50:50 H_2O_2/H_2O precursor, which was maintained at a constant partial pressure of ~ 20 mTorr. Following a delay of approximately 9 ns, OH (A, $v = 0$) was optically pumped using the $A – X$ (0,0) electronic band. Various branch types were used to prepare specific rotational levels, either in f_1 or f_2 SR manifolds. The spontaneous fluorescence was guided through polarisation-sensitive optics to a monochromator which dispersed the fluorescence before being detected using a PMT. The experiments were performed in a uniform magnetic field between 0 and 50 Gauss and were screened from external sources by μ-metal. This magnetic field caused the

precession of the rotational polarisation generated by the pump laser; the damping of the Zeeman quantum beats reflects the decay of the rotational polarisation.

For all experiments the polarisation axis of the detection optics was fixed. To measure the decay of rotational alignment the linear probe laser polarisation was rotated between horizontal and vertical, with respect to the detection optics, using a photo-elastic modulator, and between right and left circular polarisation to monitor the orientation decay. The magnetic field direction was fixed parallel to the detection optics for alignment measurements, and orthogonal to both the detection optics and probe laser propagation direction for the orientation measurements.

Essentially the rate of depolarisation is provided by the time-dependent ratio of fluorescence intensity for the two polarisations; i.e. horizontal and vertical, or left and right circular polarisation. The appropriate summation of signals from the two polarisations used provides the total rate of population removal, which would equate to k_{POP} in the context of this work. Figure 6.6 represents an example of a typical data set fit using their theoretical treatment. For extracting population removal rate constants / cross-sections, only the first 100 ns were used, to avoid any contribution from secondary collisions which re-populate the initially prepared level.

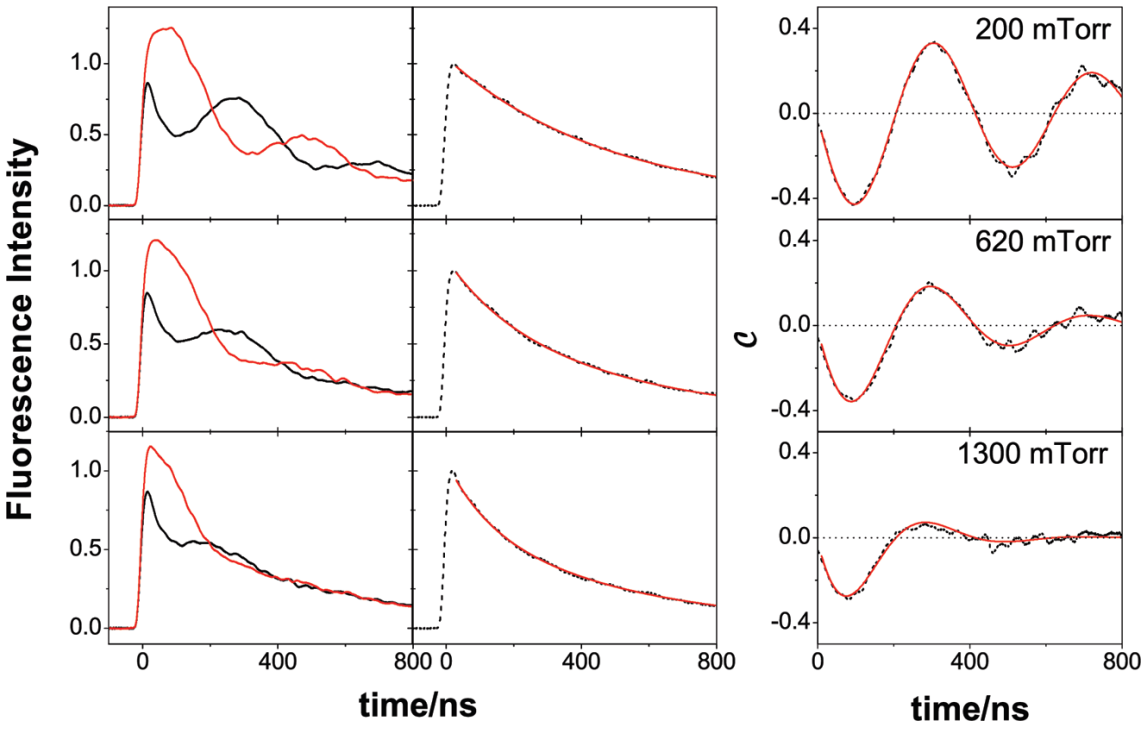

Figure 6.6: *Example decays for ZQBS experiments on OH (A) + Ar. The data were recorded subsequent to excitation on the $R_{11}(13)$ line, with the emission detected from the $P_{11}(15)$ line, at the three pressures indicated. Left panels: the signals obtained with left and right circularly polarized light. Middle panels: the population decay obtained by summing the signals obtained with left and right circularly polarized light. Right panels: the decay of the orientation quantum beat, $\mathcal{C}$. The loss of the beat structure reflects pure elastic depolarization. Taken from ref [90].*

Decay traces were collected for typically 6 pressures of buffer gas (Ar), over a range similar to that used in the TCPS measurements. In a similar fashion to the measurements of this thesis, second-order rate constants for population removal and elastic depolarisation were extracted by plotting the decay rate *versus* collision partner number density. As discussed in the opening section (6.1.1), the main collisional process responsible for population removal is RET. Non-zero intercepts are observed for the population measurements due to spontaneous fluorescence. For the depolarisation measurements, field inhomogeneities provide an additional non-collisional loss process to the non-zero intercept. Collisional processes with the precursor will also contribute to both intercepts. The rate constants were converted to thermally averaged cross-sections, and all the results obtained are reported in table 6.2 below. The results show that the efficiency of RET quickly reaches a maximum at $N = 1$ (35.8 Å^2), before falling smoothly to 6.8 Å^2 for $N = 14$. Where a comparison can be made, f_1 levels ($j = N + ½$) appear to be more robust to RET in comparison to the f_2 counterparts. For elastic 'disorientation' ($\sigma^{(1)}_{DEP}$), the cross-sections seem almost

insensitive to *N*, approximately 15 Å^2 on average and maximum for $N = 5$, f_2 (18.1 Å^2). Interestingly the cross-section for $N = 0$, where $j = 0.5$, is measured to be zero. This is consistent with the concept of the electron spin and nuclear spin (which are the only non-zero angular momenta) being spectators to collisional encounters with Ar (see section 1.1.3). The only process accessible is therefore RET. Elastic 'disalignment' ($\sigma_{DEP}^{(2)}$) also displays an almost *N*-independent trend across the range $N = 1 - 8$, dropping to the lowest value at $N = 14$, f_2 (21.8 Å^2). These values are at least the same magnitude as RET at low *N*, becoming progressively larger than RET for higher rotational levels. Averaged over all rotational levels studied, the cross-sections for disalignment are a factor of 2 greater than those for disorientation. This outcome has been seen previously from the QM scattering calculations on OH (X) + He/Ar/Xe systems discussed in chapter 4.

Table 6.2: *Experimentally determined thermally averaged cross-sections (in Å^2) for (total) rotational energy transfer and depolarisation of rotational orientation or alignment in OH (A, v = 0) + Ar collisions using ZQBS. Data taken from ref [90].*

N	*j*	σ_{RET}	$\sigma^{1)}_{ZQBS}$	$\sigma^{2)}_{ZQBS}$
0	*0.5*	*30.2 ± 6.7*	*0.0 ± 3.3*	
1	*1.5*	*35.8 ± 5.6*	*12.0 ± 5.5*	*35.3 ± 7.5*
2	*2.5*			*30.5 ± 4.3*
4	*3.5*	*32.1 ± 6.2*	*13.0 ± 5.0*	
4	*4.5*	*28.1 ± 5.1*		*32.7 ± 9.0*
5	*4.5*	*28.6 ± 6.9*	*18.1 ± 4.6*	
5	*5.5*	*26.8 ± 7.0*		*31.8 ± 9.4*
8	*7.5*	*16.6 ± 6.4*	*17.9 ± 3.5*	*30.3 ± 13.7*
14	*14.5*	*6.8 ± 3.2*	*15.7 ± 2.9*	*21.8 ± 14.6*

6.3.2 QCT Predictions

Brouard and co-workers also performed QCT calculations to evaluate cross-sections for RET and elastic depolarisation in collisions between OH (A, v = 0, N) and Ar. In addition, they performed open and closed shell QM scattering calculations, which served as a test basis for the QCT predictions of RET cross-sections. The QM calculations, similar to those presented in chapter 4, were exact CC calculations using HIBRIDON, performed on the most recent *ab initio* PES. The QCT calculations were performed for a single collision energy of 39 meV, corresponding to the mean of thermal energy at 300 K. 10^5 trajectories were run for several initial N and the final value for N was rounded to the nearest whole number to calculate the cross-sections for RET. Those trajectories whose final N varied by ± 0.5 of the initial were treated as elastic. The polarisation parameters were determined by evaluating the individual asymptotic angles between initial and final N vectors, and the depolarisation moments calculated as the ensemble average of the corresponding Legendre moments. The depolarisation rate constants / cross-sections are related to these depolarisation moments through relationships that have been previously published [29,89]. The open-shell nature of OH (A) is accounted for within the approximation that the electron and / or nuclear spin can be considered as spectators (see section 1.1.3) and therefore allows the calculation of SR changing processes and also hyperfine changing collisions. Table 6.3 below summarises the findings. Figures 6.7 and 6.8 provide a graphical comparison of

their experimental and theoretical results for RET population removal and elastic depolarisation respectively.

Table 6.3: *Open-shell QCT calculations of RET and elastic depolarisation cross-sections (in Å^2) at fixed energy (39 meV).*

N	F_1 initial levels			F_2 initial levels		
	σ_{RET}	$\sigma^{(1)}_{DEP}$	$\sigma^{(2)}_{DEP}$	σ_{RET}	$\sigma^{(1)}_{DEP}$	$\sigma^{(2)}_{DEP}$
0	36.0	0.0				
1	37.3	9.6	23.3	47.3	16.4	
2	35.8	9.4	21.4	40.4	14.7	25.1
3	34.2	9.3	20.4	37.2	12.8	23.3
4	30.1	9.9	21.6	32.3	13	24.3
5	26.5	11.3	24.3	28.5	14.2	26.7
6	22.0	12.8	27.7	23.7	15.8	30.2
7	13.4	14	30.8	14.6	17.1	33.7
8	10.1	14.1	31.6	11.1	16.9	34.7
9	8.3	13.3	30.7	9.2	15.8	33.9
14	4.2	8.6	22.2	4.5	9.8	24.6

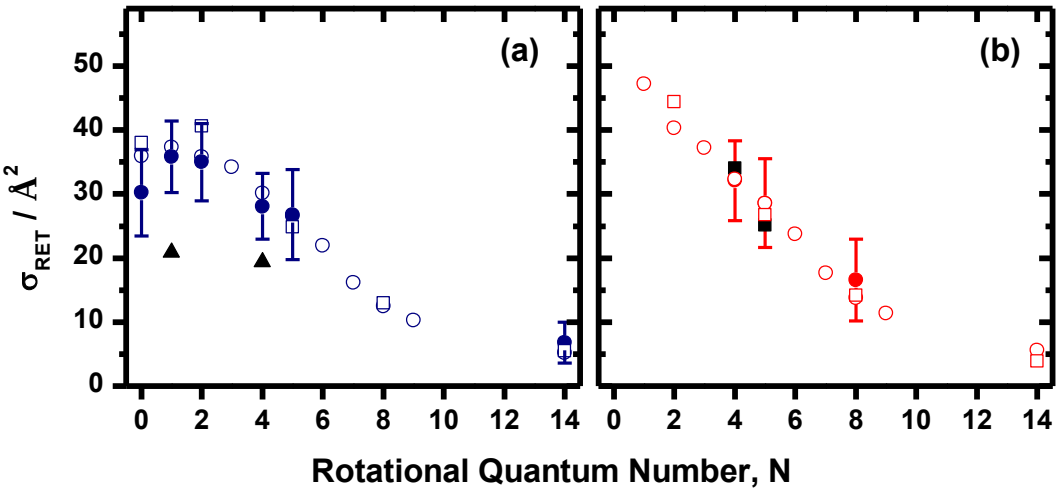

Figure 6.7: *RET Cross-sections for OH (A, v = 0) + Ar: (a) from f_1 spin-rotation levels and (b) f_2 spin-rotation levels. The data from the ZQBS experiments (filled symbols with 2σ uncertainties) are compared to the QCT predictions (open circles) and open-shell QM predictions (open squares) at a fixed energy of 39 meV. In (a) the state-to-state RET measurements, summed over all final rotational levels measured; from the work of Lengel and Crosley are reported (filled triangles). Similarly, in (b) experimental RET cross-sections, again summed over all final rotational levels, from the work of Jorg et al. are provided for comparison (filled squares).*

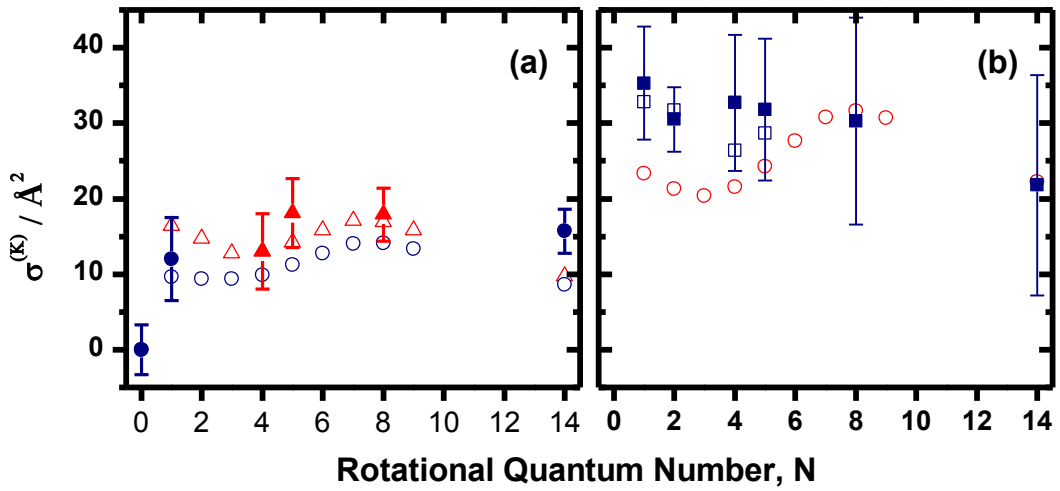

Figure 6.8: *(a) OH (A, V = 0) + Ar pure elastic disorientation cross-sections (K = 1) from the ZQBS experiments (filled symbols with 2σ uncertainties). The data are resolved into f_1 (circles) and f_2 (triangles) spin-rotation levels. The open-shell QCT data are shown as open symbols. (b) pure elastic disalignment cross-sections (K = 2) from the ZQBS experiments. The open shell QCT cross sections for pure elastic disalignment are shown as the open circles, specifically for the F_1 spin-rotation levels. The open squares are fits to simulated data that include the effects of overlapping satellite lines. The measured disalignment cross-sections are therefore enhanced by the depolarization caused by spin-rotation collisions, weighted by the satellite line strength. The effect of unresolved satellite lines is negligible for N = 8 and 14.*

Generally there is excellent agreement between the ZQBS RET measurements, and the predictions, from both open-shell QM and QCT scattering calculations on the most recent *ab initio* PES, for population removal from both f_1 and f_2 SR manifolds. For the f_2 SR manifold excellent agreement is also observed in comparison to the limited measurements of Jorg *et al.* [36] The RET measurements of Lengel and Crosley [34] however are significantly lower in magnitude than those values computed or measured in the work presented in this section. The decline of σ_{RET} as a function of initial rotational quantum state is clear to see. The QCT predictions also reproduce the measured elastic depolarisation measurements for orientation in both f_1 and f_2 SR manifolds. f_2 SR levels seem to be more robust to elastic depolarisation. Good agreement is also observed for the 'disalignment' measurements when inelastic depolarisation and dephasing contributions to $\sigma^{(2)}_{ZQBS}$ were accounted for (these 'contaminating' effects were the result of not resolving unique emission lines). The main conclusion here, and the one that will be the main focus of discussion, is that elastic depolarisation for orientation and alignment appears to be insensitive to

rotational quantum number across the range of states studied, slowly declining for $N >$ 10. It is reiterated that in all cases alignment cross-sections are larger than the orientation equivalents, on average, by a factor of ~ 2.

6.4 Discussion

6.4.1 Assessment of the Two Techniques

Because of the contrasting approaches used to measure rotational depolarisation in OH (A) + Ar, it is worth exploring the strengths and weaknesses of each technique. First of all there is the issue of resolution. Because TCPS relies only on laser radiation for excitation and detection, it is inherently of higher resolution than ZQBS, which involves dispersing emitted fluorescence with a monochromator to isolate emission from a particular quantum state. For this reason ZQBS is often incapable of probing unique rotational levels and the 'elastic' depolarisation measurements potentially overestimate the true magnitude. Unwanted depolarisation or dephasing processes are factored out using known experimental resolution and spectroscopic data. The measurements most affected in the results presented here are the ZQBS 'disalignment' measurements, $\sigma^{(2)}_{ZQBS}$. As indicated in section 6.2 TCPS does not suffer from this experimental artefact. The ZQBS measurements of RET cross-sections are sensitive to collisional re-population of the initially prepared level and so the reliable data is restricted to the first ~ 100 ns of the exponential decay, where the probability of multiple collisions is low for those Ar partial pressures used. In contrast, the TCPS measurements, which are sensitive to the bulk polarisation, are very likely to be insensitive to collisional repopulation of the initial level, because a rotational polarisation is required to produce a signal. This possibility was explored in section 4.5.4 as a possible source of underestimating the RET component of the TCPS rate constants / cross-sections. This is even less likely for OH (A) + Ar where depolarisation as a result of RET is predicted to be strong (i.e. returning molecules are unlikely to be rotationally polarised) [89]. However, because TCPS is only sensitive to the bulk polarisation of the ensemble, TCPS cannot resolve the population loss from the depolarisation contribution. ZQBS on the other hand can measure both these properties from the one experiment, but is subject to numerical handling errors and any errors incurred by changing the polarisation of the probe laser. In principle, degenerate four-wave mixing schemes related to TCPS can allow independent determination of population and polarisation properties. In practice

however, with the nanosecond-pulsed lasers used in these experiments, such measurements would be dominated by other non-collisional processes arising from the formation of spatial gratings in the sample. The ZQBS experiments almost certainly possess higher sensitivity than TCPS, where the ultimate detection sensitivity is limited by the extinction ratio of the polarisers (1×10^{-6}). In addition the non-linear nature of the technique results in a squared dependence on the number density of the initial level, restricting the range of rotational levels that can potentially be investigated.

Despite the differences, the agreement between the two independent studies is very good, as shown in figure 6.9 below. For the orientation measurements a direct comparison can be made between the two methods, by summing the $\sigma^{(1)}_{DEP}$ and σ_{RET} values obtained for each level using the ZQBS technique. To be clear, this is an independent measurement of $\sigma^{(1)}_{TCPS}$. The ZQBS measurements are, in general, slightly larger than the equivalent TCPS values, but still within the combined uncertainties. It should be highlighted that the ZQBS measurements for $N = 4$ and 5 are sensitive to f_2 SR levels, which have been found to be larger in magnitude (for RET and elastic depolarisation) than the equivalent f_1 levels that are measured with the TCPS technique. Interestingly for the lowest level, $N = 0$, the measured values are essentially the same for the two techniques. For this one level there can be no elastic depolarisation, in the limit that the electron spin can be reliably treated as a spectator in the collisional process, and so this is purely a measurement of RET.

A similar comparison can be made for the alignment data, although slightly more indirectly, because of the overlapping spectroscopic lines contaminating the $\sigma^{(2)}_{DEP}$ values obtained from the ZQBS measurements. However, the simulations of this artefact, used to compare $\sigma^{(2)}_{DEP}$ values to QCT predictions in section 6.3.2, can be used to correct the ZQBS disalignment data. Adding the corrected $\sigma^{(2)}_{DEP}$ values to the RET measurements results in the same type of comparison used for the orientation measurements, and is shown in Figure 6.9(b). The correction drops from 10 Å^2 – 4.5 Å^2 over the range $N = 1 – 5$, and is negligible for $N = 8$ and 14 where the line-strength of the satellite line that contributes is negligible. Similar to the orientation results, the ZQBS measurements are somewhat larger than the TCPS measurements, the discrepancy being largest for $N = 1$ and 5.

It should be emphasised that the two techniques probe different vibrational levels of OH (A) (ZQBS: v' = 0 and TCPS: v' = 1). The good agreement between the two data sets lends support to the view that both RET and elastic depolarisation are not strongly vibrational-level dependent. In any case, the additional quantum of vibration in the TCPS measurements would more likely result in *larger* overall cross-sections (inelastic plus elastic depolarisation) in comparison to the ZQBS equivalents, due to the anticipated increase in anisotropy of the PES that follows an increase in the nuclear excursion. This is actually the opposite of what is observed.

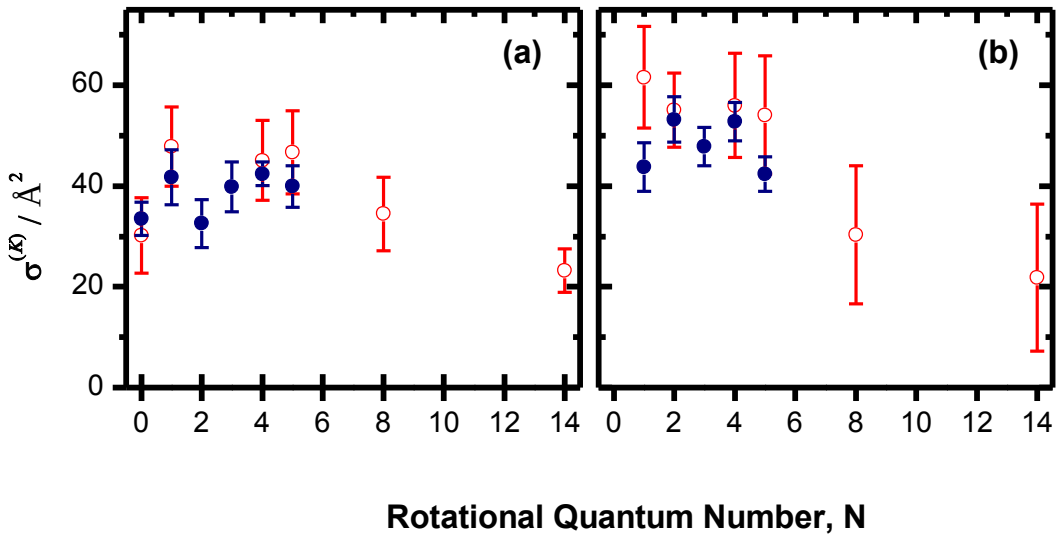

Figure 6.9: *(a) Comparison between the OH (A, v) + Ar orientation data (K = 1) obtained from the TCPS (filled circles) and the ZQBS (open circles) experiments. The latter are the sum of the RET and disorientation cross sections, and neglect small differences in the values for F_1 and F_2. (b) Comparison of the disalignment cross sections (K = 2) obtained in the two experiments. The disalignment data have been corrected for the effects of spin-rotation changing collisions based on the simulations using the QCT cross sections.*

6.4.2 OH (A) + Ar: Evaluating the Magnitude of Depolarisation

As is now known from chapter 4, assessing the absolute magnitude of elastic depolarisation requires prior knowledge of the RET contribution to the TCPS signal. This has been provided in section 6.3, at least for OH (A) + Ar. From the usual subtraction $(\sigma^{(K)}_{TCPS} - \sigma_{RET})$ the value of $\sigma^{(K)}_{DEP}$ can be established. Unfortunately, for OH (A) + He there have been no *recent* independent experimental or theoretical studies using the techniques introduced in section 6.3. The only information available, which covers the rotational quantum states investigated here (albeit for v' = 0), are QM

scattering calculations of E&W [49]. They evaluated state-to-state rate constants, as mentioned in the introduction, for OH (A, $v' = 0$, N) + He at a temperature of 298 K. The sum of the state-to-state rate constants provides the RET contribution and a comparison to the TCPS measurements is shown in figure 6.10. The rate constants for pure SR changing transitions are shown separately from all other RET processes. The RET contribution is predicted by the calculations to fall progressively from $N = 0 – 5$, with the SR changing component decreasing monotonically over the same range. Note that there is only one rotational level for $N = 0$ ($j = 1/2$), as, of course, an f_2 level ($j = N$-1/2) does not exist for this special case. More importantly, all measurements of $k_{TCPS}^{(K)}$ are larger than these QM scattering calculations, leaving a plausible positive deficit which could be attributed to elastic depolarisation. It should be noted that these calculations were performed using a fixed OH bond length, set to r_e for OH (A, $v = 0$). From similar calculations on OH (X), Esposti and Werner had found that an increase in the OH average bond length resulted in a more anisotropic PES and hence larger overall RET rate constants [15]. Given this, the RET values for $v' = 1$ may be expected to be larger, leaving less room for elastic depolarisation. This, together with the previous observation that the values of $k_{TCPS}^{(1)}$ and $k_{TCPS}^{(2)}$ are very similar (for some rotational levels $k_{TCPS}^{(1)}$ is actually larger than $k_{TCPS}^{(2)}$), indicates that it is likely that elastic depolarisation plays a relatively small role, and is at most modest, approximately < 5 Å^2. Interestingly, the best agreement is for $N = 0$ for orientation, which, in the spin-spectator model, should measure RET alone. An earlier study by Brinkman and Crosley using LIF measured depolarisation cross-sections, $\sigma_{DEP}^{(2)}$, of 9, 6 and 3 Å^2 for $N = 1$, 2 and 4 (f_1 levels), in general agreement with the modest depolarisation measured here.

On the other hand, OH (A) + Ar shows very different behaviour. Figure 6.11 compares the TCPS measurements with the RET cross-sections obtained in section 6.3. First, for the one measurement where only RET can contribute, i.e. the orientation result for $N = 0$ (figure 6.11(a)) the QCT calculation and ZQBS experiment reassuringly reproduce the TCPS value (~ 34 Å^2). The calculations also show that RET is expected to decline steadily from $N = 0 – 5$, whilst SR changing cross-sections hold their magnitude across the range of N shown and actually slightly increase and become proportionately larger as a fraction of total RET. Also reassuringly, all other TCPS measurements, with the exception of $\sigma_{TCPS}^{(1)}(N = 2)$, are larger than the QCT predictions and ZQBS measurements of RET. This is required in order to leave room for a positive

contribution from elastic depolarisation. In most cases, more so at higher rotational levels and for alignment, the deviation is statistically significant. Coupled with the observation that alignment is destroyed more efficiently than orientation, this leads to the conclusion that there must be significant elastic depolarisation for OH (A) + Ar. In addition, there is overall good agreement with the QCT prediction of the TCPS measurements. This prediction is represented by the total height of the bars in figure 6.11 (navy + blue + cyan).

Due to the very good agreement between the two independent experimental measurements, and also their agreement with the appropriate theoretical predictions, it is possible to arrive confidently at some conclusions concerning elastic depolarisation for OH(A) + Ar. The main points are that, first, the magnitude of elastic depolarisation is approximately 10 – 15 $Å^2$ for orientation and roughly twice that for alignment, namely 20 – 30 $Å^2$. This is also consistent with the only prior attempt to measure OH (A) + Ar alignment depolarisation, by Brinkman and Crosley, who obtained a value of 20 $Å^2$ for $N = 4$ (f_1). Second, the magnitude appears to be approximately constant over the range $N = 1 – 10$ before eventually decreasing with increasing N.

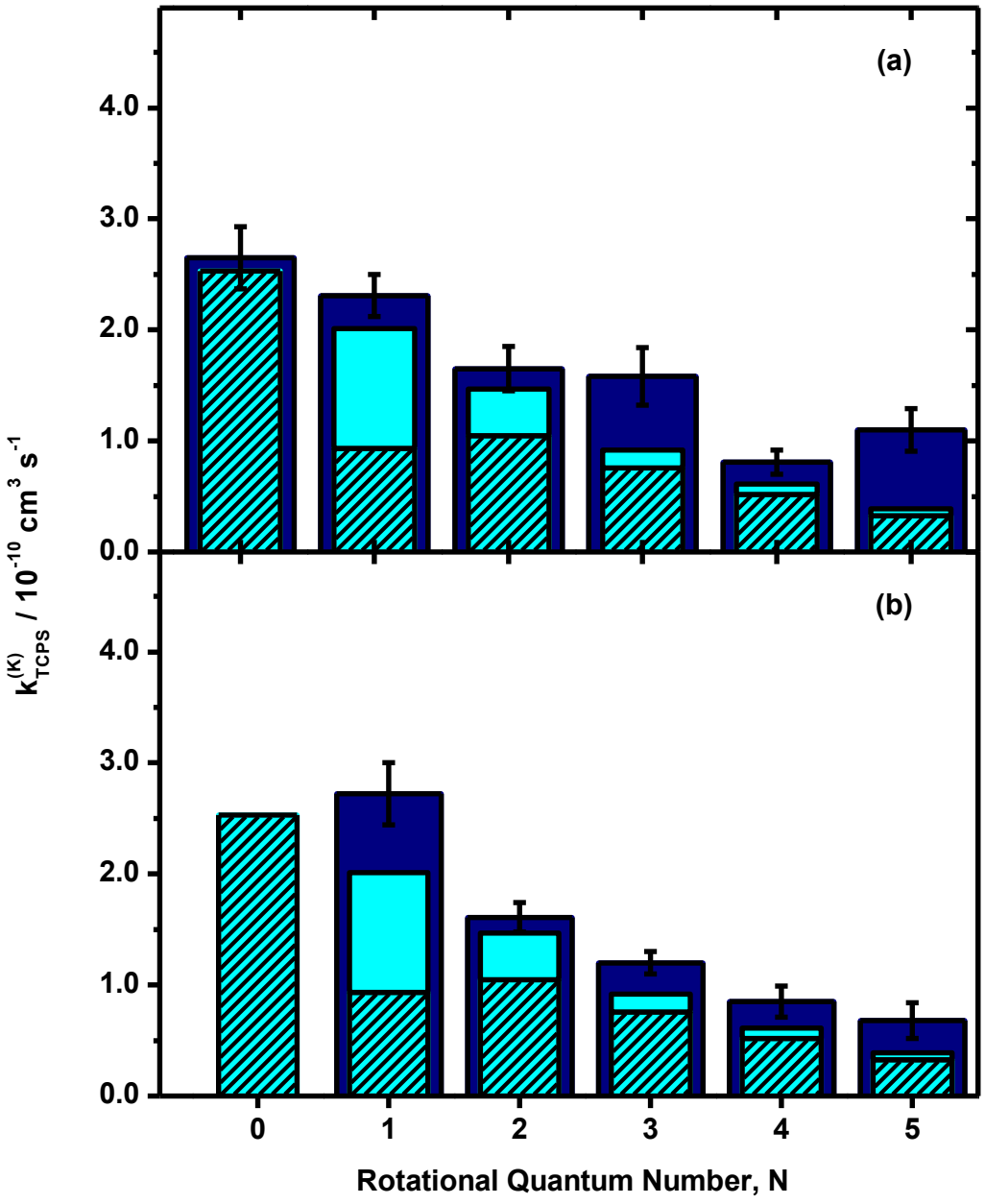

Figure 6.10: *Comparison of the measured TCPS rate constants for OH (A) + He (navy bars) with QM RET predictions from Esposti and Werner. The RET component has been decomposed into all RET processes except pure spin-rotation changing (hashed cyan) and pure spin-rotation changing alone (unhahsed cyan). (a) orientation data (K = 1) (b) alignment (K = 2).*

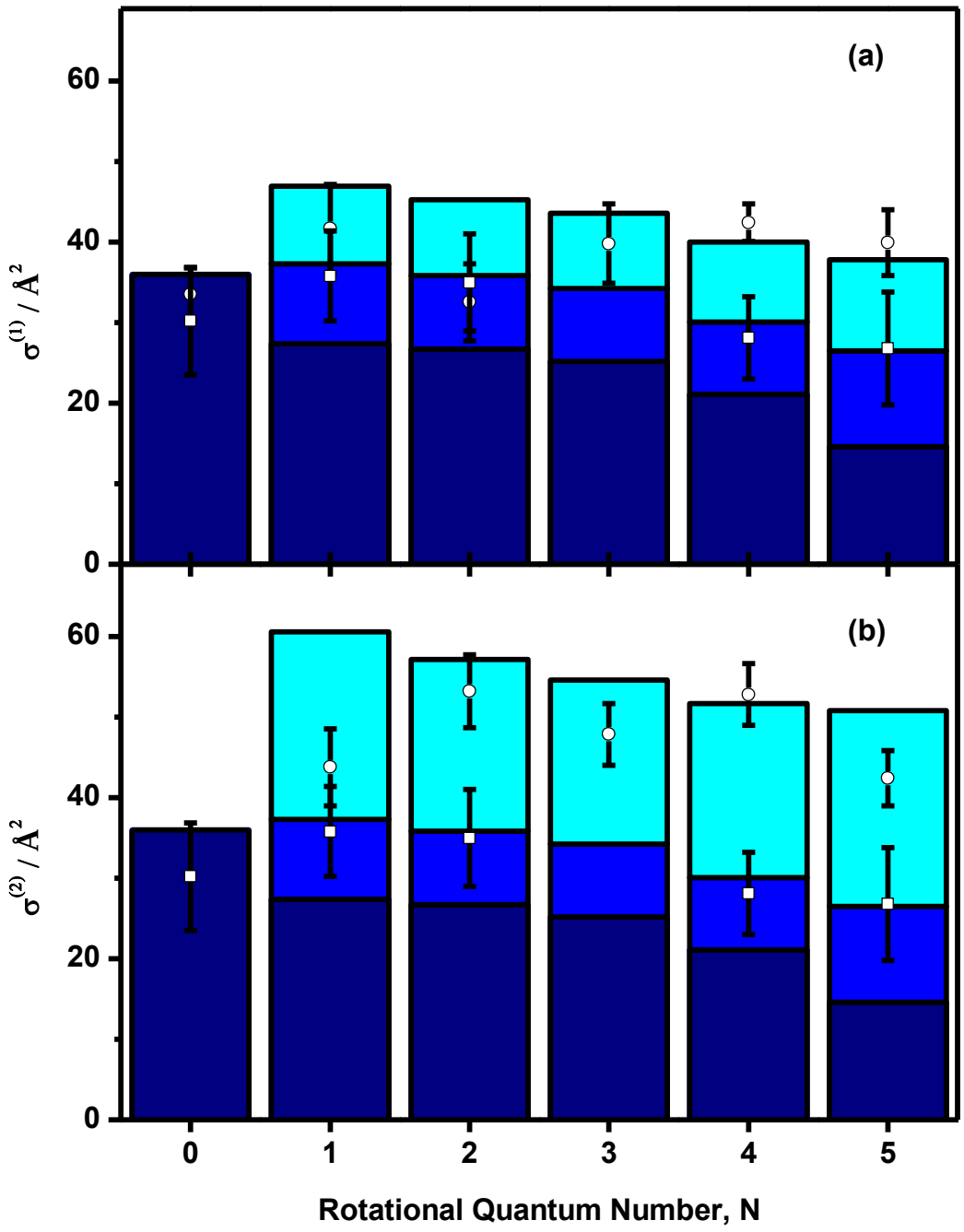

Figure 6.11: *Comparison of thermally averaged cross-sections for OH (A) +Ar obtained from the TCPS measurements (open circles) with a QCT prediction (total height of the bars). The bars have been decomposed into the various collisional processes which the TCPS experiment is sensitive to: RET excluding spin-rotation transfer (navy), pure spin-rotation transfer (blue) and elastic depolarisation (cyan). (a) orientation (K = 1) (b) alignment (K= 2). Also included are the RET measurements from the ZQBS experiment (open squares), which should be equal to the sum of the navy bars together.*

6.4.3 OH (A) *vs.* OH (X)

The systems most closely related to the results presented here, are the OH (X)-Rg systems presented in chapter 4. Figure 6.12 summarises the contrasts in TCPS results between the two electronic states, for both Ar and He. At low *N*, the cross-sections are very comparable. For OH (A) + Ar the similarity promptly disappears as *N* increases, and the cross-sections for OH (A) and OH (X) diverge. The reason for this is an interesting question.

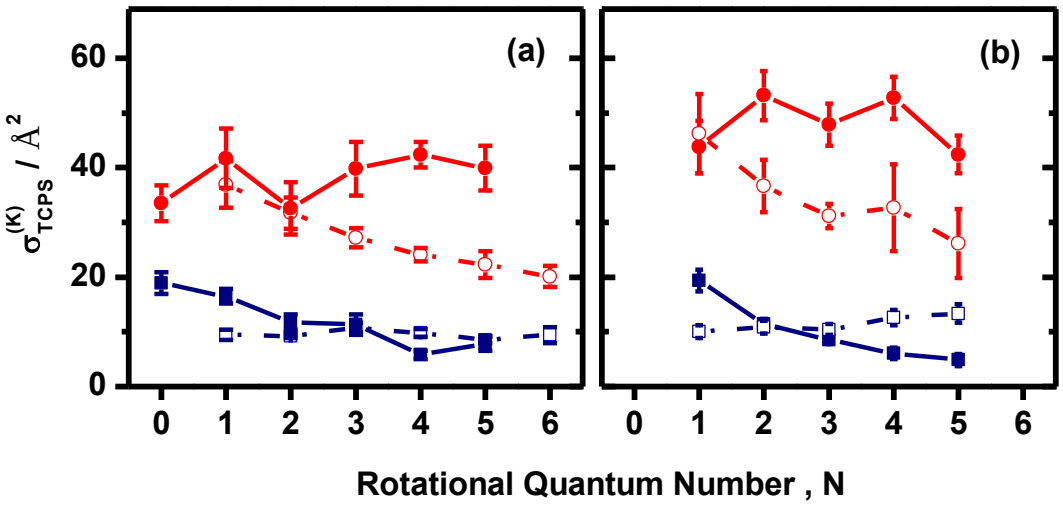

Figure 6.12: *Comparison of the measured TCPS thermally averaged cross-sections for OH (A, v = 1, N, f_1) (filled symbols) and OH (X, v = 0, N, F_1 e) (open symbols) for Ar (circles) and He (squares). Data are shown for (a) K = 1 (orientation) and (b) K = 2 (alignment).*

One important difference between OH (A) + Rg and OH (X) + Rg, which has been touched on before, is the fact that the collision dynamics for OH (A) may be approximated using the model that the electron spin is a spectator (see section 1.1.3 and figure 1.5). This has profound implications on the definition of elastic depolarisation. Figure 1.5 illustrates this by showing the vector addition of the nuclear rotation angular momentum, ***N***, and the electron spin, ***S***. Within the spin-spectator assumption, an SR changing process is essentially a reorientation of the vector ***N***, and although a quantum state changing process, it is by all accounts 'elastic' depolarisation with respect to ***N***. There is no equivalent for OH (X), where the electron spin is coupled to the electronic angular momentum. Perhaps a fairer comparison of elastic depolarisation between OH (X) and OH (A) can therefore be seen in figure 6.13. Here the QM tensor cross-sections computed by Alexander and Dagdigian [94,174] for $\sigma^{(K)}_{DEP}$ are used for OH (X) and the

QCT results of section 6.3.2 are used for OH (A). It is clear that by treating the SR components as elastic depolarisation, the difference between OH (A) + Ar and OH (X) + Ar is enhanced. In fact, it has been shown previously that the sum of the QCT calculations for elastic depolarisation and SR changing collisions equals that obtained for elastic depolarisation from a closed-shell QCT calculation [89]. For low *N*, the magnitude is also somewhat similar to the largest values obtained for OH (X) + Ar, but OH (A) is depolarised considerably more efficiently when considering the rotational levels investigated as a whole. This roughly constant *N* dependence is a combination of elastic depolarisation and SR changing processes being broadly insensitive to *N*, as shown in figure 6.11. This is in contrast to what is seen for He, where the efficiency of SR changing transitions decreases rapidly with *N* (figure 6.10).

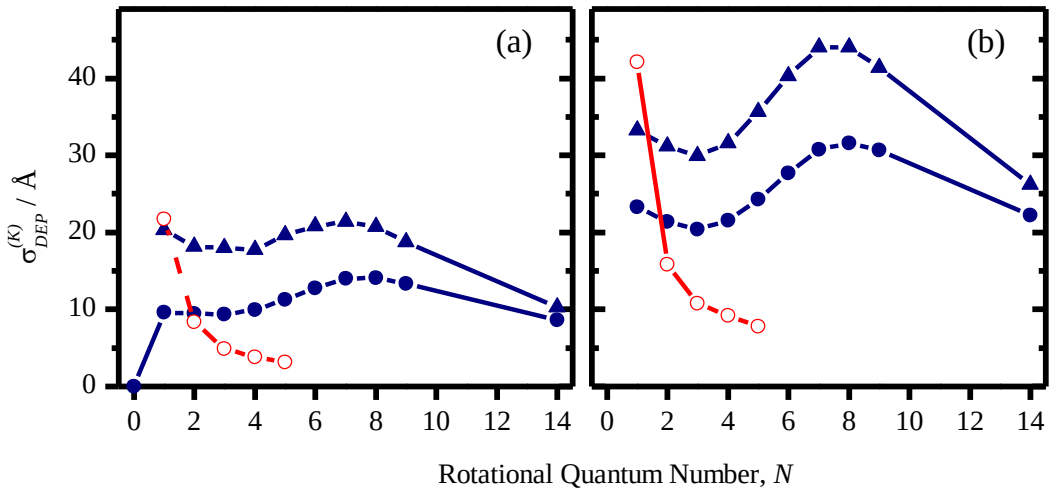

Figure 6.13: *Comparison of calculated elastic depolarization cross sections for OH (A) + Ar (filled navy symbols) and OH (X) + Ar (open red symbols), and for both (a) K = 1 and (b) K = 2. The OH (X) data are from Dagdigian and Alexander (o-s QM) [94,174] and OH (A) data are from section 7.3.2. For OH (A) + Ar, the circles represent the pure elastic depolarization and the triangles the sum of elastic depolarization and spin-rotation changing depolarization.*

6.4.4 Role of the PES

From figures 6.1 and 6.2 the extent of the differences between the PESs for OH (X) + Ar and OH (A) + Ar as well as that for OH (X/A) + He are clear to see. In chapter 4 the PESs expressed as radial expansions of Legendre polynomials (see figure 4.27) were used assess the relative magnitude of the various components that contributed to the TCPS measurements, namely RET, Λ-doublet transfer and elastic depolarisation. The isotropic term $\lambda = 0$ in the PES for He and Ar seems to be relatively independent of

electronic state (figure 6.2). This component cannot in any case contribute to any scattering process which changes the magnitude or direction of ***N***, and can only induce pure velocity changing events. The other, anisotropic terms, do influence the dynamics, and are therefore the important components to which the TCPS and ZQBS experiments are sensitive. As was argued for OH (X) (section 1.1.3), the even terms control scattering between levels of the same parity (with respect to the rotational wavefunction), and the odd terms mediate parity changing events [26]. This means that elastic depolarisation and SR changing processes are both in principle governed by the even terms in the Legendre expansion.

Inspection of figure 6.2 reveals that the *ranges* of the OH (X)-Ar and OH (A)-Ar PESs are not too dissimilar and so it is anticipated that the maximum total experimental cross-sections should be comparable also. This is indeed what is observed. Taking the average value of $\sigma_{TCPS}^{(2)}$ for OH (A) + Ar, an approximate collision radius of ~ 7.25 a_0 is found, which is well into the attractive wing of the PES. At this range, and at separations smaller than this, the OH (A)-Ar anisotropic terms are strikingly different from OH (X)-Ar, reflecting the strongly attractive OH (A)-Ar PES. The $\lambda = 2$ term is dominant, so it is not surprising that for OH (A) + Ar depolarisation (taking into account SR changing processes) is considerably more efficient than OH (X) + Ar for the majority of rotational levels measured.

The principal conclusion from this study is therefore that a more strongly anisotropic and attractive PES enhances depolarisation (the sum of elastic depolarisation and SR changing processes). In addition, the efficiency of these depolarising collisions seems to be more efficient for higher rotational levels. In a classical picture, that means the stronger and more anisotropic the forces acting, the easier it is to 'tilt' or reorient more rapidly rotating molecules. There is some evidence that the efficiency of depolarisation will decrease for rotational levels higher than $N = 14$. This is perhaps the result of increased gyroscopic stability, or that the collisions experience a full rotational average of the intermolecular forces, effectively 'smearing' out the attractive wells at the two linear configurations, $\theta = 0$ and 180°.

6.4.5 Comparison to Other Systems

Now that the dynamics of OH (X) + Rg and OH (A) + Rg have been unravelled it is worthwhile to discuss other related open-shell systems with the intention of better

understanding what influences elastic depolarisation. Given that the evidence so far presented indicates that it is the attractive parts of the PES that induce elastic depolarisation, and OH-He is essentially repulsive (hence the absence of elastic depolarisation), the focus henceforth will concentrate on collisions with Ar. The kinematically identical OH (X/A) + Rg systems presented here and in chapter 4 clearly reveal the effect of altering the PES alone, the outcome of which has been covered in detail above (6.4.4). But the influence of kinematics cannot be ruled out. Below is a summary of four related systems, but with kinematics distinct from OH + Rg (i.e. HH' + H''). Those are: NO ($X^2\Pi$) [87] + Ar, NO ($A^2\Sigma^+$) + Ar [179] and CN ($A^2\Pi$) + Ar [81].

$^2\Sigma^+$ *Systems*

Due to the common electronic term, the NO (A) + Ar work of Brouard and co-workers is the most related to the work of this chapter. Briefly, NO (A) + Ar adopts a 'linear' PES geometry, where there are minima located at $\theta = 0$ and 180°, and the magnitude of the global minimum is ≈ 100 cm^{-1}. The reduced mass of the system is 17 a.m.u. Using the ZQBS technique Brouard and co-workers measured depolarisation cross-sections for a number of NO (A, $v = 0$) rotational levels in collisions with Ar. Unfortunately they did not resolve the fluorescence as they had done for the OH measurements of section 6.3.1. Consequently, the reported cross-sections included inelastic depolarisation processes in addition to elastic ones, which, in turn, resulted in dephasing contributions that arise from the population of rotational levels with different Landé-*g* factors, and hence, different hyperfine frequencies. In an attempt to decompose their measurements into inelastic / elastic depolarisation *etc.*, QCT scattering calculations were run, analogous to those of section 6.3.2, to obtain a theoretical prediction of their measurements (including a dephasing simulation). The overall good agreement between experiment and theory provides some justification for using these computed elastic depolarisation cross-sections as reliable values. It should be noted that open-shell and closed-shell calculations were performed as well as QM scattering calculations, which provided a benchmark for QCT. They find that for initial level $N = 2$ (f_2): $\sigma_{DEP}^{(2)} = 8$ Å^2. However, as touched on above, perhaps a fairer assessment of 'elastic' depolarisation for a $^2\Sigma^+$ state is a summation of pure elastic depolarisation and SR changing cross-sections. This is provided by their closed-shell QCT calculation, for which the cross-section for $N = 2$ is approximately 18 Å^2. These two values are considerably lower than the OH (A) + Ar counterparts, which are ~ 23 and 33 Å^2 respectively (based on QM scattering

calculations [94,174]). Although closed-shell calculations were only performed for this one initial level, pure elastic depolarisation cross-sections (i.e. $\Delta N = 0$ and $\Delta j = 0$) were reported for various rotational levels covering the range $N = 2 – 14$. Despite being low in comparison to OH (A), $\sigma_{DEP}^{(2)}$ values are reasonably constant over this range of N; falling from 5.8 – 4.9 Å^2 between $N = 5 – 14$. $\sigma_{DEP}^{(1)}$ values are predicted to be the familiar factor of 2 less than their $\sigma_{DEP}^{(2)}$ equivalents, but interestingly the closed-shell QCT calculations (pure elastic depolarisation + SR changing collisions) are very similar for orientation and alignment.

$^2\Pi$ Systems

In terms of the $^2\Pi$ systems; NO (X) + Ar has a 'T-shaped' PES geometry, where the global minimum is located at $\theta = 90°$ with a depth of ≈ 100 cm^{-1} [231]. There are no reports of elastic depolarisation in the literature for this system, but it is the focus of ongoing TCPS measurements (see chapter 7). Dagdigian and Alexander have, however, performed QM scattering calculations on this system for a kinematic comparison to the OH (X) + Ar work discussed in chapter 4, and presented in figure 6.14. Elastic depolarisation tensor cross-sections, $\sigma_{DEP}^{(K)}$, were provided for orientation and alignment, with the usual factor of roughly two being observed between them. They found that, somewhat similar to NO (A) + Ar, $\sigma_{DEP}^{(2)}$ decreased from 7 to 3 Å^2 smoothly over the range of rotational levels $j = 1.5 – 7.5$. Essentially zero elastic depolarisation was found for $j = 0.5$. (Note: this is the F_1 spin-orbit manifold ($^2\Pi_{1/2}$). NO is regular, whereas OH is irregular.)

The values obtained for NO (X) + Ar are much smaller than those for OH (X) + Ar, where the same QM predictions give $\sigma_{DEP}^{(2)}$ values that decline rapidly, from 47 Å^2 to 7 Å^2 over the range $j = 1.5 – 5.5$. TCPS measurements on OH (X) provide an upper limit of approximately 20 Å^2, which is still a factor of roughly 3 greater than the NO (X) + Ar QM predictions, which by all accounts, may similarly overestimate the elastic depolarisation cross-sections, at least at low-j.

The final open-shell diatomic molecule that elastic depolarisation information is available for is CN (A) + Ar, which conforms to a $^2\Pi$ electronic term symbol, has a 'T-shaped' PES geometry with a global minimum of ≈ 130 cm^{-1} and has a reduced mass of

~ 16 a.m.u [232]. Very recently Ballingall *et al.* used Doppler-resolved frequency-modulated spectroscopy (FMS) to monitor the collisional evolution of both population and alignment moments (K = 2) from various rotational levels in CN (A, v = 4) under thermal conditions [81]. Similar to the ZQBS measurements, these experiments are able to resolve the total RET component from the elastic depolarisation, but were of higher spectroscopic resolution, and thus uncontaminated by neighbouring transitions. They reported $\sigma_{DEP}^{(2)}$ values which were on average 16 Å^2 over the range j = 1.5 – 10.5, before dropping to zero within the precision of their measurement at j= 23.5. These values are approximately a factor of 4 less than the population removal, which was found to be roughly 50 – 60 Å^2 over the range j = 1.5 – 10.5, in very good agreement with previous experiments and theoretical predictions. Orientation measurements were not possible due to the multi-pass turning mirror arrangement in their vacuum chamber. Dagdigian and Alexander have recently extended their QM calculations on OH and NO to include CN (A) + Ar (unpublished). There was good agreement between the computed and measured population transfer cross-sections (predictions roughly 10% larger), but surprisingly $\sigma_{DEP}^{(2)}$ was calculated to range from 9.5 Å^2 to 3.2 Å^2 over the range j = 1.5 – 10.5, considerably lower than the FMS measurements and with a contrasting j-dependent trend. Although these calculations were run on an older PES the contradiction makes it difficult to identify any solid trends of elastic depolarisation from this and the above case studies.

It should be remembered that the $^2\Pi$ systems are described not by one PES but at least two, i.e. V_{SUM} and V_{DIFF}. It was mentioned briefly in chapter 4 that Alexander and Dagdigian had explored the effect of setting the V_{DIFF} surface to zero. Carrying out QM scattering calculations with and without this artificial alteration revealed how large a role the V_{DIFF} surface played with respect to elastic depolarisation. It turns out that for OH (X) + Ar the V_{DIFF} contribution is very substantial; elastic depolarisation being suppressed by, on average, 86% over the range j = 1.5 – 5.5 when V_{DIFF} = 0. In contrast, for NO (X) Ar, elastic depolarisation seems to be insensitive to V_{DIFF}. It was argued that this outcome is the result of the relative magnitude of the V_{22} term (of V_{DIFF}) in comparison to the V_{20} term (of V_{SUM}) in the decomposed PES (see section 4.5.5). These potential arguments are supported by independent rotationally inelastic scattering experiments and calculations, which show that for OH (X) + Ar (section 4.4.2), spin-orbit transfer is comparatively competitive with spin-orbit conserving processes,

whereas spin-orbit transfer for NO (X) + Ar is found to be considerably weaker than spin-orbit conserving transitions [233].

In terms of CN (A) + Ar, the V_{22} component of the difference PES, similar to OH (X)-Ar, is of significant magnitude in the range of the attractive minimum in V_{SUM}. For this reason spin-orbit changing transitions are a significant proportion of all rotational transitions and consequently it may be anticipated that elastic depolarisation is strong. This is consistent with the FMS experimental results [81], but inconsistent with the CN (A) + Ar calculations of elastic depolarisation. CN (A) + Ar also has a third surface (not included in the tensor cross-section calculations) which may influence the dynamics. Indeed electronic energy transfer to CN (X) is possible *via* the V_1 coupling PES and has been shown to be as efficient as RET in previous measurements [20]. It remains unclear at this stage what influence this surface may have on elastic depolarisation.

Despite some significant advances made recently in the subject of collisional depolarisation, further experimental and theoretical investigations are clearly required to fully understand the mechanism of elastic depolarisation and what influences its magnitude.

6.5 Summary

Below are the main conclusions from chapter 6:

i. For OH (A) the rate constant for loss of alignment is larger than orientation for Ar, but not for He: elastic depolarisation is significant for Ar but not for He.

ii. The magnitude of $k_{TCPS}^{(K)}$ values are very similar for OH (X) and OH (A) at low-*j*. This is a reflection that the PESs for the two electronic states have a comparable *range*.

iii. As the rotational level increases the magnitude of $k_{TCPS}^{(K)}$ becomes progressively larger for OH (A) in comparison to OH (X).

iv. There is very good agreement between TCPS measurements and independent ZQBS measurements for OH (A) + Ar.

v. There is also very good agreement between both sets of experiments and QCT scattering calculations.

vi. For OH (A) + Ar 'pure' (quantum state conserving) depolarisation is evaluated to be approx 10 – 20 $Å^2$ for orientation and 15 – 30 $Å^2$ for alignment.

vii. Spin-rotation changing collisions (elastic in *N*) should be considered as elastic depolarisation within the spin spectator model.

viii. For Ar, elastic depolarisation (incl. spin-rotation transfer) is insensitive to initial *N* over the range $N = 1 – 10$, in contrast to that for OH (X) + Ar.

ix. $N = 0$, i.e. $j = 0.5$ does not undergo elastic depolarisation – supportive of the spin-spectator model.

x. The more attractive and anisotropic the PES, the more efficient elastic depolarisation is at higher rotational levels.

Chapter 7

Conclusions and On-going Work

7.1 Summary of Principal Conclusions

It has been demonstrated throughout this thesis that PS is a powerful spectroscopic tool to probe the collisional evolution of rotational angular momentum polarisations, using OH + atomic and molecular partners as comprehensive case studies. The fundamental understanding of depolarising collisions has advanced throughout the course of this research project, not only from the findings of the PS results presented here, but also from independent experimental and theoretical work performed in parallel.

The underlying general conclusion is that depolarising collisions, especially those elastic in nature, are significantly mediated by the attractive parts of the PES. The support for this conclusion stems primarily from the empirical observations that elastic depolarisation is more efficient for Ar than He. This was inferred directly from the difference between the PS measurements for orientation and alignment and also from the comparison of the PS measurements with rigorous QM scattering calculations on the most recent *ab initio* PES. It was shown that the magnitude of elastic depolarisation for OH (X) + Ar most probably ranges up to 20 $Å^2$ for alignment and up to 10 $Å^2$ for orientation. For He, elastic depolarisation is found to be more modest: ≤ 5 $Å^2$. Further support for the role of the attractive forces in elastic depolarisation is provided from the analysis of tensor cross-sections obtained from QM scattering calculations by Dagdigian and Alexander [93,94,174,179]. This showed that for Ar the range of the PES responsible for mediating elastic depolarisation correlates (although not entirely) with the location of attractive minimum. In addition, elastic depolarisation was predicted to have a negative energy dependence. In contrast, the same analysis for He showed that there was no contribution to elastic depolarisation at ranges that correspond

to the attractive well, together with a positive energy dependence for the elastic depolarisation cross-section.

It was also shown for OH (X) that QM predictions of the PS measurements, viewed broadly, were in good agreement with the equivalent rate constants/cross-sections obtained experimentally. However, closer inspection revealed that the calculations failed to quantitatively reproduce the PS measurements. The discrepancies are largest for the lowest rotational levels. It is clear from comparison of the calculation with the measurements that the predictions overestimate the inelastic population transfer component of the PS experiments alone, for both Ar and He. It is also very likely that the elastic depolarisation component is over predicted for both. This highlights residual inaccuracies in the best available PESs.

The magnitude of elastic depolarisation does not seem to increase progressively with the the well depth in the interaction potential. The results of OH (X) + Xe indicate that, instead, the magnitude of the total PS rate constant / cross-section follows the increased *range* of the interaction potential. It is found that the magnitude of elastic depolarisation for Xe, inferred either by the difference between the orientation and alignment measurements, or by the subtraction of the calculated inelastic population transfer component from the PS measurements, was very comparable to that found for Ar, i.e. ~ 10 $Å^2$ for orientation and 20 $Å^2$ for alignment. Comparison of the measurements with the calculated state-to-state rate constants suggests that the elastic depolarisation (mediated by the λ = even terms in a Legendre expansion of the PES), and Λ-doublet transfer (mediated by the λ = odd components) are in competition with one another. The ordering of the even/odd components in the PES seem to match the observation that Λ-doublet transfer is enhanced more than elastic depolarisation for Xe relative to Ar.

For OH (A), elastic depolarisation is found to be more efficient for Ar than He, similar to the behaviour for OH (X). There is excellent agreement between the PS measurements and independent Zeeman quantum beat spectroscopy (ZQBS) measurements and quasi-classical trajectory (QCT) scattering calculations [90] (see chapter 6). Since the electron spin can be reliably treated as a spectator to the collision dynamics for OH (A) (see section 1.1.3), collisional transfer between the closely spaced spin-rotation levels is effectively an elastic reorientation of $\boldsymbol{N}$. Therefore, a fairer comparison of elastic depolarisation between OH (X) and OH (A) may be made using the sum of the 'normal' elastic depolarisation and spin-rotation transfer rate

constants/cross-sections for OH (A). From this point-of-view, the comparatively much more attractive and anisotropic PES for OH (A) leads to an enhancement of elastic depolarisation for the lowest rotational levels. More notable, however, is the difference in *j*- or *N*-dependent trends between the two electronic states. For OH (X), the QM scattering calculations predict that elastic depolarisation decreases rapidly as a function of *j*, whereas for OH (A), elastic depolarisation seems to be largely insensitive to rotational level, across the range $N = 1 - 10$. It is clear that the more anisotropic PES is able to promote elastic depolarisation for larger values of the rotational quantum number.

Elastic depolarisation for OH (X) and OH (A) with Ar as a collision partner are significant collisional processes and are often comparable in magnitude to other inelastic processes. This contradicts models which predict that m_j is conserved in collisional processes and highlights that these models are not applicable when there are appreciable attractive forces between the collision partners.

Comparison of the results of this thesis to those obtained from other collisional systems involving open-shell diatomics made it possible to establish some key features of the interaction which appear to be responsible for elastic depolarisation. First, it is the even components of the PES, expanded in a Legendre series, which promote elastic depolarisation, which are, by definition, parity and rotational-quantum-number-conserving. Second, for significant depolarisation, these components should have appreciable magnitude at ranges of the PES that are accessed at the collision energy of the experiment. Elastic depolarisation is predicted to be strong when the even components are larger than the other anisotropic components for a given separation of collision partners. Third, for Π-states interference between the two adiabatic surfaces seems to influence the magnitude of depolarisation. In particular, the range and sign of the half-difference PES in comparison to the average PES is found to have a significant effect on the magnitude of depolarisation.

For OH (X) + N_2 and O_2 it was difficult to assess the magnitude of depolarisation due to the relatively small data sets and also the lack of QM scattering calculations to complement the experiments. Nonetheless, the PS experiments did uncover interesting differences between the two diatomic colliders. N_2 is found to be significantly more efficient than O_2 in removing the PS signal. This is believed to be primarily due to the larger dipole-quadrupole for OH-N_2 in comparison to OH-O_2. However, the most recent

ab initio calculations for OH-N_2 [197] and OH-O_2 [205,227], at restricted points on the PES, do not seem to reproduce the greater long-range attraction expected for OH (X)-N_2. Although OH (X)-O_2 has a significantly deeper attractive global minimum in the interaction potential, access to this is thought to be hindered by the presence of a barrier, elevated ~ 700 cm^{-1} from the asymptote. Clearly more experimental and theoretical work should be carried out on these systems given the striking differences observed for energy transfer between OH (X) + O_2 and OH (X) + N_2 and their importance to atmospheric chemistry.

Finally, there was very good agreement of the PS measurements with previous line-broadening measurements of various OH spectroscopic bands in the presence of He, Ar and O_2. This comparison demonstrates which collisional properties the line-broadening experiments are sensitive to. For example, the good agreement between few distinct sets of the Ar data suggests that the line broadening experiments must be sensitive to inelastic population transfer as well as elastic depolarisation. There was poor agreement between PS and line-broadening with N_2 as a collision partner. This is perhaps indicative of the line-broadening experiments being sensitive to elastic de-phasing collisions, to which the PS experiment, as implemented in this work, is not sensitive.

Although the research project discussed in this thesis has been comprehensive, there are still a number of avenues that can be explored before this area becomes exhausted. In terms of OH, it would be beneficial to have a more comprehensive study with molecular partners, such as N_2, O_2 and H_2. A key challenge here is to build on current theoretical descriptions of these systems, towards full-dimensional PESs and performing exact QM scattering calculations. This would greatly assist the interpretation of experiments which cannot resolve different collisional processes, such as PS measurements or line-broadening studies. Experiments which are sensitive to elastic depolarisation, as well as other inelastic processes, for example RET, serve to test the full-range of the best available PESs.

In terms of rotational angular momentum depolarisation, it would be interesting to measure the efficiency of depolarisation as a result of inelastic energy transfer for OH in collisions with Rg atoms. This has been investigated for CN (A) + Ar [81] and also NO (A) + Ar [87]. This is amenable to PS and preliminary data has been collected for OH (X/A) + He and Ar during the project discussed in this thesis. To do this the pump laser is used, as usual, to generate a rotational polarisation in the quantum states connected by

the transition. The probe laser may be tuned to a spectroscopic line which is resonant with a rotational level which neighbours one of the levels that is resonant with the pump laser. This approach is similar to that used to measure state-to-state RET. However, because the PS experiment is sensitive to the bulk polarisation of the sample then a PS signal would be generated only if there is population transfer between the pumped and probed levels with *retention* of polarisation. Qualitatively, very little retention of polarisation was observed. A more quantitative analysis would provide an additional test of the PES and a more complete picture of the collision dynamics.

7.2 Current Focus: NO (X) +Ar

The most recent focus of the PS experiments has been on measurements of the NO (X) + Ar system. A 'V-shaped' TCPS spectroscopic scheme was employed to monitor the collisional evolution of NO (X, $v = 0$, j) rotational polarisations. The primary motivation for this work was to make the comparison between two kinematically distinct collision systems (NO (X) + Ar and OH (X) + Ar), which have a relatively similar PESs [18,144,234]. For these measurements, the pump laser was centred on the $A - X$ (0,0) electronic band (~ 226 nm) and the probe was centred on the $A - X$ (1,0) electronic band (~ 214 nm). Selected members of the $P_1(j)$ and $Q_1(j)$ spectroscopic branches were used, for orientation and alignment measurements, respectively. Consequently, the TCPS measurements were sensitive to the rotational orientation of NO (X, $v = 0$, j e) or the rotational alignment of NO (X, $v = 0$, j f). NO was transferred into the vacuum chamber directly from its cylinder *via* a mass flow controller (MFC). The use of a MFC, and also the fact that there was no photolytic production step, meant that partial pressure of NO was much more stable as a function of time. The experimental methodology used to measure $k_{TCPS}^{(K)}$ was otherwise similar to that used in all other work in this thesis (see chapter 3 and section 4.3).

7.2.1 Results

$k_{TCPS}^{(K)}$ values were measured for two different rotational levels (j = 6.5 and 14.5) and for both $K = 1$ and $K = 2$. Example TCPS decay traces are presented in figure 7.1. It should be noted that, although there are nuclear hyperfine quantum beats for a polarised NO ensemble ($I = 1$ for ^{14}N), they are not resolved by the TCPS experiment. Plots of the

measured TCPS decay rate, $\Gamma_{TCPS}^{(K)}$, *versus* collision partner number density are shown in figure 7.2. As usual, the slopes of the linear fit to the data are equal to $k_{TCPS}^{(K)}$. The values obtained from these measurements are collected in table 7-1.

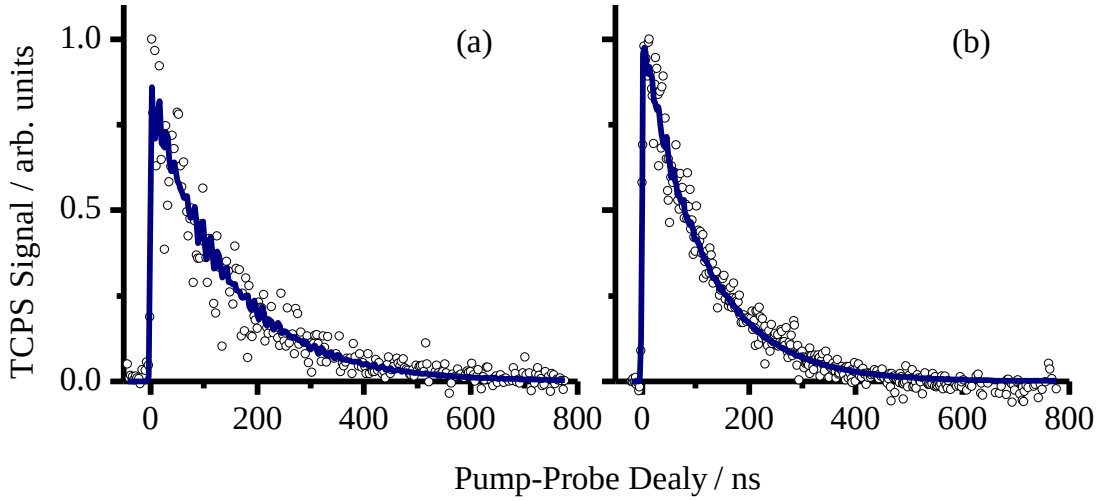

Figure 7.1: *TCPS decay traces for NO (A) + Ar. The pump laser polarisation was linear. (a) j = 6.5 and (b) j = 14.5. The open circles represent the acquired experimental data and the solid lines represent the fit to the data using the TCPS theoretical treatment [72]. For these decay traces the partial pressure of Ar was approximately 200 -300 mTorr.*

An interesting observation from figure 7.2 is that the zero-pressure intercept is substantially lower in comparison to the OH (X/A) + Ar measurements (see figures 4.14, 4.15 and 6.5). This must suggest that NO (X) + NO self collisions are very weak at promoting inelastic energy transfer and also elastic depolarisation, with the dominant loss processes likely to be fly-out of NO from the laser beam volume. It should be reminded that the OH precursor was a HNO_3/H_2O mixture and necessarily present at higher partial pressures than NO that was used here.

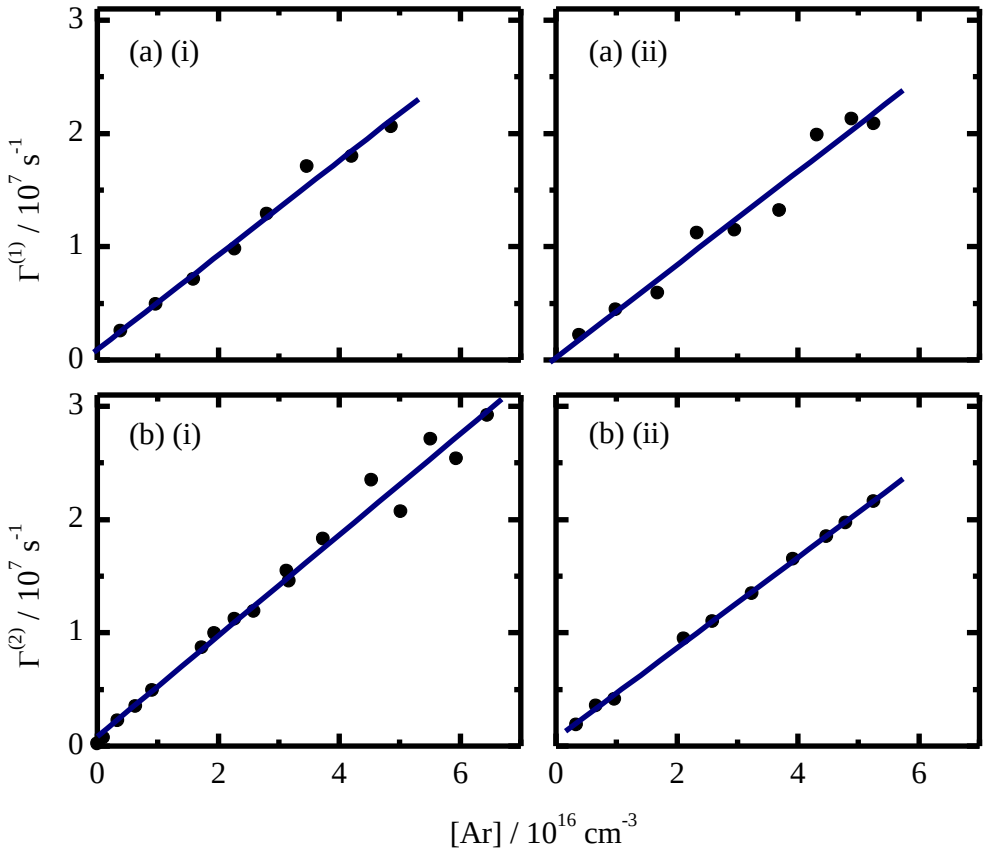

Figure 7.2: *TCPS decay rates as a function of Ar number density for (a) orientation (K = 1) and (b) alignment (K = 2). The filled circles represent the measured decay rates for a given collision partner number density and the colour-coordinated solid lines are linear regression fits to the data points. The slope of these fits yields the bimolecular rate constant,* $k_{TCPS}^{(K)}$ *. Plots are shown for (i) j = 6.5 and (ii) j = 14.5.*

Table 7-4: *NO (X) + Ar TCPS decay rate constants,* $k_{TCPS}^{(K)}$ *(in units of* 10^{-10} cm^3 s^{-1}*), and thermally averaged cross-sections,* $\sigma_{TCPS}^{(K)}$ *(in units of* $Å^2$*,) for loss of orientation (K =1) and of alignment, (K = 2) with associated 2σ statistical uncertainties. Experiments performed at room temperature (nominally 298 K).*

	$k_{\mathrm{TCPS}}^{(1)}$	$\sigma_{\mathrm{TCPS}}^{(1)}$	$k_{\mathrm{TCPS}}^{(2)}$	$\sigma_{\mathrm{TCPS}}^{(2)}$
j* = 6.5 *e	*4.17 ± 0.40*	*67.14 ± 6.44*		
j* = 6.5 *f			*4.46 ± 0.28*	*71.81 ± 4.51*
j* = 14.5 *e	*4.12 ± 0.60*	*66.33 ± 9.66*		
j* = 14.5 *f			*3.93 ± 0.20*	*63.27 ± 3.22*

The interesting features of figure 7.2 are the values of $k_{TCPS}^{(K)}$ quoted in table 7-1. Direct comparison between the orientation and alignment measurements is difficult because they are not a measure of a common rotational quantum state. However, very recent QM scattering calculations by Dagdigian and Alexander [235] on NO (X, v = 0) + Ar (which are compared to the TCPS measurements below) suggest that the rate constants for RET, Λ-doublet transfer and elastic depolarisation are not too dissimilar for the two Λ-doublet levels of the same j. However, to make the initial comparison easier, it will be assumed that, for NO(X) + Ar, the measured $k_{TCPS}^{(K)}$ values are independent of Λ-doublet level.

As noted in the previous chapters, the difference between orientation and alignment (i.e. $k_{TCPS}^{(2)}$ - $k_{TCPS}^{(1)}$) provides an indication of the magnitude of elastic depolarisation. For j = 6.5 this difference is equal to + 0.29 cm^3 s^{-1} and for j = 14.5 it is equal to (- 0.19) cm^3 s^{-1}. (Note that these differences are lower than the combined experimental uncertainties!) The negative value for j = 14.5, which suggests that orientation is destroyed faster than alignment, is quite unlikely. This is perhaps especially true for higher rotational levels approaching a classical limit. It is however consistent with elastic depolarisation being modest, requiring particularly accurate measurement of $k_{TCPS}^{(K)}$ to reveal it correctly.

As also discussed in section 4.5.3, an alternative method to assess the magnitude of elastic depolarisation is to compare measured $k_{TCPS}^{(K)}$ values to known values for inelastic population transfer, k_{POP}. Smith and co-workers [233,236] have measured state-to-state RET rate constants, excluding Λ-doublet transfer, for NO ($X^2\Pi_{1/2}$, v = 2, j = 7.5 e, 20.5 e, 31.5 e and 40.5 e). None of these quantum states match those measured here. However, the value for k_{RET} (i.e. sum of the measured state-to-state rate constants) for j = 7.5, which is the closest to the TCPS measurements presented in this section, was measured to be 3.4 x 10^{-10} cm^3 s^{-1}. Assuming that there is no significant variation of k_{RET} between j = 6.5 and 7.5, and also no variation between vibrational levels, then this would require that (k_{Λ} + $k_{DEP}^{(1)}$) is equal to 0.77 x 10^{-10} cm^3 s^{-1}, for j = 6.5, to match $k_{TCPS}^{(1)}$ = 4.17 x 10^{-10} cm^3 s^{-1}. It is not possible to resolve (k_{Λ} + $k_{DEP}^{(1)}$) further. This comparison suggests that Λ-doublet transfer and elastic depolarisation are relatively

inefficient in comparison to RET and that RET is therefore the dominant collisional process measured by TCPS for NO (X) + Ar.

Perhaps a better evaluation of $k_{DEP}^{(K)}$ can be made by comparing the TCPS measurements to recent QM scattering calculations [235] of NO (X, v = 0, j) + Ar. Figure 7.2 presents this comparison. The total height of the coloured bars represents a prediction of the TCPS measurement, decomposed into sub-components representing the collisional processes to which the TCPS measurements are sensitive overall. It is clear from this figure that the QM scattering calculations significantly under-predict the TCPS measurements. This is most likely an indication that the PES used in the calculations [234], is not accurate, which is an important conclusion given that these experiments are the best available test of the PES for this important system.

Regardless of the discrepancies of the absolute magnitude with experiments, the QM calculations indicates that the TCPS are likely to be dominated by RET, which is consistent with the experimental difference between orientation and alignment values of the same j (but, different Λ-doublets) being small. This is in contrast to the OH (X) + Ar system investigated comprehensively in this thesis (see chapter 4), where elastic depolarisation is significant, especially at low-j. However, the *total* TCPS rate-constants are substantially larger for NO (X) + Ar in comparison to OH (X) + Ar.

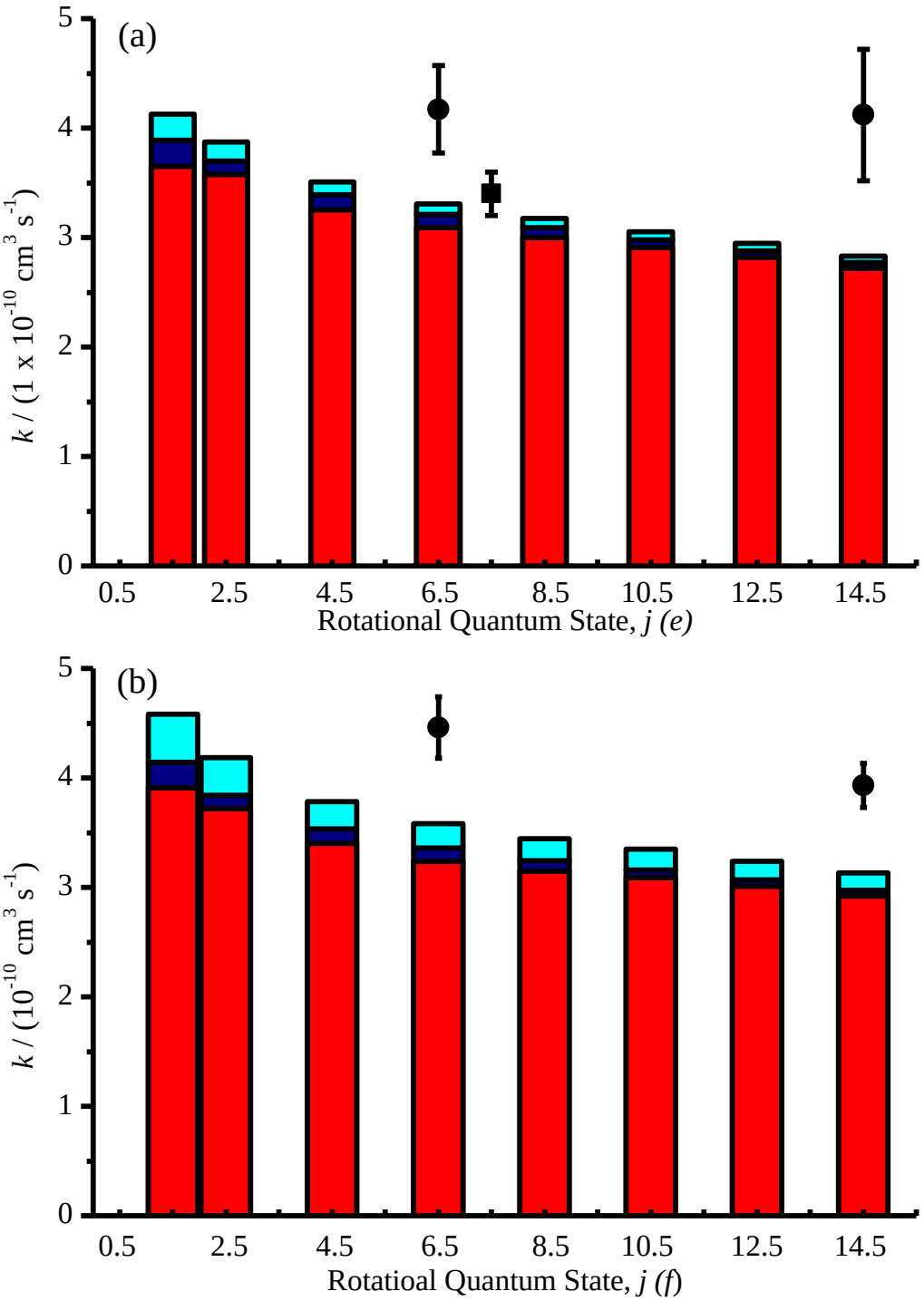

Figure 7.3: *Thermal (298 K) rate constants for NO (X, v = 0, j). QM predictions [235] are shown for* k_{RET} *(red),* k_{Λ} *(navy) and* $k_{DEP}^{(K)}$ *(cyan). Measured* $k_{TCPS}^{(K)}$ *values are shown (filled circles) with their corresponding statistical uncertainties. An independent measurement of* k_{RET} *is also shown for NO (X, v = 2, j = 7.5) ([233] Smith and co-workers, squares). (a) K = 1 (orientation) and (b) K = 2 (alignment).*

7.3 Future Directions

Future directions of this research area might be expected to be further evaluation of depolarisation for rotational orientation and alignment distributions and comparing the results to rigorous QM scattering calculations on the most recent *ab initio* PESs. Techniques which allow the independent measurement of inelastic population transfer and depolarisation provide a promising test of current theoretical descriptions. One particular experimental method which makes this possible is frequency-modulated spectroscopy (FMS). Initial results measuring the depolarisation of CN (A) + Ar using this technique [81] has already been discussed alongside the results of the work in this thesis (see section 6.4.5). One of the disadvantages of the experimental set-up used in the FMS work so far was the restriction to measuring rotational alignments and not orientations. Costen and co-workers are now re-configuring their experimental approach to make the measurement of rotational orientations possible.

A more comprehensive study of NO (X) + Ar, than that presented in this chapter, would also be of interest, not only for the direct comparison to the QM calculations of Dagdigian and Alexander, but also the measurements of Brouard and co-workers on NO (A) +Ar [87]. Investigating other diatomic molecules would be advantageous in-order to understand better what dictates the efficiency of various collisional processes. Promising candidates include NH and CH.

Bibliography

[1] A. Schiffman and D. W. Chandler, *International Reviews in Physical Chemistry* **14** (2), 371 (1995).

[2] M. L. Costen, S. Marinakis, and K. G. McKendrick, *Chem. Soc. Rev.* **37**, 732 (2008).

[3] R. P. Wayne, *Chemistry of the Atmospheres*, Third ed. (Oxford University Press, Oxford, 2002).

[4] C. J. Hayes, J. K. Merle, and C. M. Hadad, in *Advances in Physical Organic Chemistry, Vol 43* (Academic Press Ltd-Elsevier Science Ltd, London, 2009), Vol. 43, pp. 79.

[5] A. K. Bertram, A. V. Ivanov, M. Hunter, L. T. Molina, and M. J. Molina, *Journal of Physical Chemistry A* **105** (41), 9415 (2001).

[6] G. J. Minkoff and C. F. H. Tipper, *Chemistry of Combustion Reactions*. (Butterworth and Co, London, 1962).

[7] Q. V. Nguyen and P. H. Paul, *Applied Physics B-Lasers and Optics* **72** (4), 497 (2001).

[8] M. Elitzur, *Reviews of Modern Physics* **54** (4), 1225 (1982).

[9] J. Luque, LIFBASE 2.0: a database and spectral simulation programme for diatomic molecules (SRI).

[10] J. Luque and D. R. Crosley, *Journal of Chemical Physics* **109** (2), 439 (1998).

[11] J. Brown and A. Carrington, *Rotational spectroscopy of diatomic molecules*. (Cambridge University Press, Cambridge, 2003).

[12] J. B. a. A. Carrington, *Rotational Spectroscopy of Diatomic Molecules*. (Cambridge University Press, Cambridge, 2003).

[13] M. H. Alexander*et al.*, *Journal of Chemical Physics* **89** (4), 1749 (1988).

[14] G. Parlant and D. R. Yarkony, *Journal of Chemical Physics* **110** (1), 363 (1999).

[15] A. Degli Esposti, A. Berning, and H.-J. Werner, *J. Chem. Phys.* **103**, 2067 (1995).

[16] A. Degli Esposti and H.-J. Werner, *J. Chem. Phys.* **93**, 3351 (1990).

[17] J. Klos, M. H. Alexander, M. Brouard, C. J. Eyles, and F. J. Aoiz, *Journal of Chemical Physics* **129** (5), 054301 (2008).

[18] G. Paterson, S. Marinakis, M. L. Costen, K. G. McKendrick, J. Klos, and R. Tobola, *Journal of Chemical Physics* **129** (7), 074304 (2008).

[19] R. N. Zare, *Angular Momentum: Understanding Spatial Aspects in Chemistry and Physics*. (John Wiley & Sons, Inc., New York, 1988).

[20] P. J. Dagdigian, *Annual Review of Physical Chemistry* **48**, 95 (1997).

[21] A. J. McCaffery, Z. T. Alwahabi, M. A. Osborne, and C. J. Williams, *Journal of Chemical Physics* **98** (6), 4586 (1993).

[22] M. A. Osborne and A. J. McCaffery, *Journal of Chemical Physics* **101** (7), 5604 (1994).

[23] H. J. Crichton, C. Murray, and K. G. McKendrick, *Physical Chemistry Chemical Physics* **4** (23), 5768 (2002).

[24] M. H. Alexander, *Journal of Chemical Physics* **76** (12), 5974 (1982).

[25] P. J. Dagdigian, M. H. Alexander, and K. Liu, *Journal of Chemical Physics* **91** (2), 839 (1989).

[26] M. H. Alexander, *Journal of Chemical Physics* **76** (7), 3637 (1982).

[27] M. H. Alexander*et al.*, HIBRIDON: a package of programs for the time-independent quantum treatment of inelastic collisions and photodissociation.

[28] G. C. Corey and F. R. McCourt, *Journal of Physical Chemistry* **87** (15), 2723 (1983).

[29] F. J. Aoiz, M. Brouard, C. J. Eyles, J. Kłos, and M. P. d. Miranda, *Journal of Chemical Physics* **130** (4), 044305 (2009).

[30] D. Stepowski and M. J. Cottereau, *Journal of Chemical Physics* **74** (12), 6674 (1981).

[31] E. W. Rothe, Y. Gu, A. Chryssostomou, P. Andresen, and F. Bormann, *Applied Physics B-Lasers and Optics* **66** (2), 251 (1998).

[32] J. W. Daily and E. W. Rothe, *Applied Physics B-Lasers and Optics* **68** (1), 131 (1999).

[33] K. Schreel, J. Schleipen, A. Eppink, and J. J. Ter meulen, *Journal of Chemical Physics* **99** (11), 8713 (1993).

[34] R. K. Lengel and D. R. Crosley, *Journal of Chemical Physics* **67** (5), 2085 (1977).

[35] R. G. Macdonald and K. P. Liu, *Journal of Chemical Physics* **97** (2), 978 (1992).

[36] A. Jorg, U. Meier, and K. Kohsehoinghaus, *Journal of Chemical Physics* **93** (9), 6453 (1990).

[37] M. Drabbels, A. M. Wodtke, M. Yang, and M. H. Alexander, *Journal of Physical Chemistry A* **101** (36), 6463 (1997).

[38] J. J. Kay, G. Paterson, K. Strecker, M. L. Costen, K. G. McKendrick, and D. W. Chandler, *Journal of Chemical Physics*, Submitted (2010).

[39] R. G. Macdonald and K. Liu, *Journal of Chemical Physics* **91** (2), 821 (1989).

[40] J. J. Gilijamse, S. Hoekstra, S. Y. T. van der Meerakker, G. C. Groenenboom, and G. Meijer, *Science* **313**, 1617 (2006).

[41] K. Wohlfart, F. Filsinger, F. Gratz, J. Kupper, and G. Meijer, *Physical Review A* **78** (3) (2008).

[42] D. A. V. Kliner and R. L. Farrow, *Journal of Chemical Physics* **110** (1), 412 (1999).

[43] P. J. Dagdigian, edited by K. Liu and A. Wagner (World Science, Singapore, 1995, pp. 315-364), pp. 315.

[44] H. P. Broida and T. Carrington, *Journal of Chemical Physics* **38**, 136 (1963).

[45] J. C. Polanyi and K. B. Woodall, *Journal of Chemical Physics* **56**, 1563 (1971).

[46] H. Joswig, P. Andresen, and R. Schinke, *Journal of Chemical Physics* **85**, 1904 (1986).

[47] J. H. Guo, A. Ali, and P. J. Dagdigian, *Journal of Chemical Physics* **85** (12), 7098 (1986).

[48] H. Joswig, P. Andresen, and R. Schinke, *Journal of Chemical Physics* **85** (4), 1904 (1986).

[49] A. Degli Esposti, H.-J. Werner, and A. Jorg, *Journal of Chemical Physics* **93**, 8757 (1990).

[50] R. Kienle, A. Jörg, and Kohse-Höinghaus, *Appl. Phys. B* **56**, 249 (1993).

[51] T. A. Caughey and D. R. Crosley, *Journal of Chemical Physics* (69), 3379 (1978).

[52] T. A. Caughey and D. R. Crosley, *Journal of Chemical Physics* **71**, 736 (1979).

[53] P. J. Dagdigian and S. J. Bullman, *Journal of Chemical Physics* **82**, 1341 (1985).

[54] S. J. Bullman and P. J. Dagdigian, *Journal of Chemical Physics* **81**, 3347 (1984).

[55] M. C. van Beek and J. J. ter Meulen, *Journal of Chemical Physics* **115** (4), 1843 (2001).

[56] A. J. Alexander, M. Brouard, K. S. Kalogerakis, and J. P. Simons, *Chem. Soc. Rev.* **27**, 405 (1998).

[57] A. J. Orr-Ewing and R. N. Zare, *Annu. Rev. Phys. Chem.* **45**, 315 (1994).

[58] D. W. Chandler and P. L. Houston, *Journal of Chemical Physics* **87** (2), 1445 (1987).

[59] A. Eppink and D. H. Parker, *Review of Scientific Instruments* **68** (9), 3477 (1997).

[60] D. H. Parker and A. Eppink, *Journal of Chemical Physics* **107** (7), 2357 (1997).

[61] J. A. Davies, R. E. Continetti, D. W. Chandler, and C. C. Hayden, *Physical Review Letters* **84** (26), 5983 (2000).

[62] K. L. Reid, *Annual Review of Physical Chemistry* **54**, 397 (2003).

[63] E. A. Wade, K. T. Lorenz, D. W. Chandler, J. W. Barr, G. L. Barnes, and J. I. Cline, *Chemical Physics* **301** (2-3), 261 (2004).

[64] K. Thomas Lorenz, D. W. Chandler, J. W. Barr, W. Chen, G. L. Barnes, and J. I. Cline, *Science* **293**, 2063 (2001).

[65] J. I. Cline, K. T. Lorenz, E. A. Wade, J. W. Barr, and D. W. Chandler, *Journal of Chemical Physics* **115** (14), 6277 (2001).

[66] A. Gijsbertsen, H. Linnartz, and S. Stolte, *J. Chem. Phys.* **125**, 133112 (2006).

[67] C. A. Taatjes, A. Gijsbertsen, M. J. L. de Lange, and S. Stolte, *J. Phys. Chem. A* **111**, 7631 (2007).

[68] A. Gijsbertsen, H. Linnartz, J. Kłos, and S. Stolte, *Phys. Scr.* **72**, 1 (2005).

[69] M. C. van Beek, J. J. ter Meulen, and M. H. Alexander, *Journal of Chemical Physics* **113** (2), 637 (2000).

[70] M. C. van Beek, G. Berden, H. L. Bethlem, and J. J. ter Meulen, *Physical Review Letters* **86** (18), 4001 (2001).

[71] M. L. Costen, H. J. Crichton, and K. G. McKendrick, *J. Chem. Phys.* **120**, 7910 (2004).

[72] M. L. Costen and K. G. McKendrick, *J. Chem. Phys.* **122**, 164309 (2005).

[73] A. J. McCaffery, M. J. Proctor, and B. J. Whitaker, *Annual Review of Physical Chemistry* **37**, 223 (1986).

[74] V. Khare, D. J. Kouri, and D. K. Hoffman, *J. Chem. Phys.* **76**, 4493 (1982).

[75] D. J. Kouri and Y. Shimoni, *J. Chem. Phys.* **67**, 86 (1977).

[76] G. O. Sitz and R. L. Farrow, *Journal of Chemical Physics* **101**, 4682 (1994).

[77] G. O. Sitz and R. L. Farrow, *Journal of Chemical Physics* **103**, 489 (1995).

[78] A. D. Rudert, J. Martin, W. B. Gao, J. B. Halpern, and H. Zacharias, *Journal of Chemical Physics* **111** (21), 9549 (1999).

[79] J. B. Halpern, R. Dopheide, and H. Zacharias, *Astrophys. Space Sci.* **236**, 19 (1996).

[80] J. B. Halpern, R. Dopheide, and H. Zacharias, *Journal of Physical Chemistry* **99** (37), 13611 (1995).

[81] I. Ballingall, M. F. Rutherford, K. G. Mckendrick, and M. L. Costen, *Molecular Physics* **108**, 847 (2010).

[82] S. J. Silvers, R. A. Gottscho, and R. W. Field, *Journal of Chemical Physics* **74** (11), 6000 (1981).

[83] L. D. Snow, R. N. Compton, and J. C. Miller, *Journal of Chemical Physics* **88** (3), 1652 (1988).

[84] P. Bréchignac, A. Picard-Bersellini, and R. Charneau, *J. Phys. B: Atom. Molec. Phys.* **13**, 135 (1980).

[85] C. D. Pibel and C. B. Moore, *Journal of Chemical Physics* **93** (7), 4804 (1990).

[86] A. D. Rudert, J. Martin, W. B. Gao, H. Zacharias, and J. B. Halpern, *Journal of Chemical Physics* **112** (22), 9749 (2000).

[87] M. Brouard*et al.*, *Journal of Chemical Physics* **131** (10) (2009).

[88] M. Brouard*et al.*, *Molec. Phys.* **103**, 1693 (2005).

[89] M. Brouard*et al.*, *Journal of Chemical Physics* **130** (4), 044306 (2009).

[90] M. L. Costen*et al.*, *Journal of Physical Chemistry A* **113** (52), 15156 (2009).

[91] M. L. Costen and K. G. McKendrick (Private Communication).

[92] K. Blum, *Density Matrix Theory and Applications*, Second ed. (Plenum Press, New York, 1996).

[93] P. J. Dagdigian and M. H. Alexander, *Journal of Chemical Physics* **130** (16), 164315 (2009).

[94] P. J. Dagdigian and M. H. Alexander, *The Journal of Chemical Physics* **130** (9), 094303 (2009).

[95] C. Wieman and T. W. Hansch, *Physical Review Letters* **36** (20), 1170 (1976).

[96] W. Demtröder, *Laser Spectroscopy*. (Springer-Verlag, Berlin, 1981).

[97] R. Teets, R. Feinberg, T. W. Hansch, and A. L. Schawlow, *Physical Review Letters* **37** (11), 683 (1976).

[98] R. E. Teets, F. V. Kowalski, W. T. Hill, N. Carlson, and T. W. Hansch, *Laser Spectroscopy* **113**, 80 (1977).

[99] J. W. Walewski, K. Nyholm, A. Dreizler, and M. Alden, *Applied Spectroscopy* **58** (2), 238 (2004).

[100] K. Danzmann, K. Grutzmacher, and B. Wende, *Physical Review Letters* **57** (17), 2151 (1986).

[101] M. J. New, P. Ewart, A. Dreizler, and T. Dreier, *Applied Physics B-Lasers and Optics* **65** (4-5), 633 (1997).

[102] W. G. Tong and E. S. Yeung, *Analytical Chemistry* **57** (1), 70 (1985).

[103] G. Zizak, J. Lanauze, and J. D. Winefordner, *Applied Optics* **24** (20), 3319 (1985).

[104] K. Nyholm, R. Maier, C. G. Aminoff, and M. Kaivola, *Applied Optics* **32** (6), 919 (1993).

[105] K. Nyholm, *Optics Communications* **111** (1-2), 66 (1994).

[106] K. Nyholm, R. Fritzon, and M. Alden, *Optics Letters* **18** (19), 1672 (1993).

[107] B. Lofstedt, R. Fritzon, and M. Alden, *Applied Optics* **35** (12), 2140 (1996).

[108] B. Lofstedt and M. Alden, *Optics Communications* **124** (3-4), 251 (1996).

[109] A. A. Suvernev, A. Dreizler, T. Dreier, and J. Wolfrum, *Applied Physics B-Lasers and Optics* **61** (5), 421 (1995).

[110] A. Dreizler, T. Dreier, and J. Wolfrum, *Journal of Molecular Structure* **349**, 285 (1995).

[111] Z. T. Alwahabi, Z. S. Li, J. Zetterberg, and M. Alden, *Optics Communications* **233** (4-6), 373 (2004).

[112] S. Roy, R. P. Lucht, and A. McIlroy, *Applied Physics B-Lasers and Optics* **75** (8), 875 (2002).

[113] Z. S. Li, M. Rupinski, J. Zetterberg, Z. T. Alwahabi, and M. Alden, *Chemical Physics Letters* **407** (4-6), 243 (2005).

[114] Z. S. Li, M. Rupinski, J. Zetterberg, Z. T. Alwahabi, and M. Alden, *Applied Physics B-Lasers and Optics* **79** (2), 135 (2004).

[115] T. B. Settersten, R. L. Farrow, and J. A. Gray, *Chemical Physics Letters* **370** (1-2), 204 (2003).

[116] K. Nyholm, R. Fritzon, N. Georgiev, and M. Alden, *Optics Communications* **114** (1-2), 76 (1995).

[117] C. F. Kaminski, B. Lofstedt, R. Fritzon, and M. Alden, *Optics Communications* **129** (1-2), 38 (1996).

[118] J. Kiefer, Z. S. Li, J. Zetterberg, M. Linvin, and M. Alden, *Optics Communications* **270** (2), 347 (2007).

[119] A. Dreizler, R. Tadday, A. A. Suvernev, M. Himmelhaus, T. Dreier, and P. Foggi, *Chemical Physics Letters* **240** (4), 315 (1995).

[120] X. L. Chen, B. D. Patterson, and T. B. Settersten, *Chemical Physics Letters* **388** (4-6), 358 (2004).

[121] X. L. Chen and T. B. Settersten, *Applied Optics* **46** (19), 3911 (2007).

[122] H. J. Crichton, M. L. Costen, and K. G. McKendrick, *J. Chem. Phys.* **119**, 9461 (2003).

[123] G. Richmond, PhD Thesis, Heriot-Watt University, 2005.

[124] H. J. Crichton, PhD Thesis, Heriot-Watt University, 2004.

[125] M. Brouard, R. Cireasa, A. P. Clark, F. Quadrini, and C. Vallance, *Physical Chemistry Chemical Physics* **8** (47), 5549 (2006).

[126] A. A. Turnipseed, G. L. Vaghjiani, J. E. Thompson, and A. R. Ravishankara, *Journal of Chemical Physics* **96** (8), 5887 (1992).

[127] A. Schiffman, D. D. Nelson, and D. J. Nesbitt, *Journal of Chemical Physics* **98** (9), 6935 (1993).

[128] G. H. Leu, C. W. Hwang, and I. C. Chen, *Chemical Physics Letters* **257** (5-6), 481 (1996).

[129] A. Jacobs, K. Kleinermanns, H. Kuge, and J. Wolfrum, *Journal of Chemical Physics* **79** (6), 3162 (1983).

[130] G. H. Dieke and H. M. Crosswhite, *Journal of Quantitative Spectroscopy & Radiative Transfer* **2**, 97 (1962).

[131] S. Marinakis, G. Paterson, G. Richmond, M. Rockingham, M. L. Costen, and K. G. McKendrick, *J. Chem. Phys.* **128**, 021101 (2008).

[132] U. Fano and J. H. Macek, *Reviews of Modern Physics* **45** (4), 553 (1973).

[133] R. Wallenstein, J. A. Paisner, and A. L. Schawlow, *Physical Review Letters* **32**, 1333 (1974).

[134] M. Brouard, H. Chadwick, Y. P. Chang, R. Cireasa, and C. J. Eyles, *Physica Scripta* **80** (4) (2009).

[135] M. S. Ltd.

[136] K. M. Hickson, C. M. Sadowski, and I. W. M. Smith, *Physical Chemistry Chemical Physics* **4** (22), 5613 (2002).

[137] K. M. Hickson, C. M. Sadowski, and I. W. M. Smith, *Journal of Physical Chemistry A* **106** (36), 8442 (2002).

[138] S. McLean, S. Macmillan, S. Muas, V. Lesur, A. Thomson, and D. Dater, The US/UK World Magnetic Model for 2005-2010 Report No. NESDIS/NGDC-1, (unpublished).

[139] H. Radford, *Physical Reviews* **122**, 114 (1961).

[140] H. Meyer, *Journal of Chemical Physics* **102**, 3151 (1995).

[141] S. Marinakis, G. Paterson, J. Klos, M. L. Costen, and K. G. McKendrick, *Physical Chemistry Chemical Physics* **9** (31), 4414 (2007).

[142] G. Paterson, S. Marinakis, J. Klos, M. L. Costen, and K. G. McKendrick, *Physical Chemistry Chemical Physics* **11** (39), 8804 (2009).

[143] G. Paterson, S. Marinakis, M. L. Costen, and K. G. McKendrick, *Physica Scripta* **80** (4) (2009).

[144] G. Paterson, S. Marinakis, M. L. Costen, K. G. McKendrick, J. Klos, and R. Tobola, *Journal of Chemical Physics* **131** (15) (2009).

[145] M. T. Berry, M. R. Brustein, J. R. Adamo, and M. I. Lester, *Journal of Physical Chemistry* **92** (20), 5551 (1988).

[146] M. T. Berry, M. R. Brustein, and M. I. Lester, *Chemical Physics Letters* **153** (1), 17 (1988).

[147] K. M. Beck, M. T. Berry, M. R. Brustein, and M. I. Lester, *Chemical Physics Letters* **162** (3), 203 (1989).

[148] M. T. Berry, M. R. Brustein, and M. I. Lester, *Journal of Chemical Physics* **90** (10), 5878 (1989).

[149] M. T. Berry, M. R. Brustein, and M. I. Lester, *Journal of Chemical Physics* **92** (11), 6469 (1990).

[150] W. M. Fawzy and M. C. Heaven, *Journal of Chemical Physics* **89** (11), 7030 (1988).

[151] W. M. Fawzy and M. C. Heaven, *Journal of Chemical Physics* **92** (2), 909 (1990).

[152] M. C. Heaven, *Int. Rev. Phys. Chem.* **24**, 375 (2005).

[153] J. Klos*et al.*, *Journal of Chemical Physics* **112** (11), 4952 (2000).

[154] R. T. Bonn, M. D. Wheeler, and M. I. Lester, *Journal of Chemical Physics* **112** (11), 4942 (2000).

[155] M. T. Berry, M. R. Brustein, M. I. Lester, C. Chakravarty, and D. C. Clary, *Chemical Physics Letters* **178** (2-3), 301 (1991).

[156] Y. Sumiyoshi, I. Funahara, K. Sato, Y. Ohshima, and Y. Endo, *J. Chem. Phys.* **125**, 124307 (2006).

[157] J. Han and M. C. Heaven, *J. Chem. Phys.* **123**, 064307 (2005).

[158] A. Vegiri and S. C. Farantos, *Journal of Physical Chemistry* **92** (10), 2723 (1988).

[159] H.-S. Lee, A. B. McCoy, R. R. Toczyłowski, and S. M. Cybulski, *J. Chem. Phys.* **113**, 5736 (2000).

[160] M. C. van Beek, J. J. ter Meulen, and M. H. Alexander, *Journal of Chemical Physics* **113** (2), 628 (2000).

[161] K. Schreel and J. J. ter Meulen, *J. Phys. Chem. A* **101**, 7639 (1997).

[162] L. Scharfenberg, J. Klos, P. J. Dagdigian, M. H. Alexander, G. Meijer, and S. Y. T. Van De Meerakker, *Physical Chemistry Chemical Physics* **12**, 10660 (2010).

[163] I. J. Wysong, J. B. Jeffries, and D. R. Crosley, *Journal of Chemical Physics* **94** (11), 7547 (1991).

[164] K. M. Hickson, C. M. Sadowski, and I. W. M. Smith, *Phys. Chem. Chem. Phys.* **4**, 5613 (2002).

[165] J. J. Termeulen, W. A. Majewski, W. L. Meerts, and A. Dymanus, *Chemical Physics Letters* **94** (1), 25 (1983).

[166] T. H. Dunning Jr, *J. Chem. Phys.* **90**, 1007 (1989).

[167] R. A. Kendall, T. H. Dunning Jr, and R. J. Harrison, *J. Chem. Phys.* **96**, 6796 (1992).

[168] S. F. Boys and F. Bernardi, *Mol. Phys.* **19**, 553 (1970).

[169] H. J. Werner*et al.*, MOLPRO: a package of *ab initio* computer programs.

[170] D. E. Manolopoulos, *J. Chem. Phys.* **85**, 6425 (1986).

[171] G. A. Raiche, J. B. Jeffries, K. J. Rensberger, and D. R. Crosley, *Journal of Chemical Physics* **92** (12), 7258 (1990).

[172] L. R. Williams and D. R. Crosley, *J. Chem. Phys.* **104**, 6507 (1996).

[173] R. K. Lengel and D. R. Crosley, *Journal of Chemical Physics* **68** (12), 5309 (1978).

[174] P. J. Dagdigian and M. H. Alexander, *Journal of Chemical Physics* **131** (22), 229902 (2009).

[175] P. J. Dagdigian and M. H. Alexander, *Journal of Chemical Physics*, submitted for publication (2009).

[176] T. P. Rakitzis, *Physical Review Letters* **94** (8) (2005).

[177] L. Rubio-Lago, D. Sofikitis, A. Koubenakis, and T. P. Rakitzis, *Physical Review A* **74** (4) (2006).

[178] D. Sofikitis*et al.*, *Physical Review A* **76** (2007).

[179] P. J. Dagdigian and M. H. Alexander, *Journal of Chemical Physics* **130** (20), 204304 (2009).

[180] R. Tadday, A. Dreizler, A. A. Suvernev, and T. Dreier, *Journal of Molecular Structure* **410**, 85 (1997).

[181] H. R. Mayne and M. Keil, *Journal of Physical Chemistry* **88** (5), 883 (1984).

[182] G. Paterson, S. Marinakis, M. L. Costen, and K. G. McKendrick, *Physical Chemistry Chemical Physics* **11** (39), 8813 (2009).

[183] P. H. Paul, J. L. Durant Jr., J. A. Gray, and M. R. Furlanetto, *J. Chem. Phys.* **102**, 8378 (1995).

[184] I. J. Wysong, J. B. Jeffries, and D. R. Crosley, *Journal of Chemical Physics* **92** (9), 5218 (1990).

[185] B. L. Hemming, D. R. Crosley, J. E. Harrington, and V. Sick, *Journal of Chemical Physics* **115** (7), 3099 (2001).

[186] B. L. Hemming and D. R. Crosley, *Journal of Physical Chemistry A* **106** (39), 8992 (2002).

[187] J. A. Dodd, S. J. Lipson, and W. A. M. Blumberg, *Journal of Chemical Physics* **95** (8), 5752 (1991).

[188] D. V. Shalashilin, S. Y. Umanskii, and Y. M. Gershenzon, *Chemical Physics* **168** (2-3), 315 (1992).

[189] D. V. Shalashilin, A. V. Michtchenko, S. Y. Umanskii, and Y. M. Gershenzon, *Journal of Physical Chemistry* **99** (30), 11627 (1995).

[190] P. Caridade, J. Sabin, J. D. Garrido, and A. J. C. Varandas, *Physical Chemistry Chemical Physics* **4** (20), 4959 (2002).

[191] L. R. Williams and D. R. Crosley, *Journal of Chemical Physics* **104** (17), 6507 (1996).

[192] U. Rahmann, W. Kreutner, and K. Kohse-Hoinghaus, *Applied Physics B-Lasers and Optics* **69** (1), 61 (1999).

[193] K. L. Steffens and D. R. Crosley, *Journal of Chemical Physics* **112** (21), 9427 (2000).

[194] L. C. Giancarlo and M. I. Lester, *Chemical Physics Letters* **240** (1-3), 1 (1995).

[195] R. L. Schwartz, L. C. Giancarlo, R. A. Loomis, R. T. Bonn, and M. I. Lester, *Journal of Chemical Physics* **105** (23), 10224 (1996).

[196] M. D. Marshall, B. V. Pond, S. M. Hopman, and M. I. Lester, *Journal of Chemical Physics* **114** (16), 7001 (2001).

[197] M. Tsiouris, I. B. Pollack, H. O. Leung, M. D. Marshall, and M. I. Lester, *Journal of Chemical Physics* **116** (3), 913 (2002).

[198] E. L. Derro, C. Murray, T. D. Sechler, and M. I. Lester, *Journal of Physical Chemistry A* **111** (45), 11592 (2007).

[199] C. Murray, E. L. Derro, T. D. Sechler, and M. I. Lester, *Journal of Physical Chemistry A* **111** (22), 4727 (2007).

[200] E. L. Derro, T. D. Sechler, C. Murray, and M. I. Lester, *Journal of Chemical Physics* **128** (24) (2008).

[201] E. L. Derro, T. D. Sechler, C. Murray, and M. I. Lester, *Journal of Physical Chemistry A* **112** (39), 9269 (2008).

[202] C. Murray, E. L. Derro, T. D. Sechler, and M. I. Lester, *Accounts of Chemical Research* **42** (3), 419 (2009).

[203] B. J. Braams and H. G. Yu, *Physical Chemistry Chemical Physics* **10** (21), 3150 (2008).

[204] M. E. Varner, M. E. Harding, J. Gauss, and J. F. Stanton, *Chemical Physics* **346** (1-3), 53 (2008).

[205] M. E. Varner, M. E. Harding, J. Vazquez, J. Gauss, and J. F. Stanton, *Journal of Physical Chemistry A* **113** (42), 11238 (2009).

[206] S. D. Le Picard, M. Tizniti, A. Canosa, I. R. Sims, and I. W. M. Smith, *Science* **328** (5983), 1258 (2010).

[207] J. Klos, F. J. Aoiz, R. Cireasa, and J. J. ter Meulen, *Physical Chemistry Chemical Physics* **6** (21), 4968 (2004).

[208] R. Cireasa, A. Moise, and J. J. ter Meulen, *Journal of Chemical Physics* **123** (6) (2005).

[209] R. Cireasa, M. C. van Beek, A. Moise, and J. J. ter Meulen, *Journal of Chemical Physics* **122** (7) (2005).

[210] A. Moise, R. Cireasa, D. H. Parker, and J. J. ter Meulen, *Journal of Chemical Physics* **125** (20) (2006).

[211] A. Moise, D. H. Parker, and J. J. ter Meulen, *Journal of Chemical Physics* **126** (12) (2007).

[212] K. Schreel and J. J. terMeulen, *Journal of Chemical Physics* **105** (11), 4522 (1996).

[213] K. V. Chance*et al.*, *Journal of Molecular Spectroscopy* **146** (2), 375 (1991).

[214] K. Park, L. R. Zink, K. M. Evenson, K. V. Chance, and I. G. Nolt, *Journal of Quantitative Spectroscopy & Radiative Transfer* **55** (3), 285 (1996).

[215] K. Park, L. R. Zink, K. V. Chance, K. M. Evenson, and I. G. Nolt, *Journal of Quantitative Spectroscopy & Radiative Transfer* **61** (5), 715 (1999).

[216] A. Schiffman and D. J. Nesbitt, *Journal of Chemical Physics* **100** (4), 2677 (1994).

[217] C. S. Parmenter and M. Seaver, *Journal of Chemical Physics* **70** (12), 5458 (1979).

[218] H. M. Lin, M. Seaver, K. Y. Tang, A. E. W. Knight, and C. S. Parmenter, *Journal of Chemical Physics* **70** (12), 5442 (1979).

[219] J. P. Burrows, D. I. Cliff, P. B. Davies, G. W. Harris, B. A. Thrush, and J. P. T. Wilkinson, *Chemical Physics Letters* **65** (2), 197 (1979).

[220] B. Shirinzadeh, D. M. Bakalyar, and C. C. Wang, *Journal of Chemical Physics* **82** (7), 2877 (1985).

[221] S. Williams, L. A. Rahn, and R. N. Zare, *J. Chem. Phys.* **104**, 3947 (1996).

[222] A. Khachatrian, P. J. Dagdigian, D. I. G. Bennett, F. Lique, J. Klos, and M. H. Alexander, *Journal of Physical Chemistry A* **113** (16), 3922 (2009).

[223] A. Khachatrian and P. J. Dagdigian, *Journal of Physical Chemistry A* **113** (47), 13390 (2009).

[224] K. Suma, Y. Sumiyoshi, and Y. Endo, *Science* **308** (5730), 1885 (2005).

[225] D. B. Lawson and J. F. Harrison, *Journal of Physical Chemistry A* **101** (26), 4781 (1997).

[226] S. Benec'h, J. Buldyreva, and A. Chrysos, *Journal of Molecular Spectroscopy* **210** (1), 8 (2001).

[227] H. G. Yu (Personal Communication).

[228] A. S. Pine and J. P. Looney, *Journal of Molecular Spectroscopy* **122** (1), 41 (1987).

[229] A. Alagappan, I. Ballingall, M. L. Costen, K. G. McKendrick, and G. Paterson, *Physical Chemistry Chemical Physics* **9** (6), 747 (2007).

[230] S. Lee, J. Luque, J. Reppel, A. Brown, and D. R. Crosley, *Journal of Chemical Physics* **121** (3), 1373 (2004).

[231] M. H. Alexander, *Journal of Chemical Physics* **111** (16), 7426 (1999).

[232] M. H. Alexander, X. Yang, P. J. Dagdigian, A. Berning, and H. J. Werner, *Journal of Chemical Physics* **112** (2), 781 (2000).

[233] M. Islam, I. W. M. Smith, and M. H. Alexander, *Physical Chemistry Chemical Physics* **2** (4), 473 (2000).

[234] Y. Kim, J. Fleniken, H. Meyer, M. H. Alexander, and P. J. Dagdigian, *Journal of Chemical Physics* **113** (1), 73 (2000).

[235] P. J. Dagdigian and M. H. Alexander (Personal Communication).

[236] M. Islam, I. W. M. Smith, and M. H. Alexander, *Chemical Physics Letters* **305** (5-6), 311 (1999).

Appendix I

Published Papers

1. A. Alagappan, I. Ballingall, M. L. Costen, K. G. McKendrick and G. Paterson, *Phys. Chem. Chem. Phys.*, 9, (2007), 747.

"*Efficiencies of state and velocity-changing collisions of superthermal CN A($^2\Pi$) with He, Ar, N_2 and O_2*".

2. S. Marinakis, G. Paterson, J. Klos, M. L. Costen and K. G. McKendrick, *Phys. Chem. Chem. Phys.*, 9, (2007), 4414.

"*Inelastic scattering of OH ($X^2\Pi$) with Ar and He: a combined polarization spectroscopy and quantum scattering study*".

3. S. Marinakis, G. Paterson, G. Richmond, M. L. Costen, and K. G. McKendrick, *J. Chem. Phys.*, 128, 10.1063/1.2829111.

"*Rotational angular momentum polarisation: the influence of stray magnetic fields*".

4. G. Paterson, S. Marinakis, J. Klos, R. Tobola, M. L. Costen and K. G. McKendrick, *J. Chem. Phys.*, 129, 074304, (2008).

"*Orientation and Alignment Depolarisation in OH($X^2\Pi$)+Ar/He Collisions*".

5. G. Paterson, S. Marinakis, M. L. Costen and K. G. McKendrick, *Physica Scripta* 80, 048111, (2009)

"Depolarisation of Rotational Angular Momentum in Open-Shell Collisions: OH + Rare Gases"

6. G. Paterson, S. Marinakis, M. L. Costen and K.G. McKendrick, *PCCP*, 11, 8804, (2009).

"Depolarisation of rotational orientation and alignment in OH($X^2\Pi$) + Xe Collisions"

7. G. Paterson, S. Marinakis, M. L. Costen and K.G. McKendrick, *PCCP*, 11, 8813, (2009).

"*Depolarisation of rotational orientation and alignment of OH($X^2\Pi$) in collisions with molecular partners: N_2 and O_2"*

8. G. Paterson, S. Marinakis, J. Klos, R. Tobola, M. L. Costen and K. G. McKendrick, *J. Chem. Phys.*, 129, 074304, (2009).

"Erratum: *Orientation and Alignment Depolarisation in OH($X^2\Pi$)+Ar/He Collisions"*

9. M. L. Costen, R. Livingstone, K.G. McKendrick, G. Paterson, M. Brouard, H. Chadwick, Y.-P. Chang, C. J. Eyles, F. J. Aoiz and J. K los., *J. Phys Chem A.*, 113, 15156, (2009).

"Elastic Depolarisation of OH(A) by He and Ar: A Comparative Study"

10. J. J. Kay, G. Paterson, M. L. Costen, K Strecker, K.G. McKendrick, and D. W. Chandler., (Submitted to *J. Chem. Phys.*)

"Direct angle-resolved measurements of collision Dynamics with Electronically Excited Molecules"

Appendix II

Conferences Attended

1. Spectroscopy and Dynamics Discussion Group Meeting, University of Oxford, 2006 (Poster).

2. Gas Kinetics Meeting (in celebration of the career of Prof. Mike Pilling, CBE), University of Leeds, 2007 (Poster).

3. ANUMOCP, University of Leeds, 2007 (Talk).

4. SCOTChem Computational Symposium, University of Glasgow, 2008 (Poster).

5. ANUMOCP, University of Sheffield, 2008 (Talk).

6. Gas Kinetics International Conference, University of Manchester, 2008 (Talk).

7. Spectroscopy and Dynamics Discussion Group Meeting, University of Nottingham, 2009 (Poster).

8. Set for Britain, Houses of Commons, London, 2009 (Poster).

9. SCOTChem Computational Symposium, Heriot-Watt University, 2008 (Poster).

10. Dynamics of Molecular Collisions, Snowbird, Utah, 2009 (Poster).

Appendix III

Courses Attended

1. Optics for Chemists, Postgraduate Lectures (Prof. K.G. McKendrick, Dr. M. L. Costen and Dr. A. Alexander).
2. Optics, Physics UG level 3, (Prof. D. P. Hand and Dr. J. Ebbecke).
3. Spectroscopy and Dynamics, Physics UG Level 3, (Dr J. S. Barton and Dr D. Townsend).
4. Academic Paper Writing, (University of St. Andrew's).
5. Thesis Writing Workshop, (University of Edinburgh).
6. Postgraduate Training Courses (Educational Development Unit, Heriot-Watt University).
7. Departmental Seminars, (Heriot-Watt University).
8. UK National GRADSchool, Windermere (Vitae).